Assessment of needle nitrogen and phosphorus in *Pinus radiata* using functional traits estimated by physically based models and solar-induced fluorescence from airborne hyperspectral imagery

Peiye Li

ORCID ID: 0000-0002-2819-7023

Supervised by

Prof. Pablo J Zarco-Tejada

Dr. Tomás Poblete

A/Prof Jagannath Aryal

Submitted in total fulfilment for the degree of

Doctor of Philosophy

Department of Infrastructure Engineering

Faculty of Engineering and Information Technology

University of Melbourne

Submitted in September 2025

Abstract

Timely and precise detection of nutrient deficiencies in needles, especially nitrogen (N) and phosphorus (P), can facilitate sustainable forestry in *Pinus radiata* D. Don (radiata pines), where the goal is to guarantee sufficient nutrient supply for tree growth and wood production, as well as to avoid detrimental environmental impacts from over-fertilization. Airborne hyperspectral remote sensing provides detailed spectral information of vegetation targets, enabling non-destructive and on-demand monitoring.

Previous studies using airborne narrow-band hyperspectral imagery have shown that plant traits derived from radiative transfer models (RTMs) and far-red solar-induced chlorophyll fluorescence (SIF_{760}) effectively explain the observed variability in leaf N concentrations in crops. However, their contribution to leaf P concentration has not been explored. In Chapter 4, we evaluated the potential of using physiological plant traits derived from airborne narrow-band hyperspectral imagery (Full-Width at Half-Maximum [FWHM] = 5.8 nm) to estimate needle N and P concentrations in radiata pines nutrient trials. We identified four predictors, including needle pigments derived from the RTM, PRO4SAIL2-derived [i.e., chlorophyll *a* + *b* (C_{ab}), carotenoid (C_{ar}), and anthocyanin contents (A_{nth})], as well as SIF_{760}, as most effective predictors both N and P when used as inputs for Gaussian Process Regression (GPR) models, demonstrating the robustness of the physically based modelling approach. Moreover, we observed consistent contributions of the blue spectral region to P estimations but not to N. Chapter 4 revealed the distinct contribution of far-red SIF and the blue spectral region for needle P compared to needle N, opening a new avenue for the physiological assessment of nutrient levels in forest stands using hyperspectral imagery.

Motivated by the findings from Chapter 4, Chapter 5 drew closer attention to SIF evaluation in their contribution to needle nutrient assessment, specifically on the impact of sensor spectral resolution (SR) on the accuracy of airborne SIF retrievals at oxygen absorption features. We evaluated whether sub-nanometer resolution offered significant benefits for SIF applications in needle N and P estimations in radiata pines. The results showed that sub-nanometer resolution did not enhance the predictive contribution of SIF_{760} beyond what its narrow-band counterpart already did for either needle N or P. Uncertainties in SIF retrievals and the lack of validity prevented the assessment of the SIF retrieval accuracy. The further focused analysis of red SIF (SIF_{687}) at the O_2-B band and depths of Fraunhofer lines (FLs), which were only observable under the sub-nanometer resolutions, showed that SIF_{687} lack predictive capability for nutrient

content. Additionally, the depths of far-red FLs contributed more to needle N and P assessment than red FLs. These findings highlight the potential of far-red FLs, which are less affected by atmospheric effects than oxygen absorption bands, as predictors for needle P status.

The application of narrow-band hyperspectral images in operational monitoring is restrained by their high monetary and computational costs, as well as the expertise required for data processing. Multispectral cameras can be a cost-effective alternative for such purposes, though their coarser spectral resolutions and limited spectral coverage restrict their capability to fully capture the subtle spectral changes related to needle nutrient levels. Therefore, it is crucial to select optimized bandsets for the specific objectives. Chapter 6 investigated whether the commercially available 10-band multispectral camera MicaSense Dual System (FWHM = 10-54 nm) was suitable for needle N and P assessment. Furthermore, we adopted a novel clustering-based supervised band selection algorithm to identify optimized bandsets for needle N and P at a 10 nm FWHM. Our results suggest that the narrow-band-based models developed in Chapter 4 consistently outperformed all multispectral-based models. Although no multispectral bandsets could effectively explain the observed variabilities in N, multispectral-based models were better suited for needle P assessment. The newly proposed 12-band bandset, BS12P, outperformed the 10-band bandset of MicaSense for needle P prediction across four datasets, suggesting the potential of the optimised BS12P bandset for developing next-generation multispectral cameras for P assessment.

Overall, this Ph.D. study advanced the physiological interpretation of radiata pine responses to nitrogen and phosphorus variations and demonstrated the effectiveness of hyperspectral remote sensing for nutrient monitoring in coniferous species. The findings contributed to the development of precision forestry in radiata pine plantations, which holds economic significance in Australia and worldwide.

Declaration

I hereby certify that:

i. This thesis comprises only my original work towards the Doctor of Philosophy, except where indicated in the preface.
ii. Due acknowledgement has been made in the text to all other material used.
iii. The thesis is no longer than the maximum word limit in length (1000.000 words), exclusive of tables, maps, bibliographies, and appendices.
iv. The thesis comprises 100% dissertation and 0% creative outputs as agreed by the advisory committee at confirmation.

Peiye Li

Melbourne, September, 2025

Preface

The main chapters of this thesis, Chapters 4-6, are formatted as journal articles. Chapter 4 has been published. Chapters 5 and 6 are intended for future submission, subject to consultation with the supervisors. The underlying research work of the thesis is entirely based on my original contributions during my Ph.D. candidature at the University of Melbourne, including methodology development, formal analysis, and writing. No work was carried out prior to enrolment in the course. No work has been submitted for other qualifications. The research work was supervised by Prof. Pablo J. Zarco-Tejada, Dr. Tomás Poblete, and A/Prof. Jagannath Aryal at the University of Melbourne. The supervision committee member, Dr. Alberto Hornero from the Spanish National Research Council (CSIC), also provided valuable assistance to the thesis.

The research work for this thesis was supported by the Melbourne Research Scholarship funded by the University of Melbourne. I acknowledge the contributions from Peter Hopmans of Timberlands Research Pty Ltd. and Stephen Elms of HVP Plantations for their provision and management of the field trials. Generative AI was used in this thesis to improve clarity and expression. Logs of use, including dates and input text, are available on request.

The publication record of Chapters 4-6 is as follows:

- Chapter 4 (published)

  Li, P., Poblete, T., Hornero, A., Aryal, J., & Zarco-Tejada, P. J. (2025). Distinct contribution of the blue spectral region and far-red solar-induced fluorescence to needle nitrogen and phosphorus assessment in coniferous nutrient trials with hyperspectral imagery. *Remote Sensing of Environment*, 328, 114915.

- Chapter 5 (to be submitted to IEEE Transactions on Geoscience and Remote Sensing)

  Li, P., Poblete, T., Hornero, A., Aryal, J., & Zarco-Tejada, P. J. Evaluation of solar-induced fluorescence using airborne narrow-band and sub-nanometer imagery for needle nitrogen and phosphorus assessment in radiata pine

- Chapter 6 (to be submitted to Agricultural and Forest Meteorology)

Li, P., Poblete, T., Hornero, A., Aryal, J., & Zarco-Tejada, P. J. Comparison of multispectral bandsets vs. hyperspectral data for needle nitrogen and phosphorus assessment in radiata pines.

In addition to the journal articles, outputs from Chapter 4 have also been presented at the following conference:

- Li, P., Poblete, T., Aryal, J., Hornero, A., & Zarco-Tejada, P. J. (2024, July). Contribution of Solar-Induced-Fluorescence for Needle Nitrogen and Phosphorus Prediction with Airborne Hyperspectral Imagery. In IGARSS 2024-2024 IEEE International Geoscience and Remote Sensing Symposium (pp. 7893-7897). IEEE.

Acknowledgement

There were many milestones celebrated during this journey, and now it has finally come to the last one. Before I am rushed to solve the next quest of my life, I'd like to spend some non-scientific words to express my gratitude to those who have supported me over the past four years.

I am deeply grateful to my supervisors, Pablo and Tomas, for all the support and guidance. It was a privilege for me to be part of this novel and challenging research project. Pablo provided invaluable scientific insights into this work and gave me great encouragement and confidence to publish in one of the top remote sensing journals. Tomas taught me everything from the very start and managed the data collection for the project. I am also grateful for his mental support throughout the years. He made the role of supervisor human. Alberto, whom I have never met in person, provided great technical support to the project.

As much as I enjoy my spacious office at Melbourne Connect, I wish I had spent more time with the HyperSens group. I greatly appreciate all the inspiring scientific discussions with Anne, Na, Anirudh and Bowen. I will miss all the drinks and heartfelt talks with Na, Thulasi and Dannielle. I'd also like to thank Olga and Lubna from the Department of Infrastructure Engineering, who supported me like mentors during the hard time. Now, standing at the end of this journey, I also want to thank Zitian, whose encouragement was the very first reason I embarked on my Ph.D. in the first place.

The love and support from my friends and my partner Michael made life more enjoyable, despite all the academic challenges I was facing. They reminded me that my values are beyond academic achievements. My family, who are thousands of miles away, provided me with enormous and unconditional support. I hope I have made them proud.

Finally, I want to thank myself for my resilience and curiosity, for working hard, and for never giving up. I am proud of what I have achieved.

Table of Contents

List of Figures

List of Tables

Chapter 1
Introduction

1.1 Nitrogen and Phosphorus Deficiency in Radiata Pine

Pinus radiata D. Don (radiata pine), native to North America, is now widely planted in the southern hemisphere, including Australia, New Zealand and Chile, as the primary softwood plantation species. In Australia alone, radiata pine plantations cover around 707,000 ha, accounting for almost 70% of the national softwood plantation area and 40% of the total plantation area (Legg *et al.*, 2021b). Radiata pine is a fast-growing species, with a rotation period typically between 30 and 35 years (Forestry Corporation of NSW, 2016). In commercial plantations, radiata pines can grow up to 30 to 45 m high with an annual increment in volume between 16 and 21 m^3/ha per year (Legg *et al.*, 2021b). Its timber has versatile applications, such as construction, furniture making, paper and packaging. In 2023, the total volume of plantation softwood harvested reached 13,740,000 m^3 in Australia, with an estimated gross value of around 1,372 million Australian dollars (ABARES, 2024). Given its significant value as the predominant softwood plantation species, it is critical to properly apply silvicultural practices to maximize the radiata pine wood production.

Radiata pine is a nutrient-demanding species, and its growth is strongly influenced by soil nutrient storage, especially nitrogen and phosphorus (Watt *et al.*, 2005a; Turner and Lambert, 2011; Turner and Lambert, 2017). Studies have shown that the peak nutrient demand of a radiata pine stand can reach 130 and 12 kg/ha per year for nitrogen (N) and phosphorus (P), respectively (Lambert and Turner, 1988). The response of radiata pines to N and P fertilization and other growth-influencing environmental factors has been studied over the past few decades. It has been shown that N fertilization results in an increase of needle number and size, shoot production rate, tree biomass accumulation and stem growth (Nambiar and Fife, 1987b). Furthermore, N and P stress limit the branch growth more than the stem or height growth of radiata pines (Will and Hodgkiss, 1977). Benson *et al.* (1992) also demonstrated that N and water availability were intertwined in facilitating stem growth. Common symptoms of N deficiency include a high root-to-shoot ratio, yellow short needles, shedding of older needles

and thin branching and crowns, while P-deficient trees display similar visual symptoms but are typically characterized by dull green color (Will and Hodgkiss, 1977; Mead, 2013).

However, overfertilization can be detrimental to the environment and counterproductive to the goal of maximizing wood production in radiata pine plantation management. It has been found that increased N supply, and thus leaf N concentrations, is associated with decreased wood density and a lower latewood percentage of radiata pine (Beets *et al.*, 2001b), potentially impacting the quality and value of the wood. There is also the risk of excessive fertilizer runoff, such as nitrate (NO_3^-) and phosphate, into waterways, causing eutrophication (Johnston *et al.*, 2014). Hence, it is critical to detect the needle N and P stress in radiata plantations in a timely and accurate manner and apply fertilizers precisely, for the benefits of wood production and environmental protection.

1.2 Leaf Nutrient Monitoring with Hyperspectral Remote Sensing

Traditional diagnostic approaches for N and P deficiencies usually involve intensive field sampling and laboratory testing for foliage chemistry and pigment contents. Initially proposed by Ulrich and Hills (1967), the critical level method is one of the main diagnostic tools used in forestry. By comparing the measurements against the critical values, the deficiency status could thus be detected. It is critical to follow the standardized sampling procedures for proper comparison with the critical values, which differ for regions. However, the critical value method has major drawbacks, inhibiting large-scale monitoring. First, the representativeness of this method is limited when scaling up to the canopy level or extrapolating to other stands with different ages and conditions (Gregoire and Fisher, 2004; Watt *et al.*, 2019). Second, the sampling and laboratory testing procedure can be laborious and costly.

Conversely, remote sensing technology provides a non-destructive alternative for monitoring leaf nutrients at the operational scale. In particular, hyperspectral remote sensing has gained more attention due to its ability to capture detailed spectral information of the ground target. Hyperspectral imaging spectrometers typically have hundreds of spectral bands with a spectral resolution of less than 10 nm. Several spaceborne hyperspectral imaging spectrometers are in operation to date, such as the dedicated Earth observation satellites EnMAP (Guanter *et al.*, 2015), PRISMA (Cogliati *et al.*, 2021), HySIS (Mahalingam *et al.*, 2019), and DESIS onboard the International Space Station (ISS) (Krutz *et al.*, 2019). However, spaceborne hyperspectral

remote sensing faces limitations, including coarse spatial resolution (usually 10 to 30 m), dependency on revisit frequency, and atmospheric inferences. On the other hand, airborne hyperspectral imagers onboard manned or unpiloted aircraft present the advantages of on-demand flexible image acquisition and sub-meter spatial resolution, which is crucial for vegetation monitoring in heterogeneous canopies.

The basis of using spectroscopy to assess leaf nutrient status lies in how plants utilize the absorbed light energy. When the incident solar radiation reaches the plant, it is either reflected, transmitted or absorbed by pigment systems. Even under unstressed conditions, plants cannot fully utilize the absorbed light energy for photochemistry. As a result, plants need to dissipate the excitation energy through two other pathways: thermal dissipation (i.e., constitutive or regulated) and chlorophyll fluorescence (ChlF). All three pathways compete for the absorbed photosynthetic active radiation (PAR), thus the disturbance in one would affect the others. In literature and the following chapters of the thesis, the term "non-photochemical quenching (NPQ)" is used to refer to the regulated thermal dissipation process that involves photosystems. The term "quenching" represents all the processes that reduce fluorescence emissions (Krause and Weis, 1991; Mohammed *et al.*, 2019). The remote sensing of leaf N status predominantly relies on the fact that the biochemical composition of chlorophyll $a + b$ molecules contains N (Evans, 1989). N deficiency thus affects the chlorophyll content, subsequently the photosynthetic activities, ChlF emission and NPQ. These physiological responses can be reflected by the variations of reflected radiation of plants in specific wavelengths, such as chlorophyll absorption features in the visible to near infrared (VNIR) regions. P, as an essential macronutrient, participates in the formation of starch, cellulose and lignin, which impact the shortwave infrared region (SWIR) of the vegetation spectrum. It has been proven that P deficiency leads to the accumulation of starch in leaves and stems (Qiu and Israel, 1992). However, as these SWIR absorption features are not as apparent and as well studied as the chlorophyll absorption features, the study of leaf P using remote sensing is relatively limited as opposed to N. In the VNIR region, P is indirectly associated with photosynthesis. On one hand, P is a component of chloroplast membrane phospholipids. On the other hand, P plays a role in the photosynthetic electron transport to photosystem I (PSI) as it affects the ATP (adenosine triphosphate) synthase activity (Carstensen *et al.*, 2018).

Remotely sensed hyperspectral data have been widely explored to track leaf N status through either empirical or physically based models. Empirical methods exploit relevant absorption features using either reflectance bands or spectral indices. The most widely used vegetation

index, the Normalized Difference Vegetation Index (NDVI) (Rouse *et al.*, 1974a), has been broadly applied to represent the green biomass of the canopy, thus reflecting on the chlorophyll content. Nevertheless, this index is not a direct proxy for the chlorophyll content, and it is well known that the index saturates at high chlorophyll concentration. Moreover, the interpretation of the index is also confounded by the canopy structural effects and other pigments. Recently, more chlorophyll indices have focused on the red edge region (~670–780 nm) due to its high sensitivity to chlorophyll content. For example, the reflectance ratio between 750 and 710 nm was proposed to approximate chlorophyll content in forest stands and was found to be insensitive to canopy structural and shadow effects (Zarco-Tejada *et al.*, 2002). The chlorophyll red-edge index (CI) was subsequently shown to be insensitive to the effects of leaf thickness and closely related to leaf N status (Clevers and Gitelson, 2013a). Other non-chlorophyll indices have also been applied as stress indicators, including N deficiency. The Photochemical Reflectance Index (PRI) (Gamon *et al.*, 1992a; Gamon *et al.*, 1997b), calculated as the normalized reflectance difference at 531 and 570 nm, has been widely used to monitor plant photosynthetic activities and nutrient levels due to its close linkage with the xanthophyll cycle, an NPQ mechanism activated in plants under stress (Demmig-Adams and Adams III, 1996). Several studies have reported associations between PRI and water stress (Suárez *et al.*, 2009a; Zarco-Tejada *et al.*, 2013c), and leaf nitrogen status (Shrestha *et al.*, 2012; Watt *et al.*, 2020). However, these empirical relationships based on indices may be unreliable for three main reasons. First, indices do not explicitly account for the effects of canopy structure, understory and soil background, and illumination conditions at the time of image acquisition, resulting in potentially unstable prediction performance and limited transferability when applied to other sites and species (Hernández-Clemente *et al.*, 2019b). Second, indices that use only two or three bands are unlikely to capture all the spectral information of the target variable, which may be nonlinearly related to the reflectance spectrum to some extent (Berger *et al.*, 2018). Furthermore, the observed changes in the reflectance signals might be related to multiple properties and confounding factors (e.g., combined pigment and structure), consequently obscuring the true relationship between nutrient status and plant physiological responses.

On the other hand, the physically based approach relying on radiative transfer theory provides more accurate and consistent estimates of the leaf properties that are more closely related to nutrient status than simple spectral signals. Vegetation radiative transfer models (RTMs) simulate light interactions with leaves and canopies. Leaf RTMs describe the optical properties of a single leaf by considering the scattering related to leaf physical properties and absorption

by biochemical content (e.g., pigment, dry matter and water). Canopy RTMs describe directional scattering and absorptions that are related to canopy architecture (e.g., leaf area index [LAI]) and illumination geometry (e.g., solar zenith angle) (Ustin *et al.*, 2009). The coupled leaf-canopy RTMs have been used to interpret top-of-canopy (TOC) signals and to retrieve leaf biochemical properties or canopy structural parameters. As RTMs originally take leaf and canopy parameter values as inputs and output canopy reflectance, the retrieval of parameters such as the leaf chlorophyll content requires the inversion of the model. Previous studies have demonstrated the reliability of RTM-derived leaf chlorophyll content across species. Poblete *et al.* (2025) implemented the inversion of the model PRO4SAIL2 to retrieve needle chlorophyll for radiata pines from airborne hyperspectral images and achieved an estimation accuracy (R^2) of 0.82 when compared to needle chlorophyll measurements in heterogeneous grassland. Similarly, Wang *et al.* (2022) reported a strong correlation between FluSAIL-derived leaf chlorophyll content and their ground-measured counterparts ($R^2 = 0.66$) in almond orchards. Despite all the promising prospects, retrieving leaf biochemical and biophysical parameters from RTMs faces a few challenges. First, the implementation of RTM is computationally expensive. Complex models can provide a more realistic representation of the canopy reflectance, though it is more computationally demanding to invert them. Second, the ill-posed problem of RTM inversion is well known; that is, different combinations of RTM input variables can lead to the same reflectance response (Zurita-Milla *et al.*, 2015). Therefore, it is crucial to choose an RTM that balances the trade-off between canopy representativeness and computational load, and also applies measures to regularise the ill-posed inversion problem.

During the past few decades, Solar-induced Chlorophyll Fluorescence (SIF), which is chlorophyll fluorescence measured under solar illumination, has been widely investigated as an indicator for vegetation photosynthetic functioning and early stress before changes in chlorophyll content or stress-induced symptoms occur. As mentioned previously, photochemistry, NPQ, and ChlF compete for the PAR. This close physiological linkage allows the use of fluorescence to assess photosynthetic activities and to serve as an early indicator of stress. The spectral span of SIF covers the red to near-infrared (NIR) region (650-800 nm), with two maxima in red (F685) and far-red regions (F740), respectively. SIF emission in the red region is mainly attributable to PSII, while both PSI and PSII emit fluorescence in the far-red region. SIF signals superimpose on the reflected radiation, providing an opportunity to retrieve SIF from remotely sensed vegetation spectra. However, SIF retrieval is not trivial. Due to its small signals, the quantification of SIF is sensitive to various factors including atmospheric

interference, illumination conditions, canopy structural effects and sensor characterization. SIF retrieved from different platforms (e.g., ground, airborne and spaceborne) have been proven effective in detecting heat and water stress (Song *et al.*, 2018; Xu *et al.*, 2021; Wang *et al.*, 2023a), biotic stress (Calderón *et al.*, 2013; Zarco-Tejada *et al.*, 2018b; Zarco-Tejada *et al.*, 2021b), predicting leaf nutrient content (Camino *et al.*, 2018a; Camino *et al.*, 2019; Jia *et al.*, 2021; Wang *et al.*, 2022), and gross primary productivity (GPP) (Bacour *et al.*, 2019; Ma *et al.*, 2022; Pierrat *et al.*, 2024). To date, the application of airborne SIF in leaf P assessment has not been extensively investigated, particularly in coniferous species, where the complexity of the canopy structure poses challenges in interpreting the subtle SIF signals.

The promising potential of the combined use of plant functional traits retrieved from RTM, along with innovative indicators such as SIF for leaf N estimation, has been demonstrated in recent studies. Camino *et al.* (2018a) found that the incorporation of SIF improved the leaf N prediction accuracy in wheat, compared with only using functional traits estimated from the model PROSPECT-SAILH. The results from a study in the almond orchard by Wang *et al.* (2022) also showed that the FluSAIL-derived leaf chlorophyll content and airborne far-red SIF as inputs provided an improved leaf N predictive accuracy (R^2 = 0.95), as compared to the performance of the model with only leaf chlorophyll as predictors (R^2 = 0.49). As airborne SIF retrieve accuracy is known to be sensitive to spectral resolution, Belwalkar *et al.* (2022) built leaf N predictive models for crop canopies with PRO4SAIL-derived leaf chlorophyll content and airborne SIF quantified either from narrow-band (FWHM = 5.8 nm) or sub-nanometer resolution (FWHM = 0.1-0.2 nm). The authors reported a slight improvement in prediction accuracy (ΔR^2 = 0.05, ΔRMSE = -0.03 %) for leaf N when the sub-nanometer SIF was used, though they contended that narrow-band resolution is sufficient (R^2 = 0.87, *p*-value < 0.001, RMSE = 0.12 %) to differentiate the relative leaf N level across the site. This physically based modelling approach, which involves plant traits obtained from RTM inversion and SIF as leaf N predictors, has not been evaluated in coniferous species, where the unique and highly heterogeneous canopy structure heavily affects the choice of RTM and SIF retrieval accuracy. Furthermore, despite its importance in plant growth, leaf P estimation has not been investigated using the physically based approach.

From an operational perspective, airborne hyperspectral remote sensing may not be suitable for frequent needle nutrient status monitoring at large scales due to the high monetary and computational costs. Multispectral cameras could be a cost-effective alternative for such purposes. However, the coarser spectral resolution and limited spectral coverage of

multispectral cameras restrict their capability to capture the subtle spectral features induced by nutrient deficiency fully. Therefore, we intend to evaluate whether the commercially available multispectral cameras can provide reasonable needle N and P estimation accuracy, as compared to the hyperspectral-based results. Moreover, we aim to utilize our hyperspectral-based analysis to inform the selection of optimal multispectral bandsets and, consequently, the design of next-generation multispectral cameras, with the specific objective of assessing needle N and P content.

1.3 Motivations and Scope

The broad motivation of this study lies in facilitating sustainable forestry in radiata pine plantations by improving the monitoring of leaf N and P status using airborne hyperspectral remote sensing. We intend to use physically based models to assess the needle N and P variabilities, which could provide a deeper understanding of plant physiology as opposed to empirical approaches based on spectral indices. Utilizing the valuable sub-nanometer hyperspectral imager, we further investigate sub-nanometer SIF and other fluorescence indicators in terms of their contribution to explaining needle N and P variability, as opposed to narrow-band-based SIF products. In addition, considering the need for cost-effective monitoring at operational scales, we explore the potential of multispectral bandsets for estimating needle N and P concentrations, benchmarking against the hyperspectral-based predictive models.

The scope of the Ph.D. study considers the following aspects:

- Nutrient focus: the analysis is restricted to needle N and P assessment. Other macro- and micronutrients are not considered.
- Study area and species: the research is exclusively conducted on a radiata pine nutrient trial located in Durham, Victoria, Australia (see Chapter 3 for more information on the study site). The transferability of the developed models and methodology to other species and locations is beyond the scope of the study.
- Spectral range: The study is focused on the VNIR spectral range (400 – 1000 nm), which reflects the spectral coverage of the hyperspectral and multispectral sensors used. The SWIR region is not considered.

- Platforms: The study focuses on airborne hyperspectral imagery. Applications of ground-based and spaceborne platforms are not addressed.

1.4 Thesis Overview

This Ph.D. thesis comprises seven chapters. Chapter 1 introduces the background, motivations, and scope of the study, providing an overview of the thesis structure. Chapter 2 presents a literature review of current remote sensing approaches for estimating leaf nitrogen and phosphorus concentrations, from which research gaps are identified and research questions are formulated. Chapter 3 describes the study site and presents the field data collection and analysis of needle nitrogen and phosphorus measurements. These field data underpin the analysis of the following three main chapters. Chapters 4, 5 and 6 address the three identified research gaps correspondingly. Finally, Chapter 7 is a synthetic discussion of the major findings, highlighting the contributions, identifying the limitations, and providing recommendations for future research.

Chapter 2
Literature Review

This chapter reviews current hyperspectral remote sensing-based approaches for estimating leaf nitrogen (N) and phosphorus (P) status, including empirical methods and more advanced methods based on radiative transfer modelling (RTM) and solar-induced fluorescence (SIF). It discusses the strengths and limitations of these methods, with a focus on airborne applications and the specific challenges associated with complex coniferous canopies. In addition, it examines the potential of airborne multispectral bandsets for large-scale nutrient monitoring and evaluates strategies for selecting optimal bandsets for needle N and P assessment. The purpose of the review is to identify key research gaps and guide the formulation of the research questions for the Ph.D. study.

2.1 Methods for Leaf N and P Estimation using Hyperspectral data

2.1.1 Empirical methods

Empirical methods rely on assessing reflectance signals (e.g., single spectral bands or spectral indices) as proxies for plant physiological properties, based on their direct relationships with specific physiological parameters. For instance, chlorophyll content can be estimated from reflectance data by exploiting its characteristic absorption features. Given the strong physiological linkage between nitrogen (N) and chlorophyll, chlorophyll indices have been extensively investigated as indicators of leaf nitrogen content in remote sensing applications. Many index designs have taken soil background, shadows and canopy structure into account to improve the chlorophyll estimation accuracy. For instance, the Transformed Chlorophyll Absorption in Reflectance Index normalized by the Optimized Soil-Adjusted Vegetation Index (TCARI/OSAVI) (Haboudane *et al.*, 2004b) combines the chlorophyll index TCARI with the structural index OSAVI. TCARI/OSAVI has been found resilient to disturbance from soil, shadow and non-synthetic woody parts, capable of producing accurate chlorophyll estimation across species (Wu *et al.*, 2008; Poblete *et al.*, 2025). The red-edge region (~670–780 nm) has been found highly sensitive to chlorophyll variations, leading to the development of a few indices in this spectral region. For example, the reflectance ratio between 750 and 710 nm can approximate chlorophyll content in forests with low sensitivity to canopy structural and shadow

effects (Zarco-Tejada *et al.*, 2002). The chlorophyll red-edge index (CI) was subsequently shown to be insensitive to the effects of leaf thickness and closely related to leaf N status (Clevers and Gitelson, 2013a).

As changes in leaf biochemical content usually occur at a later stage of the stress development (Hernández-Clemente *et al.*, 2019b), the use of chlorophyll indices to monitor leaf N status might not be timely enough for the implementation of corrective horticultural measures. In that regard, the Photochemical Reflectance Index (PRI) (Gamon *et al.*, 1992a; Gamon *et al.*, 1997b) tracks the spectral variations around 531 nm, which is associated with the xanthophyll cycle, an NPQ mechanism activated in plants under stress (Demmig-Adams and Adams III, 1996). The xanthophyll cycle involves the de-epoxidation of violaxanthin into antheraxanthin and then zeaxanthin, which contributes to the heat dissipation (i.e., NPQ). The inter-conversion process can be detected in reflectance at 531nm. PRI is related to N and P status in the needles of radiata pine seedlings (Watt *et al.*, 2020) and water-stress conditions in various species (Suárez *et al.*, 2009a; Zarco-Tejada *et al.*, 2013c). The Normalized Phaeophytinization Index (NPQI) (Barnes *et al.*, 1992b; Peñuelas and Filella, 1998) utilizes bands in the blue spectral region to track the changes in phaeophytin content, a product of chlorophyll degradation that happens during plant senescence and under stress conditions. Previous studies have shown the sensitivity of NPQI to biotic stresses across species (Zarco-Tejada *et al.*, 2018c; Zarco-Tejada *et al.*, 2021b; Poblete *et al.*, 2023).

Other empirical methods use reflectance signals or their transformed formats as predictors for leaf nutrient concentrations, including N and P (Mutanga and Kumar, 2007; Ramoelo *et al.*, 2013; Guo *et al.*, 2018; Ye *et al.*, 2020; Lin *et al.*, 2024). Spectral transformation techniques, such as logarithmic transform, first derivative, among others, are applied to improve the signal-to-noise ratio (Li *et al.*, 2018) of the hyperspectral data. In these spectrum-based methods, a band selection strategy is often performed to reduce data redundancy and to retain the bands that are closely related to the target variable (See section 2.2.2 for more details on band selection). The selected set of informative wavelengths is then used as inputs for regression models like Partial Least Squared regression (PLSR) (Ramoelo *et al.*, 2013; Li *et al.*, 2018; Lin *et al.*, 2024), Multivariate Linear Regression (MLR) (Ye *et al.*, 2020), or machine learning (MLs) algorithms (Mutanga and Kumar, 2007; Guo *et al.*, 2018) to predict leaf nutrient concentrations. The spectrum-based empirical modelling approach is often more frequently used when working with the shortwave infrared (SWIR) region than the visible–near-infrared (VNIR) region. This is because the SWIR absorption features associated with protein, starch,

lignin etc, are less characterized than pigment absorption features in VNIR. However, several studies have shown that the significant contribution of SWIR region to leaf N and P estimations (Mutanga and Kumar, 2007; Mahajan *et al.*, 2014; Camino *et al.*, 2018a; Guo *et al.*, 2018; Li *et al.*, 2018). SWIR relates to N as proteins are one of the dominant N-containing constituents, while chlorophyll only accounts for 1.7% of total leaf N (Kokaly *et al.*, 2009b). P is essential for the formation of starch, cellulose and lignin, which affect SWIR spectral responses (Qiu and Israel, 1992).

These index- or spectrum-based empirical methods for leaf N and P monitoring, although computationally efficient, present a few drawbacks. First, they do not explicitly account for the effects of canopy structure, understory and soil background, and illumination conditions at the time of image acquisition, resulting in potentially unstable model performance and limited transferability when applied to other sites. Additionally, spectral indices only use two or three bands, leaving the rest of the spectrum unevaluated. Furthermore, the observed variations in reflectance spectrum represent a combined response to multiple factors (e.g. physiological and structural), which simple empirical methods cannot detangle.

2.1.2 Radiative transfer modelling

Radiative transfer models (RTMs) simulate the interaction between solar radiation and the vegetation target, including absorption, scattering and reflection. Leaf RTMs take the leaf internal structure and biochemical composition into account and generate leaf reflectance and transmittance spectra. Canopy RTMs describe the interaction between vegetation canopy elements and solar radiation, with emphasis on the directional scattering and absorption. Leaf and canopy RTMs can be coupled together for the interpretation of remotely sensed top-of-canopy (TOC) reflectance data at both leaf and canopy levels.

The most extensively evaluated leaf RTM is PROSPECT, developed by Jacquemoud and Baret (1990). PROSPECT uses four inputs to simulate leaf reflectance in the 400 to 2500 nm spectral range: chlorophyll *a* + *b* content (C_{ab}), equivalent water thickness (C_w), dry matter content (C_m) and the leaf mesophyll parameter (N_{mes}). The later version PROSPECT-4 (Feret *et al.*, 2008a) incorporates carotenoid content (C_{ar}). Anthocyanin content (A_{nth}) was introduced in PROSPECT-D (Féret *et al.*, 2017). A more recent version of PROSPECT-PRO (Féret *et al.*, 2021) further breaks down leaf dry matter content into proteins and carbon-based constituents. Another variation, Fluspect (Vilfan et al., 2016), further incorporates the simulation of

chlorophyll fluorescence. Fluspect is further extended to simulate spectral changes associated with xanthophyll cycle, forming Fluspect-Cx (Vilfan *et al.*, 2018). PROSPECT family was initially developed for broad leaves, though recent studies have demonstrated its applicability to coniferous species (Zarco-Tejada *et al.*, 2004; Wang *et al.*, 2018c; Poblete *et al.*, 2025).

One of the most widely used canopy RTM, 4SAIL (Verhoef *et al.*, 2007), simulates the bidirectional canopy reflectance based on the four-stream radiative transfer theory, assuming a homogeneous canopy layer. The model requires inputs of canopy structural parameters (i.e., leaf area index, leaf inclination distribution function), parameters related to viewing geometry, and leaf reflectance and transmittance used as an input from the leaf RTM. The assumption of a uniform canopy makes 4SAIL not suitable for a heterogeneous forest canopy. A later extension 4SAIL2 (Verhoef and Bach, 2007) relaxed this assumption by considering both vertical and horizontal heterogeneity in canopy structures. 4SAIL2 is a two-layer model that treats the canopy as two separate layers to track the vertical gradient in leaves: the green-leaf layer and the brown leaf layer. Two parameters control the spectral effects of the brown layer: the fraction of brown leaf area (fb) and the layer dissociation factor (D). 4SAIL2 also accounts for the canopy by the vertical crown cover percentage (Cv) and tree shape factor (ξ). The former represented the vertically projected crown cover fraction, while the latter was defined as the ratio of crown diameter to the crown height at the crown's center above the ground. Another model, INFORM (Invertible Forest Reflectance Model) (Atzberger, 2000) was initially designed to simulate reflectance at both the leaf and canopy levels. The canopy representation in INFORM requires more detailed inputs, including crown shape, radiance, density and tree height, making the model parameterization challenging. More complex three-dimensional models were developed, such as the voxel-based Discrete Anisotropic Radiative Transfer (DART) model (Gastellu-Etchegorry *et al.*, 2015) and the FLIGHT model (North, 2002), which relies on Monte Carlo simulation of photon transport. These models can provide a realistic representation of the forest canopy, albeit at the expense of high computational cost. In all, the choice of RTM should consider the representativeness of the model to the species under investigation and whether the model can be effectively inverted.

To determine the unknown biochemical and biophysical parameters from reflectance measured by remote sensing platforms, the RTM needs to be inverted (i.e., RTM inversion), to link the observed spectra with the biochemical and structural parameters. There are three commonly used RTM inversion techniques. The first approach is iterative numerical optimisation, where the observed spectrum is iteratively compared to various RTM simulations to minimise the

discrepancy between the two based on certain cost functions. Parameter values of the simulation where the minimum is found are used to represent the retrieved parameters of the observation. Optimization techniques are involved to find the minimum, such as the genetic algorithm (Fang *et al.*, 2003) and the Quasi-Newton algorithm (Jacquemoud *et al.*, 2000). This method is computationally intensive and is likely to converge at a local minimum depending on the optimization algorithm and the convergence criteria used. The second inversion technique is based on look-up tables (LUTs) (Darvishzadeh *et al.*, 2008; Rivera *et al.*, 2013; Duan *et al.*, 2014). RTMs are executed in the forward mode with various combinations of parameters to generate simulated reflectance spectra on a large scale (usually more than 10,000 simulations). Then the inversion is performed by querying the pre-computed LUT to find the simulation that is closest to the observed spectrum based on a cost function, such as root mean squared error (RMSE) between the simulated and observed spectrum. The LUT-based approach is relatively efficient compared to the iterative optimization technique, as the computationally heavy task of LUT generation is completed before the inversion process. However, the retrieval accuracy is shown to be affected by the choice of cost functions (Rivera *et al.*, 2013) and the coverage of the LUT. The third inversion technique combines LUT and machine learning (ML) algorithms, such as Artificial Neural Network (ANN) (Yang *et al.*, 2010; Wang *et al.*, 2022), Support Vector Machines (SVM) (Belwalkar *et al.*, 2022; Poblete *et al.*, 2025) and Gaussian Process Regression (GPR) (Berger *et al.*, 2020; Farmonov *et al.*, 2025). Precomputed LUTs are used to train ML algorithms that take simulated reflectance as inputs and output the biochemical and biophysical parameters. The trained ML models can then be applied to the observed spectrum to retrieve corresponding parameters. Depending on the ML algorithms used, one or more parameters can be retrieved simultaneously. The primary advantage of this LUT-ML hybrid technique is that the trained model can be applied to a different dataset, provided the training LUTs are representative enough. However, the hybrid method highly relies on the training LUT, though larger LUT sizes lead to higher training cost. Regardless of the inversion techniques, RTM inversion is known to be prone to the ill-posed problem, where several different combinations of RTM biochemical and biophysical parameters lead to the same spectral response. In other words, the inversion result is not unique. Different strategies have been proposed to relieve the ill-posed issue. For example, prior knowledge obtained from experiments and literature can be used to constrain the solution. Ecological constraints can be applied to filter out unrealistic solutions (Darvishzadeh *et al.*, 2011; Quan *et al.*, 2017; Wang *et al.*, 2018c). Baret and Buis (2008) provided a detailed review of the regularization techniques for RTM inversion.

RTM inversion has been widely implemented to retrieve leaf pigment content, including chlorophyll (Lu *et al.*, 2021; Wang *et al.*, 2023b; Poblete *et al.*, 2025), carotenoids (Zarco-Tejada *et al.*, 2013e; Miraglio *et al.*, 2020), leaf water content (Riano *et al.*, 2005; Zhu *et al.*, 2019) and the canopy structural parameter LAI (Darvishzadeh *et al.*, 2011; Miraglio *et al.*, 2020; Lu *et al.*, 2021) from hyperspectral images. A higher retrieval accuracy is usually reported for LAI and leaf chlorophyll content than carotenoids, potentially due to the spectrally restricted carotenoid absorption feature and its overlap with other pigment absorption regions. To date, no existing RTMs enable the direct retrieval of leaf nutrient content through inversion, though the RTM-derived plant traits can be used as predictors for leaf nutrient status. In the context of leaf N estimation, two RTM-based strategies have been employed in previous studies: one relies on the N-chlorophyll linkage and the other on the N-protein linkage. With the focus on the VNIR region, the first strategy uses RTM-derived leaf chlorophyll and other biochemical constituents as inputs for ML models to predict leaf N concentration (Camino *et al.*, 2018a; Belwalkar *et al.*, 2022; Wang *et al.*, 2022; Dehghan-Shoar *et al.*, 2023). This strategy has also been successfully applied to detect biotic stress (Zarco-Tejada *et al.*, 2018c; Zarco-Tejada *et al.*, 2021b; Poblete *et al.*, 2023). The second strategy requires coverage of the SWIR region to retrieve leaf protein content from advanced leaf optical models. Leaf or canopy N content is subsequently obtained based on an empirical nitrogen-protein converting factor (Verrelst *et al.*, 2021; Wang *et al.*, 2023b). At present, these strategies have only been attempted for N status evaluation in relatively homogeneous crop and orchard canopies, while their performance for leaf P estimation has not been well understood, especially for highly heterogeneous coniferous canopies.

Compared to empirical methods that depend on reflectance-based proxies, RTM inversion provides direct estimations of plant biophysical and biochemical parameters, thereby rewarding the latter with better physiological interpretability. It should be noted that RTM inversion does not necessarily produce significantly higher retrieval accuracy as compared to empirical methods, as shown in studies on leaf chlorophyll content (Wang *et al.*, 2023b; Poblete *et al.*, 2025) and LAI (Darvishzadeh *et al.*, 2011) estimation. However, RTM-based methods demonstrate the advantages of higher transferability, whereas empirical methods require extensive field measurements for model calibration (Wang *et al.*, 2023b). Cautions should be taken for RTM parameterization to achieve realistic retrievals of plant traits. Measures should be taken to alleviate the ill-posed inverse problem.

2.1.3 Solar-induced fluorescence

The incident solar radiation can be reflected, transmitted, scattered, or absorbed by the vegetation. The absorbed photosynthetically active radiation (PAR) is partially used for photosynthesis, while the remaining is either dissipated as heat or emitted as chlorophyll *a* fluorescence (ChlF) by each photosystem (PSI and PSII) at longer wavelengths. This close linkage between ChlF and other radiation pathways makes ChlF a sensitive indicator of photosynthetic functioning. The spectral span of ChlF covers the red to near-infrared (NIR) region (650-800 nm), with two maxima in red (F_{685}) and far-red regions (F_{740}), respectively. ChlF emission in the red region is mainly ascribed to PSII, while both PSI and PSII emit fluorescence in the far-red region.

ChlF can be measured by active or passive techniques. Active techniques use artificial light to excite ChlF emissions, such as the pulse-amplitude modulation (PAM) technique and the saturation pulse method (Schreiber, 2004). However, active techniques are usually restricted to leaf (e.g., handheld fluorometers) to plant scales (e.g. imaging fluorometers), making them infeasible for large-scale applications. On the other hand, passive techniques retrieve fluorescence parameters under natural solar irradiation conditions. Thus, the passively retrieved ChlF signal is also called solar-induced fluorescence (SIF). SIF can be retrieved using optical sensors deployed on various platforms, including ground-based, airborne, and spaceborne systems. This enables large-scale monitoring of SIF and facilitates the assessment of its spatial variability.

The superimposition of SIF signals on the apparent vegetation reflectance at both leaf and canopy levels was first identified by Zarco-Tejada *et al.* (2000a) and Zarco-Tejada *et al.* (2000b), forming the basis of SIF quantification strategy at the TOC level, as expressed by Eq. 2.1. Assuming a Lambertian surface for the vegetation and neglecting the atmospheric effects, the apparent upwelling radiance L*(λ) signal recorded by a sensor is the combination of the SIF signal F(λ) and the solar radiation L(λ) of the vegetation:

$$L^*(\lambda) = L(\lambda) + F(\lambda) = \frac{R(\lambda)\,E(\lambda)}{\pi} + F(\lambda) \qquad \text{Eq. 2.1}$$

where λ is the wavelength, R is the pure vegetation reflectance, and E is the down-welling irradiance.

However, SIF only account for a small portion of the total reflected radiation - less than 2% and 5.2% of the reflected radiance at 685 nm and 740 nm, respectively (Guanter *et al.*, 2010),

rendering difficulties in decoupling these two signals from remotely sensed hyperspectral data. SIF retrieval methods can be categorized based on whether SIF is retrieved at specific absorption features or the full SIF emission spectrum is obtained. In the first category, telluric and solar absorption features are used to quantify SIF based on the in-filling principle: as the solar incident radiation is significantly attenuated at these narrow spectral regions due to either the telluric or solar atmospheric absorption, the relative contribution of SIF to the reflected radiation becomes more apparent. These absorption features are sometimes collectively referred to as Fraunhofer lines (FLs), although here we use FLs to represent solar absorption features, as opposed to the oxygen absorption features in the telluric atmosphere. The oxygen absorption bands in the telluric atmosphere are commonly used as they are broader and deeper than FLs. Even though the O_2-B absorption band (687 nm) is closer to the SIF emission maximum in the red region (F_{685}), most research utilized the O_2-A band (760 nm) for SIF retrieval (F_{760}) in the NIR region, due to the broader and deeper absorption feature.

Algorithms to retrieve SIF at these absorption features include the Fraunhofer Line Depth (FLD) method (Plascyk and Gabriel, 1975; Damm *et al.*, 2011), spectral fitting method (SFM) (Meroni *et al.*, 2010; Cogliati *et al.*, 2015) and singular value decomposition (SVD) algorithm (Guanter *et al.*, 2013). FLD-based methods are the most extensively applied, due to their simplicity. In these methods, SIF is represented as the normalized difference between the absorption band depth of a non-fluorescent target and that of a fluorescent target. The absorption band depth is measured using the differential absorption technique, which requires calculating the ratio between bands within and outside the absorption feature. The major difference between the standard FLD (sFLD) and its variants, including 3FLD (Maier *et al.*, 2004) and improved FLD (iFLD) (Alonso *et al.*, 2008). The sFLD algorithm requires measurements of the incident irradiance and target radiance of two bands, one reference band and the other within the absorption feature, assuming constant reflectance and fluorescence within the absorption feature. The 3FLD method assumes a linear variation of reflectance and fluorescence over the absorption window and implements linear interpolation using two reference bands, one on the left shoulder and the other on the right shoulder of the absorption window, respectively. However, the assumption of linearity does not technically hold for the spectral shapes of oxygen absorption features, especially for the O_2-B band (Cendrero-Mateo *et al.*, 2019). Further improvements were made for iFLD, which accounts for the non-linear variation within the considered absorption window. Damm *et al.* (2011) and Cendrero-Mateo *et al.* (2019) provided comprehensive assessments of FLD-based methods for SIF retrievals at

oxygen absorption features. Other techniques, such as SFM and SVD, exploit continuous spectral information by mathematically reconstructing the fluorescence and reflectance spectra within the absorption window, allowing a more realistic representation of the spectrally variable reflectance and fluorescence. However, these methods are more computationally demanding and require complex parametrization, as compared to FLD-based methods.

Recent advances in RTM allow the retrieval of the full fluorescence spectrum from model inversion. Several studies employed the SCOPE (Soil Canopy Observation, Photochemistry and Energy fluxes) model (Van der Tol *et al.*, 2009) to study the relationship between SIF and photosynthesis (Zhang *et al.*, 2014; Verrelst *et al.*, 2016; Camino *et al.*, 2019). To simulate TOC SIF, the Fluspect leaf model has been combined with a canopy RTM, such as DART (Regaieg *et al.*, 2025) or FLIGHT (Hernández-Clemente *et al.*, 2017a) model, to account for the canopy scattering and reabsorption effects, as well as the impacts of observation and illumination geometry on the SIF signals. RTM-based SIF full-spectrum retrieval faces the challenges of complex RTM parameterization and high computational load. Moreover, Mohammed *et al.* (2019) notes that spectral information in the visible to near-infrared is required for the canopy model inputs, though dedicated fluorescence sensors with sub-nanometer spectral resolution (i.e., FWHM < 1.0 nm) usually only cover the fluorescence spectral range. This leads to the complication of co-registration of two sensors, spectrally and spatially, if imaging spectrometers are used.

The accurate estimation of SIF, especially from airborne sensors, faces multiple sources of uncertainty. The airborne sensor captures not only the reflected radiation from the ground target but also contributions from adjacent objects and path radiance, all of which are further attuned by atmospheric absorption and scattering before reaching the sensor. The impact of atmospheric absorption and scattering has been identified as the most influential factor on SIF retrieval accuracy (Guanter *et al.*, 2010; Damm *et al.*, 2014). The atmospheric intervention adds noise to the ratio between the reflectance and fluorescence emission within the absorption features, which might be confused with the SIF in-filling effects, especially for oxygen absorption bands. FLs, by contrast, suffer from less atmospheric intervention, though an ultrafine spectral resolution is required to detect these absorption features. There are two groups of atmospheric correction approaches at the oxygen bands for airborne imagery. The first method is empirical, where SIF is normalised by a non-fluorescent target (i.e., a reference board in a bare soil scene) to account for atmospheric effects. The other group hinges on more realistic atmospheric radiative transfer modelling. Canopy structure influences the correct interpretation

of TOC SIF signals, as the emitted leaf fluorescence can be re-absorbed and scattered when escaping the canopy. The re-absorption is significantly stronger in the red SIF more due to its overlap with the chlorophyll absorption region. On the other hand, far-red SIF is scattered more than red SIF (Porcar-Castell *et al.*, 2014). Previous studies (Yang and van der Tol, 2018; Dechant *et al.*, 2020) have suggested that far-red SIF is mainly affected by canopy structure rather than leaf physiology. Malenovský *et al.* (2021a) have identified that the leaf clumping effect is the most influential factor in causing multi-angular anisotropy for both red and far-red SIF.

SIF retrieval accuracy also highly depends on sensor characteristics. Simulation studies (Damm *et al.*, 2011; Julitta *et al.*, 2016) have shown that spectral resolution (SR) and signal-to-noise ratio (SNR) are the most influential factors in SIF retrievals at oxygen absorption features. Coarser spectral resolution and higher noise levels typically result in more erroneous SIF estimates. In particular, the decrease in SR leads to a decrease in the O_2-A band depth and a spectral shift of the minimum radiance toward the longer wavelengths, subsequently, the overestimation of far-red SIF (Damm *et al.*, 2011). The impacts of sensor characteristics and other influencing factors on SIF retrieval accuracy cannot be considered in isolation. Damm *et al.* (2011) evaluated the sensitivity of FLD-based far-red SIF retrievals to various sensor configurations. Their results showed that sFLD produced the least accurate retrievals compared to 3FLD and iFLD at low SR. Additionally, the iFLD method was most sensitive to high noise levels (i.e., low SNR). For FLD-based SIF retrievals, Julitta *et al.* (2016) recommend the use of sub-nanometer resolution (FWHM < 1.0 nm) for the absolute measurement of far-red SIF at O_2-A band and ultrafine resolution (FWHM < 0.5 nm) for red SIF at O_2-B band. However, previous field studies have successfully used narrow-band resolution to estimate SIF in the application of leaf N status evaluation (Camino *et al.*, 2018a; Wang *et al.*, 2022), water stress detection (Camino *et al.*, 2018c) and biotic stress detection (Zarco-Tejada *et al.*, 2018c; Poblete *et al.*, 2020; Zarco-Tejada *et al.*, 2021b). These results question the necessity of retrieving absolute SIF values at sub-nanometer resolution, given the associated large data volume and redundancy.

During the past two decades, SIF has been widely studied as an indicator for vegetation photosynthetic functioning, and thus gross primary productivity and stress conditions. Multiple studies have used SIF retrieved from spaceborne platforms for GPP monitoring in the context of global carbon flux cycle modelling (Damm *et al.*, 2010; Sun *et al.*, 2018; Zuromski *et al.*, 2018; Gao *et al.*, 2021). It has also been demonstrated that SIF is related to heat and water

stress (Song *et al.*, 2018; Xu *et al.*, 2021; Wang *et al.*, 2023a). Others have shown that SIF can be used to detect biotic stress (Calderón *et al.*, 2013; Zarco-Tejada *et al.*, 2021b). Recent studies have demonstrated the promising prospect of combining RTM-derived plant traits and SIF for leaf N estimation. Camino *et al.* (2018a) found that the incorporation of airborne far-red SIF improved the leaf N prediction accuracy in wheat (R^2 = 0.92), compared with only using functional traits (i.e., leaf chlorophyll content, dry matter content, water content) estimated from the PROSPECT-SAILH model (R^2 = 0.68-0.75). Similarly, Wang *et al.* (2022) assessed the leaf N status in the almond orchard. Their results showed that the model with the FluSAIL-derived leaf chlorophyll content and airborne far-red SIF as inputs provided an improved leaf N predictive accuracy (R^2 = 0.95), as compared to the model with only chlorophyll as predictors, which achieved moderate accuracy (R^2 = 0.49). To further investigate the potential of SIF for leaf N estimation, Belwalkar *et al.* (2022) compared the contribution of airborne far-red SIF quantified at narrow-band (FWHM = 5.8 nm) and sub-nanometer (FWHM = 0.1-0.2 nm) resolutions for leaf N estimation in crop fields, when combined with the narrow-band-based PRO4SAIL-derived leaf chlorophyll content as model inputs. The authors reported an improvement in prediction when the sub-nanometer SIF was used (R^2 = 0.93), though they contended that narrow-band resolution is sufficient (R^2 = 0.87) in differentiating various nutrient levels in crops.

The predictive power of the physically based modelling approach, which combines RTM-derived plant traits and SIF, has so far been primarily evaluated for leaf N estimation. The reliability of this method for another critical macronutrient, P, has received little attention. Furthermore, this approach has mainly been applied to homogeneous canopies, such as crops and orchards, while its transferability to more heterogeneous coniferous canopies remains largely unevaluated. Given the demonstrated importance of airborne SIF in leaf N monitoring, more attention should be directed toward assessing the accuracy of SIF retrievals, including the impact of sensor spectral resolution on SIF in the context of leaf N and P estimation.

2.2 Challenges for needle N and P monitoring in coniferous canopy

The correct interpretation of remotely sensed data over coniferous canopies is challenging, due to the unique shapes of needle leaves and the heterogeneous canopy structure. At the leaf level, needles exhibit different optical characteristics from broad leaves. Lukeš *et al.* (2013) assessed the optical properties of broadleaves (i.e., silver birch) and needles (i.e., scotch pine and

Norway spruce) from 300 to 2500 nm. The authors found that the needle transmittance of both coniferous species was lower than the reflectance, while transmittance and reflectance were similar for the broadleaf species. Furthermore, needles displayed significant discrepancies in albedo measured on exposed needles and shaded needles, which was not observed for broad leaves. At the canopy level, the incident radiation light interacts with shoots, bark and understory or soil background. Shoots are the structure formed by the spiral arrangements of needles. It is known that shoots have strong scattering in the backward direction, but little forward scattering in the visible region (Rautiainen *et al.*, 2018).

The specific spectral characteristics of coniferous species, related to the biochemical and physical properties of their needles and canopy, introduce complications into RTM inversion and SIF quantification, which in turn affects the estimation of needle N and P. Most RTMs were developed for broadleaf species, except for LIBERTY (Leaf Incorporating Biochemistry Exhibiting Reflectance and Transmittance Yields) (Dawson *et al.*, 1998). LIBERTY simulates the spectral reflectance and transmittance of conifer shoots, though the model is less widely evaluated than the PROSPECT family, which is preferred for its simplicity and computational efficiency. Despite not being intended for needles, the PROSPECT family has been previously successfully applied to retrieve needle chlorophyll content in Jack pines (Zarco-Tejada *et al.*, 2004) and radiata pine seedlings (Poblete *et al.*, 2025), indicating the potential of other PROSPECT variants for coniferous studies. The complexity of the coniferous canopy also interferes with the retrieval of top-of-canopy SIF signals, considering the fluorescence reabsorption and scattering within the canopy structure.

2.3 From Hyperspectral to Multispectral

2.3.1 The potential of multispectral bandsets for large-scale monitoring

Despite the ability of airborne hyperspectral imagery to capture detailed spectral information with fine spatial resolution (e.g., $\leqslant$1 m), its application for frequent monitoring of leaf nutrient status at large scales is constrained by several factors. First, the cost of the hyperspectral imagers is relatively high, compared to multispectral sensors or RGB cameras. Second, not all hyperspectral imagers are compatible with unmanned airborne vehicles (UAVs) due to the limited UAV payload capacity (Nex *et al.*, 2022). A manned aircraft is required to carry medium-to-heavy-weight hyperspectral imagers, which increases operational costs. There are

UAV-compatible lightweight options, but they are often limited to the VNIR spectral range and have lower radiometric quality and geometric accuracy. Lastly, the processing of large volumes of hyperspectral data requires expertise and significant computational capacity, making it less practical for non-scientific applications. On the other hand, multispectral cameras are more affordable, lightweight, and their data can be easily processed and interpreted. However, multispectral cameras capture less spectral information due to their limited spectral coverage and resolution, leading to concerns that they cannot track the subtle spectral changes associated with nutrient variations.

Many studies have attempted to quantify this potential accuracy loss in plant biochemical and biophysical traits or leaf nutrient estimation when transitioning from hyperspectral to multispectral resolution. Navarro-Cerrillo *et al.* (2014) evaluated the RTM-simulated canopy reflectance spectra with different spectral resolution (Full Width Half Maximum [FWHM] = 30 and 70 nm) for their ability to estimate needle chlorophyll *a* + *b* content in scotch pines (*Pinus sylvestris* L.). Their results from the index-based empirical models showed that coarser spectral resolution led to less accurate predictions ($R^2 \geq 0.70$ vs. $R^2 \leq 0.55$). Similarly, Zhou *et al.* (2022) simulated broad bands (FWHM = 10, 20 and 40 nm) from the obtained airborne narrow-band hyperspectral imagery (FWHM = 2.2 nm) covering the VNIR region and evaluated their performance in estimating leaf N content in potatoes with PLSR models. The authors reported a decreasing trend in model accuracy (i.e., NRMSE from 12.3% to 16.0%) as the bandwidth increases, indicating the need for high spectral resolution to capture N-associated spectral fluctuations. They also evaluated the performance of the bandsets from three commercially available multispectral cameras with four or five bands using the synthetic data derived from the hyperspectral images. Their results demonstrated that the reduced spectral coverage had a significant impact on the model accuracy, with multispectral camera bandsets achieving NRMSE greater than 20%, compared to the 12.3% produced by the hyperspectral-based models. In a study on LAI mapping in a maize field (Guo *et al.*, 2023), the authors collected both hyperspectral (ULTRIS X20 Plus) and multispectral (DJI Phantom 4 UAV, 5 band) airborne imagery and adopted an RTM-based approach to assess the utility of both imagers for LAI estimation. A higher prediction accuracy ($R^2 = 0.86$, NRMSE = 13.71 %) was yielded by the hyperspectral-based model than the multispectral-based one ($R^2 = 0.75$, NRMSE = 10.61 %), highlighting the advantages of hyperspectral data.

Other studies have suggested that hyperspectral data added only limited predictive power for various target parameters, despite its significantly higher computational cost. In their airborne-

based study, Lu *et al.* (2019) compared a hyperspectral image, a simulated three-band image and a simulated five-band red-edge image in the context of canopy chlorophyll content estimation in mixed-species canopy through empirical modelling. Their results showed that the five-band image yielded comparable prediction performance with the hyperspectral image (R^2 = 0.80 vs. 0.81). Nevertheless, the modified three-band image resulted in decreased performance (R^2 = 0.42). A leaf-level study using RTMs, Croft *et al.* (2015) showed that the hyperspectral data does not substantially improve the accuracy of leaf chlorophyll content estimation, compared to the simulated Landsat 5 TM bandset (R^2 = 0.77 and 0.75, respectively).

Therefore, hyperspectral data does not have an absolute advantage over multispectral data, due to the great data redundancy and high noise levels of the former. The extent of potential performance loss associated with the transition from hyperspectral to multispectral resolutions depends on various factors, including the target variable of focus, the species under investigation, the configurations of both hyperspectral and multispectral sensors under evaluation, the modelling methods used and others.

2.3.2 The selection of optimal bandsets

Most commercially available multispectral cameras cover a few key spectral regions, including chlorophyll absorption, the red edge, and the near-infrared regions. These bandsets are versatile, as they generally allow the calculation of widely used indices such as NDVI. Nevertheless, these bandsets are not always optimized for the application of needle nutrient monitoring. Given the economic and environmental significance of vegetation nutrient monitoring, it is practically important to design a multispectral camera with optimized bandsets for this purpose.

Numerous studies have focused on selecting optimal wavelengths for estimating plant biochemical and biophysical traits from hyperspectral data, with the primary motivation of preserving only informative bands and reducing the computational load for the following modelling process. Various supervised band selection (BS) algorithms have been evaluated on either original reflectance spectra or transformed spectra. For example, Li *et al.* (2018) assessed the performance of band selection on leaf N and P estimation in oilseed rape canopy using *in situ* hyperspectral data. The BS algorithm used was based on the variable importance in projection (VIP) scores embedded in PLSR model (Wold *et al.*, 1993). The authors reported a validation accuracy (R^2) of 0.85 and 0.78 from the optimized bandsets for leaf N and P, respectively, slightly lower than the accuracy provided by the full spectrum of hyperspectral

data (R^2 = 0.89 and 0.83), demonstrating the capability of the optimized bandset with less than 10 bands for comparable prediction accuracy and less computational demands than the full spectrum (400–1300 nm). Guo *et al.* (2018) evaluated the leaf P predictive performance of PLSR models built with the full spectrum (350-2500 nm) and those built with the BS-reduced bandset determined through the Monte Carlo-uninformative variable elimination (MC-UVE) algorithm in rubber trees. Their results showed the reduced bandset (493 bands, R^2 = 0.47) outperformed the full spectrum (2150 bands, R^2 = 0.25). Cao *et al.* (2021) investigated different combinations of BS algorithms and modelling algorithms for leaf N content estimation in summer maize. Their results suggest that the performance of the BS-reduced bandsets cannot be determined independently of the modelling algorithms. For instance, the optimized bandset determined by the successive projection algorithm (SPA) yielded an R^2 of 0.53 when used as inputs for the multiple stepwise regression (MSR) model, but an R^2 value of 0.90 was achieved when the PLSR model was adopted.

Overall, the literature shows that BS-optimized bandsets can provide similar or even improved prediction accuracy for leaf nutrient status across species, compared to the full reflectance spectrum. This implies the effectiveness of BS algorithms in removing noise from hyperspectral data and retaining informative wavelengths. However, these commonly used supervised BS algorithms in regression studies cannot fulfil our requirements of selecting bandsets for future multispectral cameras. First, we should only select around 10 bands, as most multispectral cameras typically have 10 or fewer channels. Second, the selected multispectral bandsets should cover all key spectral regions so that they can be used for other tasks, such as index calculation, in addition to N and P estimation. Nevertheless, the sizes of the optimized bandsets produced by these supervised BS algorithms highly depend on both the input spectrum and the BS algorithms used. In other words, the number of bands in the reduced bandset cannot be defined by the user. Moreover, some BS algorithms tend to produce bandsets with clustering patterns in a certain region (Cao *et al.*, 2021).

Another technique for hyperspectral dimension reduction, band clustering, can provide the user with certain control over the size of the optimized bandset. The technique has been widely used in hyperspectral image classification studies (e.g. Martínez-Usó *et al.* (2007); Su *et al.* (2011); Wang *et al.* (2019); Wang *et al.* (2020)) to improve the computational efficiency, but has been rarely explored in a regression context. In a nutshell, band clustering algorithms first group similar bands together to maximize the inter-cluster variance and minimize the intra-cluster variance. Then, one representative band is selected from each group/cluster to form the final

optimized bandset. Certain similarity measures must be chosen, such as Euclidean distance or information theory-based measures (Martínez-Usó *et al.*, 2007). The representative band selection procedure is usually unsupervised. Either the cluster centres or the most informative band determined by information theory (Wang *et al.*, 2018a) are chosen. The state-of-the-art clustering algorithm, the agglomerative clustering algorithm based on Ward's linkage (Martínez-Usó *et al.*, 2007), creates a tree structure by firstly treating each band as an individual cluster and then grouping the two most similar clusters together. The grouping is repeated until the dissimilarity threshold between two clusters is met. The user can control the final number of clusters by specifying the dissimilarity threshold. However, agglomerative clustering can produce discontinuous clusters, that is, bands within the same cluster are not spectrally adjacent to each other. More recent algorithms, such as the Fast Neighbourhood Grouping (FNG) (Wang *et al.*, 2020) and Adaptive Subspace Partitioning Strategy (ASPS) (Wang *et al.*, 2019), account for the spectral continuity by treating the spectral bands as ordered features and assuming adjacent bands have higher similarity. Both FNG and ASPS allow the user to pre-define the number of clusters, thus the size of the final bandset. Nevertheless, the unsupervised representative band selection embedded in most clustering-based algorithms does not guarantee that the most informative bands are retained for specific applications (e.g., leaf N and P estimation).

The aforementioned band selection studies, whether supervised or clustering-based, focused on dimensionality reduction and noise removal of the hyperspectral data. No one has attempted to use hyperspectral data to guide the selection of an optimised multispectral bandset for next-generation multispectral camera development. To achieve this specific goal, we intend to combine band clustering with supervised BS algorithms to identify the most informative bands for needle N and P estimation at a multispectral resolution.

2.4 Research Gaps and Questions

The following research gaps have been identified, and corresponding research questions have been formulated for the Ph.D. study.

Research Gap 1: It has been demonstrated that plant biochemical traits retrieved from RTM inversion, solar-induced fluorescence (SIF) and specific narrow-band hyperspectral indices (NBHI) can provide satisfactory prediction accuracy for leaf N content in broadleaved species using airborne hyperspectral imagery. However, the assessment of this method for quantification of other critical nutrients, such as phosphorus (P), has not been well investigated,

especially for coniferous species, where high-level heterogeneity in canopy structures and the unique needle structure pose challenges to interpreting airborne hyperspectral data.

Research Question 1: To assess the contribution of narrow-band solar-induced fluorescence (SIF) and plant functional traits derived from radiative transfer models (RTMs) for needle N and P estimation in radiata pine using airborne hyperspectral imagery.

Research Gap 2: It is known that the accuracy of SIF retrievals is affected by various factors, including spectral resolution. Previous studies have shown that sub-nanometer resolution (FWHM < 1 nm) is required to retrieve absolute SIF values from airborne platforms. However, high spectral resolution often leads to highly noisy data and heavy data volume. It has been demonstrated that airborne SIF can be quantified in a relative term from narrow-band resolution (FWHM = 5-7 nm), which is sufficient for differentiating various N levels in homogenous crop canopies. Despite this, the impact of the spectral resolution on the airborne SIF retrieval accuracy, particularly in the context of needle N and P estimation in heterogeneous coniferous canopy, remains unexplored. Given that canopy structural effects highly influence SIF retrieval accuracy, it is critical to evaluate whether sub-nanometer resolution is needed for airborne SIF retrievals to enhance the needle nutrient predictions in radiata pine.

Research Question 2: To investigate and compare the impacts of SIF quantified with narrow-band (FWHM = 5.8 nm) and sub-nanometer (FWHM = 0.1-0.2 nm) spectral resolutions for needle N and P prediction in radiata pine using airborne hyperspectral imagery.

Research Gap 3: The high monetary and computational costs of hyperspectral data, as well as the expertise required for data processing, hinder its application in large-scale nutrient mapping. Multispectral cameras can be a more affordable alternative with higher practicality. However, this comes at the expense of reduced spectral resolution and limited spectral coverage, which may limit their ability to accurately capture subtle spectral changes induced by needle N and P variations. The hypothesis is that multispectral bandsets would result in a decrease in needle N and P estimation accuracy, as compared to hyperspectral-based models. Therefore, it is important to quantify the potential performance loss and determine whether the multispectral bandsets can still yield satisfactory needle nutrient estimation accuracy.

Research Question 3: To evaluate the performance of 1) a commercially available multispectral camera and 2) an optimized multispectral bandset for needle N and P estimation in radiata pine, benchmarked against predictive models developed using hyperspectral data.

Chapter 3
Study site and field data analysis

This chapter provides a description of the study site and the field data collection process. It also presents the analytical results of the field data. The subsequent chapters (Chapters 4, 5, and 6) draw upon the same field dataset, with each chapter focusing on the analysis of different airborne images.

3.1 Study Site

The study was conducted in a radiata pine plantation in Durham, Victoria, Australia (37°44'03"S, 143°55'39"E), with an elevation of around 420 m above sea level. This region has an oceanic climate type according to the Köppen classification, characterised by cool winters and warm summers. The mean annual temperature is 12.3 °C, and the mean annual rainfall of 685.6 mm. The region typically has cool winters and warm summers. The dominant soil type, as indicated by the Australian soil classification map, is kurosols, characterised by a dark brown colour. Kurosols are characterised by contrasting textures, featuring a sandy topsoil and acidic clay-rich subsoil. Soil depth is typically between 0.75 m to 1 m at the study site, according to Soil and Landscape Grid of Australia (SLGA).

A nutrient experiment trial covering 3.26 ha was established in 1993 (Fig. 3.1), covering 34 plots in size from 770 m^2 to 1,160 m^2. Nine treatment groups (A, B, …, I) featuring various fertilization levels were replicated three or four times. Treatment A served as the control group, which received no fertilization. Treatments A to F were thinned in 2011, while Treatments G to I were thinned in 2019. Additionally, weed control measures were applied in Treatments B and D at planting.

Phosphorus (P) fertilizer was initially applied to individual trees at varying rates. Two additional rounds of broadcast fertilization with nitrogen (N), phosphorus (P), and biosolids were applied between 1998 and 2019. Over the years, Treatments C and D received 90 kg/ha of N and 100 kg/ha of P. Treatments E, F, G, and H received 72 kg/ha of N and 80 kg/ha of P. Treatment I received N at a rate of 272 kg/ha and P at 157 kg/ha. Finally, 30 t/ha biosolids were

applied to Treatments E and H and 50 t/ha to Treatment F. See Table 3.1 for a summary of fertilization history.

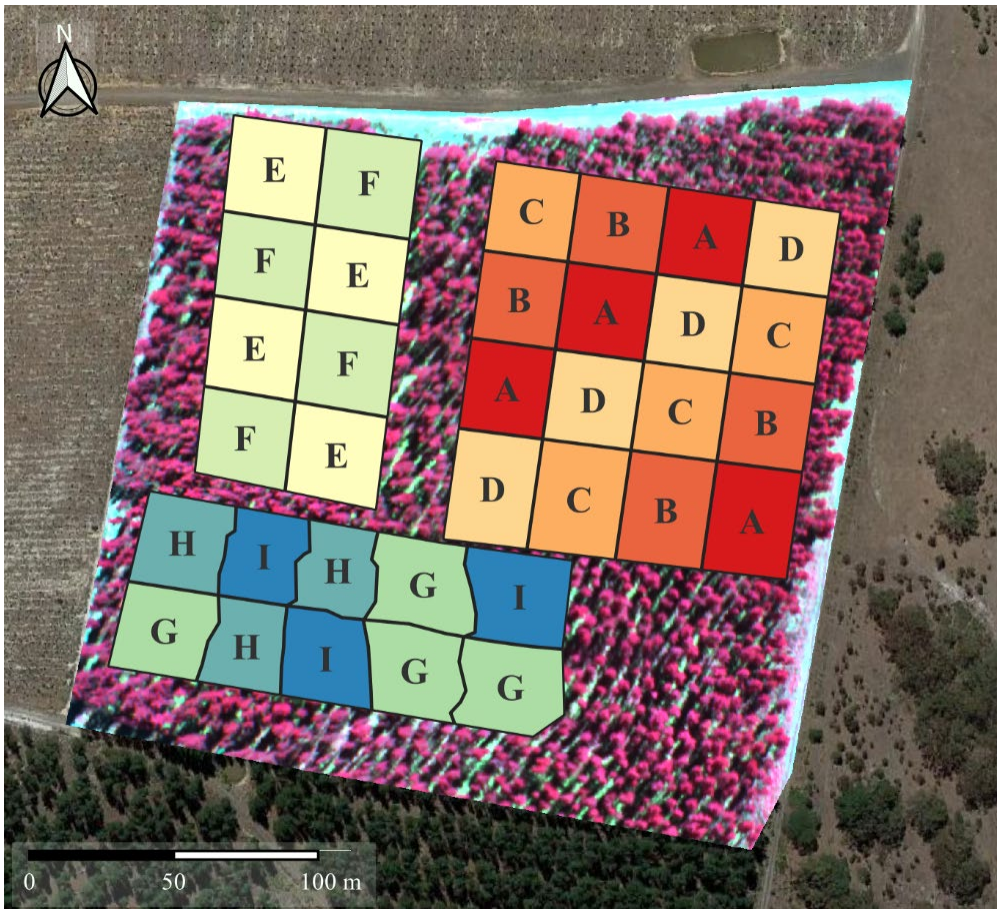

Fig. 3.1. Overview of the study site in Durham, Victoria, Australia in the near-infrared composite. The image was acquired in October 2023 as part of an airborne campaign. Polygons indicate the plot boundaries. Letters A-I represent nutrient treatments.

3.2 Field Data Collection and Analysis

3.2.1 Field data collection

Needle samples were collected from 19 plots in February 2021, and all 34 plots were sampled in October 2021, January 2023, and October 2023. Subsequently, laboratory analyses were conducted to determine needle N and P concentrations. The Dumas method was used for needle N determination (McGill and Figueiredo, 1993). Needle P concentration was measured with inductively coupled plasma optical emission spectroscopy (ICP-OES) on a nitric/hydrogen peroxide digest. One-way ANOVA was performed on ground-measured nutrient data to assess the effects of different treatments. Post-hoc analysis with Tukey's Honestly Significant

Difference at $\alpha < 0.05$ was implemented to determine the pairwise differences among treatment groups.

Table 3.1 Fertilization history for the nine treatment groups from 1993 to 2019. P fertilizers were applied to individual trees in 1993; N, P, and biosolids were applied in 1998/1999 and 2019.

Treatment	1993	1998/1999		2019		
	P (g/Tree)	N (kg/ha)	P (kg/ha)	N (kg/ha)	P (kg/ha)	Biosolids (t/ha)
A	0	0	0	0	0	0
B	100	0	0	0	0	0
C	23	90	100	0	0	0
D	23	90	100	0	0	0
E	22	72	80	0	0	30
F	22	72	80	0	0	50
G	22	72	80	0	0	0
H	22	72	80	0	0	30
I	22	72	80	200	77	0

3.2.2 Field data analysis

The ground-measured needle N and P concentration displayed different levels of variability across treatment groups and dates (Fig 3.2). Plots that received the same level of fertilization maintained a consistent nutrient concentration over the study period (p-value < 0.05 for within-treatment ANOVA).

Needle N concentration ranged from 9.02 to 12.05 g/kg across datasets (Table. 3.2). The highest mean level (13.24 g/kg) and the lowest variability (CV = 0.07) of needle N concentration were observed in the 2021-Feb dataset. The 2023-Oct dataset showed the highest variability (CV = 0.12) and mean value (12.00 g/kg) in needle N observations among four datasets. Overall, needle P measurements displayed higher level of variability (CV = 0.26-0.33) than needle N (CV = 0.07-0.12). The highest mean value of needle N was observed in the 2023-Oct dataset (1.20 g/kg), while the lowest was in the 2021-Oct dataset (0.98 g/kg). Needle P measurements in the 2023-Jan dataset displayed the highest level of variability (CV = 0.33), followed by the 2023-Oct dataset (CV = 0.29), and the two datasets in 2021 (CV = 0.26).

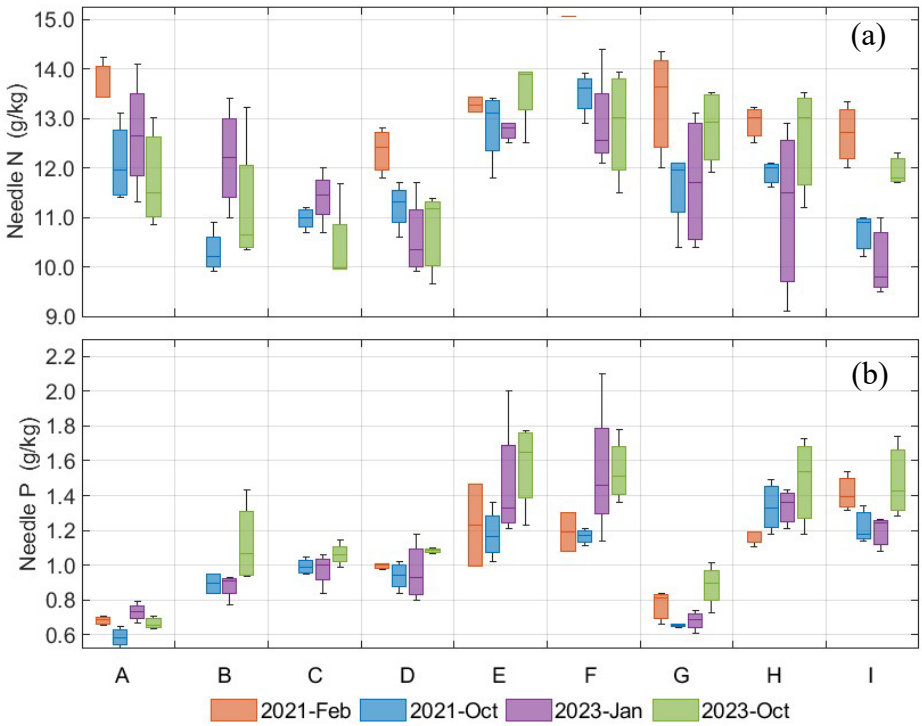

Fig 3.2. (a, b) Variability across dates and treatments for (a) needle N and (b) P concentrations (g/kg) for the four datasets. Over the years, Treatments C and D received 90 kg/ha of N and 100 kg of P. Treatments E, F, G and H received 72 kg/ha of N and 80 kg/ha of P. Treatment I received 272 kg/ha N and 157 kg/ha P. Biosolids were also applied at a rate of 30 t/ha to Treatments E and H and 50 t/ha to Treatment F.

Within each dataset, needle N and P measurements showed significant differences (p-value < 0.05) across treatment groups, reflecting the various fertilization levels. However, post-hoc analysis using Tukey's honestly significant difference procedure (See Appendix 3 Table A3.1 and Table A3.2) revealed a lack of pairwise variability in needle N concentration in the 2023-Jan and 2023-Oct datasets. Only one pair of treatments differed significantly from each other (p-value < 0.05) in N measurements for the 2023-Jan dataset, and two pairs for the 2023-Oct dataset. Therefore, the variability in N concentration in the remaining treatment groups in these two datasets was limited despite their different fertilization levels.

Table. 3.2 Summary of needle N and P measurements from four individual datasets and the combined dataset.

Dataset	Sample size *n*	Needle N (g/kg)				
		Mean	Min.	Max.	Std[a]	CV[b]
2021-Feb	19	13.24	11.80	15.06	0.94	0.07
2021-Oct	34	11.71	9.90	13.90	1.11	0.10
2023-Jan	34	11.79	9.10	14.40	1.31	0.11
2023-Oct	34	12.00	9.02	14.24	1.46	0.12
All	119	12.05	9.02	15.06	1.34	0.11
		Needle P (g/kg)				
		Mean	Min.	Max.	Std[a]	CV[b]
2021-Feb	19	1.05	0.65	1.54	0.28	0.26
2021-Oct	34	0.98	0.52	1.49	0.25	0.26
2023-Jan	34	1.07	0.61	2.10	0.35	0.33
2023-Oct	34	1.20	0.64	1.78	0.34	0.29
All	119	1.08	0.52	2.10	0.32	0.30

[a] The unit of standard deviation (Std) is (g/kg)
[b] The coefficient of variation (CV) is unitless

Chapter 4
Distinct contribution of the blue spectral region and far-red solar-induced fluorescence to needle nitrogen and phosphorus assessment in coniferous nutrient trials with hyperspectral imagery

Highlights

- SIF and RTM-derived traits effectively explained needle N and P variability across four independent datasets collected over three years.
- SIF yielded the most critical contribution among traits to explain the variability in needle P.
- RTM-derived Cab was the most important contributor when accounting for the variability in needle N.
- The blue spectral region was revealed to be sensitive to variability in needle P but not N.

Abstract

Accurate monitoring of plant nutrient status, especially nitrogen (N) and phosphorus (P) content, via remote sensing can facilitate precision forestry, with environmental and management benefits. In previous studies, plant traits derived from hyperspectral data via radiative transfer models (RTMs) and solar-induced chlorophyll fluorescence (SIF) effectively explained the observed variability in leaf N concentrations in crops. However, their contribution to leaf P concentration is unknown. Furthermore, such an approach might not be

transferrable to coniferous stands, which are structurally complex and heterogeneous. We evaluated the potential of using physiological plant traits derived from airborne hyperspectral imagery to explain the observed variability in needle N and P concentrations in *Pinus radiata D. Don* (radiata pine) with four datasets collected over three years in established nutrient trials. RTM-derived data on pigment content in needles, including chlorophyll *a+b* (C_{ab}), carotenoid (C_{ar}), and anthocyanin contents (A_{nth}), as well as SIF quantified at the O_2A absorption band (SIF_{760}), explained variability in N (R^2 = 0.67–0.97 and NRMSE = 0.07–0.30) and P concentrations (R^2 = 0.60–0.95 and NRMSE = 0.09–0.27) in needles. Although C_{ab} was the most important predictor of needle N concentration (ranking C_{ab} > A_{nth} > SIF_{760} > C_{ar}), SIF_{760} contributed the most to explain the variability of needle P concentration (SIF_{760} > A_{nth} > C_{ab} > C_{ar}). Moreover, the blue spectral region was essential for assessing P but not for explaining N variability in needles. Among all reflectance-based indices and inverted traits evaluated, the blue indices best explained the variability in needle P concentration, followed by C_{ab}, C_{ar}, and A_{nth}. The study revealed the distinct contribution of far-red SIF vs. the blue spectral region for needle P compared to needle N, describing new insights for the physiological assessment of nutrient levels in forest stands using hyperspectral imagery.

4.1 Introduction

Pinus radiata D. Don (radiata pine) is the dominant softwood species in plantation forests of Australia and worldwide, accounting for 69% of the total area of softwood plantations in Australia (Legg *et al.*, 2021a). Soil nitrogen (N) and phosphorus (P) concentration are key factors limiting radiata pine growth (Will and Hodgkiss, 1977; Watt *et al.*, 2005b). N and P deficiencies lead to reduced wood production and thus economic losses. However, the excessive application of N and P fertilizers is costly and environmentally harmful (Fields, 2004; Chen *et al.*, 2022). The timely and accurate monitoring of nutrient status in pine is vital for precision forestry and sustainability. Standard methods for assessing the nutritional status of pine trees rely on destructive sampling of needles and biochemical analysis in the laboratory, which is laborious and impractical for large-scale monitoring. Alternatively, advanced imaging spectroscopy provides non-destructive, efficient nutrient monitoring and mapping in forest stands (Wessman *et al.*, 1988; Smith *et al.*, 2002; Smith *et al.*, 2003; Townsend *et al.*, 2003; Martin *et al.*, 2008; Sims *et al.*, 2013).

Most spectral-based methods for leaf N estimation rely on chlorophyll-related indices, as N is a major component of chlorophyll protein complexes (Evans, 1989). Variations in chlorophyll levels can be captured based on fluctuations in its absorption features in the blue and red regions (McConnell *et al.*, 2010). The red-edge region (~670–780 nm) has been widely exploited due to its high sensitivity to chlorophyll. For example, the optical index R_{750}/R_{710} was proposed as an indicator of chlorophyll content that is robust in regard to the effects of canopy structure and shadows in forest stands (Zarco-Tejada *et al.*, 2001). The chlorophyll red-edge index (CI) proposed by Gitelson *et al.* (2003) was subsequently shown to be insensitive to the effects of leaf thickness and closely related to leaf N status (Clevers and Gitelson, 2013b). Nevertheless, upscaling indices to the canopy level introduces complexities due to soil background effects, canopy structure, and non-vegetation components (Haboudane *et al.*, 2002; Homolová *et al.*, 2013; Croft *et al.*, 2014). Combined indices were therefore proposed to accommodate such factors by integrating physiological and structural indices, such as the Transformed Chlorophyll Absorption Index (TCARI) normalized by the Optimized Soil-Adjusted Vegetation Index (OSAVI) in the form of TCARI/OSAVI (Haboudane *et al.*, 2002; Eitel *et al.*, 2008). However, the performance of such indices in estimating chlorophyll content is poorer in conifers than in broadleaf crop species due to the increased complexity and heterogeneity of the canopy structure and background effects in coniferous stands (Croft *et al.*, 2014). Another limitation of using chlorophyll indicators to assess leaf N concentration is saturation that occurs at high chlorophyll and high LAI levels (Wu *et al.*, 2008), hindering the accurate quantification of variations in chlorophyll content in well-managed crop and forest canopies.

Radiative transfer modelling (RTM) provides a robust alternative to chlorophyll indices for leaf N assessment by quantifying several leaf and canopy traits concurrently, exploiting the full spectrum rather than individual spectral bands and indices (Ustin *et al.*, 2009). RTMs can also account for the effects of canopy and soil background when interpreting top-of-canopy (TOC) reflectance (Meroni *et al.*, 2004). Most recent studies have adopted a hybrid approach to leaf N assessment—using plant functional traits derived by RTM inversion, e.g., equivalent water thickness (C_w), dry matter content (C_m), chlorophyll *a* + *b* content (C_{ab}), carotenoid content (C_{ar}), anthocyanin content (A_{nth}), and leaf area index (LAI) to build models to predict leaf N through an empirically-based framework. Wang *et al.* (2018b) used leaf protein content derived from the coupled PROSPECT-5 (Feret *et al.*, 2008b) and INFORM (Schlerf and Atzberger, 2006) model to predict leaf N based on canopy reflectance, achieving a prediction accuracy (R^2) of 0.64 in mixed-species forests. Camino *et al.* (2018b) demonstrated a strong relationship

between leaf N and functional traits retrieved from the coupled PROSPECT (Jacquemoud and Baret, 1990) and SAILH (Baret *et al.*, 1992) models in wheat (*Triticum aestivum*), which yielded an R^2 between 0.68 and 0.75. Although these results are promising, they are inconsistent across species regarding model choice and the selection of functional traits as indicators to explain the variability in leaf N concentration. Hence, whether this physical–empirical hybrid modelling method could be used to estimate N concentration in the needles of coniferous species requires further study to evaluate its performance and the relative contributions of the traits to explaining the variability in N concentration. Increasing efforts have focused on developing advanced models for the early detection of stress before symptoms become visible (e.g., decreases in pigment content), in order to avoid further irreversible damages such as stunt growth and yield loss. These methods rely on detecting subtle changes in photosynthetic pigment concentrations and structures by tracking radiation pathways of vegetation–light interactions (i.e., photochemistry, chlorophyll fluorescence and heat dissipation) (Hernández-Clemente *et al.*, 2019a). Even under unstressed conditions, plants absorb more radiation than they can utilize for photosynthetic activities. The excessive energy is dissipated through non-photochemical quenching (NPQ) (Müller *et al.*, 2001) or re-emitted as solar-induced chlorophyll fluorescence (SIF) (Mohammed *et al.*, 2019). When abiotic and biotic stress further restrict photosynthetic metabolism, the rates of NPQ or SIF emissions vary correspondingly, thus serving as indicators of disturbed photosynthetic activity (Müller *et al.*, 2001; Krause and Jahns, 2004). In the context of needle nutrient assessment, given that N and P are both essential for photosynthesis (Evans, 1989; Carstensen *et al.*, 2018), the nutrient deficiency would consequently disturb the partitioning of absorbed light energy and the light absorption process.

The Photochemical Reflectance Index (PRI) (Gamon *et al.*, 1992b; Gamon *et al.*, 1997a) has a close linkage with the xanthophyll cycle, an NPQ mechanism activated in plants under stress (Demmig-Adams and Adams, 1996). The xanthophyll cycle involves the inter-conversion between violaxanthin and its de-expoxidized state: antheraxanthin and then zeaxanthin, which contributes to the heat disspation (i.e., NPQ). This inter-conversion process can be detected in reflectance at 531nm, which is used for PRI calculation (Gamon *et al.*, 1997a). It has been proven that PRI is closely related to N and P status in the needles of radiata pine seedlings (Watt *et al.*, 2020) and is sensitive to water-stress conditions in olive and peach (Suárez *et al.*, 2009b), grapevine (Zarco-Tejada *et al.*, 2013d), and other crop species. However, PRI is sensitive to canopy structure, other leaf pigments, and illumination conditions (Peguero-Pina

et al., 2008; Suárez *et al.*, 2008; Hernández-Clemente *et al.*, 2011). To account for these effects, different variations of PRI indices were proposed. For instance, Garrity *et al.* (2011) multiplied PRI by the Chlorophyll Index (CI) (Gitelson *et al.*, 2003) to cancel the effect of chlorophyll on PRI and obtained an accurate estimation of carotenoid content. With the aim of eliminating the canopy effects on PRI quantification, Hernández-Clemente *et al.* (2011) proposed various PRI modifications (PRI_m) with different reference wavelengths. PRI_{m1} was found less sensitive to changes in canopy structure compared to PRI and highly related to water-stress indicators such as stomatal conductance. A normalized PRI (PRI_n) was developed by Zarco-Tejada *et al.* (2013d) to account for both canopy and pigment effects simultaneously. The authors observed a strong relationship between PRI_n and Crop Water Stress Index (CWSI) (Jackson *et al.*, 1981), a thermal indicator of water stress.

SIF has also been widely used as a pre-visual diagnostic tool for stress detection, as it competes with photosynthesis and NPQ for absorbed radiation (see Ač *et al.* (2015), Meroni *et al.* (2009), and Mohammed *et al.* (2019), for comprehensive reviews). SIF signals originating from chlorophyll *a* exhibit two peaks, in the red (685 nm) and far-red region (740 nm), respectively. Chlorophyll fluorescence can be used to track water stress (Pérez-Priego *et al.*, 2005; Zarco-Tejada *et al.*, 2009; Zarco-Tejada *et al.*, 2013b; Xu *et al.*, 2021) and nutrient levels (Corp *et al.*, 2003; Sun *et al.*, 2020). Airborne SIF improved the assessment accuracy of leaf N concentration in wheat (Camino *et al.*, 2018b) and almond (Wang *et al.*, 2022) when SIF was included along with RTM-based chlorophyll content in models that explain the observed variability in leaf N concentration. However, whether such methods can be used to estimate nutrient status in radiata pine in light of the multiple uncertainties faced with SIF quantification, especially the anisotropy of the canopy, has not been evaluated. Due to the overlap of the SIF emission spectrum with the chlorophyll absorption spectrum, the emitted fluorescence is re-absorbed and scattered by leaves (Porcar-Castell *et al.*, 2014; Hernández-Clemente *et al.*, 2017b). Malenovský *et al.* (2021b) used model simulations to investigate the impact of canopy structure on canopy SIF. They concluded that the multi-angular anisotropy of SIF in both red and far-red regions was related to the leaf-clumping effect, canopy density, and non-wood parts in heterogeneous forest stands. Hence, canopy anisotropy should be accounted for to decouple SIF signals from the apparent reflectance spectrum, especially for heterogeneous canopies such as coniferous stands.

Research on another important nutrient element, leaf P, using remotely sensed data is much more limited, although P plays a key role in plant growth (Will & Hodgkiss, 1977). The lack

of absorption features and the low levels of this nutrient lead to lower prediction accuracy (Watt *et al.*, 2019). Most studies assessing leaf P concentration have relied on empirical methods in which reflectance data or its transformed forms are used as inputs for partial least-squares regression (PLSR) models (Pimstein *et al.*, 2011; Ramoelo *et al.*, 2013; Li *et al.*, 2018), with neural networks (Mutanga and Kumar, 2007) yielding a moderate estimation accuracy (R^2 of 0.42 to 0.80). Despite the inconsistency in the reported spectral wavelengths for leaf P estimation and the different numbers of model inputs among these studies, red-edge, near-infrared (NIR), and shortwave infrared (SWIR) regions are usually selected as potential indicators for leaf P. Nevertheless, these empirically-based nutrient modelling methods suffer from the lack of transferability to other datasets. In this study, we explored plant parameters retrieved from airborne hyperspectral imagery to explain the observed variability in needle N and P concentrations using four datasets collected across three years in radiata pine nutrient trials. We evaluated the contributions of functional traits, such as SIF emission and RTM-derived biochemical constituents, for N and P assessment. We also quantified the contributions of spectral traits related to the blue spectral region (400 to 500 nm), revealing the different relative importance of blue-related traits and indices to explain the variability in needle N and P concentrations.

Several studies have attempted to predict N and P using hyperspectral data (Mutanga and Kumar, 2007; Wu *et al.*, 2008; Pimstein *et al.*, 2011; Ramoelo *et al.*, 2013; Abdel-Rahman *et al.*, 2017; Li *et al.*, 2018; Siedliska *et al.*, 2021a; Liu *et al.*, 2023). Nevertheless, the present study's novelty lies in the application of RTM-derived functional traits combined with SIF for explaining the variability of needle N and P in a coniferous nutrient trial. Such an approach has been previously proven successful in agriculture for leaf N status assessment (Camino *et al.*, 2018b; Belwalkar *et al.*, 2022; Wang *et al.*, 2022) although the investigation of SIF and the blue region for needle P variability assessment has not been carried out. This is the first attempt to adopt such a physically based modelling approach to explain the variability of needle P in a nutrient trial across years, as the majority of studies on leaf P still rely on empirical modelling without a detailed assessment of the physiological traits that are more sensitive to needle P deficiency.

4.2 Methods

4.2.1 Airborne data collection and processing

Narrow-band hyperspectral images (Fig. 4.1a) were acquired concurrently with field sampling on February 2, 2021, October 27, 2021, January 11, 2023, and October 2, 2023 under clear sky at solar noon using a line-scanning hyperspectral sensor onboard the piloted Cessna-172 aircraft operated by HyperSens Laboratory, the University of Melbourne's Airborne Remote Sensing Facility. The hyperspectral imager acquired 358 bands covering the 400–1000 nm spectral region with a full width at half-maximum (FWHM) of 5.8 nm and an angular field of view (FOV) of 66° (Headwall Photonics, Fitchburg, MA, USA). The images were collected at 350 m above ground level (AGL), resulting in a spatial resolution of 0.2 m. Radiometric calibration was performed in an optics laboratory using a CSTM-USS-2000C integrating sphere (Labsphere, XTH2000C, Labsphere Inc., North Sutton, NH, USA) to convert digital numbers to radiance. We used the irradiance simulated by the SMARTS model (Gueymard, 1995a) to perform the atmospheric correction on the radiometrically-calibrated imagery. The SMARTS model simulated the downwelling irradiance by simple transmittance parameterizations, accounting for various atmospheric extinction process, including Rayleigh scattering, aerosol extinction, the absorption by Ozone, Nitrogen dioxide, water vapor and mixed gas. The required meteorological inputs for the SMARTS model, including relative humidity and air temperature, were acquired from the nearest weather station. The aerosol optical depth at 550 nm was measured using a Microtops II Sunphotometer (Solar Light Co., Philadelphia, PA, USA) during the airborne campaigns. Image orthorectification was carried out using PARGE software (ReSe Applications Schlapfe, Wil, Switzerland): the inputs were recorded by the onboard inertial measuring unit (VN-300-VectorNav Technologies LLC, Dallas, TX, USA) and synchronized with the hyperspectral imager.

Image segmentation was applied to the reflectance imagery to identify pure vegetation pixels and to delineate individual tree crowns (Fig. 4.1b) using Fiji software (Abràmoff *et al.*, 2004). Local thresholding algorithms were first applied to a NIR band (810 nm) and a structural index layer (NDVI > 0.6) in combination to separate the sunlit vegetation pixels from the soil background and within-crown shadows. The identified vegetation pixels were clustered to each object (i.e., individual tree crowns) using the watershed object-based approach with Euclidean distance (as in Zarco-Tejada *et al.* (2018a)). Delineated tree-crown polygons were then reduced by 75% to account for the high heterogeneity in the coniferous stands and the sensitivity of pigment and SIF to illumination conditions. In addition, spectral binning (binning factor = 3) and spectral smoothing with the Savitzky-Golay algorithm (Savitzky and Golay, 1964) were applied to the tree-crown reflectance to increase the signal-to-noise (SNR) ratio. The mean

reflectance and radiance of the tree-crown pixels belonging to the same plot were used to represent the plot-level spectral information. The segmentation results are illustrated in Fig. 4.1c and Fig. 4.1d.

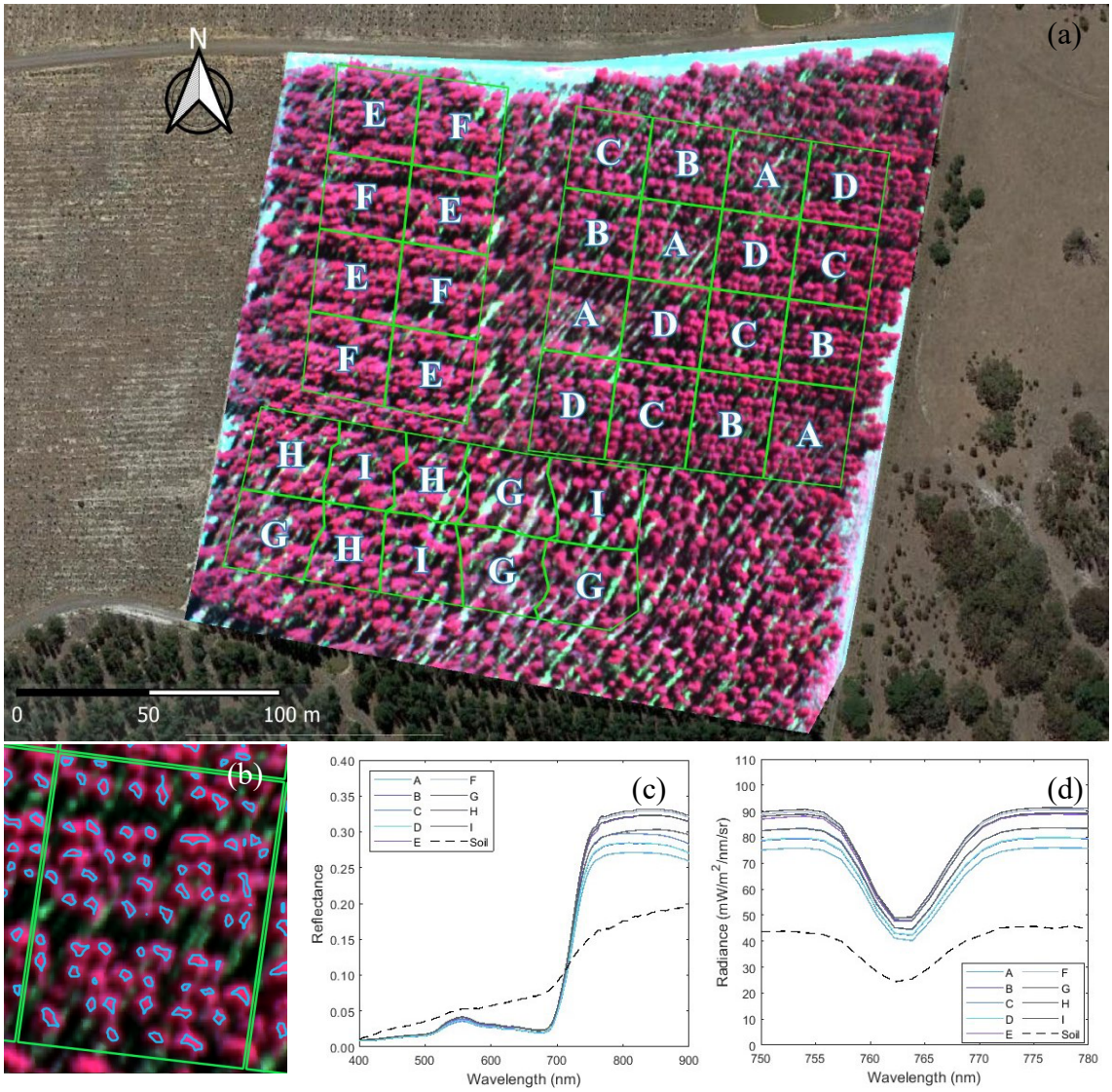

Fig. 4.3. Overview of the study site in Durham, Victoria, Australia in the near-infrared composite. The image was acquired in October 2023 as part of an airborne campaign. Green polygons indicate the plot boundaries. Letters A-I represent nutrient treatments. (b) Example of segmented tree crowns. (c, d) The reflectance (c) and radiance spectra (d) of different scene components: soils (black dashed lines) and average vegetation spectra of the nine treatment groups (solid lines).

4.2.2 Plant trait retrieval by PRO4SAIL2 model inversion

The two-layer RTM PRO4SAIL2 model, which couples PROSPECT-D (Féret et al., 2017) and 4SAIL2 (Verhoef and Bach, 2007), was employed to retrieve the biochemical and structural parameters of needles from pure tree crowns, including needle C_{ab}, C_{ar}, and A_{nth} and LAI. The choice of RTM was made based on two considerations: how realistic the model simulations represented the canopy architecture and whether the model could be efficiently inverted. Single-layer models like SAIL treat the canopy as homogeneous, which could not realistically represent coniferous canopies. Its updated version 4SAIL2 instead considers both the vertical and horizontal heterogeneity in the canopy. In a recent study conducted on radiata pines (Poblete et al., 2025), the authors compared the needle chlorophyll *a* + *b* retrieval accuracy from PRO4SAIL and PRO4SAIL2 inversion and concluded that the latter was more accurate due to the consideration of crown-level clumping effects in 4SAIL2 model. More complex three-dimensional models can provide more comprehensive descriptions of forest canopies, such as the voxel-based Discrete Anisotropic Radiative Transfer (DART) model (Gastellu-Etchegorry et al., 2004) and the FLIGHT model (North, 1996) based on Monte Carlo simulation of photon transport. However, the parametrization and inversion of these three-dimensional model could be rather difficult and computationally expensive.

The selected 4SAIL2 model, which simulates the canopy as two separate layers, was initially designed to account for the vertical gradient in leaves (Verhoef and Bach, 2007). In the evergreen coniferous stands investigated in this study, the second layer represented the understory. Two parameters were varied to track the spectral effects of the understory layer: the fraction of brown leaf area (f_b) and the layer dissociation factor (D). Additionally, the canopy clumping effects were accounted for by the vertical crown cover percentage (C_v) and tree shape factor (ξ). The former represented the vertically projected crown cover fraction, while the latter was defined as the ratio of crown diameter to the crown height at the crown's center above the ground. The soil background was considered a non-Lambertian surface in the integrated RTM. These clumping parameters were then used to modulate the optical quantities of the canopy layer so that they could approximate the heterogeneous canopy. Soil scattering effects were simulated by a Bidirectional Reflectance Distribution Function (BRDF) model. Additionally, the effect of soil moisture on soil reflectance was accounted for by the soil moisture parameter ranging between 0 and 1. The interaction between the soil background and the canopy layer was integrated using the four-stream adding method. In our study, we used the 4SAIL2-based soil reflectance and adjusted the value of the soil moisture parameter for each dataset.

PRO4SAIL2 was inverted using a look-up-table (LUT)-based approach in the wavelet domain (Suárez *et al.*, 2021). For each dataset of plot-mean reflectance, a LUT with 500,000 simulations was generated, where parameter values were randomly drawn from the uniform distribution within the pre-defined ranges. Parameter ranges (Table 4.1) were adjusted so that the simulated spectra enclosed the observed spectra and the median of simulated spectra was close to the median of observed spectra where the closeness was assessed based on RMSE values. Some parameter values were fixed to reduce the potential for multiple solutions. For example, Fig. 4.2 shows the agreement between simulated and observed reflectance spectra for the 2023-Oct dataset. Original simulated reflectance (400 to 2500 nm, FWHM = 1 nm) was then resampled to match the spectral characteristics of the hyperspectral imager (400–1000 nm, FWHM = 5.8 nm) using a Gaussian convolution method (Belwalkar *et al.*, 2022).

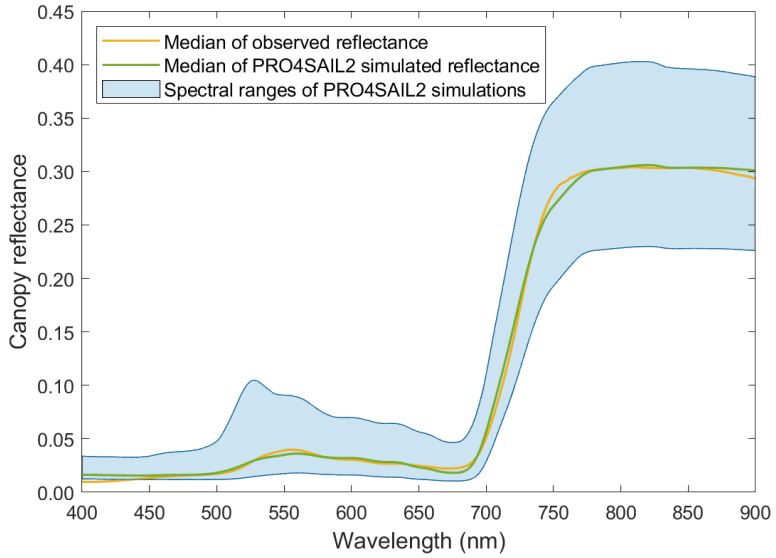

Fig. 4.4. Agreement between the median of the observed reflectance spectrum (orange line) and the median of the PRO4SAIL2 simulated spectrum (green line) for the 2023-Oct dataset. The spectral ranges of 500,000 PRO4SAIL2 simulations are indicated by the shaded blue area.

Continuous wavelet transform (CWT) (Strang and Nguyen, 1996) is an effective signal-processing method that enables the decomposition of complex signals at various scales. In the context of plant trait retrieval using hyperspectral data, CWT helps decouple the overlapping absorption features and remove noises. After the transformation of original spectra, broad absorption features were captured at higher scales while the narrow features were made perceivable at lower scales, thus improving the estimation accuracy of target plant

trait(Blackburn, 2007; Rivard *et al.*, 2008). Several studies have employed CWT on the leaf or canopy reflectance spectrum to identify effective spectral features in the wavelet domain for the estimation of leaf chlorophyll content (Blackburn and Ferwerda, 2008; Xiao *et al.*, 2024), leaf water content (Cheng *et al.*, 2011), leaf dry matter content and specific leaf area (Ali *et al.*, 2016). Recently, (Suárez *et al.*, 2021) combined CWT with the inversion of the coupled Fluspect-Cx and 4AIL model to retrieve leaf pigments from airborne hyperspectral data collected over shiraz vineyards. The authors found strong relationships between the retrieved traits and their target variables related to grape aromatic components.

Table 4.3 Ranges of PRO4SAIL2 input parameters for LUT generation for individual datasets.

Parameter	Unit	Value/range			
		2021-Feb	2021-Oct	2023-Jan	2023-Oct
Leaf/needle parameters (Layer 1: green layer)					
Chlorophyll *a*+*b* content (C_{ab})	µg/cm^2	[20, 88]	[15, 80]	[25, 65]	[20, 60]
Carotenoid content (C_{ar})	µg/cm^2	[5, 20]	[5, 20]	[1, 20]	[1, 20]
Anthocyanin content (C_{brown})	µg/cm^2	[1, 5]	[1, 5]	[1, 6]	[1, 10]
Brown pigment content (A_{nth})	µg/cm^2	0			
Dry matter content (C_m)	g/cm^2	[0.005, 0.016]	[0.012, 0.027]	[0.012, 0.027]	[0.011, 0.020]
Equivalent water thickness (C_w)	g/cm^2	0.08	0.08	0.08	0.09
Mesophyll structure coefficient (N_{struct})	-	[1.8, 2.5]	[1, 2.3]	[1, 2]	[1, 2.3]
Leaf/needle parameters (Layer 2: brown layer)					
Chlorophyll *a*+*b* content (C_{ab}_b)	µg/cm^2	20	22	28	20
Carotenoid content (C_{ar}_b)	µg/cm^2	6	10	15	12
Anthocyanin content (A_{nth}_b)	µg/cm^2	4	4	5	4
Brown pigment content (C_{brown}_b)	µg/cm^2	0	0.2	0.2	0.2
Dry matter content (C_m_b)	g/cm^2	0.040	0.024	0.018	0.010
Equivalent water thickness (C_w_b)	g/cm^2	0.080	0.070	0.030	0.060
Mesophyll structure coefficient (N_{struct}_b)	-	1.3	1.3	1.3	1.3

Parameter	Unit	Value/range			
		2021-Feb	2021-Oct	2023-Jan	2023-Oct
Canopy structural parameters					
Total crown leaf area index for clumped vegetation (LAI)	m^2/m^2	[1.0, 6.8]	[1.5, 6]	[2.0, 6.4]	[2.5, 6.5]
Leaf inclination distribution function parameter a ($LIDF_a$)	-	-0.35			
Leaf inclination distribution function parameter b ($LIDF_b$)	-	-0.15			
Vertically projected crown cover fraction (C_v)	-	[0.87, 0.97]	[0.96, 0.99]	[0.48, 0.76]	[0.66, 0.98]
Tree shape factor (ξ)	-	[0.50, 0.60]	[0.30, 0.50]	[0.60, 0.80]	[0.55, 0.75]
Fraction brown leaf area (f_B)	-	0.15	[0.35, 0.50]	[0.45 0.55]	[0.30, 0.35]
Layer dissociation factor (D)	-	0.30	0.70	0.75	0.07
Hot spot parameter (Hot)	-	0.01			
Sun zenith angle (tts)	deg.	52.73	42.79	71.77	51.74
Observed angle (tto)	deg.	0			
Relative azimuth angle (psi)	deg.	0			

In this study, we applied CWT to both the observed plot-mean reflectance spectra and simulated section in LUTs. The second-derivative Gaussian wavelet was chosen as the kernel function, as it best described the shapes of absorption features in the canopy reflectance (le Maire *et al.*, 2004). CWT was implemented over six scales using the R package 'ifultools' (Constantine and Kaluzny, 2022), with the shift parameter set to 5. The accuracy of estimating N and P concentrations in needles retrieved at each wavelet scale was estimated via modelling, as described in Section 4.2.5. For each dataset, the wavelet scale at which the retrieved functional traits provided the best overall performance for predicting needle N or P concentrations was selected. The overall performance of a certain wavelet scale was represented by the average R^2 of needle N or P models with different combinations of functional traits as inputs.

The RTM inversion was carried out in MATLAB (Statistics and Machine Learning toolbox; MathWorks Inc., Natick, MA, USA). Using the wavelet-transformed spectra for each dataset,

the LUT was queried to identify the closest 1% of simulations with each observed spectrum, where the RMSE represents the closeness between the simulation and observation (Eq. 4.1).

$$\mathrm{RMSE} = \sqrt{\frac{1}{n}\sum_{k=1}^{n}(r_{obs}^{k} - r_{sim}^{k})} \quad \text{Eq. 4.1}$$

where r_{obs}^{k} and r_{sim}^{k} represent the observed and simulated reflectance at the k^{th} band in the wavelet domain, respectively, and n is the total number of bands. The plant trait values of each observation were then calculated as the weighted average of plant functional traits in these 1% simulations (Eq. 4.2), where Y is the trait value for the observation; W_i is the weight of the i^{th} simulation in the selected S LUT entries (i.e., 500); and X_i is the corresponding trait value of the i^{th} simulation.

$$Y = \sum_{i=1}^{S}(W_i \times X_i) \,/\, \sum_{i=1}^{S} W_i \quad \text{Eq. 4.2}$$

The weight of each simulation was determined by the RMSE value using Eq. 4.3.

$$W_i = 1 - [((\mathrm{RMSE}_i - \min(\mathrm{RMSE})) \,/(\max(\mathrm{RMSE}) - \min(\mathrm{RMSE}))] \quad \text{Eq. 4.3}$$

This inversion strategy allowed all four target variables (i.e., C_{ab}, C_{ar}, A_{nth}, and LAI) to be retrieved simultaneously.

Due to the lack of measurements of needle pigment concentration and LAI, the accuracy of retrieved plant traits based on PRO4SAIL2 inversion couldn't be assessed. However, we applied the methodology to a synthetic dataset for a better understanding of the errors embedded in the designed retrieval method. A set of 1,000 simulations was extracted from the LUT with 500,000 entries. Another 100,000 simulations were extracted from the same LUT to create a small LUT. We then added 1% signal-dependent noise to the 1,000 simulations to represent the reflectance extracted from the image prone to noise related to atmospheric correction and other factors intrinsic to the sensors. Plant traits (i.e., $C_{\neg ab}$, C_{ar}, A_{nth} and LAI) were retrieved from the small LUT for both the 1,000 simulations and those with noise. Results of the synthetic validation are presented in Fig. 4.3.

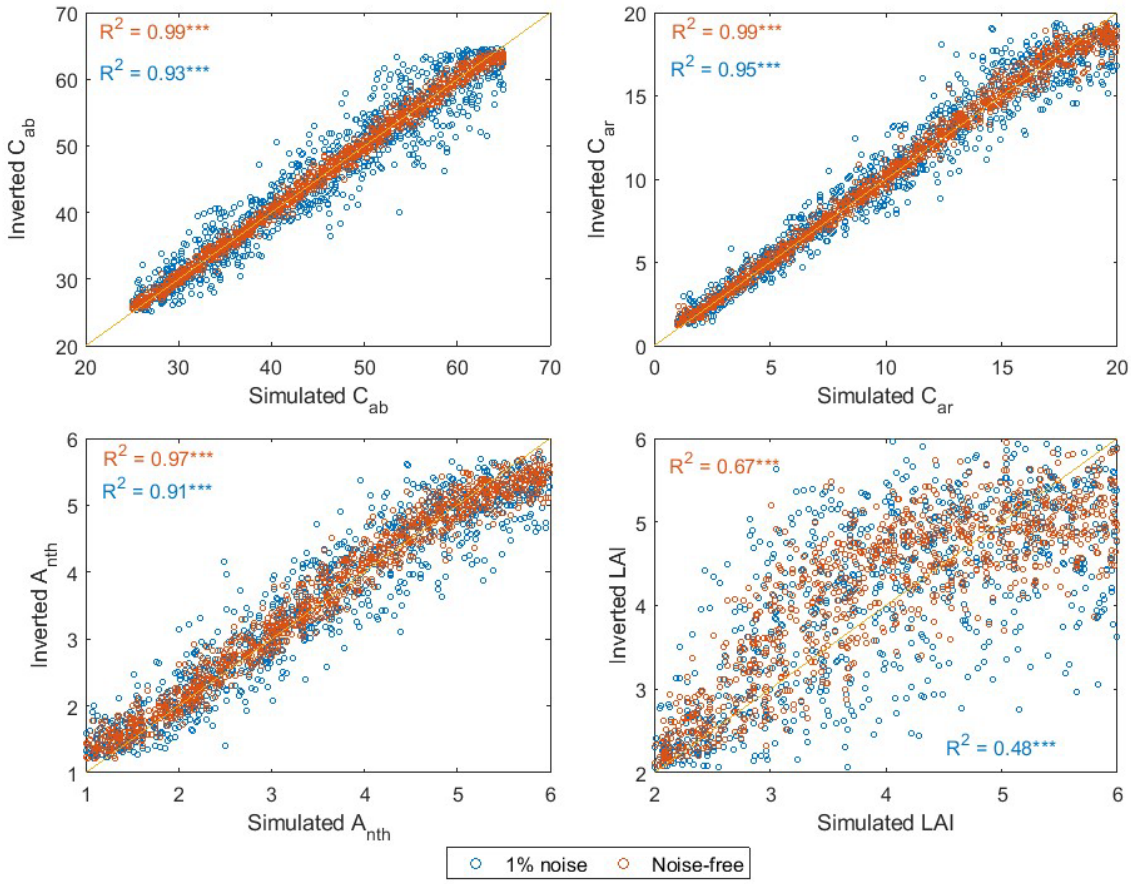

Fig. 4.5. Results of inverted plant traits using a synthetic dataset of 1000 simulations from the LUT (n = 100,000) without noise (orange) and with 1% random noise (blue). **p*-value<0.05; ***p*-value<0.01; ****p*-value< 0.001; n.s.=not significant

4.2.3 Calculation of narrow-band Hyperspectral indices (NBHIs)

A selection of 66 NBHIs was quantified from the plot-mean reflectance (Table 4.2; see Appendix Table A4.1 for the comprehensive list). These NBHIs were used as indicators of canopy structure (e.g., Normalized Difference Vegetation Index [NDVI], Enhanced Vegetation Index [EVI], Optimized Soil-Adjusted Vegetation index [OSAVI]), chlorophyll content (e.g., TCARI/OSAVI, Modified Chlorophyll Absorption Index [MCARI]), xanthophyll content (e.g., Photochemical Reflectance Index [PRI] and its variations), and blue indices (e.g., BF_x, NPQI). The multi-collinearity among plot-level NBHIs was then assessed using variance inflation factor (VIF) analysis (Gareth *et al.*, 2013). Indices with VIF > 5 (Akinwande *et al.*, 2015) were considered to be collinear and discarded. Only non-collinear NBHIs were used as predictors for needle N and P concentrations.

Table 4.4 Equations of narrow-band hyperspectral indices (NBHIs) presented in this study. R_λ represents the reflectance at λ nm wavelength.

Index	Equation	Reference
Structural indices		
NDVI	$(R_{800} - R_{670})/(R_{800} + R_{670})$	Rouse *et al.* (1974b)
EVI	$2.5(R_{800} - R_{670})/(R_{800} + 6R_{670} - 7.5R_{400} + 1)$	Liu and Huete (1995)
RDVI	$(R_{800} - R_{670})/\sqrt{(R_{800} + R_{670})}$	Roujean and Breon (1995)
OSAVI	$(1 + 0.16) \times (R_{800} - R_{670})/((R_{800} + R_{670} + 0.16)$	Rondeaux *et al.* (1996)
MCARI	$[(R_{700} - R_{670}) - 0.2(R_{700} - R_{550})] \times (R_{700}/R_{670})$	Daughtry *et al.* (2000)
$MCARI_1$	$1.2[2.5(R_{800} - R_{670}) - 1.3(R_{800} - R_{550})]$	Haboudane *et al.* (2004a)
Chlorophyll *a* + *b* indices		
TCARI	$3[(R_{700} - R_{670}) - 0.2(R_{700} - R_{550}) \times (R_{700}/R_{670})]$	Haboudane *et al.* (2002)
TCARI/ OSAVI	$\frac{3[(R_{700}-R_{670})-0.2(R_{700}-R_{550})\times(R_{700}/R_{670})]}{(1+0.16)(R_{800}-R_{670})/(R_{800}+R_{670}+0.16)}$	Haboudane *et al.* (2002)
CTR_1	R_{695}/R_{420}	Carter (1994)
SRPI	R_{430}/R_{680}	Peñuelas *et al.* (1995b)
$PSSR_a$	R_{800}/R_{675}	Blackburn (1998)
$PSSR_b$	R_{800}/R_{635}	Blackburn (1998)
$PSSR_c$	R_{800}/R_{470}	Blackburn (1998)
$PSND_c$	$(R_{800} - R_{470})/(R_{800} + R_{470})$	Blackburn (1998)
NPCI	$(R_{680} - R_{430})/(R_{680} + R_{430})$	Peñuelas *et al.* (1994)
$DC_{ab}C_{xc}$	$R_{672}/(R_{550} \times 3R_{708})$	Datt (1998)
$DNC_{ab}C_{xc}$	$R_{860}/(R_{550} \times R_{708})$	
PSRI	$(R_{680} - R_{500})/R_{750}$	Merzlyak *et al.* (1999)
VOG_1	R_{740}/R_{720}	Vogelmann *et al.* (1993)
VOG_2	$(R_{734} - R_{747})/(R_{715} + R_{726})$	Vogelmann *et al.* (1993)
VOG_3	$(R_{734} - R_{747})/(R_{715} + R_{720})$	Vogelmann *et al.* (1993)
CI	R_{750}/R_{710}	Zarco-Tejada *et al.* (2001)
PRI indices		
PRI	$(R_{570} - R_{531})/(R_{570} + R_{531})$	Gamon *et al.* (1992b)
PRI_{515}	$(R_{515} - R_{531})/(R_{515} + R_{531})$	Hernández-Clemente *et al.* (2011)
PRI_{m1}	$(R_{512} - R_{531})/(R_{512} + R_{531})$	Hernández-Clemente *et al.* (2011)
PRI_{m2}	$(R_{600} - R_{531})/(R_{600} + R_{531})$	Gamon *et al.* (1992b)
PRI_{m3}	$(R_{670} - R_{531})/(R_{670} + R_{531})$	Gamon *et al.* (1992b)
PRI_{m4}	$(R_{570} - R_{531} - R_{670})/(R_{570} + R_{531} + R_{670})$	Hernández-Clemente *et al.* (2011)
PRI_n	$PRI_{570}/[RDVI \times (R_{700}/R_{670})]$	Zarco-Tejada *et al.* (2013d)
PRI·CI	$[(R_{570} - R_{530})/(R_{570} + R_{530})](R_{760}/R_{700} - 1)$	Garrity *et al.* (2011)

Index	Equation	Reference
Blue indices		
NPQI	$(R_{415} - R_{435})/(R_{415} + R_{435})$	Peñuelas *et al.* (1995b)
BF_1	R_{400}/R_{410}	Zarco-Tejada *et al.* (2018a)
BF_2	R_{400}/R_{420}	Zarco-Tejada *et al.* (2018a)
BF_3	R_{400}/R_{430}	Zarco-Tejada *et al.* (2018a)
BF_4	R_{400}/R_{440}	Zarco-Tejada *et al.* (2018a)
BF_5	R_{400}/R_{450}	Zarco-Tejada *et al.* (2018a)
BRI_1	R_{400}/R_{690}	Zarco-Tejada *et al.* (2012)
BRI_2	R_{450}/R_{690}	Zarco-Tejada *et al.* (2012)

4.2.4 Quantification of solar-induced fluorescence

Solar-induced fluorescence (SIF) was quantified using the Fraunhofer Line Depth (FLD) method (Plascyk and Gabriel, 1975), which is based on the SIF in-filling effects at narrow dark absorption bands where the solar irradiance is largely reduced, allowing the contribution of SIF to the apparent radiance to be more easily detected. SIF quantified through FLD methods at a moderate spectral resolution (> 1.0 nm FWHM) shows sensitivity to plant stress, including nutrient status (Camino *et al.*, 2018b; Watt *et al.*, 2020; Belwalkar *et al.*, 2022; Raya-Sereno *et al.*, 2022; Wang *et al.*, 2022), water stress (Zarco-Tejada *et al.*, 2012; Panigada *et al.*, 2014), and biotic stress (Calderón *et al.*, 2013; Zarco-Tejada *et al.*, 2018a).

The 3FLD method (Maier *et al.*, 2004) was used to calculate far-red SIF at the O_2-A absorption band (SIF_{760}) from the radiance data at the plot level. This method requires irradiance (E) and radiance (L) spectra as inputs. E was simulated by the SMARTS model using meteorological inputs from weather stations near the study site and Microtops II Sunphotometer measurements (i.e., aerosol optical depth at 500 nm, angstrom wavelength exponent below 500 nm, and relative air mass). To implement the 3FLD method, E and L measurements at three bands were identified for each spectrum: one within the O_2-A absorption window, and the other two reference bands located at the left and right shoulder of the absorption feature, respectively. For narrow-band hyperspectral imagery, the absorption band was located at 762 nm, corresponding to the E or L minimum in the absorption window (755–765 nm); the reference bands were located at the E or L minimum at 750–755 nm and 771–776 nm. An empirical rescaling approach using non-fluorescent targets (i.e., bare soil pixels in the scene) as

references was used to correct the negative raw airborne SIF values resulting from atmospheric effects and the calibration process (Bandopadhyay *et al.*, 2019).

4.2.5 Modelling methods to explain the variation in needle N and P concentrations

Predictive models for needle N and P concentrations were built independently for the 2021-Feb, 2021-Oct, 2023-Jan, and 2023-Oct datasets at the plot level. Each dataset contained the ground needle N and P measurements used for model training and validation and airborne-derived parameters, including 1) four plant traits retrieved from PRO4SAIL2 (i.e., C_{ab}, C_{ar}, A_{nth}, and LAI); 2) SIF_{760}; and 3) non-collinear NBHIs. The models were built using Gaussian regressors (GPR) (Rasmussen, 2004), with inputs selected from the predictor pool composed of airborne-based parameters. The hyperparameters of the GPR algorithm were automatically tuned in parallel for each target variable with the Bayesian optimizer in MATLAB (Statistics and Machine Learning toolbox; MathWorks Inc., Natick, MA, USA), over 120 iterations. A Leave-One-Out Validation (LOOV, 19 folds for 2021-Feb dataset, 33 folds for the others) scheme was adopted to quantify the model performance, with the normalized root mean squared error (NRMSE) and the coefficient of determination (R^2) as the main metrics. NRMSE was calculated as the ratio between RMSE and the range of needle nutrient measurements.

A two-stage feature selection process was used to identify the best input combination. In the first stage, an exhaustive feature selection procedure was implemented whereby the performances of all possible combinations of Predictor Pool 1 parameters (PRO4SAIL2-derived plant traits and SIF_{760}) for estimating target nutrient concentrations were evaluated when used as GPR model inputs. Subsequently, a set of plant traits that provided the best prediction accuracy for the target nutrient among all input combinations was retained for the next stage. In the second stage, Predictor Pool 2 comprised stage 1–retained plant traits and non-collinear NBHIs. The predictive performances of models whose inputs consist of stage 1–retained parameters and any combinations of non-collinear NBHIs or NBHIs only were evaluated for N and P. The second stage of feature selection was performed to test if NBHIs could add more information to the explanation of the observed variability in the concentrations of the target nutrients, as the leaf RTM is not highly sensitive to subtle spectral changes in the blue and green regions induced by stress dynamics. Through the second stage of feature selection of non-collinear NBHIs, we intended to evaluate whether simple index-based models

could match the performance of more complex, plant trait-based models—potentially questioning the need for computationally intensive RTM inversion.

After two-stage feature selection, the final set of parameters was selected to explain each dataset's observed variability in needle N and P concentrations. Finally, the contribution of each parameter to target nutrient estimation was quantified using the Out-Of-Bag (OOB) permutation score embedded in the Random Forest model (Liu and Zhao, 2017).

The uncertainty in needle N and P predictions was quantified by GPR models. GPR model could provide the uncertainty estimation, thanks to its probabilistic nature (see Williams and Rasmussen (2006) for more details). During the LOOCV process, GPR model made the prediction on the left-out sample and provided the confidence interval of the prediction at 95% confidence level. The uncertainty of the prediction was represented by the margin of error, which was calculated as the confidence interval divided by two.

The modelling methods were applied to the tree-crown reflectance and radiance to obtain the needle N and P predictions for each tree. The spatial interpolation algorithm kriging (Oliver and Webster, 1990) was then implemented to generate the airborne variability maps for the whole study site, using the SmartMap plugin in QGIS (Pereira *et al.*, 2022).

4.3 Results

4.3.1 Relationships of narrow-band Hyperspectral indices (NBHIs) to needle N and P concentrations

Hyperspectral indices derived from the airborne images at the treatment level were related to ground-measured needle N and P concentrations, with different levels of correlation (Fig. 4.4). Overall, there was a weak correlation between needle N concentration and the selected hyperspectral indices across dates, even for C_{ab}-related indices used in previous studies as a proxy of N (Fig. 4.4a). For example, TCARI, TCARI/OSAVI, and CTR_1 displayed significant correlations only with needle N in the 2021-Feb dataset (R^2 of 0.79, 0.89, and 0.73, respectively, p-value < 0.05), with no significant relationships in the remaining datasets. Moreover, no strong correlation existed between needle N and structural indices. PRIs, which are used as proxies for xanthophyll content, showed strong relationships only with needle N in the 2023-Oct dataset. For instance, PRI_{m3} and PRI_{m4} yielded $R^2 > 0.9$ (p-value < 0.001). PRI_{515}, PRI_{m1}, and PRI_{m2} displayed correlations (R^2) of ~0.7 (p-value < 0.01).

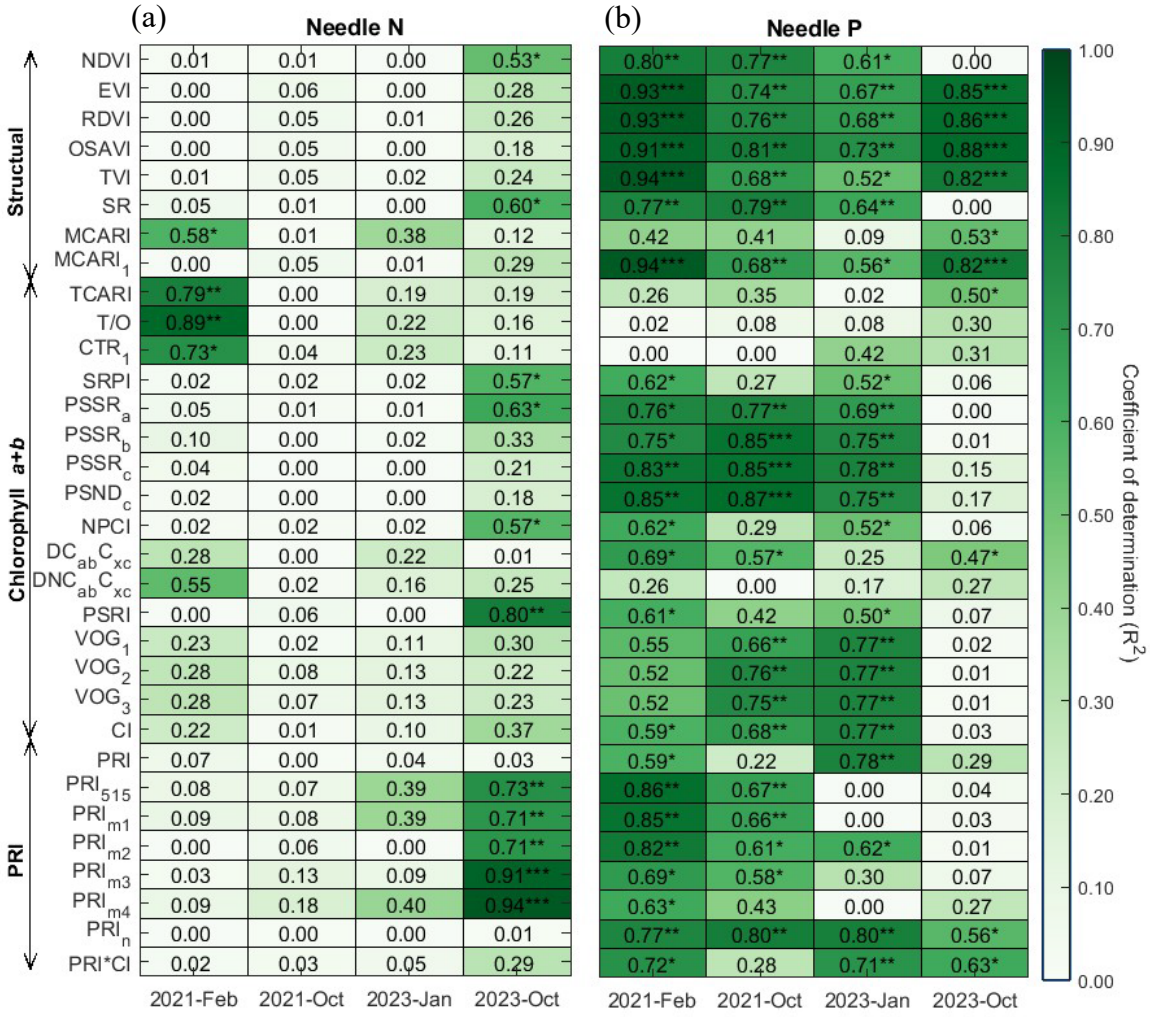

Fig. 4.6. Coefficients of determination (R^2) between hyperspectral indices of various categories (e.g. structural indices, chlorophyll *a+b* indices and PRI indices) and measurements of (a) needle N and (b) P concentrations (g/kg) at the treatment-mean level for the four datasets. * *p*-value < 0.001, ** *p*-value < 0.01, * *p*-value < 0.05.**

By contrast, a strong relationship was observed between specific indices of all categories and needle P concentrations (Fig. 4.4b). Structural indices displayed consistent relationships with needle P concentrations across datasets, often with stronger correlations in the 2021-Feb and 2023-Oct datasets. Specifically, needle P showed strong correlations with EVI, RDVI, OSAVI, and $MCARI_1$ ($0.82 \leq R^2 \leq 0.94$, *p*-value < 0.001) in 2021-Feb and 2023-Oct, while the relationships were less significant in the other two datasets ($0.56 \leq R^2 \leq 0.81$, *p*-value < 0.01). Furthermore, chlorophyll indices, particularly $PSSR_a$, $PSSR_b$, $PSSR_c$, and $PSND_c$, were significantly related to needle P concentrations in three out of the four datasets, with $R^2 > 0.69$ (*p*-value < 0.01). The red-edge Chlorophyll Index (CI) (Zarco-Tejada *et al.*, 2001) also

exhibited strong relationships ($R^2 \geq 0.59$, *p*-value < 0.01) with needle P in the two 2021 datasets and the 2023-Jan dataset. Moreover, significant relationships ($R^2 \geq 0.66$, *p*-value < 0.01) were observed in the 2021-Oct and 2023-Jan datasets between needle P and VOG indices, which focused on the red-edge region. PRIs also showed variable relationships with needle P concentrations. For instance, PRI_n was consistently correlated to P, with $R^2 \geq 0.77$ (*p*-value < 0.01) for the 2021-Feb, 2021-Oct, and 2023-Jan datasets and R^2 of 0.56 (*p*-value < 0.05) for the 2023-Oct dataset. PRI_{515}, PRI_{m1}, PRI_{m2}, and PRI_{m3} showed more significant correlations with P in 2021 ($0.59 \leq R^2 \leq 0.86$ for 2021-Feb, and $0.58 \leq R^2 \leq 0.67$ for 2021-Oct, *p*-value < 0.05) than in the 2023 datasets.In general, NBHIs of all categories were more strongly correlated with needle P measurements, rather than N.

4.3.2 Relationships with RTM-based plant traits and SIF_{760}

A summary of the relationships between ground-measured nutrient levels in needles and PRO4SAIL2-derived plant traits and SIF_{760} is provided in Fig. 4.5 at the treatment (*n* = 7 for 2021-Feb, *n* = 9 for the others) and plot levels (*n* = 19 for 2021-Feb, *n* = 34 for the others). A significant correlation (*p*-value < 0.05) between C_{ab} and needle N was consistently observed across years at the treatment level, with the highest R^2 of 0.90 (*p*-value < 0.001) observed in the 2023-Oct dataset and the lowest R^2 of 0.56 (*p*-value < 0.05) in 2023-Jan. The relationship became moderate at the plot level, where R^2 ranged from 0.15 to 0.46 (*p*-value < 0.05). By contrast, SIF_{760} showed no significant correlation with needle N concentrations in any of the four datasets (*p*-value > 0.05). LAI only exhibited a significant relationship with N in the 2023-Oct dataset (*p*-value < 0.001), with R^2 increasing from 0.29 at the plot level to 0.85 at the treatment level.

Conversely, needle P concentration showed no significant correlation (*p*-value > 0.05) with pigment content in any dataset except 2023-Oct. Specifically, C_{ab}, C_{ar}, and A_{nth} were slightly related to needle P in the 2023-Oct dataset at the plot level, with R^2 ranging from 0.17 to 0.29 (*p*-value < 0.05). The relationship between LAI and needle P was significant in both the 2021-Feb and 2023-Jan datasets at both levels. Moreover, the relationships were stronger at the treatment level (R^2 = 0.86 and 0.59, respectively, *p*-value < 0.05) than at the plot level (R^2 = 0.53 and 0.31, respectively, *p*-value < 0.001). SIF_{760} was consistently correlated with needle P concentration across the years. The relationship tended to be stronger at the treatment level (R^2 of 0.54 to 0.92, *p*-value < 0.05) than at the plot level (R^2 of 0.29 to 0.58, *p*-value < 0.01) as

well. The significant correlation between PRO4SAIL2-derived C_{ab} and needle N, and that between SIF_{760} and needle P, was also reflected in the following modelling results.

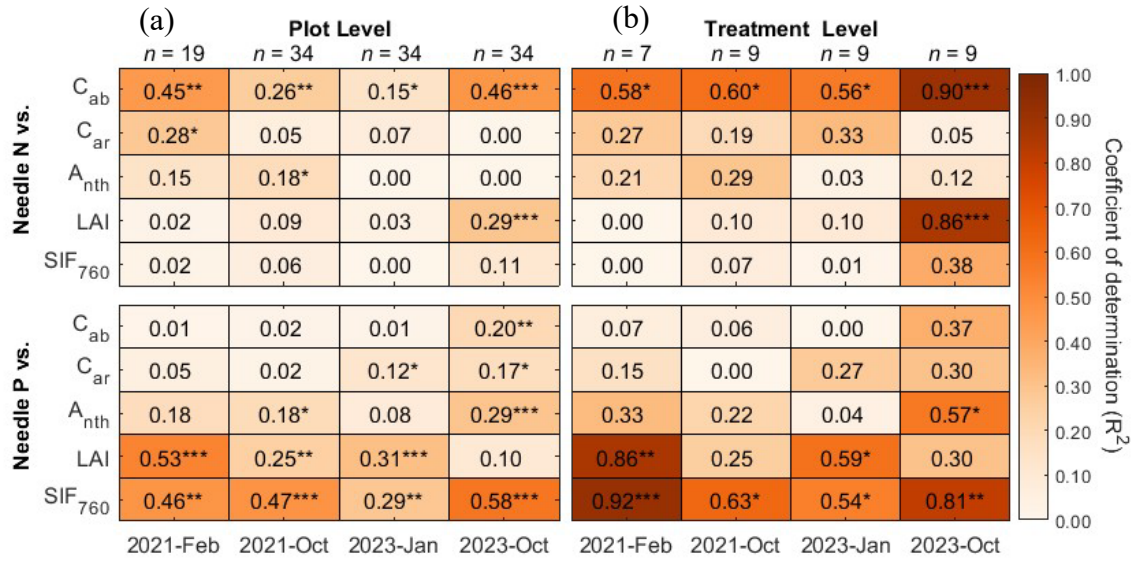

Fig. 4.7. Coefficient of determination between PRO4SAIL2-derived plant functional traits and SIF and measured needle N and P concentrations at (a) plot level and (b) treatment level. *n* represents the sample size of each dataset. **p*-value < 0.05, ***p*-value < 0.01, ****p*-value < 0.001.

4.3.3 Contributions of RTM-derived plant traits and SIF_{760} to explaining variability in needle N and P concentrations

We identified the RTM-derived biochemical constituents C_{ab}, C_{ar}, A_{nth}, and SIF_{760} as predictors sensitive to variability in both needle N and P concentrations, outperforming structural parameters such as LAI. We detected a non-significant relationship between N and this set of parameters in only one dataset (R^2 = 0.25; *p*-value > 0.05 for 2023-Jan, Fig. 4.6a), which could be explained by the low variability in ground-measured needle N concentrations (see Chapter 3 for more details on field data analysis).

The GPR model built with these four input parameters, N = *f*(C_{ab}, C_{ar}, A_{nth}, SIF_{760}), explained the variability in needle N concentrations, with an R2 of 0.27 to 0.76 (*p*-value < 0.001) and NRMSE of 0.14–0.22 at the plot level for four datasets. The aggregated treatment-level results (Fig. 4.6a) displayed higher model accuracy (R^2 = 0.56-0.93, NRMSE = 0.08-0.25, *p*-value < 0.05) for the two datasets in 2021 and the 2023-Oct dataset, as the aggregation process reduced within-treatment-group variance and the errors embedded in the needle nutrient measurements

However, the N modelling results for 2023-Oct lost significance (p-value > 0.05) when averaged to the treatment level. This could be explained by the lack of significant differences in needle N measurements between treatments in this specific dataset.

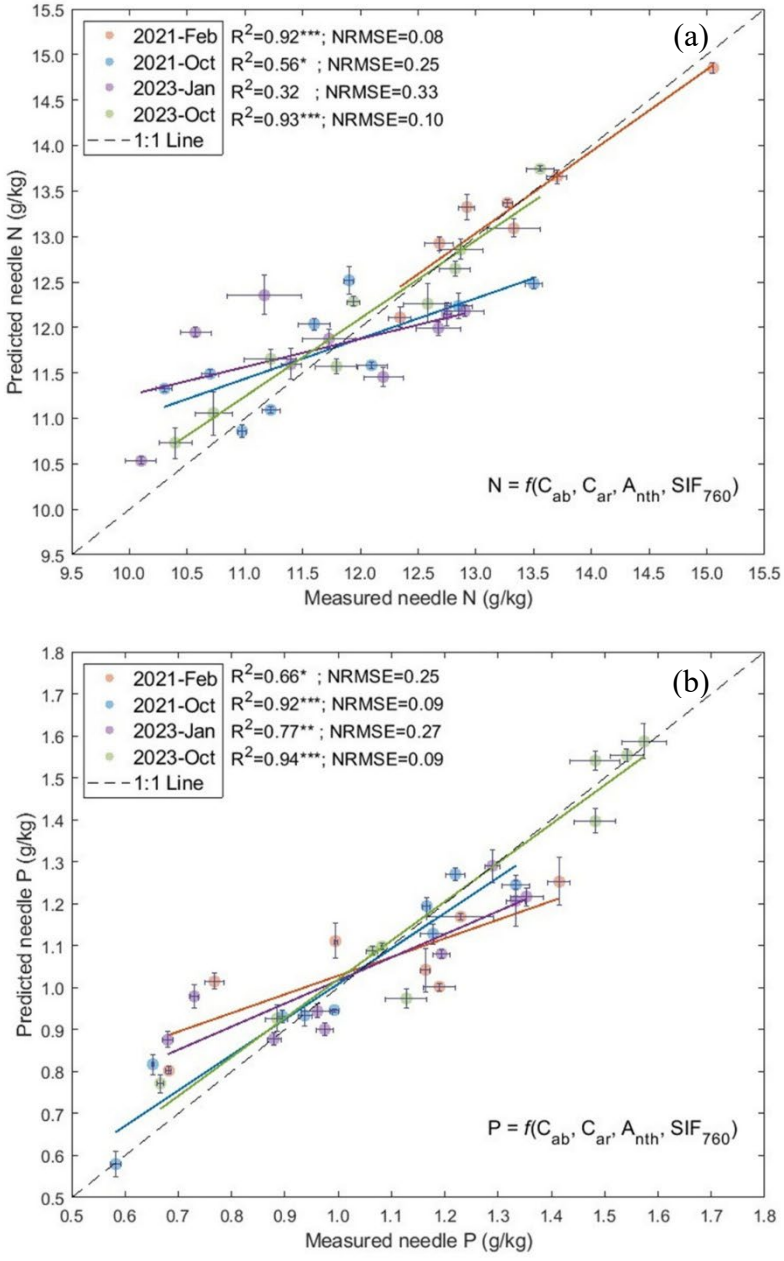

Fig. 4.8. Relationships between measured nutrient concentrations in needles and concentrations predicted by the GPR models with inputs of PRO4SAIL2-derived C_{ab}, C_{ar}, A_{nth}, and SIF_{760} for (a) needle N and (b) P concentrations for the four datasets at the treatment level. Error bars represent standard errors (SE) within each treatment. *p-value < 0.05, **p-value < 0.01, ***p-value < 0.001.

The model P = f(C_{ab}, C_{ar}, A_{nth}, SIF_{760}) yielded prediction accuracy for needle P concentration with R^2 of 0.24–0.95 and NRMSE of 0.13–0.27, p-value < 0.001 for four datasets at the plot level. Similarly, the treatment level results (Fig. 4.6b) have seen the improvement in needle P estimation accuracy (R^2 of 0.66–0.94 and NRMSE of 0.09–0.27, p-value < 0.05).

The uncertainty analysis (Fig. 4.7) revealed that the median margin of error of the model N = f(C_{ab}, C_{ar}, A_{nth}, SIF_{760}) were around 1.7 – 2.5 g/kg for four datasets at the plot level, with predictions for 2021-Feb and 2023-Jan datasets displaying slightly higher margin of error (median value 2.18 and 2.01 g/kg, respectively) than the other two datasets. Needle P predictions by P = f(C_{ab}, C_{ar}, A_{nth}, SIF_{760}) exhibited various levels of uncertainty for four datasets. The median values of values for 2021-Feb and 2023-Jan datasets were around 0.74 and 0.90 g/kg, respectively, higher than those for 2021-Oct dataset (0.31 g/kg) and 2023-Oct dataset (0.24 g/kg).

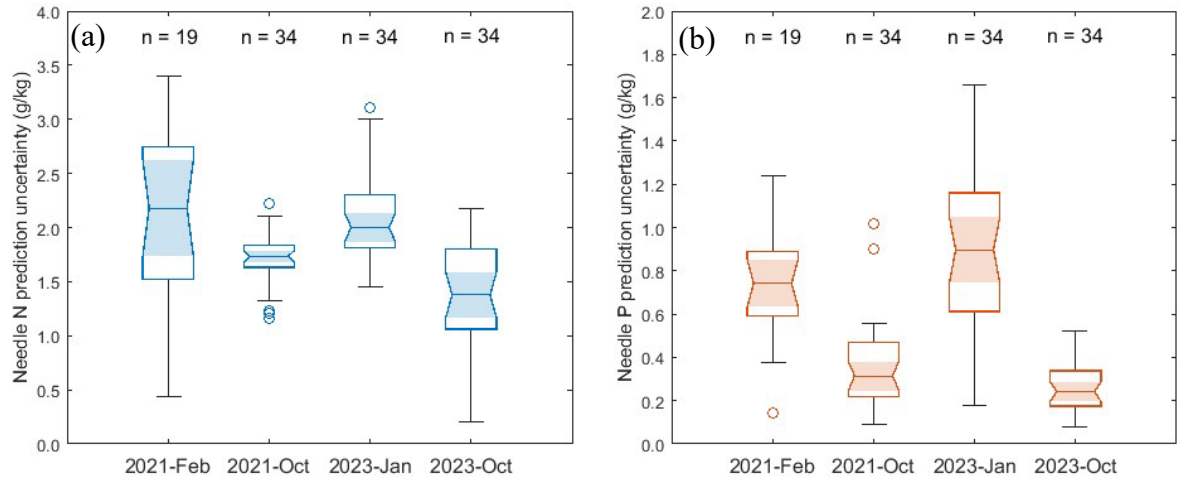

Fig. 4.9. Uncertainties in (a) needle N and (b) needle P predictions provided by GPR models with RTM-derived C_{ab}, C_{ar}, A_{nth} and SIF_{760} as inputs for four datasets at the plot level. *n* represents the sample size. Uncertainties (i.e., Margin of Error or MOE) were estimated by GPR models.

We performed N and P model analysis with the focus on evaluating the relative contributions of the predictors to explaining the variability in N and P concentrations among trials, instead of optimizing the prediction accuracies of the models. A careful analysis of the importance of each parameter (Fig. 4.8) demonstrated the distinct contributions of pigments and SIF to N (Fig 4.8a) vs. P concentrations in needles (Fig 4.8b). The estimated C_{ab} content best explained the variability in needle N concentration across all datasets, with the highest relative importance

score (Fig 4.8a). C_{ab} contributed at least 49% of the relative importance in the N model, with the highest value (78%) observed in the 2023-Oct dataset. A_{nth} was ranked as the second most important parameter to explain the variability in needle N concentration for both datasets in 2021, whereas SIF_{760} was the second most important parameter for the 2023 datasets. The contributions of the three pigments (C_{ab}, C_{ar}, and A_{nth}) varied depending on the dataset across all years, but the contribution of SIF_{760} was ~10% for all datasets. The most critical parameter for explaining the variability in needle P concentration was SIF_{760} (Fig 4.8b), with a relative contribution ranging from 55% to 68% across the four datasets. The remaining contribution was variably distributed across the three pigments. A_{nth} made the second most important average relative contribution (6% to 28%), followed by C_{ar} (4% to 16%). C_{ab} was the least important parameter for P in both the 2021-Feb and 2023-Jan datasets, with a relative contribution < 10%. These results demonstrated the potential of pigment content and SIF to assess needle N and P levels in radiata pine stands. Notably, PRO4SAIL2-derived C_{ab} contributed the most to explaining viability in N levels, whereas SIF_{760} was the leading contributor to the assessment of P levels.

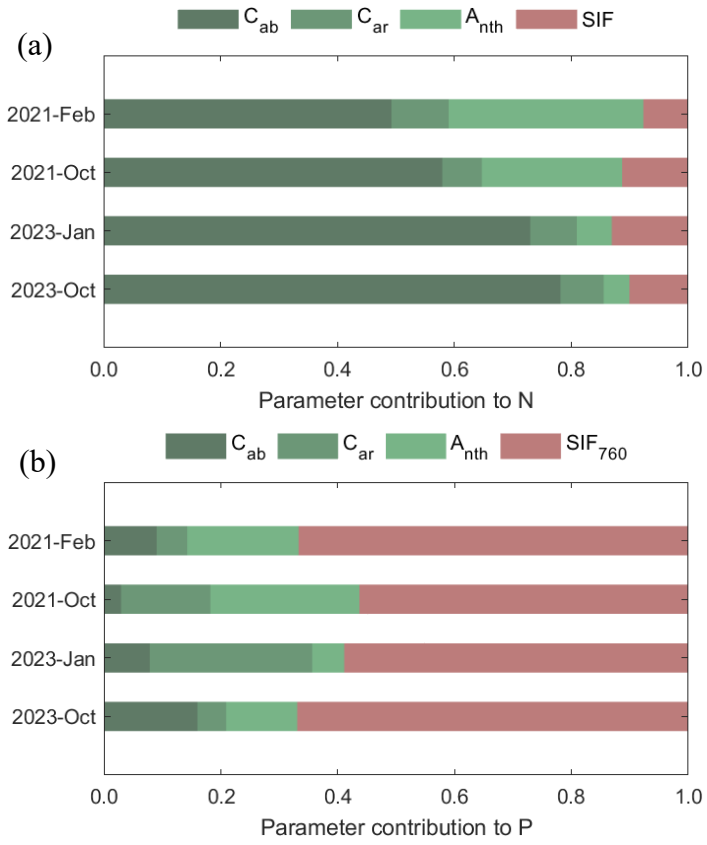

Fig. 4.10. Relative contributions of hyperspectral-derived C_{ab}, C_{ar}, A_{nth}, and SIF_{760} values to explaining the variability in needle (a) N and (b) P concentrations in the nutrient trials.

The interpolated maps based on airborne predictions for the 2023-Oct dataset from the model $N = f(C_{ab}, C_{ar}, A_{nth}, SIF_{760})$ (Fig. 4.9b) and $P = f(C_{ab}, C_{ar}, A_{nth}, SIF_{760})$ (Fig. 4.10b) revealed high spatial variabilities of needle N and P across the study site. The overall spatial patterns of the airborne predictions agreed with those observed in the field measurements for both needle N (Fig. 4.9a) and P (Fig. 4.10a), implying the potential of spatial mapping of needle nutrient content with our proposed models.

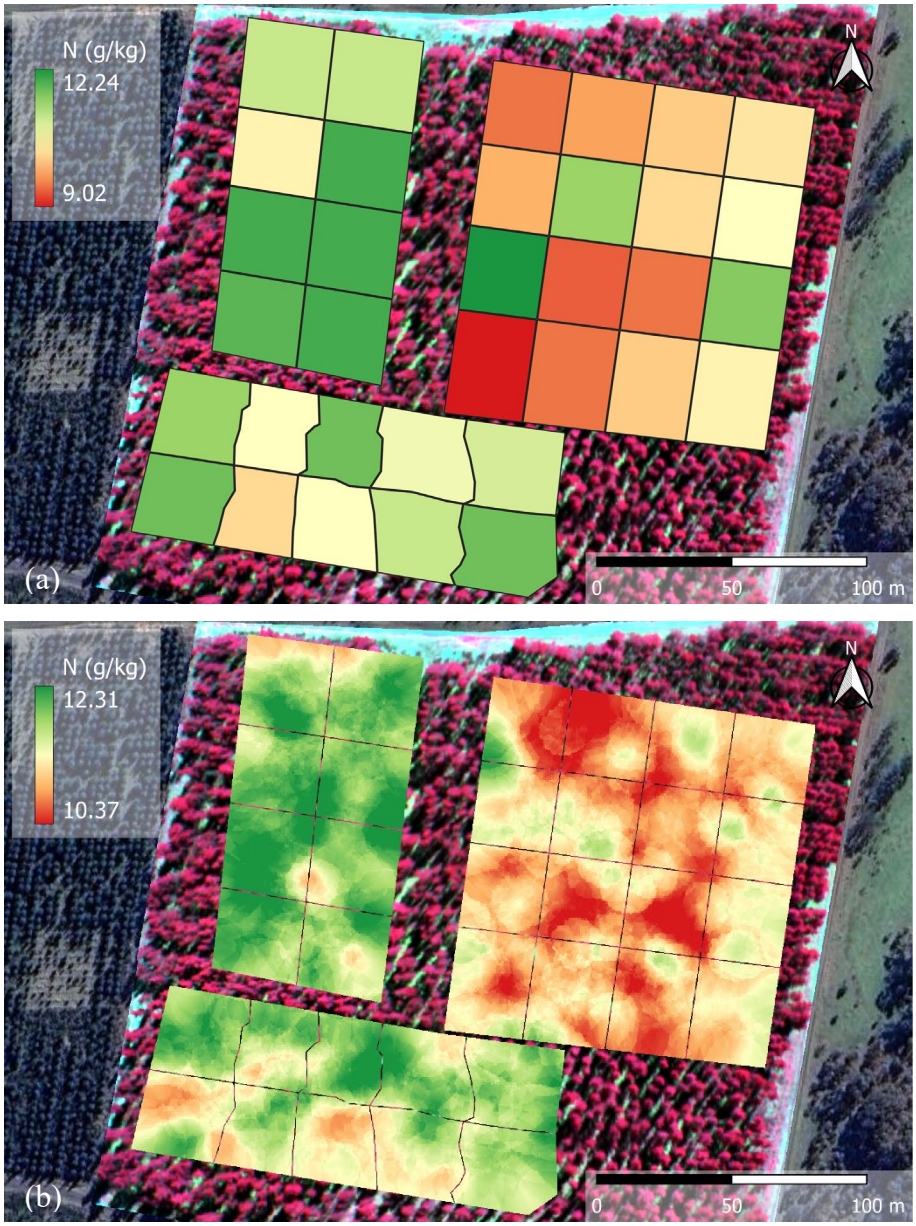

Fig. 4.11. Variability maps of needle N for the 2023-Oct dataset, where (a) is based on the field measurements of needle N, (b) is interpolated using needle N predictions from the model $N = f(C_{ab}, C_{ar}, A_{nth}, SIF_{760})$.

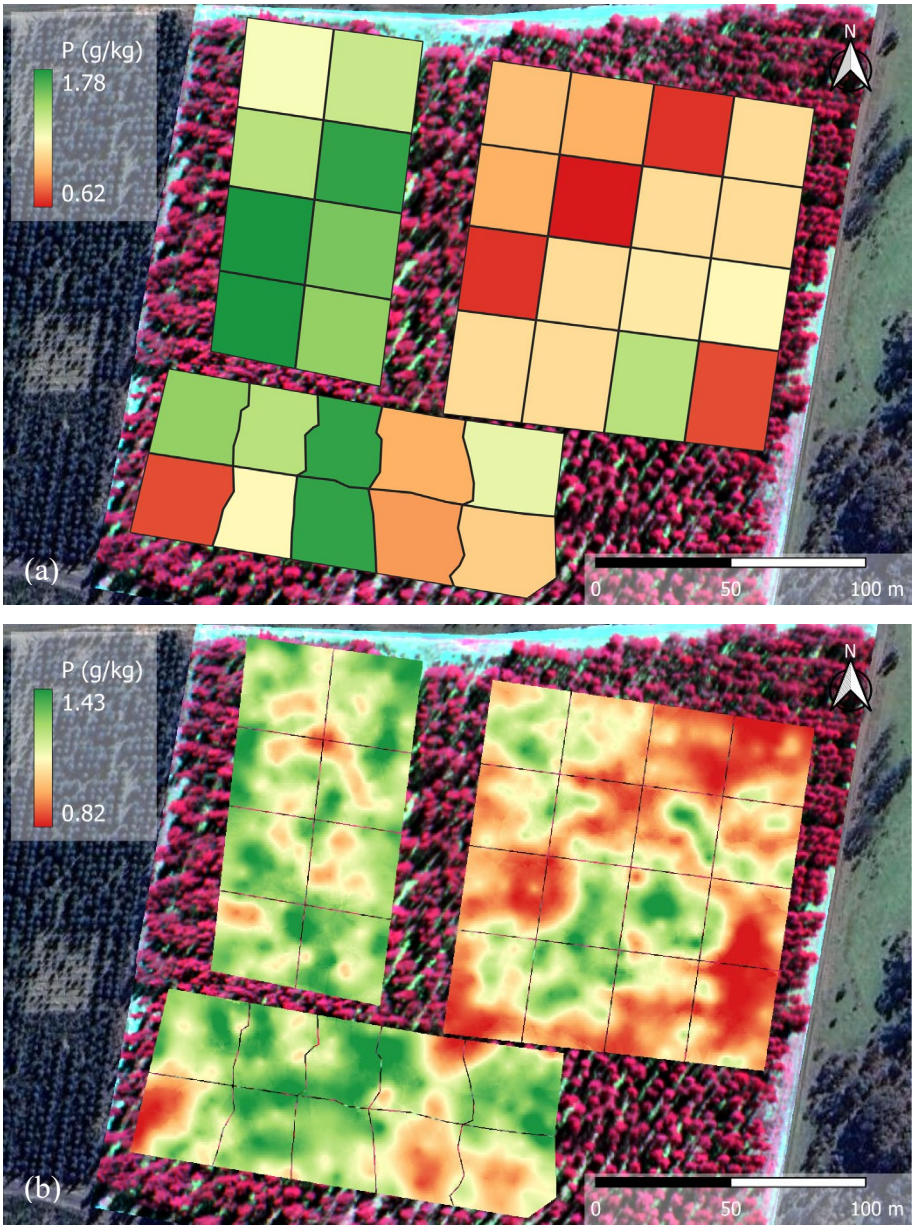

Fig. 4.12. Variability maps of needle P for the 2023-Oct dataset, where (a) is based on the field measurements of needle P, (b) is interpolated using needle P predictions from the model P = *f*(C_{ab}, C_{ar}, A_{nth}, SIF_{760}).

4.3.4 Contributions of the blue region to explain the variability in needle N and P concentrations

We employed the GPR model using non-collinear (VIF < 5) NBHIs such as BF_1, BRI_1, and PSND as inputs, which provided comparable performance for explaining the variability in needle P concentrations to the model with plant functional traits described in the previous section, P = *f*(C_{ab}, C_{ar}, A_{nth}, SIF_{760}). The model P = *f*(BF_1, BRI_1, $PSND_c$) yielded R^2 of 0.86 for 2021-Feb, 0.87 for 2021-Oct, 0.72 for 2023-Jan, and 0.64 for 2023-Oct (*p*-value < 0.01) at the

treatment level. At the plot level, R^2 values of 0.53, 0.69, 0.45 and 0.49 (p-value < 0.001) were obtained for these four datasets, respectively. A careful assessment of these selected indices sensitive to the variability in needle P concentrations showed that they incorporated one or more bands from the blue spectral region. BF_1 (Zarco-Tejada *et al.*, 2018a) is calculated with bands R_{400} and R_{410}, BRI_1 (Zarco-Tejada *et al.*, 2012) with bands R_{400} and R_{690}, and $PSND_c$ (Blackburn, 1998) with bands R_{470} and R_{800}. This intriguing result encouraged us to perform a detailed assessment of the relative contributions of all blue-region-related indices (i.e., indices calculated with at least one wavelength in the blue spectral region) to explain the variability in needle N and P concentrations.

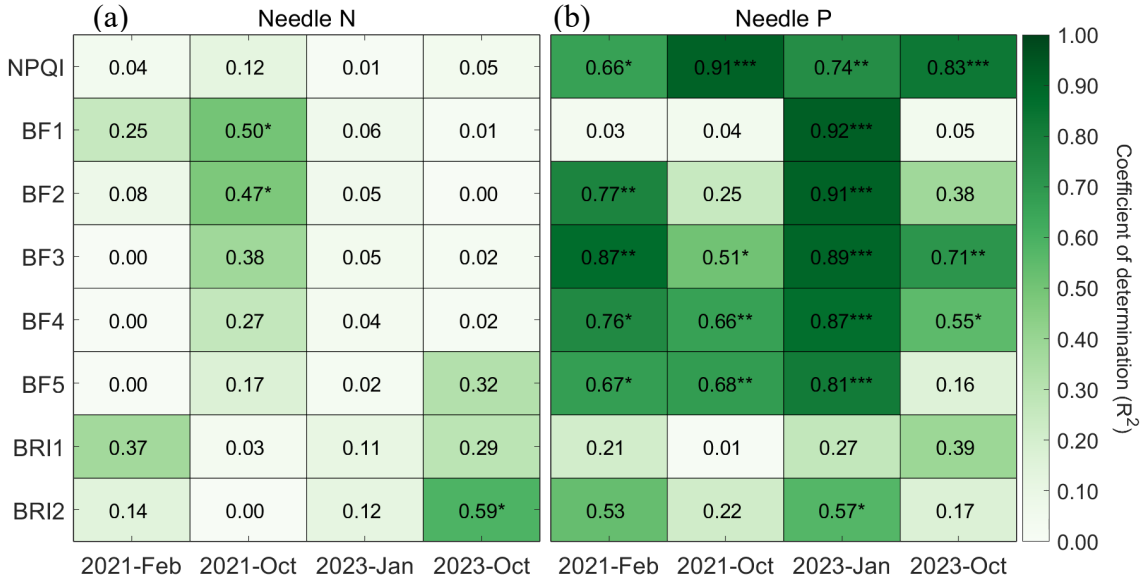

Fig. 4.13. Coefficients of determination (R^2) obtained between hyperspectral indices calculated in the blue spectral region and (a) needle N and (b) P concentrations (g/kg) at the treatment level for all datasets.

Correlation analysis demonstrated that variability in needle N concentrations was barely explained by blue indices (Fig. 4.11a). Nevertheless, needle P concentrations consistently exhibited strong sensitivity to a few hyperspectral indices calculated in the blue region (Fig. 4.11b). For instance, NPQI and needle P yielded R^2 of 0.66–0.91 (p-value < 0.05). Needle P concentration in the 2023-Jan datasets exhibited a significant correlation with the BF_x family (R^2 of 0.81–0.92, p-value < 0.01). The significant relationships between needle P vs. BF_3 and BF_4 were consistent across the years, with R^2 of 0.51–0.89 (p-value < 0.05).

We compared the results of the analysis of the contributions of plant pigments, SIF_{760}, and the blue indices to explain the variability in needle N and P concentrations (Fig. 4.12) against the

previous results from N or P = f(C_{ab}, C_{ar}, A_{nth}, SIF_{760}). The blue indices and pigments together yielded comparable prediction accuracies for needle N concentration (NRMSE = 0.11 for 2021-Feb, 0.17 for 2021-Oct, and 0.11 for 2023-Oct, p-value < 0.05). High prediction accuracy for needle N concentration always required plant pigments in the model inputs, especially for the 2021-Feb and 2023-Oct datasets (Fig. 4.12a).

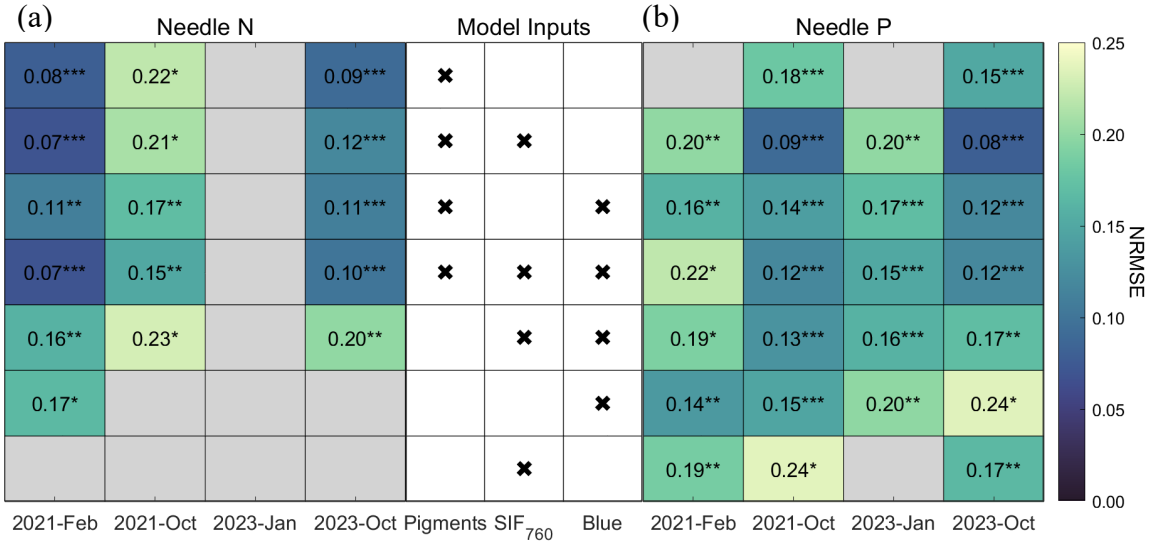

Fig. 4.14. NRMSE between needle nutrient measurements and predictions by the GPR models with inputs of different categories at the treatment level. (a) Needle N and (b) needle P concentrations. **p*-value < 0.05, ***p*-value < 0.01, ****p*-value < 0.001. Inputs were categorized as follows: Pigments include PRO4SAIL2-derived C_{ab}, C_{ar}, A_{nth}, SIF_{760}; blue includes the selected blue indices of the BF_x, BRI_x, and PSI_x groups. BF_x represents the collection of BF_1, BF_2, BF_3, BF_4, and BF_5; BRI_x includes BRI_1 and BRI_2; PSI_x includes $PSSR_a$, $PSSR_b$, $PSSR_c$, and $PSND_c$.

The consistently high prediction accuracy for needle P concentrations across datasets was associated with the incorporation of blue indices in the GPR model inputs (Fig. 13b). Plant pigments alone successfully explained the observed variability in needle P concentrations for the 2021-Oct and 2023-Oct datasets (NRMSE = 0.15 and 0.18, respectively, p-value < 0.001), but not for the 2021-Feb or 2023-Jan datasets (p-value > 0.05). SIF_{760} alone provided NRMSE of 0.17 to 0.24 (p-value < 0.01) for three out of four datasets, while the model performance for the 2023-Jan dataset was not significant (p-value > 0.05).

Compared to the benchmark model P = f(C_{ab}, C_{ar}, A_{nth}, SIF_{760}) (NRMSE of 0.08–0.20), the model built with plant pigments and the blue indices, P = f(C_{ab}, C_{ar}, A_{nth}, blue index), provided comparable overall performance (0.12 ≤ NRMSE ≤ 0.17). Specifically, there was a slight

increase in NRMSE (of 0.05) for the 2021-Oct and 0.04 for 2023-Oct datasets. Nevertheless, minor improvements were observed in the other two datasets, where NRMSE decreased by 0.04 for 2021-Feb and 0.03 for 2023-Jan. Moreover, the quantification of blue indices is more straightforward and less computationally demanding than plant traits like SIF_{760}, which further awards the model built with C_{ab}, C_{ar}, A_{nth} and blue index a greater computational advantage. When only blue indices were used to explain the variability in observed needle P concentration, the GPR model achieved an accuracy of 0.14 for 2021-Feb, 0.15 for 2021-Oct, 0.20 for 2023-Jan, and 0.24 for 2023-Oct in terms of NRMSE (Fig. 4.12b).

Analysis of the relative contributions of different parameters revealed the dynamic role of the blue region in explaining the variability in needle N and P concentrations in the nutrient trials (Fig. 4.13). The blue region, assessed by incorporating blue indices into the GPR model inputs, was the most crucial parameter for P for the two 2021 datasets and the 2023-Jan dataset, with a relative contribution >60% (Fig. 4.13b). Hyperspectral-derived plant pigments were highly important for evaluating needle N concentration, with a combined relative contribution of 70% in all datasets (Fig. 4.13a). In summary, the blue region was critical when explaining the observed variability in needle P but not N concentration. In fact, C_{ab} was still the most important input for explaining the variability in needle N concentration among all three pigment parameters (Fig. 4.13a), with relative contributions ranging from 34% to 65%. C_{ar} and A_{nth} were almost equally important for the 2021-Feb and 2023-Oct datasets. For 2021-Oct, A_{nth} (14%) contributed more strongly to needle N concentration than C_{ar} (6%). For 2023-Jan, C_{ar} was the second most important plant pigment parameter (14%), followed by A_{nth} (5%). Regarding P concentration, C_{ab} was the pigment parameter that best explained the variability in needle P concentration for the 2023-Oct dataset, with a relative contribution of 40%, whereas A_{nth} was the most important pigment to needle P variability for the other three datasets (Fig. 4.13b).

Our analysis revealed that the blue indices contributed to explaining the variability in needle P, implying the sensitivity of the blue spectral region to variations in P levels in radiata pine needles.

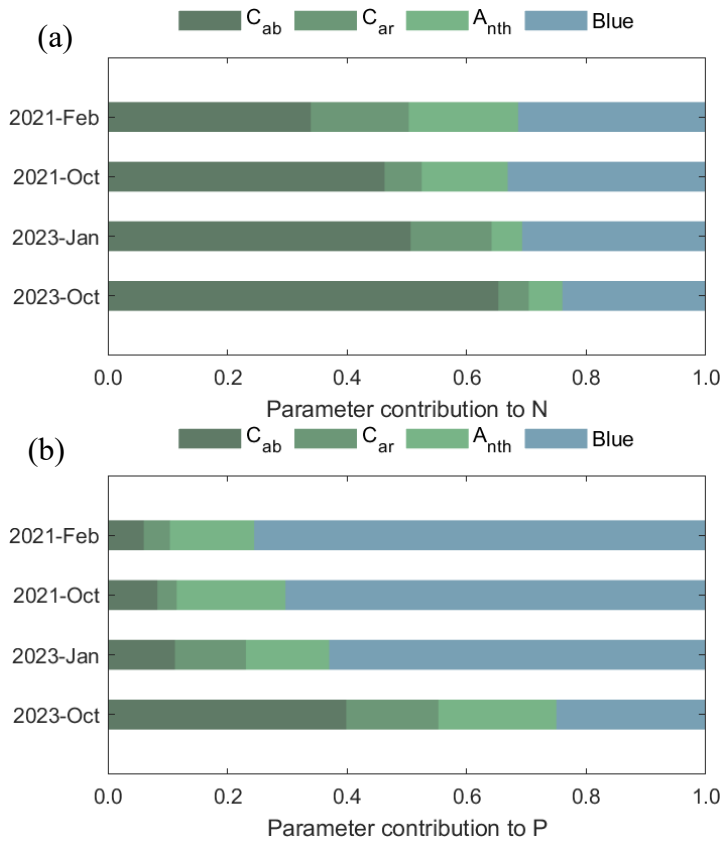

Fig. 4.15. Relative contributions of hyperspectral-derived C_{ab}, C_{ar}, and A_{nth} and the selected indices calculated in the blue region (BF_x, BRI_x, and PSI_x) to the explained variability in needle (a) N and (b) P concentrations at the treatment level. BF_x includes BF_1, BF_2, BF_3, BF_4, and BF_5; BRI_x includes BRI_1 and BRI_2; PSI_x includes $PSSR_a$, $PSSR_b$, $PSSR_c$, and $PSND_c$.

4.4 Discussion

We successfully used hyperspectral imagery and RTMs to analyze how physiological traits contribute to explaining the variability in N and P concentrations in radiata pine needles in long-term nutrient trials. We determined that hyperspectral-derived biochemical parameters are more sensitive to variations in needle N and P concentrations than the structural parameters (i.e., LAI) that are generally tracked by NDVI and other standard remote sensing methods (Fang *et al.*, 2019). We found that LAI is weakly related to needle N and P variability, though it remains inconclusive whether LAI can potentially contribute to needle nutrient estimation, considering the retrieval performance using the proposed method. The synthetic validation results (Fig. 4.3) revealed that LAI was retrieved with lower accuracy (R^2 = 0.67, p-value < 0.001 without noise, R^2 = 0.48, p-value < 0.001 with 1% noise) than the plant pigments. This could be caused by the small wavelet scale (i.e., 3 or 4) used for the retrieving process, which

failed to represent broader features like LAI, but also due to the structural characterization of the canopy by SAIL2. Moreover, LAI retrievals might not be representative enough for the canopy structure, as the parameter was retrieved from crown-level data, where the segmentation process likely reduced the variability in canopy structure.

Despite the indirect link with LAI, needle P concentration displayed moderate relationships with structural indices such as EVI, RDVI, MCARI1, and OSAVI, and red-edge indices such as VOG indices and CI. Indeed, previous studies showed that the NIR and the red-edge region are sensitive to leaf P concentration. For example, Mutanga and Kumar (2007) estimated leaf P concentration in grass with six predictors, including two red-edge bands (710 and 742 nm), three bands in the SWIR region and the red edge position (REP). Their best model yielded an R^2 of 0.63 for estimating leaf P concentration in grass. Similarly, among the set of wavelengths selected by Li *et al.* (2018) for predicting leaf P concentration in oilseed rape, five bands were located between 832 and 1267 nm, and the remaining band was in the red edge (755 nm). The authors reported an R^2 of 0.78 for the leaf P predictive model. Among the 10 effective bands selected by (Lin *et al.*, 2024) for leaf P concentration estimation ($R^2 = 0.70$) in summer maize, two were located in the red edge (700 and 730 nm) and four in the NIR region (795, 838, 858, 870nm). Overall, all three studies achieved a slightly lower prediction accuracy for leaf P concentration than our study ($0.66 \leq R^2 \leq 0.94$). The widely observed linkage between leaf or needle P concentrations and the red-edge region could be potentially related to the SIF signals, given that chlorophyll fluorescence effects were observed in the red-edge region of the leaf apparent reflectance spectrum, with two peaks around 690 and 750 nm, respectively (Zarco-Tejada *et al.*, 2000). These index- and band-level findings were aligned with our plant-trait level analysis below.

RTM-inverted C_{ab} and airborne narrow-band SIF_{760} were indicative of needle N and P concentrations, with C_{ab} playing a more pronounced role in predicting N than P. Previous studies assessing leaf N concentrations in other species produced similar results. For instance, Camino *et al.* (2018b) determined that including SIF quantified at the O_2A absorption band improved the prediction accuracy of leaf N levels to R^2 of 0.92 compared with the model using only functional traits (C_{ab}, C_m, and C_w) derived from PROSPECT-SAILH, with an $R^2 \leq 0.77$. Similarly, Wang *et al.* (2022) built predictive models for leaf N levels in almond trees over two years and achieved an accuracy of R^2 of 0.95 with input parameters including narrow-band SIF and C_{ab} concentration retrieved from the FluSAIL model. The predictive capacity of SIF and C_{ab} for N status has a well-studied physiological basis. N deficiency affects plant

photosynthetic activities in various ways, such as by influencing the contents of chlorophyll, thylakoid proteins, and other components of the photosynthetic apparatus (Mu and Chen, 2021). As photosynthetic activities are reduced, plants also vary the partitioning of absorbed energy among other radiation pathways, such as chlorophyll fluorescence emission, along with adjusting the light absorption to maintain the balance of radiation utilization and absorption.

The responses of C_{ab} and SIF to needle P levels might be linked to the photosynthetic electron transport chain. Laboratory studies on chlorophyll fluorescence kinetics have revealed that P deficiency results in a reduction in ATP synthesis and lumen acidification in chloroplasts, thereby inhibiting electron transport to photosystem I (PSI) (Carstensen *et al.*, 2018). Watt *et al.* (2020) detected a strong positive correlation between SIF and photosynthetic variables, such as the maximal rate of carboxylation (V_{cmax}) and electron transport (J*max)* in radiata pine seedlings under N- and P-stress conditions. These findings support the hypothesis that SIF reflects the impact of P on the photosynthetic electron transport chain and are aligned with our results that SIF has a pronounced effect in explaining variability in needle P concentration.

Anthocyanins and carotenoids regulate plant responses to abiotic stress (such as nutrient deficiency) due to their photoprotective and antioxidant properties (Landi *et al.*, 2015; Sachdev *et al.*, 2021). Under stress conditions, the incident radiation energy exceeds the maximum that plants can use or dissipate, leading to the excessive production of reactive oxygen species (ROS). To prevent oxidative damage, plants activate anthocyanin biosynthesis to scavenge the excessive ROS induced by abiotic stress, thereby reducing cellular damage (Landi *et al.*, 2015; Naing and Kim, 2021; Li and Ahammed, 2023). Besides anthocyanins, certain types of carotenoids, such as β-carotene, also detoxify ROS as a response to stress (Demmig-Adams, 1990; Posch *et al.*, 2008).

Xanthophyll, another type of carotenoid, also plays a crucial photoprotective role in dissipating excess energy. In the xanthophyll cycle, violaxanthin is de-epoxidized into antheraxanthin and then zeaxanthin, contributing to heat dissipation (i.e., NPQ) (Demmig-Adams and Adams, 1996). The Photochemical Reflectance Index (PRI) and its variants are thought to track the epoxidation state of the xanthophyll cycle, thus reflecting the stress level of the plant. For example, Suárez *et al.* (2009b) determined that PRI was effective for detecting water stress across species due to its significant correlation with canopy temperature ($R^2 \geq 0.65$), reflecting stomatal conductance. Shrestha *et al.* (2012) determined that the variation in PRI values could reflect the increase in xanthophyll cycle activity induced by N deficiency in rice (*Oryza sativa*)

leaves. However, in the current study, we observed no significant relationships between PRI or its variants and measured needle N concentrations, except for the 2023-Oct dataset. Needle P measurements only displayed consistent relationships with PRI_n. The lack of correlation in our study could be related to the effects of canopy structure, illumination conditions, and viewing geometry, which affect the sensitivity of PRIs to the epoxidation state of xanthophyll (Hernández-Clemente *et al.*, 2011).

Our results reveal the importance of the blue spectral region, represented by indices with blue spectral wavelengths, in explaining the variability in needle P concentration in the nutrient trials. Three indices from the BF_x, BRI_x, and PSI_x groups provided good prediction accuracy for needle P concentrations, with NRMSE of 0.14–0.24 at the plot level, and 0.13- 0.24 at the treatment level. Despite the slightly reduced performance for explaining variability in P levels, compared to the benchmark model P = *f*(C_{ab}, C_{ar}, A_{nth}, SIF_{760}), these predictive models built with only indices as inputs have great computational advantages over those built with RTM-based functional traits and/or SIF, suggesting that a multispectral sensor centred at bands in the blue and NIR spectral regions could be used for large-scale monitoring of P. Our findings at the index level comply with those from band-level predictions of leaf P concentrations. For instance, Guo *et al.* (2018) selected a set of hyperspectral bands for estimating leaf P levels in using the spectral measurements of leaf samples from rubber trees. Their empirical regression model achieved NRMSE ~0.08 using seven wavelengths as inputs (437, 713, 1144, 1405, 1686, 2243, and 2249 nm). With the *in-situ* canopy reflectance measured over summer maize (*Zea mays*) canopies, Lin *et al.* (2024) built an empirical model to predict leaf P concentration that yielded an R^2 of 0.70. Ten wavelengths were included in their model: four in the visible region (442, 479, 572, and 630 nm), two in the red-edge region (700 and 730nm) and four in the NIR region (795, 838, 858 and 870 nm). The blue indices used in our needle P assessment also utilize bands in the blue and NIR regions. To further illustrate the potential of blue indices for explaining variability in needle P, we evaluated another index-based model, with TCARI/OSAVI, PRI, NPQI and the curvature index (CUR) as inputs, in terms of their needle P prediction performance. These indices were chosen as they were proxies for the plant functional traits used in the benchmark model: TCARI/OSAVI, PRI, NPQI were indicators for needle pigment content, and CUR was a proxy for SIF. The results showed (see Appendix Table A4.2) the model P = *f*(TCARI/OSAVI, PRI, NPQI, CUR) failed to provide statistically significant predictions for the 2021-Feb and 2023-Oct datasets, and yielded lower accuracy for the remaining two datasets, compared to the blue-index-based model. Hence, the consistent

performance of blue indices in needle P estimation was unlikely to be incidental, and it implied the physical relationship between P and the blue spectral region, which has not been well understood but is noteworthy.

The mechanism of the responses of the blue spectral region to variations in leaf P levels is not yet fully understood by the remote sensing community due to limited studies on this topic. Different hypotheses exist to explain how the blue spectral region responds to the variability in needle P concentration, one of which is related to blue fluorescence. When excited by UV light, green plants emit fluorescence not only in the red spectral region (i.e., chlorophyll fluorescence) but also in the blue-green region, with a blue maximum near 450 nm (BF) and a green shoulder around 530 nm (GF) (Chappelle *et al.*, 1984; Lang and Lichtenthaler, 1991; Subhash *et al.*, 1999). The blue fluorescence originates from cinnamic acids bound to the cellulosic cell walls (Harris and Hartley, 1976) and soluble substances bound to cell vacuoles, including cinnamic acids, flavones, and flavonols (Lichtenthaler and Miehé, 1997). Fluorescence ratios (e.g., BF/SIF, GF/SIF and BF/GF) are highly responsive to stresses, such as heat, nutrient deficiency, and pathogen infection (Lichtenthaler and Miehé, 1997; Subhash *et al.*, 1999; Bürling *et al.*, 2011). These observed stress responses at the leaf level might be related to the reduced reabsorption of blue fluorescence due to lower photosynthetic pigment concentration induced by long-term stress (Lichtenthaler and Miehé, 1997). An alternative hypothesis hinges on the degradation of chlorophyll into phaeophytin under stress conditions (Hörtensteiner, 2013). As a proxy for phaeophytin content, the Normalized Phaeophytinization Index (NPQI) (Barnes *et al.*, 1992a; Peñuelas *et al.*, 1995b) was proven to be sensitive to various stresses (Zarco-Tejada *et al.*, 2018a; Zarco-Tejada *et al.*, 2021a; Poblete *et al.*, 2023). In the current study, NPQI, a blue-region-related index, also displayed significant relationships with needle P concentrations across dates.

The uncertainties in the needle N and P prediction could be attributed to various sources. Firstly, the small sample size might result in uncertainties in parameter estimations of the GPR models. The limitation of small sample size was reflected in the relatively higher uncertainty in the 2021-Feb dataset (n = 19), compared to the other three datasets (n = 34). Low level of variances in the needle nutrient measurements (See Chapter 3 Table 3.2) likely led to a restricted learning range for the GPR models during the training phase, and thus impaired the prediction accuracy on the "unseen" samples during the predicting phase. The low level of variability in needle N measurements (CV = 0.07-0.12), compared to those of needle P (CV = 0.26-0.33), partially explained the lower accuracy of needle N estimation than that of P by the benchmark model

N/P = f(C_{ab}, C_{ar}, A_{nth}, SIF_{760}). Moreover, the uncertainties in needle N and P measurements could potentially undermine the reliability of the trained GPR model.

The obtained SIF_{760} values (2.5-23.2 mW/m^2/nm/sr. See Appendix Fig. 4.1), despite being higher than what is expected for healthy vegetation (0–3 mW/m^2/nm/sr), succeeded in differentiating nutrient treatments. Thus, the quantified SIF_{760} should be regarded as relative values, rather than absolute values. Several studies have also reported that airborne SIF values quantified from data with 3–7 nm FWHM were higher than the typical ranges (Zarco-Tejada *et al.*, 2013b; Camino *et al.*, 2018b; Belwalkar *et al.*, 2022; Wang *et al.*, 2022). Simulation studies using RTMs (Damm et al., 2011; Belwalkar et al., 2022) revealed that coarser spectral resolution (SR) led to overestimated far-red SIF values based on FLD principles. Belwalkar et al. (2022) also evaluated the suitability of airborne SIF quantified at 0.1-nm FWHM and that at 5.8-nm FWHM for monitoring crop leaf N status. They concluded that although sub-nanometer resolution was necessary to retrieve SIF in absolute units, a coarser resolution was sufficient for detecting SIF differences in the context of vegetation stress detection. A potential focus of future research can be comparing airborne SIF quantified at sub-nanometer resolution (<1.0-nm FWHM) and moderate resolution (>1.0-nm FWHM) to decide whether the sub-nanometer resolution is required for a more accurate assessment of needle nutrient content in coniferous forests.

Similarly, the retrieved C_{ab}, C_{ar} and A_{nth} should be regarded as relative values, rather than absolute values of pigment content, as we lack the pigment measurements to validate the accuracy of the retrievals. The synthetic validation results indicated that pigment retrievals are more robust to noise than LAI. A previous study by Poblete *et al.* (2025) also showed the high agreement between PRO4SAIL2-derived C_{ab} content with the needle chlorophyll measurements for radiata pine (R^2 = 0.80-0.89). Similarly, Darvishzadeh *et al.* (2008) found a strong relationship between PRO4SAIL-derived C_{ab} content and the ground measurements (R^2 = 0.70) in heterogeneous grassland. In the study conducted in almond orchards (Wang *et al.*, 2022), a strong correlation between FluSAIL-derived C_{ab} and their ground-measured counterparts (R^2 = 0.66) was reported. Therefore, we believe that the RTM-based needle pigment retrievals, though they cannot represent the absolute levels of pigment content, are sufficient to differentiate plots/trees from different fertilization levels.

Due to the lack of coverage in the SWIR region by the narrow-band hyperspectral imager used in this study, we only focused on the visible-near infrared (VNIR) region for needle nutrient

analysis. However, it should also be noted that chlorophyll only accounts for 1.7% of total leaf N (Kokaly *et al.*, 2009a), while there are more predominant N-containing biochemical constituents, such as proteins. It has been shown that the shortwave infrared (SWIR) region, where the protein absorption is prominent, can be used for leaf N content. Previous studies have reported that leaf N concentration displayed a stronger relationship with NIR/SWIR-based indices than with VNIR indices in wheat (Camino *et al.*, 2018b) and potato (Herrmann et al., 2010). The advancement in RTM also enabled the retrieval of leaf protein content. Wang *et al.* (2018b) investigated the potential of RTM-derived leaf protein content for assessing leaf and canopy N status in mixed temperate forests. The authors obtained a higher prediction accuracy for canopy N ($R^2 = 0.64$) than for leaf N content ($R^2 = 0.46$). Several studies also reported the importance of the SWIR region for leaf P assessment (Guo *et al.*, 2018; Li *et al.*, 2018; Gao *et al.*, 2019). Future studies could extend our methodology to evaluate and compare the importance of VNIR-related plant traits (e.g., C_{ab}, C_{ar}, A_{nth} and SIF_{760}) and SWIR-related traits (e.g., leaf protein content) for needle N and P prediction accuracy in radiata pine forests.

Overall, our findings shed light on the importance of biochemical constituents, SIF, and the blue spectral region in explaining the variability in needle N and P concentrations. Distinct dynamics were observed for these two nutrients, whereby C_{ab} best explained the variability in needle N concentration, whereas SIF and the blue spectral region played crucial roles in explaining the variability in needle P concentration.

4.5 Conclusions

Our study is the first to demonstrate that a physically based modelling approach—using plant functional traits, including biochemical constituents and solar-induced fluorescence (SIF)—can be effectively applied to explain the observed variability in needle nitrogen (N) and phosphorus (P) concentration in coniferous forests. Moreover, as opposed to most studies relying on empirical methods (e.g., using spectral indices or spectral bands as PLSR model inputs), our physically based approach yielded a robust accuracy to explain needle P variability, with the advantage of improved model interpretability, which relied on physiological traits instead of vegetation indices without physical meaning.

Using the four sets of airborne hyperspectral imagery and field data collected from radiata pine over three years of established nutrient trials, we demonstrated that RTM-derived needle

pigment content (i.e., C_{ab}, C_{ar}, and A_{nth}) and far-red SIF_{760} could be used to explain the observed variability in needle N concentration across years. Using GPR models, these four traits explained the variability in needle N (R^2 = 0.67–0.97, NRMSE = 0.07–0.30) and needle P concentration (R^2 = 0.60–0.95, NRMSE = 0.09–0.27). C_{ab} played a critical role in explaining the observed variability in needle N concentration, whereas SIF_{760} was the main contributor to the explained variability in needle P concentration. Our analysis of the pool of hyperspectral indices and RTM-inverted traits revealed the essential contribution of the blue spectral region in explaining the variability in needle P but not needle N concentration. Blue indices (i.e., BF_x, BRI_x and PSI_x), when combined with RTM-derived plant pigments (i.e., C_{ab}, C_{ar}, and A_{nth}) as inputs in the GPR models, improved the assessment of needle P in the nutrient trials. This new insight regarding the blue spectral region playing a major role in explaining the observed variability of needle P concentration opens new options for screening of nutrient trials, and it suggests the potential of using multispectral sensors with bands centred at the blue wavelengths to monitor needle P status at an operational scale. Further studies are required to evaluate different hypotheses to explain the divergent contributions of the blue region to needle N and P concentrations, such as the potential effects of blue fluorescence and the degradation of chlorophyll *a* + *b* into other compounds under nutrient-stress conditions.

Chapter 5
Evaluation of solar-induced fluorescence using airborne narrow-band and sub-nanometer imagery for needle nitrogen and phosphorus assessment in radiata pines

Highlights

- Sub-nanometer-based SIF_{687} was less effective than SIF_{760} for needle N and P estimation.
- Far-red FLs contributed to needle N and P estimation more than red FLs and sub-nanometer-based SIF did.
- Further work is needed to understand the impact of sub-nanometer vs. narrow-band resolution for SIF_{760} quantification to assess needle N and P variability.

Abstract

Solar-induced chlorophyll fluorescence (SIF) is an early indicator of plant stress, as it is directly linked to photosynthetic activity. Its retrieval accuracy strongly depends on sensor characteristics, especially spectral resolution (SR). Simulation studies have shown that sub-nanometer resolution (Full-Width at Half-Maximum [FWHM] < 1.0 nm) is required for the retrieval of SIF in the absolute term. Nevertheless, for large-scale monitoring on airborne platforms, sub-nanometer imagers inevitably lead to higher operational and computational cost, compared to narrow-band imagers (FWHM > 3 nm). This studyaims to investigate whether sub-nanometer resolution offers significant benefits for SIF applications in assessing needle nitrogen (N) and phosphorus (P) in radiata pine (*Pinus radiata D. Don)* canopies. We collected data on two dates using two airborne hyperspectral imagers in tandem, with an FWHM of 5.8 nm and less than 0.2 nm, respectively, we quantified far-red and red SIF (SIF_{687}, SIF_{760},

respectively) as well as depths of Fraunhofer line (FL) features. We then evaluated the needle N and P prediction performance of Gaussian Process Regression (GPR) models built with inputs including SIF, FLs and narrow-band-based needle pigment content derived from radiative transfer models (RTMs).

Contrary to our initial hypothesis, sub-nanometer resolution did not enhance the predictive capacity of SIF_{760} beyond that of the narrow-band benchmark model for either needle N or P. Potential uncertainties in SIF retrievals—such as atmospheric effects, canopy structure, and retrieval errors—could not be entirely attributed to in this study, leaving the quantification of SIF using FL inconclusive. The analysis of sub-nanometer data showed that SIF_{687} lack predictive capability for nutrient content, potentially due to stronger fluorescence re-absorption and scattering within the canopy in the red spectral region. However, sub-nanometer data enabled the exploration of 16 FLs across 670–780 nm, among which far-red FLs (particularly FL_{16} at 774.8990 nm) exhibited significant potential, yielding robust N predictions ($R^2 = 0.62$, p-value < 0.001, NRMSE = 0.17) and comparable P estimation performance to SIF-based models ($R^2 = 0.36$-0.51, p-value < 0.001, NRMSE = 0.17-0.25). These findings highlight the potential of FLs, especially far-red FLs, obtained at the sub-nanometer resolution, for needle N and P estimations in coniferous canopies.

5.1 Introduction

Solar-induced chlorophyll fluorescence (SIF) has received growing attention over the past two decades as an indicator for plant photosynthesis and stress. When the incident solar radiation reaches the plant, it is either reflected, transmitted or absorbed by pigment systems. The absorbed photosynthetically active radiation (PAR) cannot be fully utilized for photochemistry. Consequently, plants need to dissipate the excitation energy through the other two pathways: thermal dissipation and chlorophyll fluorescence (ChlF). ChlF is the re-emission of absorbed energy by chlorophyll *a* at longer wavelengths, with the emission spectrum covering 650 to 800 nm characterized by two peaks – one in the red region (F_{685}) and the other in the far-red region (F_{740}). Red fluorescence is primarily contributed by photosystem II (PSII), and the far-red fluorescence emissions are ascribed to both PSI and PSII. Since both photosynthesis and chlorophyll fluorescence emission compete for PAR, ChlF can serve as a probe for the photosynthetic activities. The optical signal of ChlF can be remotely sensed under solar illumination (i.e., SIF), which is superimposed on the reflected radiation. However, SIF signals

only account for a small portion of the total reflected radiation - less than 2% and 5.2% of the reflected radiance at 685 nm and 740 nm, respectively (Guanter *et al.*, 2010), rendering difficulties in decoupling these two signals from remotely sensed hyperspectral data. More comprehensive reviews on the fluorescence basics are available (Meroni *et al.*, 2009; Frankenberg and Berry, 2017; Mohammed *et al.*, 2019).

The primary strategy of estimating SIF is associated with the SIF in-filling effect at strong absorption regions in the solar or telluric atmosphere. As the solar incident radiation is significantly attenuated in these narrow spectral regions, the relative contribution of SIF to the reflected radiation becomes more apparent. The widely investigated absorption features are the oxygen absorption bands in the terrestrial atmosphere, as they are broader and deeper than the solar absorption features or Fraunhofer lines (FLs). O_2-A absorption band around 760 nm is used to estimate far-red SIF due to its proximity to the far-red SIF (SIF_{760}), while the red SIF is retrieved from the O_2-B absorption band at 687 nm (SIF_{687}). Far-red SIF is more commonly retrieved than red SIF because the O_2-A absorption band is relatively broad, requiring lower sensor spectral resolution (SR), whereas sub-nanometer resolution is needed to observe the much narrower O_2-B band. On the other hand, FLs associated with solar atmospheric absorptions have not been comprehensively investigated, due to the requirement of ultra-high SR. However, SIF retrievals from FLs do not require complex atmospheric correction as the absorption happens in the solar atmosphere, unlike those from oxygen absorption bands in the terrestrial atmosphere, which is an important factor to consider in airborne or spaceborne applications. The most widely used algorithms to estimate SIF from restricted absorption features are based on the Fraunhofer Line Depth (FLD) principle (Plascyk and Gabriel, 1975), and its variants such as 3FLD (Maier *et al.*, 2004) and iFLD (GomezChova *et al.*, 2006). FLD-based methods rely on the contrast between the radiance levels within and outside the absorption feature to quantify SIF. Meroni *et al.* (2009) and Damm *et al.* (2011) provided detailed explanations and analysis of FLD-based approaches. Another extensively evaluated alternative for SIF retrievals from absorption features is the spectral fitting method (SFM), which decouples the fluorescence from the reflected radiation through mathematical parametric regressions (e.g., Guanter *et al.* (2010); Cendrero-Mateo *et al.* (2019); Albert *et al.* (2023)). SFM allows a more realistic representation of the reflectance and fluorescence spectrum within the absorption window, compared to FLD-based approaches. It is also less sensitive to sensor noise as more bands are used. The advancement in radiative transfer modelling (RTM) enabled the incorporation of leaf fluorescence in the simulations. Particularly, the SCOPE (Soil Canopy

Observation, Photochemistry and Energy Fluxes) model proposed by Van der Tol *et al.* (2009), which simulates SIF in vertically heterogeneous canopies, has been widely used in studying the relationship between SIF and photosynthesis (Zhang *et al.*, 2014; Verrelst *et al.*, 2016; Camino *et al.*, 2019). The leaf optical model Fluspect (Vilfan *et al.*, 2016), when coupled with canopy models such as the 3-D model DART (Discrete Anisotropic Radiative Transfer) (Gastellu-Etchegorry *et al.*, 2015), has also been used to study top-of-canopy (TOC) SIF (Regaieg *et al.*, 2025). These models incorporate the effects of canopy structure, illumination and observation geometry, thus enabling accurate SIF interpretation.

SIF retrieved from different platforms (e.g., ground, airborne and spaceborne) have been proven effective in detecting heat and water stress (Song *et al.*, 2018; Xu *et al.*, 2021; Wang *et al.*, 2023a), biotic stress (Calderón *et al.*, 2013; Zarco-Tejada *et al.*, 2018b; Zarco-Tejada *et al.*, 2021b), predicting leaf nutrient content (Camino *et al.*, 2019; Jia *et al.*, 2021; Wang *et al.*, 2022; Li *et al.*, 2025), and gross primary productivity (GPP) (Bacour *et al.*, 2019; Ma *et al.*, 2022; Pierrat *et al.*, 2024). Airborne platforms offer opportunities for on-demand monitoring of SIF with a higher spatial resolution than spaceborne platforms, and a larger spatial coverage than ground-level systems. However, the accurate SIF estimates from airborne sensors are challenging due to multiple sources of uncertainty. In particular, reliable SIF retrievals at the oxygen absorption features require proper accounting for atmospheric scattering and absorption (Guanter *et al.*, 2010; Damm *et al.*, 2014), since the atmospheric intervention adds noise to the true ratio between the reflected radiation and fluorescence emission within the absorption features, which might be confused with the SIF in-filling effects. Damm *et al.* (2014) also emphasized that the characterisation of atmospheric effects is intertwined with observational and illumination geometries. Canopy structure plays a key role in the correct interpretation of TOC SIF signals (Dechant *et al.*, 2020; Malenovský *et al.*, 2021a), due to the re-absorption and scattering of emitted fluorescence within the canopy. Compared to far-red SIF, red SIF undergoes significantly stronger re-absorption because of its substantial spectral overlap with chlorophyll absorption regions. In their study covering ground, airborne and spaceborne analysis, Dechant *et al.* (2020) suggest that far-red SIF is mainly affected by canopy structure and radiation rather than leaf physiology. They proposed an approximation of far-red SIF as the product of fluorescence quantum yield and NIR_vP, which is a parameter representing canopy effects and illumination conditions. NIR_vP was found to be strongly related to SIF at different temporal and spatial scales, indicating that observed variability in far-red SIF resulted from changes in canopy structure and radiation levels. Malenovský *et al.* (2021a) conducted

3-D model simulations for both crop and forest canopies. They found that the leaf clumping effect is the most influential factor in causing multi-angular anisotropy for both red and far-red SIF. They also highlighted the effects of non-photosynthetic woody material on forest canopy SIF due to the wood shadowing affecting the PAR absorption by leaves.

Sensor cacharcteristics affect SIF retrieval accuracy, as proven by simulation studies (Damm *et al.*, 2011; Julitta *et al.*, 2016). In particular, spectral resolution (SR) and signal-to-noise ratio (SNR) are the most influential factors in SIF retrievals at oxygen absorption features. It is shown that coarser spectral resolution and higher noise levels usually lead to more erroneous SIF estimates. Julitta *et al.* (2016) recommended the use of sub-nanometer resolution (FWHM < 1.0 nm) for the absolute measurement of far-red SIF at O_2-A band and ultrafine resolution (FWHM < 0.5 nm) for red SIF at O_2-B band. Nevertheless, higher spectral resolution is usually accompanied by higher noise levels and data redundancy. In the context of leaf nutrient status monitoring, far-red SIF retrieved at narrow-band resolution has been successfully used to estimate leaf nitrogen (N) content, along with other RTM-derived leaf biochemical parameters, in both homogenous (Camino *et al.*, 2019; Belwalkar *et al.*, 2022) and heterogenous canopies (Wang *et al.*, 2022; Li *et al.*, 2025). Furthermore, Belwalkar *et al.* (2022) compared the performance of far-red SIF quantified at narrow-band (FHWM = 5.8 nm) and sub-nanometer (FWHM = 0.1-0.2 nm) airborne images to explain leaf N variability in crops. The authors reported an improvement in prediction accuracy (ΔR^2 = 0.5, ΔRMSE = -0.03 %) for leaf N, ascribed to the sub-nanometer resolution, though they contended that narrow-band resolution is sufficient (R^2 = 0.87, *p*-value < 0.001, RMSE = 0.12 %) to differentiate the relative leaf N level across the site. However, such a comparison study has not been performed in more complex canopies, such as forests, to help determine whether sub-nanometer resolution is necessary for vegetation nutrient monitoring. Li *et al.* (2025) have shown that SIF_{760} quantified from narrow-band airborne images (FWHM = 5.8 nm), when combined with RTM-derived needle pigment content chlorophyll *a* + *b*, carotenoids and anthocyanins—yielded a prediction accuracy (R^2) greater than 0.56 for needle N and 0.66 for needle P in radiata pine plantation. The authors also highlighted that far-red SIF was the most dominant contributor to needle P assessment through the variable importance analysis. Building on these previous findings, this study aims to evaluate and compare airborne far-red SIF quantified at the narrow-band resolution (FWHM = 5.8 nm) and that at the sub-nanometer resolution (FWHM = 0.1-0.2 nm) in terms of their contributions to explaining the variability in needle N and P content in radiata pines. We aim to determine if narrow-band resolution is sufficient for SIF_{760} quantification in

monitoring needle nutrient status. The hypothesis is that sub-nanometer-based SIF_{760} is more accurate and thus contributes more to nutrient estimation. Furthermore, we explore other absorption features related to solar-induced fluorescence, such as red SIF (SIF_{687}) and solar FLs that are only apparent at the sub-nanometer resolution.

5.2 Methods

5.2.1 Airborne data collection and processing

Two airborne campaigns were conducted over the radiata pine study site in Durham, Victoria, on October 27th, 2021, and January 11th, 2023, with two line scanning hyperspectral imaging spectrometers onboard a piloted aircraft Cessna-172 operated by the HyperSens Laboratory, University of Melbourne. The first hyperspectral sensor was a Hyperspec VNIR E-Series model (Headwall Photonics, Fitchburg, MA, USA) with narrow-band resolution, covering the 400-1000 nm spectral region with a FWHM of 5.8 nm, with an FOV of 66°. The second hyperspectral sensor was a Solar-Induced Fluorescence imaging sensor (Headwall Photonics, Fitchburg, MA, USA), covering the SIF emission spectrum from 670-780 nm with an ultra-high spectral resolution of 0.1-0.2 nm FWHM, with an FOV of 23.5°. The two spectrometers were hereafter referred to as narrow-band imager and sub-nanometer sensors, respectively. More details of the spectral characteristics of the two hyperspectral imagers were summarised in Table 5.1. Narrow-band images and sub-nanometer images were collected at 350 m and 500 m above ground levels, respectively, resulting in a spatial resolution of 0.2 m for both imagers. Radiometric calibrations were performed for both imagers in an optics laboratory using a CSTM-USS-2000C integrating sphere (Labsphere, XTH2000C, Labsphere Inc., North Sutton, NH, USA). Atmospheric correction was further applied to the radiometrically calibrated narrow-band images using the SMARTS model (Gueymard, 1995b) with the aerosol optical depth measured at 550 nm by a Microtops II Sunphotometer (Solar Light Co., Philadelphia, PA, USA) during the airborne campaigns. The output of this step was the narrow-band reflectance images. Image orthorectification was implemented on all images using PARGE software (ReSe Applications Schlapfe, Wil, Switzerland) with the inputs recorded by the onboard inertial measuring unit (VN-300-VectorNav Technologies LLC, Dallas, TX, USA) and synchronized with the hyperspectral imager. More details on the image pre-processing can be found in Chapter 4. Fig. 5.1 presents an overview of the study site and an example of the sub-nanometer image.

Table 5.5 Spectral characteristics of the narrow-band and sub-nanometer sensors used in this study. *With spectral binning

	Headwall Hyperspec VNIR *E*-Series imager (Hyperspectral sensor)	Headwall Solar-Induced Fluorescence Imaging Sensor (Sub-nanometer sensor)
Spectral range	400-1000 nm	670-780 nm
Number of bands	371	2160
Spectral sampling interval	1.626 nm	0.051 nm
FWHM	5.8 nm	0.1-0.2 nm
Field of view	66°	23.5°
Signal-to-Nose Ratio	> 300:1*	> 300:1*
Bit depth	16	16

An object-based segmentation procedure was implemented on the narrow-band reflectance images image and radiance images from both narrow-band and sub-nanometer sensors using the Fiji software (Abràmoff *et al.*, 2004) to extract pure tree crowns. Local thresholding algorithms were applied to an NIR band (810 nm) and a structural index layer (NDVI > 0.6) in combination to separate the sunlit vegetation pixels from the soil background and within-crown shadows. The watershed algorithm was then applied to extract tree crown polygons. Delineated tree-crown polygons were further restricted to the central 25% area, considering the sensitivity of SIF to the illumination conditions and canopy structure (Zarco-Tejada *et al.*, 2013f; Malenovský *et al.*, 2021a). Due to the spatial misalignment between the narrow-band and sub-nanometer image, a manual selection process was then employed to identify and label trees that were visible in both images. This step ensured a fair comparison between narrow-band and sub-nanometer-based analysis. Eventually, 512 trees (n = 512) from 30 plots belonging to 9 treatments were selected for the 2021-Oct dataset. 576 trees (n = 576) from 33 plots belonging to 9 treatments were selected for the 2023-Jan dataset. The mean reflectance and radiance of the tree crowns in the same plot were used to represent the plot-level products.

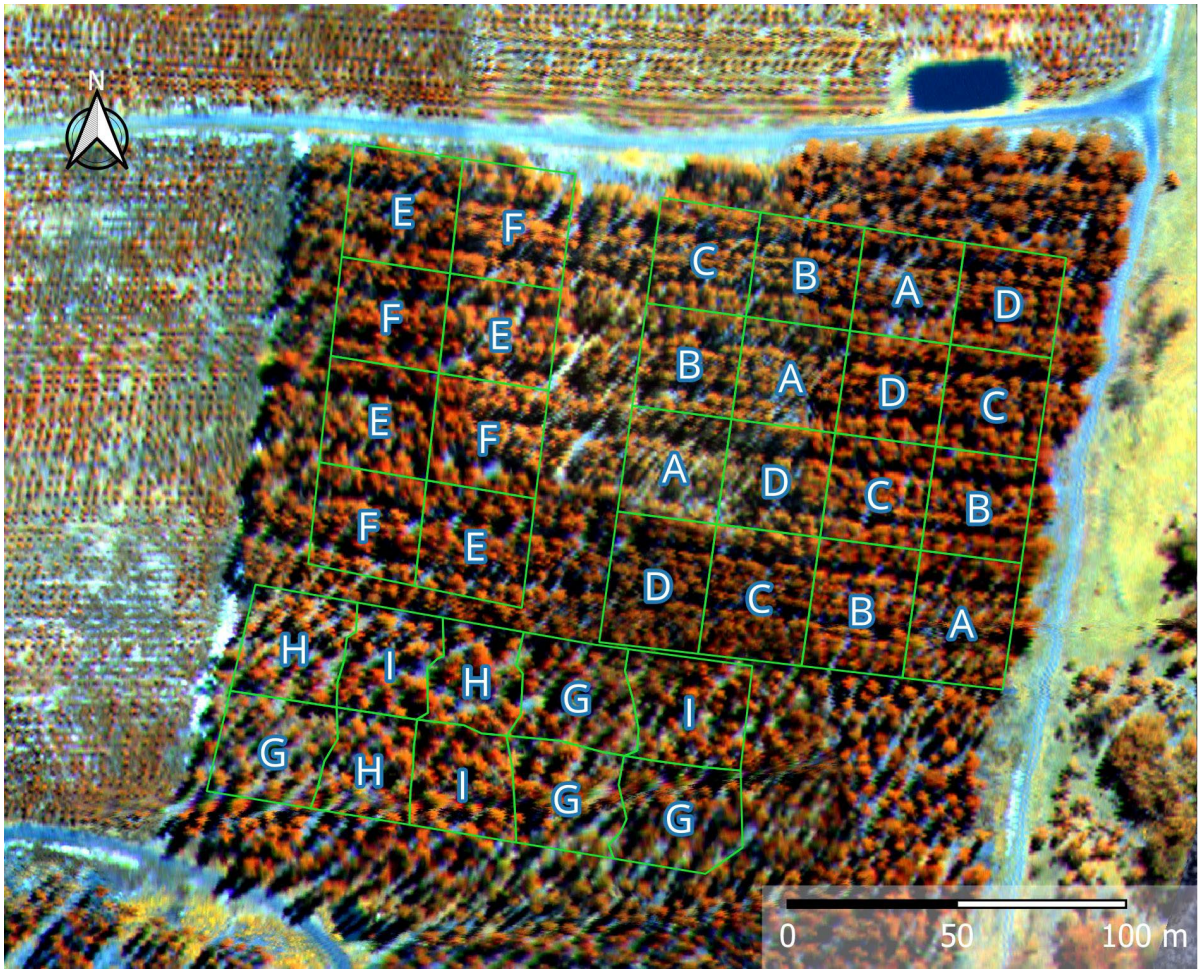

Fig. 5.16. Overview of the study site as shown in the sub-nanometer radiance mosaic (composite: 760 (R), 710 (G) and 680 (B) nm) obtained on October 27th, 2021. Plot boundaries are green. Letters A-I represent the treatment group. See Chapter 3 for more information on the study site.

5.2.2 SIF quantification

We implemented FLD-based methods for SIF quantification, as they are computationally efficient and well-established. 3FLD was used to quantify SIF at the O_2-A absorption feature (SIF_{760}), as the retrieval accuracy for far-red SIF based on the 3FLD method was less affected by sensor characteristics compared to other FLD-based methods (Damm *et al.*, 2011). While SIF_{760} was retrieved from both narrow-band and sub-nanometer data, SIF_{687} was only quantified at the sub-nanometer resolution, as the O_2-B absorption feature was not evident at the narrow-band resolution (Fig. 5.1). SIF_{687} was retrieved through the sFLD method, as the assumption of linear spectral variations in 3FLD was invalid for the O_2-B absorption region. It has also been found in the previous study that SIF_{687} retrieval errors through FLD-based

methods were highly dependent on the selection of absorption windows and reference shoulders, while sFLD was less affected than 3FLD (Cendrero-Mateo *et al.*, 2019).

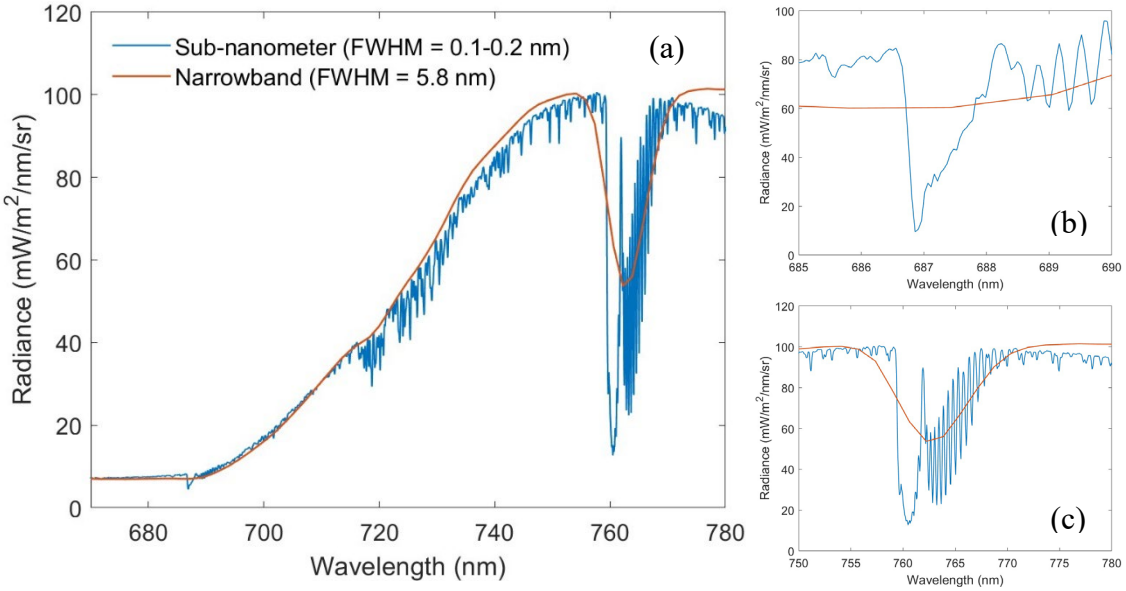

Fig. 5.17. Comparison between narrow-band and sub-nanometer radiance spectra extracted from one of the plots in the (a) fluorescence spectral region and zoomed-in views for the (b) O2-B (685-690 nm) and (c) O2-A absorption region (750-780 nm).

The general formulation of FLD-based chlorophyll fluorescence quantification can be expressed by:

$$F = \frac{L^{\uparrow}in - \frac{E^{\downarrow}in}{E^{\downarrow}out} L^{\uparrow}out}{1 - \frac{E^{\downarrow}in}{E^{\downarrow}out}} \qquad \text{Eq. 5.1}$$

Where F is the chlorophyll fluorescence in units of radiance. $L^{\uparrow}$ and $E^{\downarrow}$ are upwelling radiance and downwelling irradiance, respectively. Suffix in indicates the wavelength where the maximum absorption occurs in the absorption feature, while the suffix out is the reference wavelength outside the absorption feature. One reference band at the left shoulder of the absorption feature is required by the sFLD method. For the 3FLD method, one band at the left shoulder and one at the right shoulder are used to obtain the virtual reference band through linear interpolation at the maximum absorption wavelength.

The minimum radiance in the absorption window characterizes the maximum absorption wavelength. The reference band is determined by searching for the maximum radiance in the

reference shoulder intervals (Table 5.2). Considering the noises present in the sub-nanometer data, the mean values of the bands within 1-nm distance from the determined shoulder maximum are used to represent $L^{\uparrow}{}_{out}$ and $E^{\downarrow}{}_{out}$. The irradiance was recorded by the HR2000 spectrometer (Ocean Optics, Dunedin, FL, USA) concurrently with the flights. An empirical correction method was then employed to account for the atmospheric effects, using the non-fluorescent target (i.e., bare soil pixels) in the scene.

We also quantified the absolute depth of O_2-A and O_2-B absorption features by taking the difference between the maximum radiance on the left shoulder and the minimum radiance within the absorption window.

Table 5.6 Spectral intervals used to calculate SIF_{760} and SIF_{687} using FLD-based methods.

	Method	Left shoulder interval	Absorption window	Right shoulder interval
SIF_{760}	3FLD	750-755 nm	755-765 nm	771-776 nm
SIF_{687}	sFLD	684.5-685.5 nm	686-689 nm	-

5.2.3 Fraunhofer line identification and depth calculation

A total of 16 Fraunhofer lines (FLs) were identified in the spectral range from 670-780 nm from the sub-nanometer data (Fig. 5.3), with spectral regions heavily affected by water vapour and oxygen absorption avoided during the selection (Albert *et al.*, 2023; Belwalkar *et al.*, 2023). The FLs were further categorized into red FLs and far-red FLs based on their spectral locations, resulting in 5 red FLs and 11 far-red FLs. The absolute FL depth was defined as the difference between the left shoulder maximum radiance and the minimum radiance within the FL absorption feature. The minimum radiance was found within the pre-defined spectral interval (Table 5.3) for each FL. The local maxima within the 1-nm range to the bottom of the FL absorption feature were used as the left shoulder radiance.

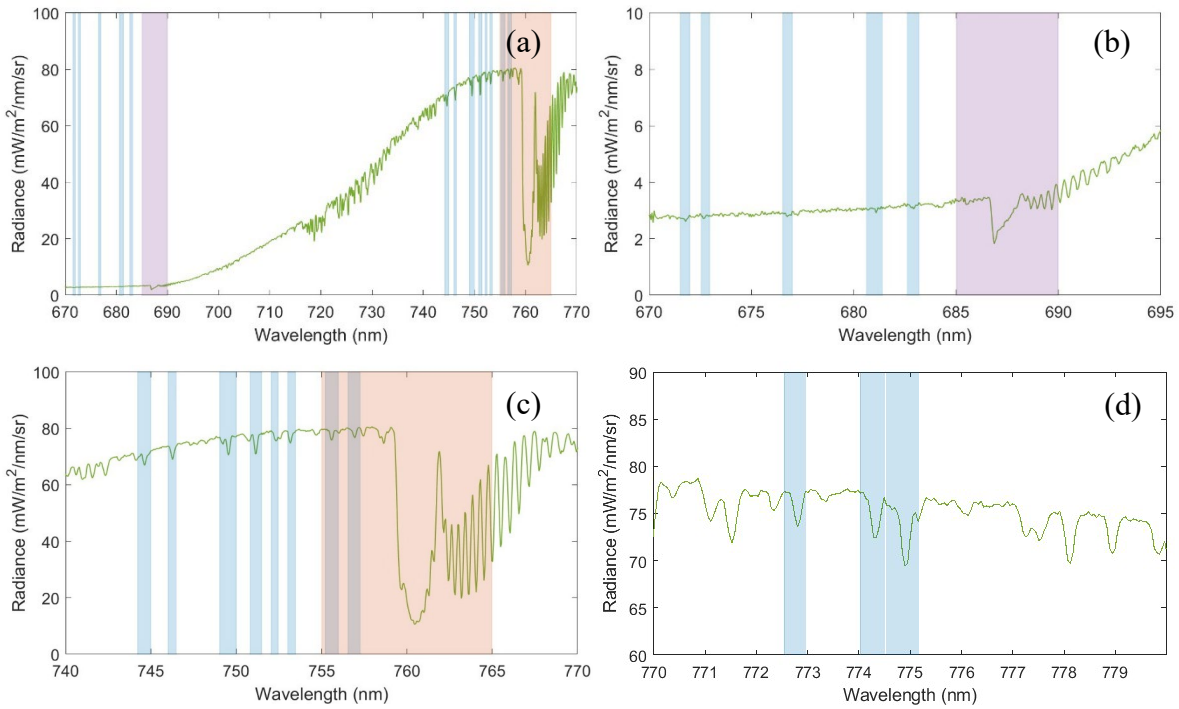

Fig. 5.18. Vegetation radiance spectrum (green lines) with sub-nanometer resolution (FWHM = 0.1-0.2 nm) overlaid with the selected 16 Fraunhofer lines (FLs) (blue shading), O_2-B absorption feature (purple shading) and O_2-A absorption feature (red shading) (a) across the 670-780 nm region; (b) zoomed-in view for five red FLs and O_2-B region; (c, d) zoomed-in view for 11 far-red FLs and O_2-A region. The width of the shaded area represents the spectral interval used to calculate depths of absorption features (FLs, O_2-A and O_2-B), SIF_{760} and SIF_{687}.

5.2.4 Plant trait retrieval from PRO4SAIL2 inversion

We retrieved leaf pigment content from the narrow-band reflectance data through the inversion of the RTM PRO4SAIL2 [PROSPECT-D + 4SAIL2] (Verhoef and Bach, 2007; Féret *et al.*, 2017) with a look-up-table (LUT) based approach. For each of the two narrow-band datasets of plot-mean reflectance, we generated a LUT with 500,000 simulations by running PRO4SAIL2 in the forward mode. To match the spectral characteristics of the narrow-band hyperspectral imager (400 – 1000 nm, FWHM = 5.8 nm), spectral convolution with a Gaussian function was then applied to the simulated spectra (400 – 2500 nm, FWHM = 1 nm). We also employed continuous wavelet transform (CWT) with the second-derivative Gaussian kernel to the simulated and observed spectra, as this method has been proven effective in decoupling overlapping absorption features such as leaf pigment. Inversion was then carried out on the transformed spectra by identifying the top 1% of simulated spectra that were most similar to the observations, as determined by the root mean square error (RMSE). From this process, we

retrieved needle chlorophyll *a* + *b* (C_{ab}), carotenoid (C_{ar}) and anthocyanins (A_{nth}) content for both datasets. Further details of PRO4SAIL2 inversion are provided in Chapter 4 and Li *et al.* (2025).

Table 5.7 Spectral intervals used to define FLs for the sub-nanometer data and the wavelength at the minimum radiance within the FL intervals. Note: the wavelength at the bottom of the FL is not fixed and may differ for different radiance spectra. The wavelengths listed in the table only represent the most frequently selected wavelengths in our datasets.

	Spectral interval (nm)	Wavelength at the minimum radiance (nm)
Red FLs		
FL_1	671.5-672.0	671.7770
FL_2	672.5-673.0	672.6404
FL_3	676.5-677.0	676.8390
FL_4	680.6-681.4	681.0820
FL_5	682.6-683.2	682.8702
Far-red FLs		
FL_6	744.2-745.0	744.6320
FL_7	746.0-746.5	746.2680
FL_8	749.0-750.0	749.5400
FL_9	750.8-751.5	751.1760
FL_{10}	752.0-752.5	752.3520
FL_{11}	753.0-753.5	753.1700
FL_{12}	755.2-756.0	755.6240
FL_{13}	756.5-757.3	756.9530
FL_{14}	772.5-773.0	772.8020
FL_{15}	774.0-774.5	774.3360
FL_{16}	774.5-775.2	774.8990

5.2.5 Needle N and P modelling

For each of the two datasets, Gaussian Process Regression (GPR) models (Rasmussen, 2004) were trained to predict concentrations of needle N and P at the plot level with various inputs. The benchmark model was selected based on results from Chapter 4, which included RTM-derived needle pigment content (i.e., C_{ab}, C_{ar}, A_{nth}) and $SIF_{760\text{-}narrow}$ as inputs. With a further focus on SIF evaluation in the needle nutrient monitoring context, we then replaced $SIF_{760\text{-}narrow}$ in the benchmark inputs with 1) $SIF_{760\text{-}subnano}$, 2) $SIF_{687\text{-}subnano}$. We further incorporated FL depths into the GPR input sets to understand the distinct contribution of red and far-red FL depths, and thus photosystem I and photosystem II, to explain needle N and P variabilities in radiata pines. More specifically, we built GPR models with inputs consisting of RTM-derived needle pigment content (i.e., C_{ab}, C_{ar}, A_{nth}) and 1) one red FL depth at a time; 2) one far-red FL depth at a time; 3) $O_2\text{-}A_{subnano}$ depth or $O_2\text{-}B_{subnano}$ depth; 4) any combination of one red FL and

one far-red FL depths; 4) $SIF_{760\text{-}subnano}$ and any of the 16 FL depths; and 5) SIF_{687} and any of the 16 FL depths.

The hyperparameters of the GPR algorithm were automatically tuned for each target variable with the Bayesian optimizer in MATLAB using the parallel computing toolbox (Statistics and Machine Learning toolbox; MathWorks Inc., Natick, MA, USA). The model performance was determined through a Leave-One-Out Validation (LOOV) procedure. The normalized root mean squared error (NRMSE), and the coefficient of determination (R^2) were used as the primary metrics for model prediction accuracy. NRMSE was calculated as the ratio between RMSE and the range of needle nutrient measurements of the dataset.

5.3 Results

5.3.1 SIF_{760} from narrow-band and sub-nanometer images

The preliminary analysis of O_2-A absorption band depths revealed a moderate relationship between two hyperspectral imagers for both datasets (R^2 = 0.63 and 0.54 for 2021-Oct and 2023-Jan datasets, respectively, *p*-value < 0.001) (Fig. 5.4a). $O_2\text{-}A_{subnano}$ depth displayed a higher magnitude (58-106 mW/m^2/nm/sr) than $O_2\text{-}A_{narrow}$ depth (24-57 mW/m^2/nm/sr), as the O_2-A absorption feature showed a shallower bottom at the narrow-band resolution than the sub-nanometer resolution (Fig. 5.1).

The narrow-band- and sub-nanometer-based SIF_{760} quantified through the 3FLD method were moderately correlated (Fig. 5.4b), with a higher R^2 observed in the 2021-Oct dataset (0.63, *p*-value < 0.001) than for the 2023-Jan dataset (0.51, *p*-value < 0.001). Notably, SIF_{760} quantified at the narrow-band resolution was significantly larger than their sub-nanometer counterparts: $SIF_{760\text{-}narrow}$ values were at least three times higher than $SIF_{760\text{-}subnano}$ values for the 2021-Oct dataset, and about two times higher for the 2023-Jan dataset. It should also be clarified that our retrievals of SIF_{760} from both hyperspectral imagers were higher than the expected values for healthy vegetation (0.5-3 mW/m^2/nm/sr).

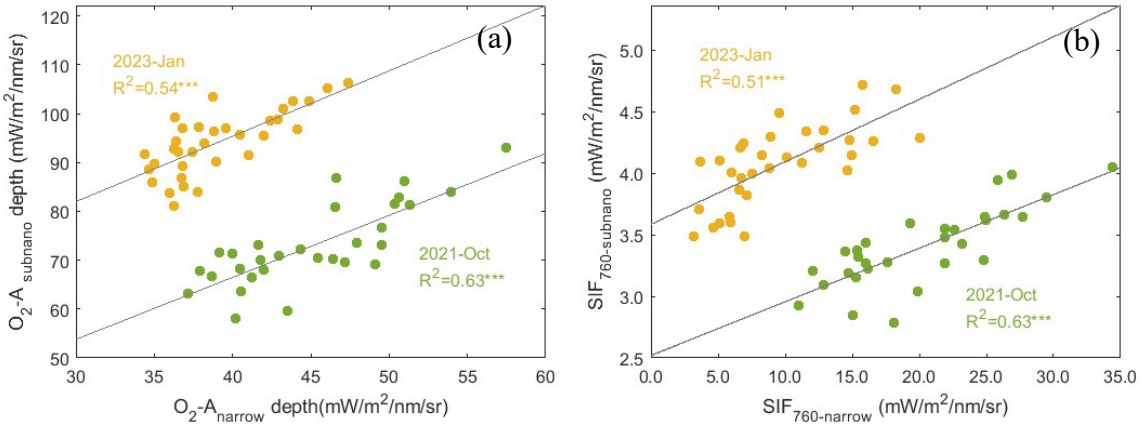

Fig. 5.19. Correlation (R^2) between (a) O_2-A absorption band depth and (b) SIF_{760} values from the narrow-band and sub-nanometer data for the 2021-Oct (green) and 2023-Jan (yellow) datasets at the plot level. ***p-value < 0.001; **p-value < 0.01; *p-value < 0.05; ns: not significant.

Regarding the O_2-B absorption region (Fig. 5.5a), we noted a narrower range of the O_2-B band depth in the 2023-Jan dataset (3.2-4.8 mW/m^2/nm/sr) than the 2021-Oct dataset (1.2-3.4 mW/m^2/nm/sr). Due to the different image acquisition dates and thus the differences in the illumination conditions, the band depths are not directly comparable. SIF_{687} determined by the sFLD method (Fig. 5.5b) showed a lower magnitude and narrower ranges for the 2021-Oct dataset (0.3-1.1 mW/m^2/nm/sr) than for the 2023-Jan dataset (2.2-3.2 mW/m^2/nm/sr).

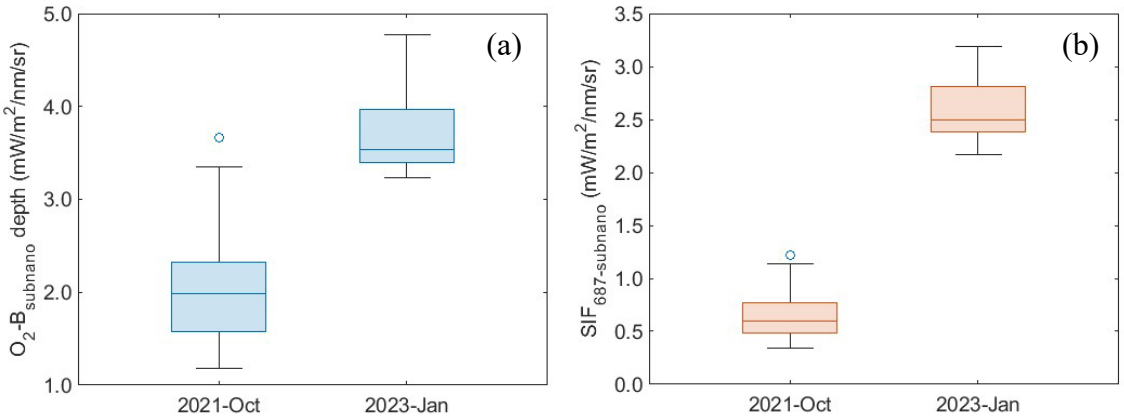

Fig. 5.20. Pairwise correlation (R^2) of sub-nanometer-based absorption features, including Fraunhofer line (FL) depths and O_2 absorption feature depths for the (a) 2021-Oct and (b) 2023-Jan datasets at the plot level.

5.3.2 Fraunhofer line depth and SIF_{687} from sub-nanometer images

The assessment of pairwise correlation for the depths of absorption features obtained from the sub-nanometer data, including FLs and O_2-A and O_2-B regions, is presented in Fig. 5.6. The pattern of strong correlation between depths of far-red absorption features (i.e., far-red FLs and O_2-A) were observed in both datasets, especially for features located between FL_7 to O_2-A region (746-760 nm) in the 2021-Oct dataset (Fig. 5.6a). By contrast, the pairwise comparison within the red spectral region (i.e., red FLs and O_2-B depths) showed weaker correlation in both datasets, potentially due to the strong influence of re-absorption by pigment in this region and the intrinsic sensor noise effects on subtle red absorption features. Furthermore, depths of red absorption features were weakly correlated with those in the far-red region, which was more distinct in the 2023-Jan dataset (Fig. 5.6b).

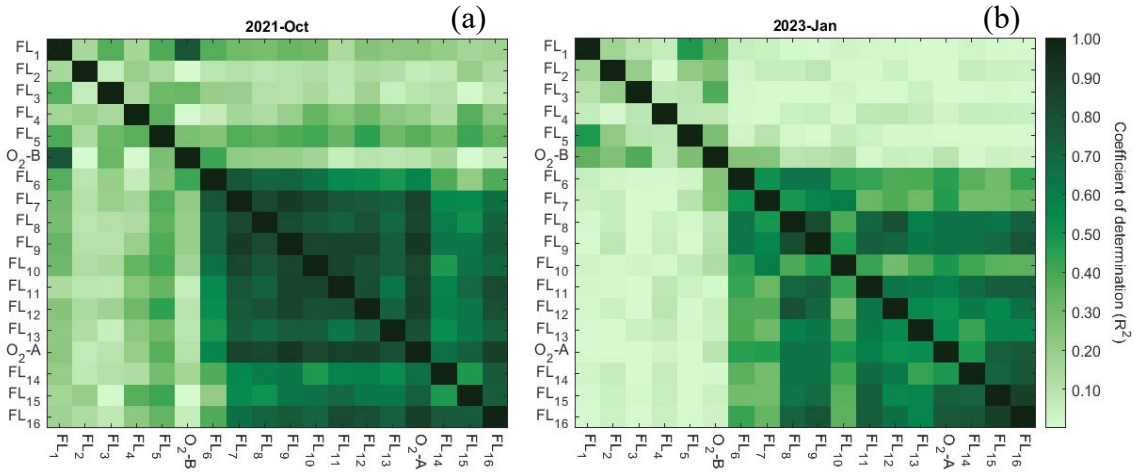

Fig. 5.21. Distributions of (a) O_2-B absorption feature depth and (b) SIF_{687} values quantified from sub-nanometer data for the 2021-Oct and 2023-Jan datasets at the plot level. The sample sizes (*n*) are 30 and 33 for the 2021-Oct and 2023-Jan datasets, respectively.

5.3.3 Model performance for needle N and P predictions

The linear relationships between variables, including SIF and depths of absorption features, and measured needle N and P concentrations, were evaluated before the GPR modelling process. Overall, all variables of interest were better correlated with needle P measurements than needle N (Table 5.4). A weak linear relationship ($R^2 < 0.2$) was consistently observed between needle N and all variables for both datasets, regardless of the spectral regions (i.e., red and far-red) or the spectral resolutions (i.e., narrow-band and sub-nanometer) from which those variables were derived. On the other hand, a stronger relationship was found between needle P measurements and SIF or band depths in the 2021-Oct dataset compared to the 2023-Jan dataset. Within each dataset, needle P was better related to far-red variables than the red variables

derived from the sub-nanometer data. For instance, $SIF_{760\text{-}subnano}$ presented an R^2 of 0.52 and 0.26 with needle P for the 2021-Oct and 2023-Jan datasets, respectively, while the correlation between $SIF_{687\text{-}subnano}$ and needle P was weaker (R^2 = 0.01 for 2021-Oct, and 0.05 for 2023-Jan). Similarly, the depth at the O_2-A absorption feature was more closely related to needle P in both datasets (R^2 = 0.36 and 0.19, respectively) than the O_2-B absorption depth (R^2 = 0.00 and 0.15, respectively).

Table 5.8 Correlation (R^2) between measured needle N and P concentrations and variables quantified from the sub-nanometer data (i.e., 16 Fraunhofer line [FL] depths and O_2-$B_{subnano}$ absorption band depth, $SIF_{687\text{-}subnano}$ and $SIF_{760\text{-}subnano}$) and variables quantified from the narrow-band data (i.e., O_2-A_{narrow} absorption band depth and $SIF_{760\text{-}narrow}$) for the 2021-Oct and 2023-Jan datasets at the plot level. The blue shading of the cell indicates the magnitude of R^2, with a darker color representing stronger correlation.

	Needle N (g/kg)		Needle P (g/kg)	
	2021-Oct	2023-Jan	2021-Oct	2023-Jan
FL_1	0.05	0.00	0.01	0.15
FL_2	0.00	0.08	0.01	0.08
FL_3	0.01	0.00	0.00	0.13
FL_4	0.00	0.01	0.03	0.06
FL_5	0.01	0.00	0.04	0.04
O_2-$B_{subnano}$	0.09	0.09	0.00	0.15
FL_6	0.05	0.06	0.06	0.00
FL_7	0.07	0.10	0.19	0.00
FL_8	0.07	0.01	0.24	0.04
FL_9	0.05	0.03	0.29	0.06
FL_{10}	0.02	0.00	0.17	0.01
FL_{11}	0.04	0.02	0.28	0.12
FL_{12}	0.02	0.00	0.34	0.06
FL_{13}	0.04	0.01	0.23	0.08
O_2-$A_{subnano}$	0.08	0.02	0.36	0.19
FL_{14}	0.19	0.00	0.21	0.09
FL_{15}	0.03	0.01	0.19	0.25
FL_{16}	0.10	0.00	0.36	0.22
$SIF_{760\text{-}subnano}$	0.05	0.01	0.52	0.26
$SIF_{687\text{-}subnano}$	0.06	0.13	0.01	0.05
$SIF_{760\text{-}narrow}$	0.07	0.00	0.46	0.44
O_2-A_{narrow}	0.07	0.00	0.47	0.37

Comparing variables obtained at different spectral resolutions, it is noticed that narrow-band-based variables (i.e., $SIF_{760\text{-}narrow}$ and O_2-A_{narrow}) generally had a stronger relationship with needle P than the sub-nanometer-based counterparts (i.e., $SIF_{760\text{-}subnano}$ and O_2-$A_{subnano}$) in both

datasets, with the only exception of needle P with SIF_{760} relationship for the 2021-Oct dataset (R^2 = 0.46 for $SIF_{760\text{-}narrow}$ vs 0.52 for $SIF_{760\text{-}subnano}$).

Needle N

Benchmarking against the narrow-band-based model developed in Chapter 4, N = f(C_{ab}, C_{ar}, A_{nth}, $SIF_{760\text{-}narrow}$), we evaluated whether sub-nanometer-based variables could further improve the needle N prediction accuracy by replacing the narrow-band-based SIF_{760} with SIF or absorption feature depths (i.e., FLs and O_2) derived from the sub-nanometer data. The performance of GPR models for needle N predictions is summarized in Table 5.5. It is apparent that none of the evaluated models yielded statistically significant or accurate prediction results for needle N in the 2023-Jan dataset. The probable cause is the lack of significant differences between needle N concentration measurements from various fertilization treatments in the specific dataset. More details of field data analysis are available in Chapter 3.

In the case of the 2021-Oct dataset, substituting the narrow-band-based SIF_{760} in the benchmark model [N = f(C_{ab}, C_{ar}, A_{nth}, $SIF_{760\text{-}narrow}$)] with the sub-nano-based values [N = f(C_{ab}, C_{ar}, A_{nth}, $SIF_{760\text{-}subnano}$)] did not significantly affect the prediction accuracy, with the NRMSE value of 0.20 for both models. The focused analysis of sub-nanometer data showed that variables quantified from the red region contributed less to the needle N predictions than those from the far-red region. When red SIF ($SIF_{687\text{-}subnano}$) was used in the GPR inputs, the prediction accuracy dropped dramatically ($\Delta R^2 \leq$ -0.19, ΔNRMSE = 0.04), as compared to the models built with far-red SIF ($SIF_{760\text{-}subnano}$). Similarly, the model with O_2-B band depth (R^2 = 0.30, p-value < 0.001, NRMSE = 0.25) was more erroneous than the one built with O_2-A band depth (R^2 = 0.47, p-value < 0.001, NRMSE = 0.22). Furthermore, the model with the best-performing red FL depth, N = f(C_{ab}, C_{ar}, A_{nth}, FL_4), produced lower accuracy (R^2 = 0.49, p-value < 0.001, NRMSE = 0.21) than N = f(C_{ab}, C_{ar}, A_{nth}, FL_{16}), the model with the best performing far-red FL depth (R^2 = 0.62, p-value < 0.001, NRMSE = 0.17). Notably, the latter was also the most accurate model among all for needle N predictions for the 2021-Oct dataset. It is also evident that all the models that outperformed the narrow-band-based benchmark for needle N predictions contained the depth of a far-red FL in the inputs. Moreover, the model with the best-performing combination of red and far-red FL depths, N = f(C_{ab}, C_{ar}, A_{nth}, FL_1, FL_{16}), showed a decrease in prediction accuracy due to the addition of the red FL_1 ($\Delta R^2 \leq$ -0.04, ΔNRMSE = 0.02), implying the adverse effects of red FL depths in explaining needle N variabilities in this study. Finally, it is important to emphasize that our results on needle N analysis might not be conclusive due to the limited availability of effective datasets.

Table 5.9 Performance of GPR models for needle N predictions at the plot level for the 2021-Oct and 2023-Jan datasets with inputs including PRO4SAIL2-derived needle pigment content (C_{ab}, C_{ar}, A_{nth}) from the narrow-band data; SIF_{760} and O_2-A absorption band depth quantified from sub-nanometer ($SIF_{760\text{-}subnano}$ and $O_2\text{-}A_{subnano}$) and narrow-band ($SIF_{760\text{-}narrow}$ and $O_2\text{-}A_{narrow}$) data; $SIF_{687\text{-}subnano}$, depths of Fraunhofer lines (FLs) and $O_2\text{-}B_{subnano}$ absorption feature calculated from the sub-nanometer data. *n* represents the sample size. ***p-value < 0.001; **p-value < 0.01; *p-value < 0.05; ns: not significant.

	2021-Oct (n = 30)		2023-Jan (n = 33)	
	R^2	NRMSE	R^2	NRMSE
Narrow-band-based models				
$N = f(C_{ab}, C_{ar}, A_{nth}, SIF_{760\text{-}narrow})$	0.56***	0.20	0.08^{ns}	0.23
$N = f(C_{ab}, C_{ar}, A_{nth}, O_2\text{-}A_{narrow})$	0.57***	0.19	0.06^{ns}	0.24
Sub-nanometer-based models				
$N = f(C_{ab}, C_{ar}, A_{nth}, SIF_{760\text{-}subnano})$	0.50***	0.20	0.03^{ns}	0.25
$N = f(C_{ab}, C_{ar}, A_{nth}, SIF_{687\text{-}subnano})$	0.31**	0.24	0.04^{ns}	0.24
$N = f(C_{ab}, C_{ar}, A_{nth}, O_2\text{-}A_{subnano})$	0.47***	0.22	0.08^{ns}	0.23
$N = f(C_{ab}, C_{ar}, A_{nth}, O_2\text{-}B_{subnano})$	0.30**	0.25	0.24**	0.22
$N = f(C_{ab}, C_{ar}, A_{nth}, FL_4)$	0.49***	0.21	0.10^{ns}	0.23
$N = f(C_{ab}, C_{ar}, A_{nth}, FL_{16})$	0.62***	0.17	0.16*	0.22
$N = f(C_{ab}, C_{ar}, A_{nth}, FL_1, FL_{16})$	0.58***	0.19	0.13^{ns}	0.22
$N = f(C_{ab}, C_{ar}, A_{nth}, SIF_{760\text{-}subnano}, FL_{16})$	0.57***	0.19	0.11^{ns}	0.23
$N = f(C_{ab}, C_{ar}, A_{nth}, SIF_{687\text{-}subnano}, FL_{12})$	0.49***	0.20	0.01^{ns}	0.25

Needle P

Overall, higher prediction accuracies were obtained for needle P predictions than for needle N for both datasets (Table 5.6). The narrow-band-based benchmark $P = f(C_{ab}, C_{ar}, A_{nth}, SIF_{760\text{-}narrow})$ showed a significant advantage over any of the sub-nanometer-based models for the 2021-Oct datasets, with an R^2 of 0.69 (p-value < 0.001) and a NRMSE value of 0.13. For the 203-Jan dataset, the advantage of the benchmark model was less evident, as two sub-nanometer-based models produced similar prediction accuracy (R^2 = 0.49-0.50, p-value < 0.001, NRMSE = 0.21-0.22): $P = f(C_{ab}, C_{ar}, A_{nth}, O_2\text{-}A_{subnano})$ and $P = f(C_{ab}, C_{ar}, A_{nth}, SIF_{760\text{-}subnano}, FL_{14})$. The replacement of narrow-band-based SIF_{760} with the sub-nanometer-based SIF_{760} in the GPR model inputs resulted in a reduction in needle P prediction accuracy for both datasets (ΔR^2 = -0.20 and -0.14, ΔNRMSE = 0.04 and 0.03, for 2021-Oct and 2023-Jan, respectively).

Table 5.10 Performance of GPR models for needle P predictions at the plot level for the 2021-Oct and 2023-Jan datasets with various inputs: PRO4SAIL2-derived needle pigment content (C_{ab}, C_{ar}, A_{nth}) from the narrow-band data; SIF_{760} and O_2-A absorption band depth quantified from sub-nanometer ($SIF_{760\text{-}subnano}$ and $O_2\text{-}A_{subnano}$) and narrow-band ($SIF_{760\text{-}narrow}$ and $O_2\text{-}A_{narrow}$) data; $SIF_{687\text{-}subnano}$, depths of Fraunhofer lines (FLs) and $O_2\text{-}B_{subnano}$ absorption feature calculated from the sub-nanometer data. *n* represents the sample size. ****p*-value < 0.001; ***p*-value < 0.01; **p*-value < 0.05; ns: not significant.

	2021-Oct (*n* = 30)		2023-Jan (*n* = 33)	
	R^2	NRMSE	R^2	NRMSE
Narrow-band-based models				
$P = f(C_{ab}, C_{ar}, A_{nth}, SIF_{760\text{-}narrow})$	0.69***	0.13	0.49***	0.22
$P = f(C_{ab}, C_{ar}, A_{nth}, O_2\text{-}A_{narrow})$	0.61***	0.15	0.50***	0.22
Sub-nanometer-based models				
$P = f(C_{ab}, C_{ar}, A_{nth}, SIF_{760\text{-}subnano})$	0.49***	0.17	0.35***	0.25
$P = f(C_{ab}, C_{ar}, A_{nth}, SIF_{687\text{-}subnano})$	0.19*	0.23	0.22**	0.27
$P = f(C_{ab}, C_{ar}, A_{nth}, O_2\text{-}A_{subnano})$	0.49***	0.18	0.50***	0.21
$P = f(C_{ab}, C_{ar}, A_{nth}, O_2\text{-}B_{subnano})$	0.17*	0.22	0.33***	0.25
$P = f(C_{ab}, C_{ar}, A_{nth}, FL_1)$	0.37***	0.20	0.34***	0.25
$P = f(C_{ab}, C_{ar}, A_{nth}, FL_{16})$	0.51***	0.17	0.36***	0.25
$P = f(C_{ab}, C_{ar}, A_{nth}, FL_3, FL_{16})$	0.46***	0.18	0.45***	0.23
$P = f(C_{ab}, C_{ar}, A_{nth}, SIF_{760\text{-}subnano}, FL_{14})$	0.49***	0.18	0.52***	0.21
$P = f(C_{ab}, C_{ar}, A_{nth}, SIF_{687\text{-}subnano}, FL_{12})$	0.46***	0.18	0.31***	0.25

Among the sub-nanometer-based models, the superiority of far-red variables over red variables for needle P predictions was observed. There was a decrease in needle P prediction accuracy when the red SIF ($SIF_{687\text{-}subnano}$) was used alongside PRO4SAIL2-derived pigments as inputs for the GPR models (R^2 = 0.19 and 0.22, NRMSE = 0.23 and 0.27, for 2021-Oct and 2023-Jan, respectively), as opposed to the case where the far-red SIF ($SIF_{760\text{-}subnano}$) was added (R^2 = 0.49 and 0.35, NRMSE = 0.17 and 0.25). A similar level of discrepancy in needle P prediction performance was found between the model with $O_2\text{-}B_{subnano}$ depth and the one with $O_2\text{-}A_{subnano}$ depth, with the latter showing higher accuracy for both datasets. Comparing the FL-involved models, the model with the best-performing red FL depth (i.e., FL_1) yielded relatively poor accuracies for both datasets (R^2 = 0.37 and 0.34, *p*-value < 0.001, NRMSE = 0.20 and 0.25 for 2021-Oct and 2023-Jan, respectively). The model with the best-performing far-red FL depth (i.e., FL_{16}) was the most accurate for the 2021-Oct dataset (R^2 = 0.51, *p*-value < 0.001, NRMSE = 0.17). Moreover, when pigments and SIF (e.g., $SIF_{687\text{-}subnano}$ or $SIF_{760\text{-}subnano}$) were fixed in the GPR inputs and one FL depth was added to the input set at a time, the best-performing FL

depths selected were both in the far-red region (e.g., FL_{12} and FL_{14}), demonstrating the importance of far-red FL depths in needle P predictions over red FL depths.

5.4 Discussion

Our results based on two datasets suggest that the sub-nanometer-based SIF_{760} did not further contribute to the needle P prediction accuracy than the narrow-band-resolved SIF_{760} already did, when SIF_{760} was used as the input of GPR predictive models along with needle pigment content derived from PRO4SAIL2. It remains inconclusive whether the sub-nanometer resolution would contribute more compared with SIF_{760} as a predictor for needle N content, due to the limited availability of needle N measurements. These results on P estimations are against our hypothesis that SIF_{760} quantified at the sub-nanometer resolution can provide more information on needle nutrient status than that from the narrow-band resolution. The hypothesis is established on the findings from simulation studies (Damm *et al.*, 2011; Belwalkar *et al.*, 2022) that finer spectral resolutions enable more accurate quantification of SIF at the O_2-A absorption region through 3FLD methods. Our findings also contradict those of a previous study on the application of airborne SIF for leaf N assessment in crop canopies. Belwalkar *et al.* (2022) found that SIF_{760} quantified from sub-nanometer images (FWHM = 0.1-0.2 nm) contributed more than SIF_{760} from narrow-band images (FWHM = 5.8 nm) to the leaf N predictions, when used as machine learning regression model inputs along with RTM-derived leaf chlorophyll $a + b$ content (R^2 = 0.93 vs 0.87, RMSE = 0.09 vs 0.12). Additionally, we observed only moderate correlation (R^2 = 0.51 and 0.63, for 2021-Oct and 2023-Jan datasets, respectively) between the narrow-band-based and sub-nanometer-based SIF_{760}, lower than the correlation reported by Belwalkar *et al.* (2022). The reduced agreement in our study can be partially attributed to the segmentation process, which introduced spatial and spectral discrepancies in the tree crowns extracted from narrow-band and sub-nanometer images (e.g., pixel mixture and tree crown sizes), and the canopy complexities.

The deviation of our results from the initial hypothesis or previous studies can be partially explained by the SIF_{760} retrieval accuracy from both imagers, which subsequently affected the needle nutrient predictions. The retrievals, either from narrow-band or sub-nanometer images, were beyond the expected ranges for far-red SIF (0.5-3 $mW/m^2/nm/sr$). Higher values of SIF_{760} were consistently obtained from narrow-band images, which can be explained by the coarser spectral resolution. This is consistent with findings from previous studies (Damm *et al.*, 2011;

Julitta *et al.*, 2016; Cendrero-Mateo *et al.*, 2019; Belwalkar *et al.*, 2022) that narrow-band resolution (FWHM > 1 nm) results in overestimates of FLD-based SIF_{760} values. Therefore, SIF_{760} retrievals in this study can only be considered as relative indicators of plant physiological responses induced by various fertilization levels across the study site, instead of as absolute quantifications of SIF. In practice, absolute errors in airborne SIF estimates could hardly be quantified, unless sophisticated radiative transfer modelling is involved. Some airborne-based studies (Damm *et al.*, 2014; Belwalkar *et al.*, 2022) employed SIF quantified from ground-level TOC spectral measurements from handheld spectrometers as the baseline values, as they are free of errors related to atmospheric effects and observation geometry. This strategy is less practical in our case, given the heights and shape of radiata pine trees. Some studies also use steady-state chlorophyll fluorescence measured by active techniques (e.g., fluorometers) at the leaf level to compare with the canopy-level SIF retrievals (Zarco-Tejada *et al.*, 2013a; Hernández-Clemente *et al.*, 2017a; Wang *et al.*, 2022). However, the leaf chlorophyll measurements do not always strongly correlate with the airborne TOC SIF due to the differences in active and passive measuring mechanisms and the scale mismatch (Cendrero-Mateo *et al.*, 2016). Additionally, the special circumstances of coniferous canopy restrain the implementation of *in-situ* steady-state fluorescence measurements, such as the canopy height and the small foliar surface area. The latter renders the use of leaf clips more challenging for fluorometer measurements. In summary, the comparison between airborne narrow-band- and sub-nanometer-based SIF_{760} lacks validity, as the accuracy of SIF_{760} estimates remains unknown. Future research could use drones to acquire low-altitude TOC spectral measurements as an alternative to validate SIF_{760} obtained by a piloted aircraft at a higher altitude.

Airborne SIF retrieval accuracy at O_2 absorption features is known to be susceptible to atmospheric effects. Non-fluorescent targets, such as bare soil pixels, have been used in the current and previous studies to account for the atmospheric effects and observational geometry, to correct the out-of-range SIF estimates (Damm *et al.*, 2014; Belwalkar *et al.*, 2022; Wang *et al.*, 2022). However, our post-correction SIF values are still higher than expected, implying the insufficiency of such an empirical atmospheric correction method in our case. It is recommended that the reference soil target be in the vicinity of the plant target with a similar radiance level (Guanter *et al.*, 2010; Damm *et al.*, 2014). Both studies used a spatially interpolated soil layer as a reference to guarantee high spatial adjacency. However, the vicinity criterion was hardly met in our analysis since barely any clear soil targets were identified closer to the trees. Instead, they were located along the road as shown in the scene. We recommend

implementing radiative transfer modelling for comprehensive atmospheric correction for heterogeneous canopies in the future.

We found $SIF_{687\text{-}subnano}$ was poorly related to needle N and P status in both datasets, compared to other sub-nanometer-derived variables. This aligns with the previous study by Belwalkar *et al.* (2023), where SIF_{687} contributed little to the leaf N estimations when used as GPR model inputs alongside RTM-derived leaf C_{ab} content. The authors contend that the collinearity between SIF_{687} and C_{ab} resulted in the low prediction accuracy. Nevertheless, we did not notice strong correlations between $SIF_{687\text{-}subnano}$ and any RTM-derived needle pigment in our datasets. Several factors could partially explain the limited contribution of SIF_{687} for needle nutrient assessment. First, the sFLD method used in this study did not account for canopy re-absorption and scattering effects on SIF_{687}. It is known that leaf chlorophyll fluorescence emitted in the red spectral region suffers more from chlorophyll re-absorption, compared to fluorescence emitted in the far-red region. The coniferous canopy structure further complicates the interpretation of at-sensor SIF_{687} signals. Second, red SIF retrievals based on the FLD principle are prone to errors. Cendrero-Mateo *et al.* (2019) evaluated uncertainties in red SIF retrievals through various methods, including sFLD, 3FLD, iFLD and SFM, against model-simulated chlorophyll fluorescence at the red peak. Their results indicated that both sFLD and 3FLD methods produced less accurate red SIF retrievals than more advanced methods such as iFLD and SFM. The selection of shoulder wavelengths and the definition of absorption windows were identified as the major sources of errors in FLD-based retrievals. Given all these complexities, we suggest the use of advanced RTMs such as SCOPE, Fluspect coupled with canopy model (e.g., 4SAIL2 and FLIGHT) for SIF_{687} quantification in heterogeneous canopies in the future.

FL absorption features, which are largely unaffected by atmospheric effects, provide an opportunity to track the response of chlorophyll fluorescence emissions to abiotic stressors without requiring complex atmospheric correction. Our results indicate that far-red FL depths contribute more to the needle N and P estimation than the depths of red FLs. The GPR model built with RTM-derived pigment (i.e., C_{ab}, C_{ar}, and A_{nth}) and FL_{16} (774.8990 nm) provided improved prediction accuracy for both needle N (R^2 = 0.62, *p*-value < 0.001, NRMSE = 0.17) and P (R^2 = 0.36-0.51, *p*-value < 0.001, NRMSE = 0.17-0.25), compared to the models with sub-nanometer-based SIF and red FL depths. This may be attributed to the generally deeper and wider absorption feature in the far-red region, making far-red FL depths less sensitive to noise and spectral shifting effects. From a physiological perspective, the stronger association

between far-red FL depths and needle nutrient status likely reflects the involvement of both photosystems in stress responses. While the fluorescence in the red region is primarily contributed by PSII, the far-red spectral region is influenced by chlorophyll fluorescence emissions from both PSI and PSII. In conclusion, these results indicate the potential of FL depths, especially far-red FLs, obtained at the sub-nanometer resolution, for needle N and P monitoring in coniferous canopies. Future research could more extensively evaluate various combinations of FL depths, with or without RTM-derived traits, in the context of needle N and P estimations.

5.5 Conclusions

Built upon previous findings that RTM-derived needle pigment content and far-red SIF (SIF_{760}) quantified from airborne narrow-band (FWHM = 5.8 nm) images are effective predictors for needle N and P concentrations in radiata pines, this study focused on the comparison of SIF obtained from narrow-band and sub-nanometer (FWHM = 0.1-0.2 nm) images and their impact on needle N and P estimation, using two datasets. We also investigated the contribution of FLs that were only evident at sub-nanometer resolution to the assessment of needle N and P concentration. Our results showed that the sub-nanometer resolution did not further improve the contribution of SIF_{760} to needle N and P estimations, compared to the narrow-band-based benchmark model with RTM-derived pigment content and SIF_{760} as inputs. These findings contradicted our hypothesis that finer spectral resolution enables more accurate SIF_{760} retrievals, which subsequently contribute more to the needle N and P estimation. However, as the uncertainties in the SIF_{760} retrievals from both imagers could not be quantified in this study, it remains inconclusive whether sub-nanometer resolution is superior to the narrow-band resolution for SIF_{760} application in needle N and P estimations. Potential sources of errors in SIF_{760} estimates include atmospheric effects, viewing geometry and errors related to the applied 3FLD method. For future research in heterogeneous coniferous canopies, we recommend using SIF (red and far-red) retrieved from low-altitude drone-acquired sub-nanometer spectral measurements as the baseline to validate SIF estimates from higher altitudes. Atmospheric RTMs should be implemented to account for the atmospheric effects and viewing geometry properly.

The sub-nanometer resolution provided the valuable opportunity to explore red SIF (SIF_{687}) and FLs for needle nutrient assessment. We found that SIF_{687} was ineffective in explaining

needle N and P variabilities. This could be partially attributed to the canopy re-absorption and scattering effects for red fluorescence, as well as the retrieval errors embedded in the sFLD method, which collectively complicated the interpretation of at-sensor SIF_{687}. It is suggested that advanced leaf-canopy RTMs should be employed in the future to obtain more reliable SIF_{687} estimates. The analysis of 16 FLs spanning between 670 and 780 nm revealed that far-red FL depths contributed more than red FL depths to both needle N and P estimations. More specifically, when combined with narrow-band-based RTM-derived pigments as GPR model inputs, the depth of FL_{16} (774.8990 nm) yielded the highest needle N prediction accuracy (R^2 = 0.62, *p*-value < 0.001, NRMSE = 0.17) for the 2021-Oct dataset, and provided needle P prediction accuracy that was comparable to the models with sub-nanometer-based far-red SIF for both datasets (R^2 = 0.36-0.51, *p*-value < 0.001, NRMSE = 0.17-0.25). Overall, our results indicate the potential of FL depths, especially far-red FL depths, obtained at the sub-nanometer resolution, for needle N and P estimations in coniferous canopies.

Chapter 6
Comparison of multispectral bandsets vs. hyperspectral data for needle nitrogen and phosphorus assessment in radiata pines

Highlights

- Hyperspectral-based models have demonstrated their superiority over multispectral-based models for needle N and P monitoring.
- Multispectral bandsets covering the VNIR range are better suited for needle P estimation than N.
- We proposed a 12-band bandset with 10-nm FWHM for needle P assessment, which outperformed the 10-band commercial MicaSense RedEdge-MX Dual camera bandset.

Abstract

Hyperspectral remote sensing provides rich information for assessing physiological changes experienced under needle nitrogen (N) and phosphorus (P) deficiency in radiata pine forests. However, the high monetary and computational costs of hyperspectral images prohibit their application in operational monitoring at large scales. Multispectral cameras could be a cost-effective alternative for such purposes. Nevertheless, their coarser spectral resolution and limited number of bands restrict their capability to fully capture the subtle spectral features associated with needle nutrient variabilities. Therefore, optimal bandsets must be selected for specific objectives (i.e., estimation of needle N and P content in this case) to guide the bandset design and future development of multispectral cameras.

In this study, we assessed the utility of multispectral data (Full Width at Half Maximum (FWHM) ≥ 10nm) for explaining needle N and P variability, against benchmark models built with narrow-band hyperspectral data (FWHM = 5.8 nm) covering the visible-near infrared

(VNIR) region. We investigated whether the commercially available 10-band multispectral camera Micasense Dual-MX System (FWHM = 10-54 nm) could be used for needle N and P assessment. Furthermore, we explored if other multispectral bandsets with 10-nm FWHM could yield higher accuracy for needle N and P estimation compared with the standard Micasense bandset, using the narrow-band-convolved FWHM-10nm data. Using four datasets collected over three years at a nutrient experiment site of radiata pines, we developed Gaussian Process Regression (GPR) algorithm to estimate needle N and P using multispectral reflectance as inputs. Three sources of multispectral data were investigated: 1) Micasense data with 10 bands acquired during two airborne campaigns in 2023; 2) Simulated Micasense data derived through convolving narrow-band data collected over four airborne campaigns from 2021 to 2023; 3) the proposed optimal multispectral bandsets with a 10-nm FWHM derived from the same four narrow-band datasets. Optimal multispectral bandsets were selected through a clustering-based approach where the redundant bands were removed, and informative bands were retained for successfully explaining needle N and P variability. The N/P prediction performance of these multispectral-based models were compared with that of the hyperspectral-based benchmark models, of which the GPR inputs included four parameters retrieved from the narrow-band data: needle chlorophyll $a + b$, carotenoid and anthocyanin content derived from the radiative transfer model (RTM), PRO4SAIL2 applied to pure crown vegetation pixels, and far-red solar-induced fluorescence (SIF_{760}) quantified through the 3FLD method.

We found that narrow-band hyperspectral-based benchmark models built with physiological traits displayed a more consistent prediction performance for both needle N (R^2 = 0.41-0.53, NRMSE = 0.20-0.24, p-value < 0.001) and P (R^2 = 0.52-0.77, NRMSE = 0.12-0.21, p-value < 0.001), compared with all multispectral-based models evaluated. We did not identify any multispectral-based model with robust prediction performance for needle N across datasets, with the best performance achieved by the model built with a proposed bandset (named as BS12N2) consisting of 12 bands at 10-nm FWHM (R^2 = 0.17-0.53, NRMSE = 0.19-0.30, p-value < 0.05). However, multispectral-based models were better suited for explaining the variability in needle P than needle N, in terms of the prediction robustness and accuracy across datasets. The newly proposed 12-band bandset BS12P (R^2 = 0.37-0.72, NRMSE = 0.13-0.25, p-value < 0.01) outperformed the simulated 10-band Micasense bandset (R^2 = 0.26-0.62, NRMSE = 0.15-0.27, p-value < 0.05) for needle P prediction for four datasets. These results suggest thatdespite the slight compromise in model accuracy compared to the hyperspectral-

based benchmark, the proposed 12-band bandset with 10 nm FWHM, BS12P, could potentially be used for the development of a multispectral camera specifically for needle P estimation on an operational scale.

6.1 Introduction

Pinus radiata D. Don (radiata pines) is extensively planted as the main softwood species worldwide, as well as in Australia. The wood productivity is prone to the effects of nutrient deficiency, such as nitrogen (N) and phosphorus (P) (Turner and Lambert, 1986). More specifically, needle N status has been found closely related to wood density and latewood percentage (Beets *et al.*, 2001a). Insufficient N and P supply results in premature shedding of needles, stunted stem growth, decreased branch production and thin crowns (Will and Hodgkiss, 1977; Nambiar and Fife, 1987a). Precise and accurate monitoring of needle nutrient status, of N and P, is critical for optimising wood production of radiata pines.

The advancement in hyperspectral remote sensing using narrow-band hyperspectral sensors (Full width at half maximum [FWHM] < 10 nm) has provided abundant and detailed spectral information on ground targets (e.g., plants), enabling the quantification of plant biophysical and biochemical parameters closely related to nutrient status. Recent studies have shown that leaf pigment content (e.g., chlorophyll a + b, carotenoid and anthocyanins) retrieved from radiative transfer model (RTM) inversion and far-red solar-induced fluorescence (SIF) derived from airborne hyperspectral data are informative indicators of leaf N or P status (Belwalkar *et al.*, 2022; Wang *et al.*, 2022; Li *et al.*, 2024). However, several factors are hindering the application of hyperspectral imagery in the operational-scale monitoring of leaf nutrient status on a regular basis. First, the vast data volume imposes high computational costs and requires expertise and domain knowledge for data analysis and interpretation. Second, the higher cost of hyperspectral cameras contributes to their lower popularity in practical applications. Furthermore, the weights of hyperspectral cameras usually exceed the payloads of unmanned aerial vehicles (UAVs), restricting their suitability for UAV applications (Nex *et al.*, 2022). Alternatively, multispectral cameras with usually 4 to 12 bands offer the advantages of affordability, lightweight and smaller data volume for processing. Nevertheless, these benefits inevitably come at the expense of information loss due to the coarser spectral resolution.

Multiple studies have thus focused on comparing the performance of multispectral and hyperspectral cameras for estimating plant biochemical and biophysical parameters. For instance, Zhou *et al.* (2022) reported a more significant advantage of hyperspectral data (R^2 = 0.78) compared with the simulated data ($R^2 \leq 0.35$) of three commonly used five-band multispectral cameras (i.e., P4 Multispectral, Parrot Sequoia+ and MicaSense RedEdge MX) in the application of potato leaf N concentration estimation. Lee *et al.* (2004) evaluated AVIRIS hyperspectral data and AVIRIS-derived Landset ETM+ and MODIS data for leaf area index (LAI) retrievals in various biomes and concluded that hyperspectral AVIRIS data with selected wavelengths offered the best accuracy among all. Guo *et al.* (2023) demonstrated that the UAV-acquired hyperspectral data yielded higher accuracy (ULTRIS X20 Plus, R^2 = 0.86) than the acquired multispectral data (DJI Phantom 4, R^2 = 0.75) for LAI estimation in maize. In some cases, multispectral data can provide comparable modelling performance to hyperspectral data, questioning the necessity of expensive hyperspectral imagery. Lu *et al.* (2019) simulated MicaSense RedEdge-MX image from hyperspectral data and found that the hyperspectral-based model only achieved a marginally higher accuracy (R^2 = 0.81) for leaf chlorophyll estimation than the model based on the simulated multispectral data (R^2 = 0.80). Croft *et al.* (2015) reported similar accuracy for leaf chlorophyll content estimation from hyperspectral data and simulated Landsat 5 TM data (R^2 = 0.77 and 0.75, respectively). It should be noted that, in most cases mentioned above, researchers used simulated multispectral images derived from the obtained hyperspectral data to avoid discrepancies caused by environmental and instrumental effects, thereby ensuring a fair comparison. In short, there is no universal answer to the question of whether hyperspectral cameras are superior to multispectral cameras for certain modelling purposes. The answer is specific to the modelling process, the target variable to be retrieved, the band center and width of multispectral bands of interest and the spectral coverage. In this study, we aim to evaluate the suitability of the recent MicaSense RedEdge-MX Dual imaging system with 10 bands covering the visible to near infrared (VNIR) region for needle N and P estimation in a radiata pine plantation and compare its performance against the hyperspectral-based models which include plant functional traits as inputs.

Hyperspectral data can be used not only to simulate and assess the performance of existing multispectral sensors for various modelling applications but also to identify the most informative spectral bands for specific target variables, thereby guiding the design and development of next-generation multispectral sensors. Numerous studies have focused on selecting informative bands from hyperspectral data in the context of regression applications,

with the primary motives of eliminating spectral noise, reducing computational load, and avoiding overfitting to achieve model transferability. Band selection (BS) algorithms are applied to the original reflectance spectrum (Guo *et al.*, 2018; Li *et al.*, 2018; Cao *et al.*, 2021) or to the transformed spectrum (Mutanga and Kumar, 2007; Lin *et al.*, 2024), where spectral transformation techniques (e.g., continuum removal, log transform, first-order derivative) are used to enhance the absorption feature and improve the signal-to-noise ratio. Mutanga and Kumar (2007) implemented forward feature selection with and Artificial Neural Network on the continuum-removed to extract a subset of 6 bands that are informative for leaf P content in savanna grass. Guo *et al.* (2018) evaluated the effect of Monte Carlo-uninformative variable elimination (MC-UVE) combined with the successive projection algorithm (SPA) on leaf P predictions in rubber trees. The authors reported an improvement in estimation accuracy when the subset of optimal bands was used, compared to the full spectrum. Cao *et al.* (2021) compared multiple BS algorithms, including LASSO regression, Elastic net and SPA, in terms of their capability of leaf N estimation in summer maize. Another commonly used BS algorithm is based on the variable importance in projection (VIP) embedded in the partial least square regression (PLSR) models (Li *et al.*, 2018; Lin *et al.*, 2024). However, such BS algorithms might not be compatible with our objective of identifying multispectral bandsets for needle N and P assessment for a few reasons. First, bands selected through these BS techniques often tend to cluster in certain spectral regions, and the final number of selected bands varies depending on the BS technique and the criteria used. In contrast, we aim to select no more than 15 bands with a relatively uniform distribution across the whole spectrum. The criterion of even coverage ensures that selected bandsets remain suitable for other tasks, such as spectral index calculation. Second, most studies select bands at narrow-band resolutions, without evaluating the impact of coarser spectral resolution on the modelling accuracy.

On the other hand, clustering-based BS algorithms, despite their widespread popularity in hyperspectral image classification (Datta *et al.*, 2015; Wang *et al.*, 2019, 2021), are seldom used for regression tasks. One of the few exceptions is the study by Latorre-Carmona *et al.* (2013), which evaluated hierarchical clustering algorithms (Martínez-Usó *et al.*, 2007) for leaf chlorophyll content estimation. Band clustering algorithms typically involve two steps: first, bands with high similarity are grouped into the same clusters based on certain similarity measures; second, a representative band is selected from each cluster, forming the final selection of bands (see (Sun and Du, 2019) for a detailed review). Given that adjacent bands are similar among them, these clustering-based BS methods can produce a reduced subset of

bands with a relatively even coverage of the spectrum. Nonetheless, the representative band selection is often an unsupervised process in most of the studies, which does not align with the objective of the current study to identify bandsets optimized for explaining the N and P variability. Therefore, in this study, we intend to explore the utility of band clustering algorithms combined with a supervised band selection process to identify the optimal bandsets for needle N and P assessment at a multispectral resolution.

The overall objective of the current study is to evaluate multispectral bandsets for needle N and P assessment in radiata pine trees, as a more affordable alternative to hyperspectral narrow-band imagery. Specifically, we compare the performance of a hyperspectral narrow-band benchmark model, which uses plant functional traits as predictors, with that of the bandset from a commercially available MicaSense RedEdge-MX Dual multispectral camera for N and P estimation. Furthermore, we aim to identify optimal bandsets, different from the Micasense 10 bands, for needle N/P estimation through a clustering-based band selection with a 10 nm FWHM.

6.2 Methods

6.2.1 Airborne data collection and processing

Four airborne campaigns were conducted on February 2, 2021, October 27, 2021, January 11, 2023, and October 2, 2023, under clear sky conditions at solar noon, using the piloted Cessna 172 aircraft operated by the HyperSens Laboratory, the University of Melbourne's Airborne Remote Sensing Facility. Narrow-band hyperspectral images were acquired during all four campaigns with the line-scanning Hyperspec VNIR E-Series sensor covering the 400–1000 nm spectral region with 358 bands at a full width at half-maximum (FWHM) of 5.8 nm and an angular field of view (FOV) of 66° (Headwall Photonics, Fitchburg, MA, USA). Multispectral images were collected during the 2023-Jan and 2023-Oct campaigns with the MicaSense RedEdge-MX Dual Camera Imaging System (MicaSense, Seattle, WA, USA), consisting of 10 bands in the visible and near infrared (VNIR) region with FWHM from 10 to 54 nm (Table 6.1) and an angular FOV of 35.4°. Narrow-band and Micasense images were collected at 350 m and 570 m above ground level (AGL), respectively, resulting in the same spatial resolution of 0.2 m. The pre-processing of narrow-band and MicaSense images, including radiometric

calibration, atmospheric correction and orthorectification, can be found in Chapter 4, Section 4.2. Fig. 6.1 presents an overview of the study site and an example of the sub-nanometer image.

Fig. 6.22. Overview of the study site as shown in the MicaSense reflectance mosaic (infrared-colour composite) obtained on October 2nd, 2023. Plot boundaries are green. Letters A-I represent the treatment group. See Chapter 3 for more information on the study site.

Tree crowns were delineated through a segmentation process on the narrow-band and MicaSense reflectance images, respectively. Automatic segmentations were performed on all narrow-band and Micasense images at first in the Fiji software (Abràmoff *et al.*, 2004). Local thresholding algorithms were first applied to an NIR band (810 nm) and a structural index layer (NDVI > 0.6) in combination to separate the sunlit vegetation pixels from the soil background and within-crown shadows. The identified vegetation pixels were clustered to each object (i.e.,

individual tree crowns) using the watershed object-based approach with Euclidean distance. Delineated tree-crown polygons were then reduced by 75% of the original area to account for the high heterogeneity in the coniferous stands and the sensitivity of pigment and SIF to illumination conditions. Given the spatial misalignment between Micasense and narrow-band images of the two datasets collected in 2023 and occasional image quality issues, automatically delineated tree crowns were further manually selected for these two datasets for a fair comparison in the following analysis. Eventually, 428 trees (n = 428) from 29 plots belonging to 9 treatments were selected for the 2023-Jan dataset. 575 trees (n = 575) from 30 plots belonging to 9 treatments were selected for the 2023-Oct dataset. For the other two datasets collected in 2021, the automatically delineated tree crowns cover the whole study sites of 34 plots, with 1374 trees (n = 1374) from the 2021-Feb dataset, and 2047 trees (n = 2047) for the 2023-Oct dataset, respectively. The mean reflectance and radiance of the tree crowns in the same plot were used to represent the plot-level spectral information.

Table 6.11 Spectral characteristics of the hyperspectral and multispectral sensors used in this study. * With spectral binning.

	Headwall VNIR *E*-Series Sensor (Hyperspectral sensor)	**MicaSense RedEdge-MX Dual imaging system (Multispectral sensor)**
Spectral range	400-1000 nm	444, 475, 531, 560, 650, 668, 705, 717, 740, 842 nm
Number of bands	371	10
FWHM	5.8 nm	28, 32, 14, 27, 16, 14, 10, 12, 18, 57 nm
Field of view	66°	
Signal-to-Nose Ratio	> 300:1*	> 300:1*
Bit depth	16	12

To compensate for the limited availability of MicaSense data, Gaussian spectral convolution was applied to the narrow-band reflectance data (FWHM = 5.8 nm) to match the MicaSense spectral characteristics, resulting in four simulated MicaSense datasets. Additionally, narrow-band data were convolved to 10-nm FWHM with the bands centered at 405, 415, 425, …, 895 nm. The resulting multispectral data with 10-nm FWHM were then used for the selection of optimal bandsets for needle N and P assessment.

6.2.2 Multispectral bandset selection

We proposed a clustering-based band selection algorithm to identify the optimal multispectral wavelengths for needle N and P estimation. Band selection was performed on the simulated 10 nm-FWHM reflectance data covering the 400 to 900 nm region obtained from the hyperspectral imagery. The process involved two main steps: 1) group similar bands together through the fast neighbourhood grouping (FNG) algorithm. Clustering was performed on tree-level reflectance spectra (n = 4424) from all four datasets, as it is an unsupervised process; 2) select one representative band from each cluster using PLS-VIP or the recursive feature selection algorithm with PLS regression (PLS-RFE). Plot-level reflectance spectra from four datasets (n = 112) were used for this step for the supervised selection. Detailed descriptions of the bandset selection process are provided below.

Band clustering

Fast neighbourhood grouping (FNG) algorithm (Wang *et al.*, 2021) was chosen for two reasons: first, FNG considered the spectral bands as ordered, thus bands adjacent to each other are more similar, which ensures that bands in the same clusters are continuous; second, it allowed a predefined number of clusters, which was aligned with our objective to select 10 to 15 bands. FNG adopted a coarse-fine strategy to partition the spectrum into clusters. The whole spectrum was first divided into k even groups (i.e., coarse partition), where k was the user-defined number of clusters. Then, the initial clusters were repartitioned by adjusting the cluster label of bands based on their similarity to the two adjacent cluster centres, eventually resulting in ununiform clusters. The process aimed to maximize the inter-cluster variance while minimizing the intra-cluster variance.

A distance-like similarity measure must be chosen for the clustering algorithm. We used a normalized mutual information (MI)-based distance-like similarity measure in this study as defined in (Martínez-Usó *et al.*, 2007). Let vectors X_1, X_2, …, X_L be the bands of a hyperspectral image. Assuming a hyperspectral image has L bands, vectors X_1, X_2, …, X_L represent individual bands. The mutual information I between the i^{th} and j^{th} bands is expressed in terms of entropy H

$$I(X_i, X_j) = H(X_i) + H(X_j) - H(X_i, X_j) \quad \text{Eq. 6.1}$$

$$H(X) = -\sum_{x \in \Omega} p(x)\, log_2\, p(x) \quad \text{Eq. 6.2}$$

Where p(x) is the probability of event x.

The mutual information was further normalized using Eq. 6.3.

$$NI(X_i, X_j) = \frac{2 \cdot I(X_i, X_j)}{H(X_i) + H(X_j)} \quad \text{Eq. 6.3}$$

As the clustering algorithm accept distance-like measure (i.e., larger values indicate lower similarity), the MI-based distance like similarity measure was finally defined as

$$D_{NI}(X_i, X_j) = \left(1 - \sqrt{NI(X_i, X_j)}\right)^2 \quad \text{Eq. 6.4}$$

The pairwise MI-based distance at 10 nm FWHM is presented in Fig 6.2. The obtained D_{NI} values were multiplied by 100 for better visualization in the figure.

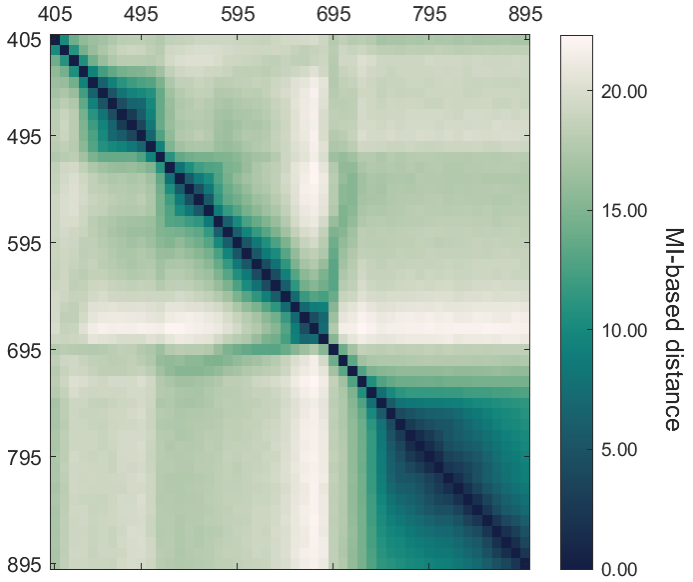

Fig 6.23. Pairwise normalized mutual information (MI) of simulated 10 nm-FWHM multispectral bands determined on tree-level reflectance spectra collected from four airborne campaigns (n = 4424). Lighter colors indicate lower similarity between corresponding band pairs.

We investigated the clustering performance for 10 to 20 clusters and chose the optimal number of clusters based on two criteria. The first one was the quality of the clustering, which was indicated by the Silhouette score (Rousseeuw, 1987). Silhouette score measures how well a data point (i.e., band) belongs to its assigned cluster compared to the remaining clusters by accounting for the inter-cluster and intra-cluster distance.

For each data point i, the silhouette score s(i) is calculated as

$$s(i) = \frac{b(i) - a(i)}{\max[a(i), b(i)]} \quad \text{Eq. 6.5}$$

Where a(i) is the mean distance between i and all other points in the same cluster; b(i) is the smallest mean distance of i to all the points in any other cluster. For special cases when there is only one data point in the cluster, s(i) = 0. The mean silhouette score of all data points was used to represent the clustering quality. It ranged from -1 to 1, with a higher value indicating better quality. MI-based distance-like similarity measure was used to calculate the Silhouette score in our case.

The second criteria was the stability of the clustering algorithm. Stability is an important property of band selection algorithms and represents the robustness of the algorithm to perturbations in the training dataset (Kalousis *et al.*, 2007). Here, we adapted the concept of stability to evaluate the clustering algorithm. We assumed that a stable algorithm would be able to produce the same clustering results (i.e., same cluster partitioning points) despite the changes in the training dataset. Jaccard index was chosen as the stability metric (Jaccard, 1901; Liu *et al.*, 2017). Let S_i and S_j be two vectors representing the partitioning points of the same length. Jaccard index is defined as:

$$J(S_i, S_j) = \frac{|S_i \cap S_j|}{|S_i \cup S_j|} \qquad \text{Eq. 6.6}$$

A Jaccard index closer to 1 implies that two vectors are identical, while 0 indicates complete dissimilarity. We performed a 10-fold evaluation and computed the mean of pairwise Jaccard index values to measure the clustering algorithm stability.

Representative band selection

We implemented two PLS-based supervised feature selection algorithms to identify the representative band from each cluster. PLS was chosen as it was widely used for high-dimensional data analysis and could handle the multicollinearity by transforming the spectrum into uncorrelated latent variables (Wold, 1966).

The first band selection algorithm employed was PLS-based Recursive Feature Elimination with cross-validation (PLS-RFE). Initially, all bands within the same cluster were included as inputs to the PLS model. The importance of each band was assessed based on its impact on the mean squared error (MSE) in a five-fold cross-validation. One band was removed at a time, and a new PLS model was built using the remaining bands. The change in MSE resulting from the removal indicated the importance of the excluded band. After each iteration, the least essential band—i.e., the one whose removal caused the largest absolute change in MSE—was eliminated. This process was repeated until only a single band remained.

The second was a ranking-based selection method where the Variable Importance in Projection (VIP) scores obtained from the PLS model were utilized (PLS-VIP) (Wold *et al.*, 1993). Bands within the same cluster were used to build a PLS model. VIP scores for each band were then computed according to Eq. 6.7. The band with the highest VIP scores was retained.

$$VIP_j = \sqrt{p \cdot \frac{\sum_{a=1}^{A}\left[SSY_a \cdot \left(\frac{w_{ja}}{\|w_a\|}\right)^2\right]}{\sum_{a=1}^{A} SSY_a}} \quad \text{Eq. 6.7}$$

Where j represents the j^{th} band; p is the number of bands; A is the number of latent variables (LVs) in the PLS model; w_{ja} is the weight of band j on LV; $\|w_a\|$ is the norm of the weight vector for LV a; SSY_a represents the amount of variance in the response variable explained by LV a as defined by Eq. 6.8.

$$SSY_a = \sum_{i=1}^{n}(xs_{ia} \cdot yl_a)^2 \quad \text{Eq. 6.8}$$

Where n is the number of samples; xs_{ia} is the score of the i^{th} sample on LV a; yl_a is the loading for the response variable on LV a.

The optimal number of LVs was determined through the leave-one-out cross-validation process for all the PLS models mentioned above. The stability of the two band selection algorithms was evaluated using a 15-fold cross-validation, with stability measured by the Jaccard index. Within each cluster, the bands most frequently selected across the 15 folds were retained as the cluster representatives.

6.2.3 Multispectral-based modelling for needle N and P

Gaussian process regression (GPR) algorithm (Rasmussen, 2004) was used to predict needle N and P concentrations for each plot with multispectral bands as inputs for individual datasets. Four sources of multispectral data were used to build GPR models separately: 1) measured MicaSense data for 2023-Jan and 2023-Oct datasets; 2) simulated MicaSense data for all four datasets (2021-Feb, 2021-Oct, 2023-Jan and 2023-Oct) from narrow-band hyperspectral imagery; 3) the multispectral bandset with 10-nm FWHM selected by PLS-RFE algorithm for needle N/P for all four datasets; 4) the multispectral bandset with 10-nm FWHM selected by PLS-VIP algorithm for needle N/P for all four datasets. The hyperparameters of the GPR algorithm were automatically tuned in parallel for each target variable with the Bayesian optimizer in MATLAB (Statistics and Machine Learning toolbox; MathWorks Inc., Natick,

MA, USA). A Leave-One-Out Validation (LOOV) scheme was adopted to quantify the model performance, with the normalized root mean squared error (NRMSE) and the coefficient of determination (R^2) as the main metrics. NRMSE was calculated as the ratio between RMSE and the range of needle nutrient measurements.

We further quantified the relative contribution of individual bands to the explanation of needle N/P variabilities using the PLS-based VIP scores. PLS models were built with all the bands in the bandset as inputs and needle N/P concentration as the response variable. The number of LVs in PLS models was determined through a leave-one-out validation process.

6.2.4 Hyperspectral-based benchmark modelling for needle N and P

GPR models built with inputs derived from the narrow-band hyperspectral data were used as the benchmark for plot-level needle N and P estimation. The training process of GPR models was the same as described in Section 6.2.3. Narrow-band-based inputs were plant functional traits, including needle chlorophyll *a* + *b* (C_{ab}), carotenoid (C_{ar}), anthocyanins (A_{nth}), retrieved from the inversion of the PRO4SAIL2 model [PROSEPCT-D (Féret *et al.*, 2017) + 4SAIL2 (Verhoef and Bach, 2007)], and solar-induced fluorescence quantified at O_2-A absorption feature (SIF_{760}) The hyperspectral-based benchmark model was denoted by N/P = f(C_{ab}, ,C_{ar}, A_{nth}, SIF_{760}) hereafter.

PRO4SAIL2 was inverted through a look-up-table (LUT) based approach with RMSE as the cost function. For each of the four datasets of plot-mean reflectance, a LUT with 500,000 simulations was generated by running PRO4SAIL2 in the forward mode. The simulated spectra (400 – 2500 nm, FWHM = 1 nm) were then convolved to match the spectral characteristics of the narrow-band hyperspectral imager (400 – 1000 nm, FWHM = 5.8 nm). We also employed continuous wavelet transform (CWT) with the second-derivative Gaussian kernel to the simulated and observed spectra. Then, the inversion was performed on the transformed spectra. SIF_{760} was retrieved from the plot-level hyperspectral radiance data using the Fraunhofer Line Depth (FLD) method (Plascyk and Gabriel, 1975) with two reference bands outside the absorption feature at O_2-A (Maier *et al.*, 2004). The relative contribution of these obtained functional traits to needle P and N estimation was quantified by the out-of-bag (OOB) permutation scores in random forest (RF) (Liu and Zhao, 2017). The details of PRO4SAIL2 inversion, SIF_{760} retrieval and parameter importance evaluation via RF-OOB were described in Chapter 4.

The proposed data analysis workflow for this study is illustrated in Fig. 6.3. We did not retrieve plant functional traits from multispectral data due to its limited spectral coverage. Given the absence of ground-truth measurements for functional traits such as needle pigment content, retrieving these traits from datasets with varying spectral resolutions could further complicate the interpretation of needle nutrient estimation results.

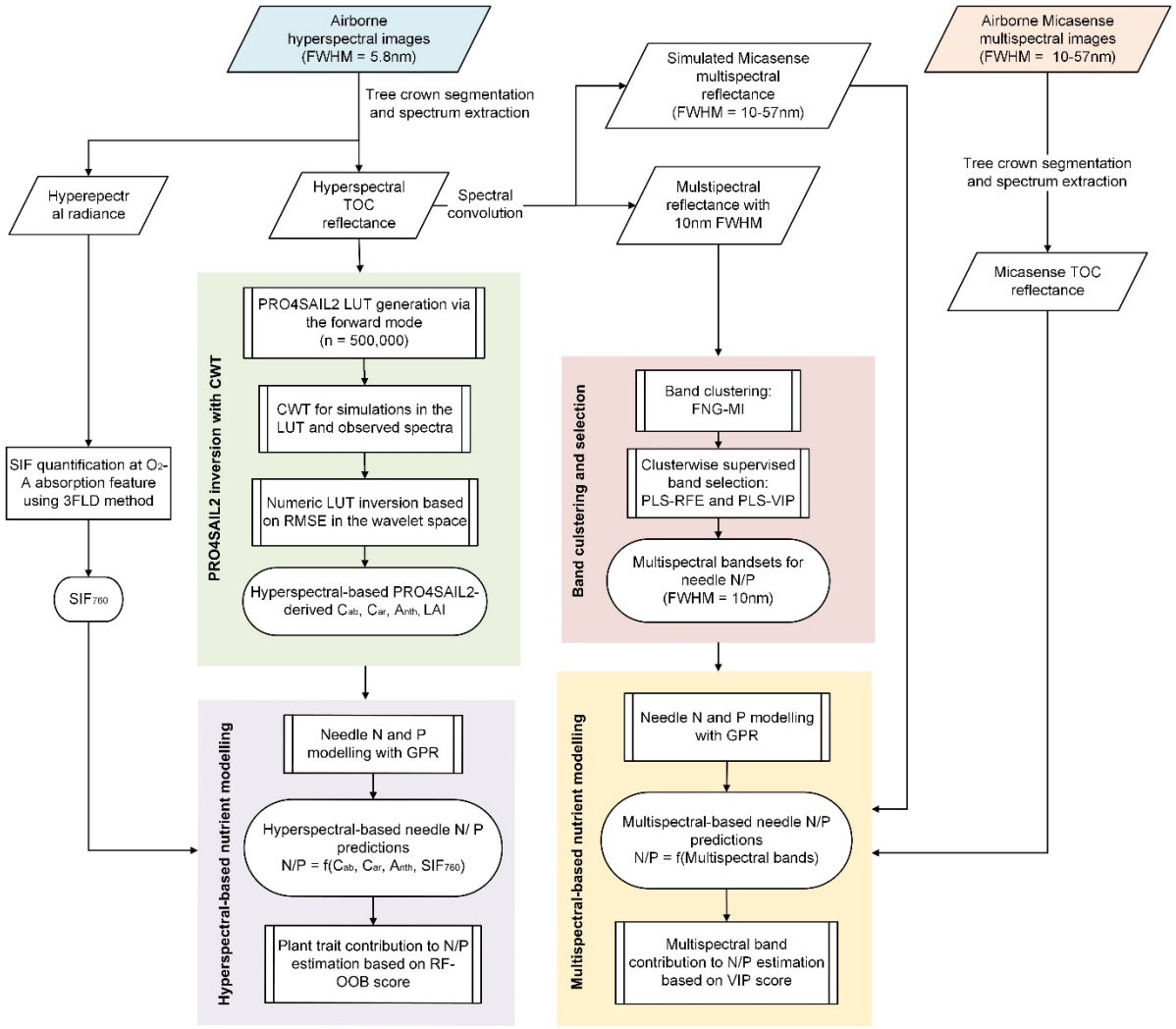

Fig. 6.24. Illustrative diagram of the proposed data analysis process

6.3 Results

6.3.1 Agreement between measured and simulated MicaSense data

Varying levels of agreement were observed between the measured and simulated MicaSense reflectance data across the plots. At the tree crown level, the measured and simulated reflectance displayed similar magnitude and variations in some plots, such as Example Plot A (Fig. 6.4). In other cases, the overlaps between the measurements and simulations were limited, such as Example Plot B (Fig. 6.4). Additionally, tree-level comparisons across the 10 MicaSense spectral bands (Appendix 6 Fig. A6.1) showed a moderate positive relationship at all wavelengths, with higher levels of agreement observed in the 2023-Oct dataset (R^2 = 0.47-0.59, *p*-value < 0.001) than the 2023-Jan dataset (R^2 = 0.40-0.55, *p*-value < 0.001). A consistent pattern was observed across both datasets, that the agreement was generally lower for MicaSense bands in the far-red and NIR regions than for those in the visible regions.

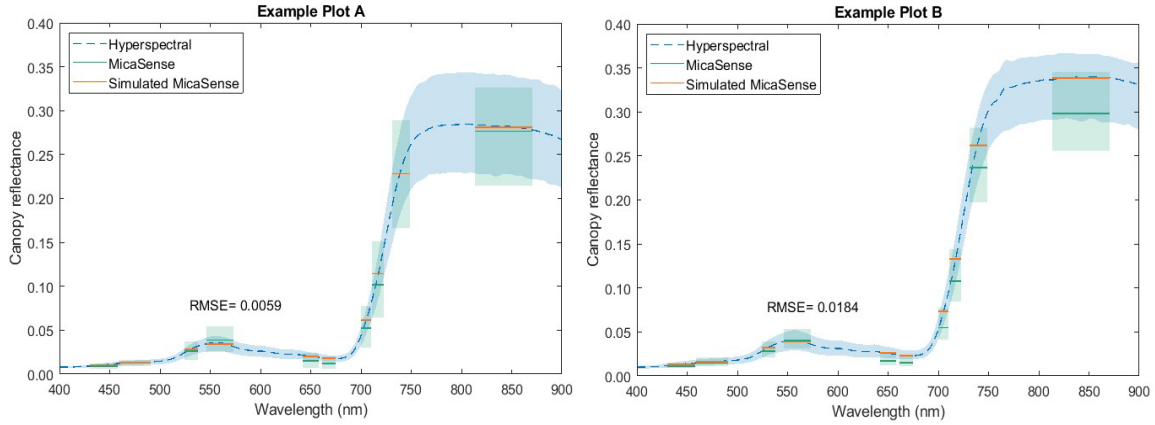

Fig. 6.25 Comparison between measured and simulated MicaSense reflectance spectra for two example plots (A and B) from the 2023-Oct dataset. The dashed blue lines indicate the mean hyperspectral reflectance of all the trees within the plot, while the shaded blue areas represent the range of tree-level hyperspectral reflectance. Simulated MicaSense reflectance spectra (orange lines) were derived by convolving hyperspectral data to match the spectral characteristics of the MicaSense sensor; the horizontal extent of each segment corresponds to the bandwidth (FWHM) of the respective band. The green lines represent the mean of the measured tree-level MicaSense reflectance spectra, with green shading representing the tree-level variation within each plot. RMSE values quantify the spectral agreement between the measured and simulated MicaSense reflectance at the plot level.

At the plot level, the agreement between the measured and simulated MicaSense reflectance was higher for the 2023-Oct dataset (RMSE = 0.0071 to 0.0189, with the median of 0.0107 and the mean of 0.0113) than for the 2023-Jan dataset (RMSE = 0.0115 to 0.0210, with the median and also the mean equal to 0.0135). Overall, the comparison between the measured and the

simulated MicaSense data showed that the simulations were reliable proxies for the measured MicaSense data to some extent.

6.3.2 Selected multispectral bandsets for needle N and P

The quality and stability of the clustering algorithm FNG-MI, for the cluster number from 10 to 20, were indicated by the Silhouette score and Jaccard index (J), respectively (Fig. 6.5a). A Silhouette score closer to one implies better separation (i.e., how well each band suits within its assigned cluster). In general, a Silhouette score above 0.5 is considered indicative of good clustering quality. However, due to the contiguous nature and high collinearity inherent in spectral data, the obtained Silhouette scores were expectedly low (~0.20 – 0.28). A Jaccard index closer to one reflects high stability – that is, the algorithm performance was robust against data perturbation and noise. Based on the cross-validation results, the clustering quality and stability were the best when 12 clusters were used. Therefore, the spectrum from 400 to 900 nm at 10nm FWHM was divided into 12 clusters (Fig. 6.5b).

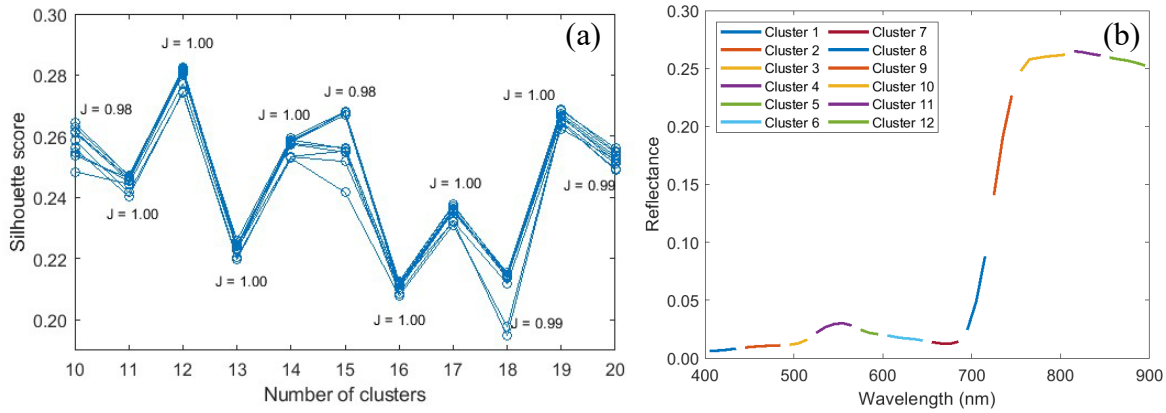

Fig. 6.26. (a) Mean Silhouette scores of FNG-MI clustering algorithm from 10-fold evaluation, applied to the 10nm-FWHM tree reflectance (n = 4424), for cluster numbers ranging from 10 to 20. J denotes the mean Jaccard index across 10 folds. (b) Clustering results using the FNG-MI algorithm with 12 clusters, illustrated with example vegetation reflectance spectrum from 400-900 nm.

Following the clustering process, which grouped the spectrum into 12 clusters, two supervised band selection algorithms were implemented to select the representative bands from each cluster. The stability analysis of the two algorithms (Fig. 6.6), as indicated by Jaccard index (J), showed that both algorithms displayed higher stability for P bandset selection than N. PLS-RFE had lower uncertainties for N bandset selection than PLS-VIP, while PLS-VIP was more stable for P bandset selection than N. The final bandsets selected via these two algorithms for needle N and P estimation were summarised in Table 6.2 and illustrated in Fig. 6.7.

Table 6.12 Center wavelengths of multispectral bandsets (FWHM = 10 nm) selected via two band selection algorithms (PLS-RFE and PLS-VIP) for needle N and P estimation. BS12N and BS12P denote the needle N and P bandsets with 12 bands selected for needle N and P via PLS-RFE algorithm. BS12N2 and BS12P2 are the 12-band bandsets selected via PLS-VIP algorithm for needle N and P, respectively.

Needle N bandsets		
PLS-RFE	435,475,495,555,595,645,655,715,745,765,815,895 nm	BS12N
PLS-VIP	435,485,495,555,575,645,665,705,745,765,815,865 nm	BS12N2
Needle P bandsets		
PLS-RFE	435,475,515,545,575,605,655,705,745,775,835,865 nm	BS12P
PLS-VIP	435,485,505,545,575,635,675,715,735,755,815,865 nm	BS12P2

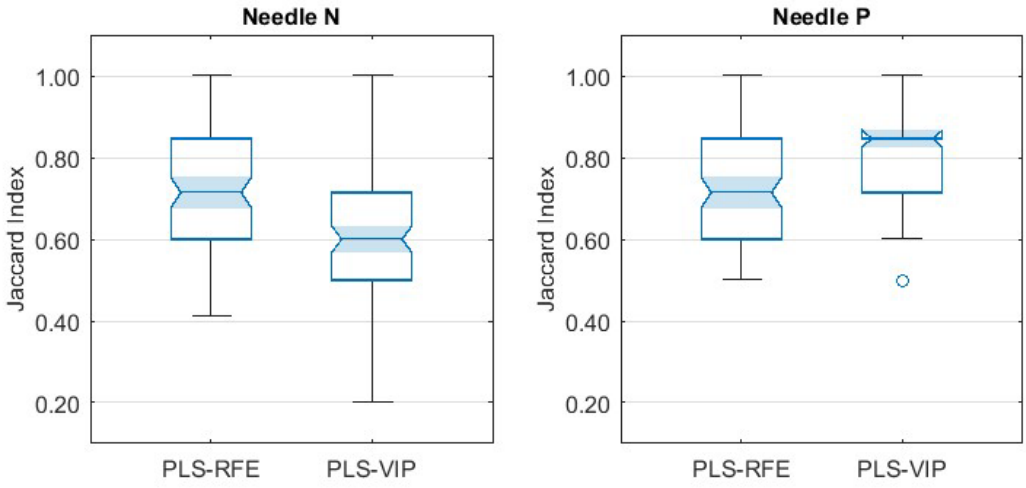

Fig. 6.27. Jaccard index of two band selection algorithms (PLS-RFE and PLS-VIP) for needle N and P estimation. Stability was evaluated across 15 folds using the 10-nm FWHM plot-mean reflectance spectra (n = 112). The central line of the box represents the median; the upper and lower bounds of the box indicate the interquartile range (IQR); whiskers extend to 1.5×IQR; notches represent the 95% confidence interval of the median and circles represent outliers.

6.3.3 Model performance for needle N and P estimation

Needle N

The comparison between needle N prediction accuracy from hyperspectral-based benchmark models and that from multispectral-based models is summarised in Fig. 6.8. It should be noted that the interpretation of model accuracy solely based on the coefficient of determination (R2) was misleading in the case of the 2023-Jan dataset. Despite BS12N- and BS12N2-based models yielded higher values of R^2 (0.24 and 0.29, respectively, p-value < 0.01) than the benchmark model (R^2 = 0.08, p-value > 0.5), the NRMSE values of the BS12N- and BS12N2-based models

(0.26 and 0.25, respectively) were higher than that of the benchmark model (NRMSE = 0.23). The poor predictive performance for needle N in the 2023-Jan and 2023-Oct datasets can be primarily attributed to the lack of statistically significant differences between treatments in terms of needle N concentration measurements in both datasets. See Chapter 3 for more details on field data analysis.

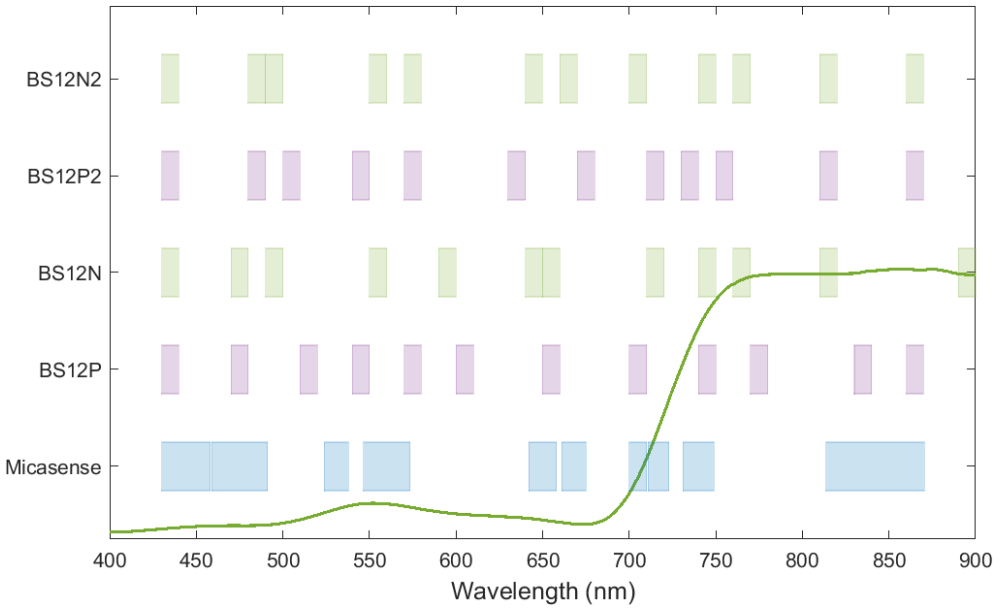

Fig. 6.28. Illustration of distribution of MicaSense bandsets and the proposed multispectral bandsets (FWHM = 10 nm) along the 400 to 900 nm region. BS12N and BS12P denote the needle N and P bandsets with 12 bands selected for needle N and P via PLS-RFE algorithm. BS12N2 and BS12P2 are the 12-band bandsets selected via PLS-VIP algorithm for needle N and P, respectively. The green line represents an example vegetation reflectance spectrum.

The performance of models built with MicaSense bandsets, and the simulated MicaSense bandsets, achieved similar results for the 2023-Jan and 2023-Oct datasets, implying that the simulated data was representative of the MicaSense sensor obtained data to some extent. MicaSense bandsets produced R^2 of 0.037 and 0.017 (p-value > 0.05) and NRMSE values of 0.24 and 0.33, respectively. An R^2 of 0.08 was obtained for both datasets (p-value > 0.05), with NRMSE of 0.25 and 0.30 by simulated MicaSense-based models for the 2023-Jan and 2023-Oct datasets, respectively.

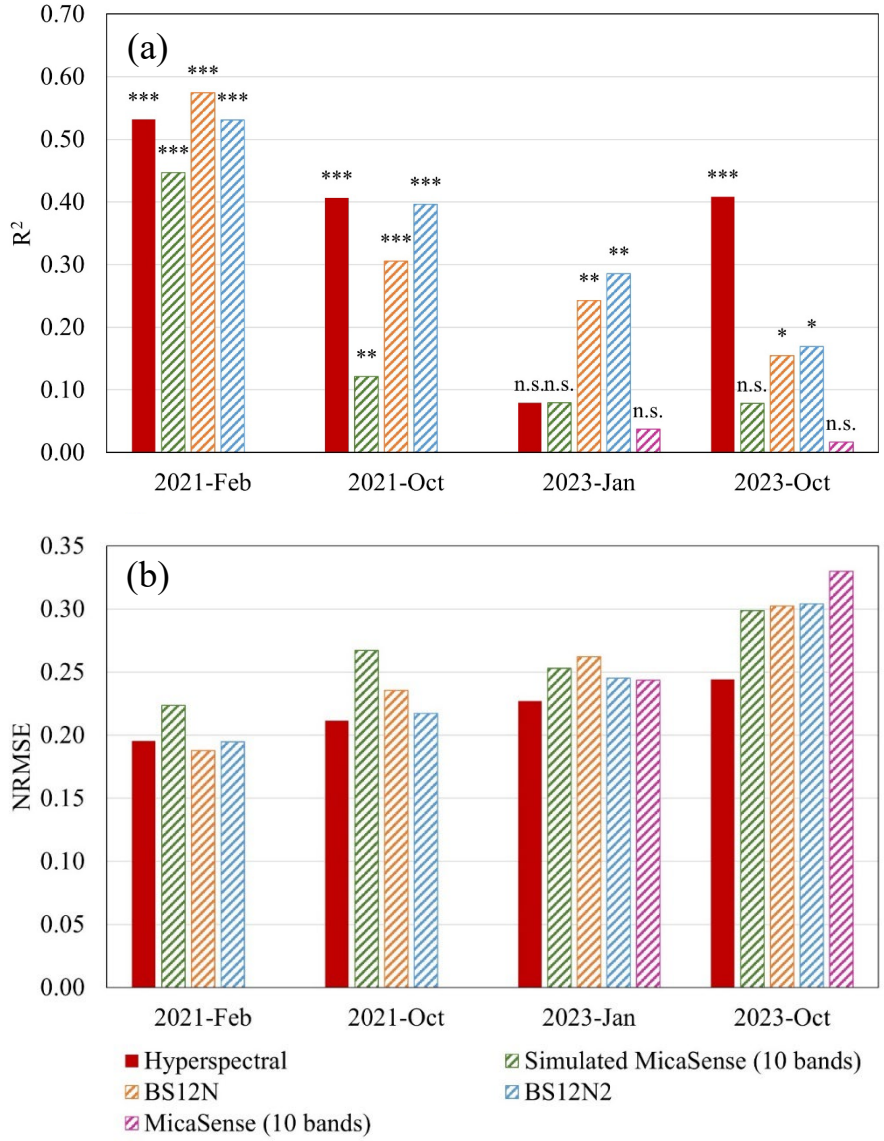

Fig. 6.29. Needle N prediction accuracy by GPR models for needle N estimation with various sources of inputs. (a) coefficient of determination (R^2). (b) Normalized root mean squared error (NRMSE). The hyperspectral-based benchmark model includes plant functional traits as inputs N = $f(C_{ab}, C_{ar}, A_{nth}, SIF_{760})$. Multispectral-based models have reflectance bands as inputs. BS12N and BS12N2 denote the needle N bandsets with 12 bands selected via PLS-RFE and PLS-VIP algorithm respectively. ***p-value < 0.001; **p-value < 0.01; *p-value < 0.05; n.s. = not significant.

For all four datasets, the newly proposed two bandsets, BS12N and BS12N2, explained the variability in needle N more accurately than the simulated MicaSense bandsets. BS12N2-based models outperformed BS12N-based models for three datasets with an increase in R^2 between 0.01 and 0.04 and a decrease in NRMSE of around 0.02, except for the 2021-Feb dataset (R^2 = 0.53 vs. 0.05, p-value < 0.001, NRMSE = 0.195 vs. 0.189). Hence, the BS12N2 bandset

selected through the PLS-RFE algorithm was determined to be the final selection of optimal bandsets for needle N estimation at 10-nm FWHM.

BS12N2-based models achieved comparable N prediction accuracy to the hyperspectral-based benchmark models for the 2021-Feb ($R^2 \approx 0.53$, p-value < 0.001, NRSME ≈ 0.19) and 2021-Oct datasets ($R^2 \approx 0.40$, p-value < 0.001, NRSME ≈ 0.21). Nonetheless, BS12N2 provided low accuracy for the 2023-Oct datasets ($R^2 = 0.17$, p-value < 0.05, NRMSE = 0.30), while the benchmark still achieved an R^2 of 0.41 (p-value < 0.001) with NRMSE of 0.30. Therefore, the hyperspectral-based benchmark model still demonstrated the advantage of consistent performance (R^2 = 0.47-0.53, p-value < 0.005, NRMSE = 0.20-0.24 for three datasets) for needle N estimation over the best multispectral-based models.

Needle P

The performance of hyperspectral-based benchmark models and multispectral-based models for needle P concentration is shown in Fig. 6.9. The simulated MicaSense data produced results comparable to the measured MicaSense data for both 2023-Jan (R^2 = 0.34 vs. 0.28, p-value < 0.01, NRSME = 0.20 vs. 0.26) and 2023-Oct (R^2 = 0.47 vs. 0.53, p-value < 0.001, NRSME = 0.23 vs. 0.20) datasets, supporting the use of simulated data as reliable proxies for actual MicaSense observations.

The proposed bandsets BS12P and BS12P2 provided similar performance for needle P estimation in all datasets, though BS12P displayed a stronger advantage in the 2021-Oct dataset (R^2 = 0.72, p-value < 0.001, NRMSE = 0.14) over BS12P2 (R^2 = 0.57, p-value < 0.001, NRMSE = 0.17). Hence, the BS12P bandset determined by the PLS-VIP algorithm was chosen as the final selection bandset for needle P estimation at 10-nm FWHM. BS12P-based models (R^2 = 0.38-0.72, p-value < 0.01, NRMSE = 0.14-0.25) also outperformed the simulated MicaSense-based models for all datasets (R^2 = 0.26-0.62, p-value < 0.01, NRMSE = 0.16-0.26).

The highest prediction accuracy for needle P concentration was achieved by the hyperspectral-based benchmark models for all datasets (R^2 = 0.52-0.77, p-value < 0.001, NRMSE = 0.12-0.21). The benchmark model displayed more significant advantages over multispectral-based models in the 2021-Feb dataset (R^2 = 0.55 vs. $R^2 \leq 0.43$, p-value < 0.05, NRSME = 0.21 vs. NRMSE ≥ 0.24). Nevertheless, multispectral-based using the proposed BS12P bandset, were able to achieve moderate to high accuracy for needle P estimation (R^2 = 0.37-0.72, p-value <

0.01, NRMSE = 0.14-0.25) with the advantage of greater simplicity in the modelling process, compared to the hyperspectral-based benchmark models.

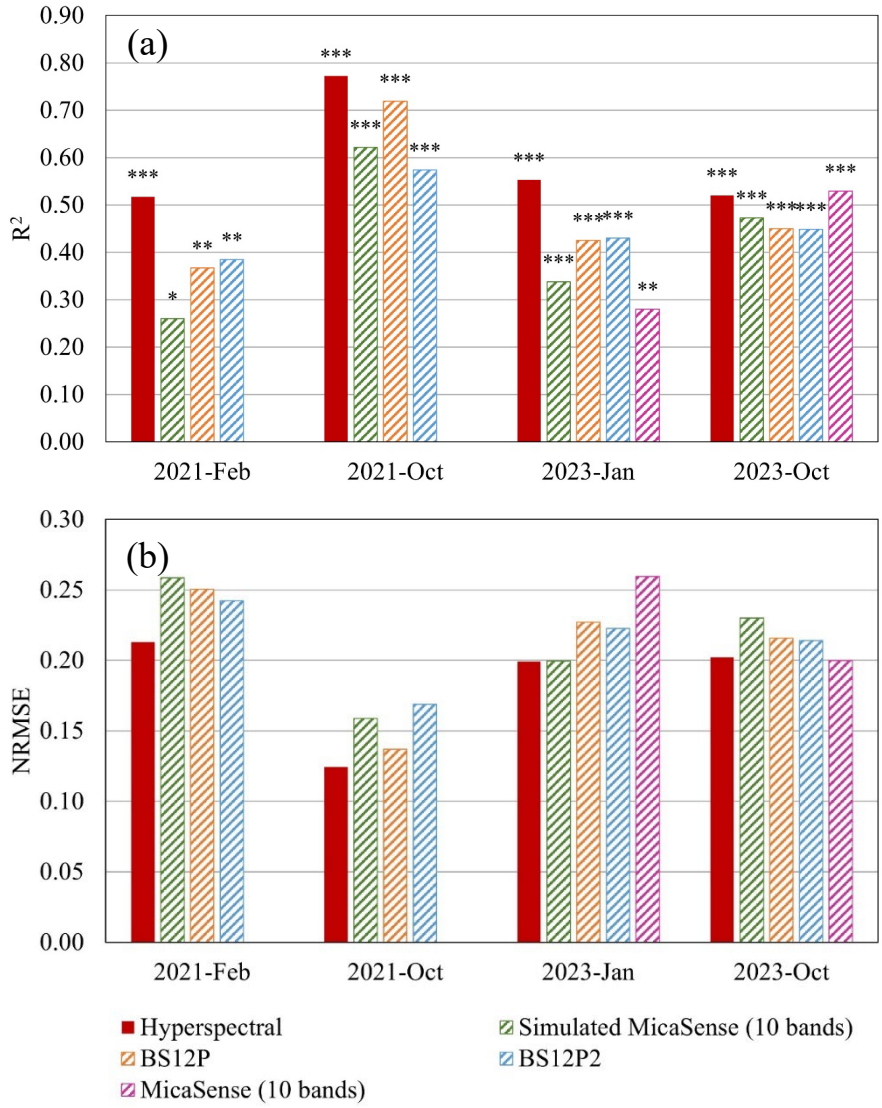

Fig. 6.30. Needle P prediction accuracy by GPR models for needle P estimation with various sources of inputs. (a) coefficient of determination (R^2). (b) Normalized root mean squared error (NRMSE). The hyperspectral-based benchmark model includes plant functional traits as inputs P = *f*(C_{ab}, C_{ar}, A_{nth}, SIF_{760}). Multispectral-based models have reflectance bands as inputs. BS12P and BS12P2 denote the needle P bandsets with 12 bands selected via PLS-RFE and PLS-VIP algorithm, respectively. ****p*-value < 0.001; ***p*-value < 0.01; **p*-value < 0.05; n.s. = not significant.

6.3.4 Multispectral band contribution to needle N and P estimation

We further evaluated the contribution of individual bands in the proposed bandsets BS12N2 (Fig. 6.10a) and BS12P (Fig. 6.10b) to understand the informative wavelengths for needle N and P estimation. It was observed that two bands centred at 555 nm and 575 nm, located within the green absorption region, consistently showed high contribution to needle N estimation across four datasets (Fig. 6.10a). Moreover, the band centered at 705 nm, falling within the red edge region, displayed relatively high VIP scores in the three datasets, except for 2023-Oct. There also existed the pattern of strong contribution from the band located at 435 nm in the blue region in all four datasets. The primary contributors for needle P estimation were in the red edge and NIR region, including bands centred at 745, 775, 835 and 865 nm (Fig. 6.10b). In the visible region, the band centred at 655 nm also exhibited higher VIP scores than other bands in all four datasets, especially the 2021-Feb, 2021-Oct and 2023-Jan datasets.

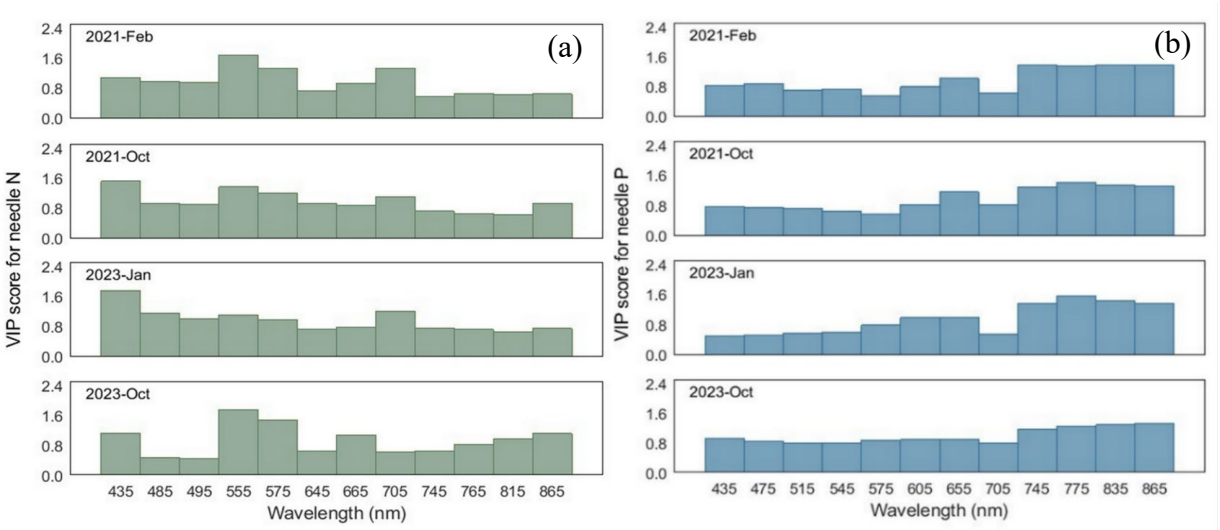

Fig. 6.31. VIP scores of (a) the selected BS12N2 bandset (FWHM = 10 nm) for estimating needle N concentration and (b) the selected BS12P bandset (FWHM = 10 nm) for estimating needle P concentration for four datasets. Higher VIP scores indicate greater contribution of corresponding wavelengths to the model performance.

6.4 Discussion

Our results confirmed, as expected, the superior performance of hyperspectral-based models for needle N and P prediction in radiata pine plantations over any multispectral-based models evaluated in this study. The hyperspectral-based benchmark models with plant functional traits (i.e., PRO4SAIL2-derived needle C_{ab}, C_{ar}, A_{nth} content and SIF_{760}) were able to produce comparable estimation accuracy across datasets for both needle N (R^2 = 0.47-0.53, *p*-value < 0.005, NRMSE = 0.20-0.24 for three datasets) and P concentration (R^2 = 0.52-0.77, *p*-value <

0.001, NRMSE = 0.12-0.21). Overall, lower accuracy was obtained for needle N estimation than for needle P, regardless of whether hyperspectral-based or multispectral-based models are used. This potentially resulted from the low level of variance in needle N measurements, posing challenges for the GPR models to learn the pattern.

Multispectral-based models performed poorly for needle N estimation, especially those based on MicaSense bandsets, compared to the hyperspectral-based benchmarks. It is known that the prediction of leaf N using the VNIR region primarily relies on chlorophyll content due to the biochemical composition of chlorophyll *a* + *b* pigments, which contain N (Evans, 1989). The analysis of the benchmark model showed that PRO4SAIL2-derived needle C_{ab} content was the most important contributor to needle N estimation. Together, the three PRO4SAIL2-derived pigments (i.e., C_{ab}, C_{ar}, A_{nth}) accounted for more than 80% of the contribution to estimating needle N concentration (See Chapter 4 and (Li *et al.*, 2025)). However, multispectral-based models might not capture the variations in pigment changes due to the limited spectral information in the pigment absorption region (~400-680 nm), subsequently affecting the nutrient estimation accuracy. Previous studies have also demonstrated the impact of spectral resolution and the number of bands for leaf chlorophyll estimation. Wei *et al.* (2025), found that the index-based retrievals of leaf chlorophyll content were sensitive to the spectral resolution based on their simulation study. Zhou *et al.* (2022) evaluated the impact of spectral resolution on the leaf N estimation by the PLS model. The authors reported an increase in NRMSE by 0.037 from 2.2-nm FWHM to 40-nm FWHM. Apart from the spectral resolution, the band placement was also crucial for needle N assessment. The proposed bandsets BS12N2 with 10-nm FWHM outperformed MicaSense bandsets for several probable reasons, including two more bands and finer spectral resolution, as well as the band placement. Our results showed that the three bands centred at 435, 555 and 575 nm had a significant contribution to needle N estimations in the BS12N2-based models. By contrast, MicaSense covered these regions with one band at 444 nm (FWHM = 28 nm) and the other at 560 nm (FWHM = 27 nm). It has been found that the 550-560 nm region is sensitive to changes in pigment content (Gitelson and Merzlyak, 1994), likely related to anthocyanin content. Moreover, 435 nm was closer to the absorption peak of chlorophyll a in the blue region (~430 nm). Therefore, it is suggested that higher spectral resolutions in the pigment absorption region can help with needle N estimation by multispectral-based models. Nevertheless, to ensure consistent and reliable predictions across diverse datasets, the use of hyperspectral data is recommended.

Our results indicate the potential of the proposed multispectral bandset BS12P to explain variabilities in needle P concentration in radiata pines. The BS12P-based models offered moderate to high accuracy (R^2 = 0.38-0.72, *p*-value < 0.01, NRMSE = 0.14-0.25) across four datasets. The slight compromise in prediction accuracy, compared to hyperspectral-based benchmark models, brought benefits such as reduced data volume and a simplified modelling process, in favour of operational-scale monitoring. In the hyperspectral-based P model, SIF_{760} played a key role in needle P estimation, contributing to more than 50% among all four inputs (i.e., RTM-derived C_{ab}, C_{ar}, A_{nth} and SIF_{760}) (See Chapter 4 and (Li *et al.*, 2025)). Due to the coarse spectral resolution, multispectral data could not capture the subtle SIF signals. The band importance analysis for multispectral-based models revealed the pronounced contributions of the red-edge (745 nm) and NIR region (775, 835 and 865 nm) for needle P prediction using the BS12P bandset. These findings were in congruence with previous studies focusing on effective hyperspectral bands selection for leaf P estimation. Siedliska *et al.* (2021b) assessed the effective wavelengths for leaf P estimation for strawberries, celery and sugar beet and identified the NIR (650-900 nm) region as the common effective region for distinguishing various P fertilisation rates in all three species. Specifically, the authors argued that the red to far-red region was related to leaf P levels through chlorophyll, as they detected variabilities in the measured leaf total chlorophyll content as responses to the different P rates applied during the nutrient experiments. Lin *et al.* (2024) also identified eight effective wavelengths (442, 479, 572, 630, 740, 795, 838 and 858 nm) within the VNIR region for leaf P estimation in potatoes. Li *et al.* (2018) selected six informative wavelengths from 400-1300 nm, with four located in the NIR region (755, 832, 891 and 999 nm) and two in the SWIR region (1196 and 1267 nm). Both studies evaluated the importance of various spectral regions using VIP scores with PLS models, and there was a shared pattern of higher VIP scores in the NIR region than the visible region, consistent with our findings. It is known that the red edge region is sensitive to chlorophyll concentrations. In turn, P could be related to leaf chlorophyll content in multiple ways. First, P is a component of chloroplast membrane phospholipids. Meanwhile, P participates in the photosynthetic electron transport chains, which in turn affects the ATP synthase activity (Carstensen *et al.*, 2018). It is widely accepted that the canopy reflectance in the NIR region is indirectly linked to leaf P levels, as the disruption in photosynthetic activities by P deficiency eventually leads to changes in biomass and thus canopy structure.

Commercially available multispectral cameras rarely cover the SWIR region (Nex *et al.*, 2022; Zhou *et al.*, 2022). However, given the proven importance of this region for leaf N and P

estimations, it is suggested that the SWIR region could be evaluated in future research using the proposed band selection framework in this study. Mutanga and Kumar (2007) reported improved estimation accuracy (ΔNRMSE = 0.3) for leaf P concentration in savanna grass, when SWIR features were added into the inputs of neural network models, along with VNIR features. Effective wavelengths were widely identified in the SWIR region for leaf N and P status estimations in hyperspectral-based studies (Ramoelo *et al.*, 2013; Camino *et al.*, 2018a; Li *et al.*, 2018; Fan *et al.*, 2019; Lin *et al.*, 2024). The plant reflectance characteristic in SWIR region was sensitive leaf water content and leaf dry matter content, with main components of proteins, starch, cellulose and lignin etc. It is known that chlorophyll only accounts for 1.7% of the total leaf N, while proteins are one of the primary N-containing biochemical constituents, which have strong absorption features in the SWIR region (Kokaly *et al.*, 2009a). P deficiency was found related to starch accumulation in leaves and stems (Qiu and Israel, 1992).

The discrepancy between measured MicaSense and simulated MicaSense data in terms of spectral agreement and performance for needle nutrient estimation was confounded by multiple factors. First, the segmentation was performed on the multispectral MicaSense images and narrow-band hyperspectral and the multispectral images independently. The image distortion and geometric misalignment caused by two sensors made it impossible to identify the same target trees, despite our efforts to manually match individual tree crowns in each hyperspectral-multispectral image pair. Usually, the pushbroom hyperspectral sensors display more complex geometric distortions than the frame-based multispectral cameras (Akhoundi Khezrabad *et al.*, 2022). Second, the mechanical differences between the two sensors led to the difference in the radiometric qualities (e.g., bit depth, signal-to-noise ratio etc.). Third, as the spectral response functions of the MicaSense camera were not publicly available, we used Gaussian convolution to simulate MicaSense data from hyperspectral data, further contributing to the discrepancy between measured and simulated MicaSense data.

Future research can focus on improving the stability and reliability of the proposed band selection methodology. It has been found that image denoising could significantly affect the band selection outcomes. For example, Latorre-Carmona *et al.* (2013) investigated the impact of hyperspectral image denoising on six unsupervised band selection algorithms, including a clustering-based method, in the context of regression tasks. Their results for both simulated and real hyperspectral data showed that denoising significantly improved the accuracy for leaf chlorophyll content estimation. Similarly, Rivera-Caicedo *et al.* (2017) also found that noises in the hyperspectral data adversely affect the performance of various dimensionality reduction

methods in terms of LAI retrieval. Thus, it is suggested that integrating a hyperspectral image denoising step prior to band selection could help achieve more robust band selection results in the future. Additionally, the PLS-based band selection algorithms employed in this study, despite being widely used and well established, were limited to only capturing the linear relationship between features and the target variable. Other non-linear variations could be explored, such as kernel PLS (Rivera-Caicedo *et al.*, 2017) and non-linear PLS (Ramoelo *et al.*, 2013).

6.5 Conclusions

This study evaluated the suitability of multispectral bandsets for explaining the variability of needle nitrogen (N) and phosphorus (P) concentrations in radiata pine plantations, as well as the performance of a commercially available multispectral camera, MicaSense RedEdge-MX Dual. The goal was to assess the potential of multispectral cameras for operational-scale nutrient monitoring in comparison to hyperspectral-based (FWHM = 5.8 nm) benchmark models. Additionally, hyperspectral data were used to guide the selection of optimal multispectral bandsets (FWHM = 10 nm) for N and P estimation through a clustering-based band selection approach. We obtained a bandset with 12 bands for needle N and P estimation, respectively.

Results from four datasets collected over three years confirmed the superior performance of hyperspectral data for both N and P estimation. Moreover, it was suggested that multispectral data in the VNIR range were insufficient for accurately estimating needle N concentrations. However, a proposed bandset with 12 bands at 10-nm FWHM was proven moderately effective for estimating needle P concentrations, with greater modelling simplicity compared to hyperspectral data. Furthermore, the proposed optimal bandset outperformed the MicaSense bands in explaining needle P variability, highlighting its potential for informing the design of next-generation multispectral sensors optimized for leaf nutrient assessment.

Future research should explore the integration of the shortwave infrared (SWIR) region into this methodology, given its known importance in leaf nutrient estimation. Additionally, the impact of hyperspectral image denoising on the performance of the proposed band selection method should be comprehensively assessed. Other band selection algorithms could also be explored within the proposed framework.

Chapter 7
Synthetic discussion and conclusions

This chapter synthesizes the main findings of the Ph.D. study, highlighting its contributions to precision forestry through airborne hyperspectral remote sensing and physically based modelling of needle nitrogen (N) and phosphorus (P). It also considers limitations of the study and proposes directions for future research.

7.1 Research Contributions

7.1.1 Robust needle N and P estimation through physically based modelling

Remote sensing technology enables the non-destructive monitoring of leaf N and P status at field scales. Conventional methods rely on empirical relationships between spectral indices or spectral bands and leaf nutrient concentrations, which lack the physiological interpretability and transferability since factors including canopy structure, soil background and observation geometry are usually not thoroughly accounted for. These constraints can be resolved by the physical models based on radiative transfer modelling. Previous studies on broadleaf crop species have shown that plant functional traits derived from radiative transfer models (RTMs) and far-red solar-induced fluorescence (SIF_{760}) quantified from airborne narrow-band imagery (FWHM = 5.8 nm) are effective indicators for leaf N concentrations (Camino *et al.*, 2018a; Wang *et al.*, 2022). However, these studies are restricted to relatively homogenous canopies, where the interpretation of remotely sensed top-of-canopy (TOC) signals is less challenging than in highly heterogeneous coniferous canopies. Furthermore, such a physically based modelling approach has not yet been applied for phosphorus assessment, whereas most studies on leaf P estimations still rely on empirical methods.

Using four datasets collected at the nutrient experiment site of radiata pines, we demonstrated the robustness of the physically based modelling method for both needle N and P estimation. Specifically, we identified four informative predictors derived from airborne narrow-band imagery, for needle N and P: PRO4SAIL2-derived needle chlorophyll *a* + *b* (C_{ab}), carotenoid (C_{ar}), anthocyanin (A_{nth}) and SIF_{760}. When used as inputs for Gaussian Process Regression

(GPR) models, these four parameters together yielded high predictive accuracy for needle N (R^2 = 0.67-0.97 and NRMSE = 0.07-0.30) and P (R^2 = 0.60-0.95 and NRMSE = 0.09-0.27) at the treatment level. GPR models built with various combinations of narrow-band hyperspectral indices (NBHIs) could not match such consistent performances.

The use of plant functional traits as predictors rewarded the advantage of higher interpretability of the plant physiological responses to nutrient variations. Predictor importance analysis further revealed that PRO4SAIL2-derived C_{ab} consistently contributed the most to explaining the observed variability in needle N, which was aligned with the known physiological knowledge that N is present in chlorophyll molecules (Evans, 1989). On the other hand, SIF_{760} was the most prominent contributor to needle P estimation in all four datasets. The SIF response to P variations might be related to the role of P in photosynthetic activities, including energy supply and membrane solubility. This P-photosynthesis linkage has been previously reported in the laboratory study on chlorophyll fluorescence kinetics (Carstensen *et al.*, 2018), as well as the greenhouse ground-level hyperspectral studies on radiata pine seedlings (Watt *et al.*, 2020). Our results implied that airborne SIF could track the P-related influence on photosynthetic functioning.

Overall, building on previous studies in other species, Chapter 4 demonstrated the generalizability of the physically based modelling method for leaf N estimations to coniferous species, and further extended its application to leaf P assessment. Unlike conventional index-based empirical models, which typically lack consistency in predictive performance across datasets, RTM-derived pigments and SIF are more reliable and physiologically meaningful indicators for needle N and P status.

7.1.2 Potential of the blue spectral region for needle P estimation

Chapter 4 sheds light on the potential of remotely sensed signals in the blue spectral region for estimating needle P concentrations. Our analysis of narrow-band hyperspectral indices (NBHIs) showed that GPR models with blue indices and PRO4SAIL2-derived needle pigments (i.e., C_{ab}, C_{ar}, A_{nth}) as inputs produced comparable estimation accuracy for needle P concentrations to those built with PRO4SAIL2-derived pigments and SIF_{760} (NRMSE = 0.12-0.17 vs. 0.08-0.20 for four datasets), though blue-index-based models performed poorly for needle N estimation. Despite the slight compromise in the prediction accuracy for P, blue indices offered the

advantage of modelling simplicity. Further analysis of predictor importance revealed that blue indices are the primary contributors to the prediction accuracy of needle P concentrations.

The consistency of these results across four datasets suggests a physiological linkage between the blue region and needle P level. Nevertheless, the mechanism of the blue-P linkage is not well understood. We proposed two hypotheses to explain the response of the blue spectral region to P variations: one was associated with the potential blue fluorescence emission (Chappelle *et al.*, 1984), and the other was based on the chlorophyll degradation into phaeophytin (Barnes *et al.*, 1992b; Peñuelas *et al.*, 1995a; Hörtensteiner, 2013). This study is among the first to report such a P-blue region relationship, highlighting the previously underexplored blue spectral region for phosphorus monitoring in radiata pines. Future research can focus on evaluating the proposed hypotheses and understanding the physiological basis of the relationship, which can guide the evolution of hyperspectral-based nutrient monitoring strategies

7.1.3 Role of red and far-red Fraunhofer line depths for needle P estimation

It has been proven in simulation studies that the accuracy of SIF retrievals based on the FLD principle at oxygen absorption features is susceptible to sensor specifications, especially spectral resolution (SR) and the signal to noise ratio (SNR) (Damm *et al.*, 2011; Julitta *et al.*, 2016). A sub-nanometer resolution (FWHM < 1.0 nm) is recommended for SIF_{760} estimates at the O_2-A band and an ultrafine resolution (FWHM < 0.5 nm) for red SIF (SIF_{687}) at the O_2-B band. However, finer spectral resolution causes larger data volumes and higher spectral noise levels, challenging the data processing. Considering previous studies have shown that SIF_{760} quantified in a relative term from the narrow-band resolution (FWHM = 3-7 nm) is sufficient for differentiating various leaf nitrogen levels in homogenous canopies (Belwalkar *et al.*, 2022; Wang *et al.*, 2022), it questions the necessity of sub-nanometer resolution for SIF application in needle N and P estimation in heterogeneous coniferous canopies.

Based on the narrow-band analysis in Chapter 4, Chapter 5 first evaluated the role of SIF_{760} quantified from the narrow-band (FWHM = 5.8 nm) and sub-nanometer imagery (FWHM = 0.1-0.2 nm) for needle N and P estimation, when SIF_{760} and narrow-band-based needle pigments derived from PRO4SAIL2 were used as GPR model inputs. Our results based on two datasets showed that sub-nanometer resolution did not make a significant contribution to SIF_{760} in the context of needle N and P assessment under the current modelling framework. However,

further work is required to determine whether the sub-nanometer resolution provides more accurate SIF retrievals than the narrow-band resolution, due to the lack of validity of SIF, which is discussed in Section 7.2.2.

Chapter 5 further explored the Fraunhofer line (FL) depths, SIF indicators that are only evident under sub-nanometer resolution, for needle N and P status monitoring. FLs are largely unaffected by the atmospheric absorption and scattering effects, which are among the most influential factors for accurate SIF retrievals at oxygen absorption features. However, FL absorption features are less evaluated than oxygen absorption bands in airborne applications, due to the requirement of high spectral resolution. Chapter 5 is one of the few to evaluate FL depths for needle nutrient monitoring purposes. The results highlighted that the depths of far-red FLs were more effective indicators for needle N and P status than those of red FLs. More specifically, the far-red FL located at 774.9 nm, together with narrow-band-based PRO4SAIL2-derived pigment (i.e., C_{ab}, C_{ar}, and A_{nth}) as inputs for GPR models, provided improved prediction accuracy for both needle N (R^2 = 0.62 and NRMSE = 0.17) and P (R^2 = 0.36-0.51 and NRMSE = 0.17-0.25), as opposed to the model built with narrow-band-based pigments and sub-nanometer-based SIF.

These results highlighted the advantages of using sub-nanometer-resolved far-red FL depths as SIF indicators for needle N and P assessment in airborne applications. Future research could refine SIF retrievals from FLs and assess their contributions to needle nutrient estimations.

7.1.4 Optimized multispectral bandsets for large-scale needle P monitoring

The application of airborne hyperspectral imagery for frequent needle nutrient monitoring at an operational scale faces several constraints, including high monetary and computational costs, as well as the expertise required for hyperspectral data processing. Multispectral cameras are more affordable and accessible alternatives, though they may not be able to capture vegetation spectral changes associated with plant physiological responses due to their coarse spectral resolution and limited spectral coverage. Therefore, it is essential to evaluate the performance of any commercially available multispectral camera in terms of its suitability for predicting needle N and P concentrations. In addition, given that the bandsets of most multispectral cameras are not designed to capture N- or P-sensitive wavelengths, an optimised multispectral bandset can guide future camera designs for this specific monitoring purpose.

In Chapter 6, the performance of the set of 10 bands from the commercially available multispectral camera MicaSense RedEdge-MX for needle N and P estimation was first evaluated and compared to the narrow-band-based benchmark model developed in Chapter 4, where PRO4SAIL2-derived pigments and SIF were used as GPR inputs. In addition, a novel approach was adopted to identify informative bandsets for needle nutrient concentrations by combining band clustering with supervised band selection algorithms. The predictive power of the newly proposed bandsets was then evaluated.

Our results showed that the narrow-band-based models outperformed all the multispectral-based models for both needle N and P estimation in terms of accuracy and consistency (R^2 = 0.47-0.53 and NRMSE = 0.20-0.24 for N; R^2 = 0.52-0.77 and NRMSE = 0.12-0.21 for P). Despite that none of the multispectral-based models yielded satisfactory N estimates across datasets, the potential of using multispectral bandsets for needle P estimation is promising. Specifically, the newly proposed optimised bandsets for P, with 12 bands (R2 = 0.37-0.72 and NRMSE = 0.14-0.25), produced higher accuracy than the MicaSense bandsets (R2 = 0.26-0.62 and NRMSE = 0.16-0.26). Although the optimized 12-band-based models yielded slightly less accurate yet still consistent performance, compared to the narrow-band-based model, the former exhibited a greater advantage of computational simplicity. A closer analysis of the proposed 12 bands revealed that the NIR and red-edge regions were critical for estimating needle P concentrations, which was in congruence with other studies on optimal P wavelength selection.

This study provided an opportunity to design next-generation multispectral cameras dedicated to needle nutrient monitoring. We recommend VNIR cameras to adopt the bandset consisting of 12 bands entered at 435, 475, 515, 545, 575, 605, 655, 705, 745, 775, 835, and 865 nm with a 10-nm FWHM. Such a camera can facilitate the cost-effective monitoring of needle P status in radiata pine plantations, thus supporting the timely horticultural interventions and precision forestry practices.

7.2 Research Limitations

7.2.1 Validity of RTM-derived plant traits

We shall clarify that the PRO4SAIL2-derived plant traits in Chapters 4,5, and 6 can only be considered as relative values. Due to the lack of needle measurements of pigment content (i.e.,

C_{ab}, C_{ar}, A_{nth}) and the in-situ measurements of the structural parameter LAI, we could not determine the accuracy of the RTM-based retrievals. Nevertheless, we contend that our PRO4SAIL2-derived parameter values reflect the relative distribution of the parameter among plots, which is sufficient for the differentiation of various fertilization levels. The synthetic validation test in Chapter 4 also supports this claim.

However, it is recommended that leaf measurements be taken in future research for two reasons. First, these measurements can be used to regularize LUT generation, a measure to alleviate the ill-posed inverse problem. Second, it enables the retrieval of plant biochemical and biophysical properties in absolute terms. This, in turn, enables N and P modelling using mixed datasets, which increases the training data size for the GPR algorithm and likely improves model performance. It also opens the possibility of time series analysis of needle nutrient concentrations.

7.2.2 Accuracy of SIF retrievals

Similar to RTM-derived traits, our SIF retrievals from either narrow-band or sub-nanometer images are relative values only, as their accuracy cannot be validated. Consequently, we cannot draw any conclusions from Chapter 5 on whether the narrow-band or the sub-nanometer images yielded more reliable SIF estimates.

The common practice for verifying airborne SIF retrievals relies on in-situ radiance and irradiance measurements taken just above the canopy, typically using a handheld spectroradiometer. SIF retrieved from the ground-level measurements is considered free of atmospheric interference, thus serving as a baseline for airborne retrievals. However, it is impractical to do so in radiata pine forests due to the height of the trees. We suggest that future research utilise drones to acquire low-altitude TOC radiance and irradiance measurements for baseline SIF, which can then be used for the validation of SIF obtained by a piloted aircraft at a higher altitude. Moreover, given the sensitivity of SIF to atmospheric absorption and scattering (Guanter *et al.*, 2010), it is recommended that comprehensive atmospheric correction based on radiative transfer models be implemented to acquire TOC spectral signals, as opposed to the currently applied empirical correction method.

7.2.3 Sample size and generalizability

The labelled samples (i.e., measurements of needle N and P concentrations) were very limited in this study (n = 19 or 34), as the measurements were averaged to the plot level. The small sample size may have limited the training of the GPR models and the predictive accuracy for needle N and P concentrations. More importantly, GPR models trained on small datasets cannot be readily used for predictions on an independent dataset due to their limited generalizability. Consequently, when applied to the tree crown-level information, the trained GPR model likely generated less reliable nutrient variability maps for the study site due to the extrapolation.

The small sample size also affects the representativeness of the optimized bandsets in Chapter 6, where supervised selection algorithms were involved. Although the band selection was implemented on the combined dataset (n = 119), the reliability of the band selection algorithm can be improved by a larger sample size.

It is suggested that extensive sampling, despite being time-consuming and laborious, should be conducted to determine needle N and P concentrations at the tree level, thereby enhancing the generalizability of the models and the reliability of the optimised bandsets.

7.3 Future Research Directions

7.3.1 Exploring the SWIR region

This study focused on VNIR data analysis, although it is known that the SWIR region contains valuable information for leaf N and P estimations. The analysis of N in the VNIR region mainly relies on the N-chlorophyll linkage. However, it should be noted that chlorophyll only accounts for 1.7 % of total leaf N (Kokaly *et al.*, 2009a), while there are more predominant N-containing biochemical constituents that have strong absorptions in the SWIR region, such as proteins. Studies on leaf P estimations using hyperspectral reflectance spectra often report SWIR wavelengths as more effective indicators than other spectral regions, due to the physiological linkage between P and leaf dry matter content, such as cellulose, lignin and starch (Qiu and Israel, 1992), which can be detected in the SWIR region.

The evaluation of SWIR can be incorporated into the methodological framework of Chapters 4 and 6. For instance, more advanced leaf RTM (e.g., PROSPECT-PRO (Féret *et al.*, 2021)) can be applied to the narrow-band reflectance to retrieve protein content as nitrogen indicators,

and other carbon-based constituents as phosphorus predictors. In addition, the VNIR-SWIR coverage enables the RTM inversion from the optimized multispectral bandsets as well, whereas the current VNIR coverage is not suitable for such tasks. Previous studies have shown that leaf biochemical constituents can be reliably retrieved from VNIR-SWIR multispectral data through RTM inversion (Quan *et al.*, 2017; Wang *et al.*, 2025). The discrete spectrum and coarse spectral resolution of multispectral data limit RTM-based retrieval to only broad absorption features such as chlorophyll, LAI and dry matter content, among which VNIR only covers the full absorption region of chlorophyll. Therefore, the incorporation of SWIR will allow the physically based modelling to be applied to the optimized multispectral bandsets for needle N and P assessment.

7.3.2 Exploring the blue spectral region

Our findings on the contribution of blue indices to needle P levels highlight the underexplored blue spectral region. We recommend that future research focus on testing the two proposed hypotheses regarding the linkage between phosphorus and the blue spectral region to deepen the understanding of plant physiological responses to P variations.

In the first theory, it is hypothesized that phosphorus variations are related to the blue-green fluorescence emission, which exhibits two emission peaks around 450 and 530 nm, respectively. Different from red fluorescence, which is emitted by chlorophyll, blue-green fluorescence originates from cinnamic acids bound to the cellulosic cell walls (Harris and Hartley, 1976) and soluble substances bound to cell vacuoles (Lichtenthaler and Miehé, 1997). Previous laboratory studies have pointed out that fluorescence ratios are associated with various stress conditions (Lichtenthaler and Miehé, 1997; Subhash *et al.*, 1999; Bürling *et al.*, 2011). Further analysis is needed to understand the relationship between phosphorus levels and fluorescence ratios.

The alternative hypothesis is that the blue spectral response is a result of chlorophyll degradation into phaeophytin under P deficiency. Phaeophytin has strong absorption in the blue region, which can be approximated by the index NPQI (Harris and Hartley, 1976; Peñuelas *et al.*, 1995a; Hörtensteiner, 2013). We observed a strong relationship between needle P measurements and NPQI across datasets. Further research should be undertaken to measure phaeophytin content and confirm its relationship with needle P concentrations.

7.3.3 Improving the reliability of band selection

Since the purpose of the optimized multispectral bandsets is to guide the design of next-generation multispectral cameras, the reliability and representativeness of the selected bandsets are critical. The transferability of the selected bandsets should be tested on different study sites or even different species for monitoring leaf N and P.

Apart from increasing the sample size (see Section 7.2.3), we suggest two other measures for future research to enhance the reliability of the band selection algorithm as proposed in Chapter 6. First, the hyperspectral image should be denoised before the subsequent data extraction. Research has shown that the denoising process affects the results of band selection algorithms (Latorre-Carmona *et al.*, 2013; Rivera-Caicedo *et al.*, 2017). Second, Chapter 6 only implemented PLS-based selection algorithms, which cannot account for non-linear relationships between spectral bands. Other non-linear variations could be explored, such as kernel PLS (Rivera-Caicedo *et al.*, 2017) and non-linear PLS (Ramoelo *et al.*, 2013).

7.4 General Conclusions

This Ph.D. study was established in the broad context of precision forestry, where remote sensing has provided the opportunity for non-destructive vegetation monitoring at a large scale. With a focus on *Pinus radiata* D. Don (radiata pine), the overall objective was to evaluate needle N and P status using airborne hyperspectral imagery, thereby guiding the implementation of fertilization interventions and avoiding wood production loss. The three research questions (Chapters 4-6) addressed different aspects of the overarching goal, with Chapters 4-5 emphasizing the physiological understanding of the plant response to nutrient variations, and Chapter 6 considering the practical application of operational scale monitoring.

Chapter 4 evaluated whether the physically based modelling approach, which had been successfully applied for leaf N assessment in crop and orchard species, could be used for needle N and P estimations in coniferous species, where the distinct needle shape and heterogeneous canopy structure presented challenges to the interpretation of remotely sensed signals. Importantly, Chapter 4 is the first study to evaluate needle/leaf P status using a physically based model, while most studies implemented empirical methods for P estimations. We achieved high prediction accuracy for both nutrients, demonstrating the robustness of the physically based modelling approach, which utilised RTM-based plant traits and SIF derived from narrow-band

images as needle nutrient predictors. More specifically, four parameters were identified as effective predictors for both N and P: PRO4SAIL2-derived C_{ab}, C_{ar}, A_{nth} content and SIF_{760}. Among them, C_{ab} contributed the most to explaining the observed variability in needle N, while SIF played a critical role in P estimations. In addition, we discovered that blue indices were associated with needle P levels, leading to the proposal of two hypotheses on the mechanisms of blue responses to P variations. This novel finding opened a new avenue for future research on needle phosphorus monitoring.

Given that SIF_{760} displayed great importance for needle N and P assessment in Chapter 4, Chapter 5 drew closer attention to SIF quantification, examining the impact of sensor spectral resolution on SIF retrieval accuracy. Based on the previous simulation studies, we hypothesized that sub-nanometer resolution (FWHM = 0.1-0.2 nm) could provide more accurate SIF retrievals at oxygen absorption features than the narrow-band resolution (FWHM = 5.8 nm), thereby improving the contribution of SIF to needle N and P estimations. Our analytical results contradict the hypothesis: sub-nanometer resolved SIF_{760} underperformed its narrow-band resolved counterparts in terms of needle N and P estimation accuracy. However, it remains inconclusive whether sub-nanometer SIF_{760} was more accurate than the narrow-band SIF_{760}, due to the lack of validity for airborne SIF retrievals. It is suggested that comprehensive atmospheric correction and the acquisition of baseline SIF retrievals from low-altitude drone-obtained radiance measurements are needed for a firm conclusion on the question. Nevertheless, the analysis of FLs identified in the sub-nanometer radiance spectra showed that the depths of far-red FLs were more effective indicators for needle N and P status than those of red FLs. Chapter 5 is one of the few to evaluate FL depths for needle nutrient monitoring purposes. Future research can focus on SIF quantification from FLs, which does not require complex atmospheric correction, and evaluate their contributions to needle nutrient estimations.

Recognizing the limitations of large-scale needle nutrient monitoring with airborne hyperspectral imagery (FWHM = 5.8 nm), including high financial and computational costs as well as the expertise required for data processing, Chapter 6 shifted the focus to evaluating multispectral bandsets as a more affordable and accessible alternative. We first evaluated the commercially available MicaSense RedEdge-MX multispectral camera for its N and P prediction capability. Then we adopted a novel approach combining band clustering with supervised band selection algorithms to identify informative bandsets for needle N and P concentrations, and evaluated the predictive performance of N and P. Our comparison between multispectral and narrow-band-based models (Chapter 4) demonstrated the robustness of the

latter for consistent estimation accuracy across datasets. Although multispectral bandsets in the VNIR regions were found to be insufficient for explaining the observed variability in needle N, they hold promise in providing satisfactory estimation accuracy for needle P, with the advantage of computational simplicity. Moreover, our newly proposed optimized bandsets (FWHM = 10 nm) with 12 bands outperformed the MicaSense 10 bands for needle P estimations. The design of next-generation cameras that focus on phosphorus monitoring can consider adopting the proposed bandsets.

Our research has important implications for facilitating precision forestry practices in radiata pine plantations, which hold enormous economic importance in Australia. While certain limitations remain, particularly in the validation of RTM-derived traits and SIF retrievals, this Ph.D. study advanced the understanding of plant physiological responses to nitrogen and phosphorus variations and demonstrated the advantage of hyperspectral remote sensing for nutrient monitoring in coniferous species.

Reference

ABARES, 2024. Australian forest and wood production statistics *Australian Bureau of Agricultural and Resource Economics and Sciences: Canberra, Australia,*

Abdel-Rahman, E.M., Mutanga, O., Odindi, J., Adam, E., Odindo, A., & Ismail, R., 2017. Estimating Swiss chard foliar macro- and micronutrient concentrations under different irrigation water sources using ground-based hyperspectral data and four partial least squares (PLS)-based (PLS1, PLS2, SPLS1 and SPLS2) regression algorithms. *Computers and Electronics in Agriculture, 132*, 21-33

Abràmoff, M.D., Magalhães, P.J., & Ram, S.J., 2004. Image processing with ImageJ. *Biophotonics international, 11*, 36-42

Ač, A., Malenovský, Z., Olejníčková, J., Gallé, A., Rascher, U., & Mohammed, G., 2015. Meta-analysis assessing potential of steady-state chlorophyll fluorescence for remote sensing detection of plant water, temperature and nitrogen stress. *Remote Sensing of Environment, 168*, 420-436

Akhoundi Khezrabad, M., Valadan Zoej, M.J., & Safdarinezhad, A., 2022. A new approach for geometric correction of UAV-based pushbroom images through the processing of simultaneously acquired frame images. *Measurement, 199*, 111431

Akinwande, M.O., Dikko, H.G., & Samson, A., 2015. Variance inflation factor: as a condition for the inclusion of suppressor variable (s) in regression analysis. *Open journal of statistics, 5*, 754

Albert, L.P., Cushman, K., Zong, Y., Allen, D.W., Alonso, L., & Kellner, J.R., 2023. Sensitivity of solar-induced fluorescence to spectral stray light in high resolution imaging spectroscopy. *Remote Sensing of Environment, 285*, 113313

Ali, A.M., Skidmore, A.K., Darvishzadeh, R., van Duren, I., Holzwarth, S., & Mueller, J., 2016. Retrieval of forest leaf functional traits from HySpex imagery using radiative transfer models and continuous wavelet analysis. *ISPRS Journal of Photogrammetry and Remote Sensing, 122*, 68-80

Alonso, L., Gomez-Chova, L., Vila-Frances, J., Amoros-Lopez, J., Guanter, L., Calpe, J., & Moreno, J., 2008. Improved Fraunhofer Line Discrimination method for vegetation fluorescence quantification. *IEEE Geoscience and Remote Sensing Letters, 5*, 620-624

Atzberger, C., 2000. Development of an invertible forest reflectance model: The INFOR-model. *A decade of trans-European remote sensing cooperation*, 39-44

Bacour, C., Maignan, F., MacBean, N., Porcar-Castell, A., Flexas, J., Frankenberg, C., Peylin, P., Chevallier, F., Vuichard, N., & Bastrikov, V., 2019. Improving estimates of gross primary productivity by assimilating solar-induced fluorescence satellite retrievals in a terrestrial biosphere model using a process-based SIF model. *Journal of Geophysical Research: Biogeosciences, 124*, 3281-3306

Bandopadhyay, S., Rastogi, A., Rascher, U., Rademske, P., Schickling, A., Cogliati, S., Julitta, T., Mac Arthur, A., Hueni, A., & Tomelleri, E., 2019. Hyplant-derived sun-induced fluorescence—A new opportunity to disentangle complex vegetation signals from diverse vegetation types. *Remote sensing, 11*, 1691

Baret, F., & Buis, S., 2008. Estimating Canopy Characteristics from Remote Sensing Observations: Review of Methods and Associated Problems. In S. Liang (Ed.), *Advances in Land Remote Sensing: System, Modeling, Inversion and Application* (pp. 173-201). Dordrecht: Springer Netherlands

Baret, F., Jacquemoud, S., Guyot, G., & Leprieur, C., 1992. Modeled analysis of the biophysical nature of spectral shifts and comparison with information content of broad bands. *Remote Sensing of Environment, 41*, 133-142

Barnes, J.D., Balaguer, L., Manrique, E., Elvira, S., & Davison, A., 1992a. A reappraisal of the use of DMSO for the extraction and determination of chlorophylls a and b in lichens and higher plants. *Environmental and Experimental Botany, 32*, 85-100

Barnes, J.D., Balaguer, L., Manrique, E., Elvira, S., & Davison, A.W., 1992b. A reappraisal of the use of DMSO for the extraction and determination of chlorophylls a and b in lichens and higher plants. *Environmental and Experimental botany, 32*, 85-100

Beets, P., Gilchrist, K., & Jeffreys, M., 2001a. Wood density of radiata pine: effect of nitrogen supply. *Forest Ecology and Management, 145*, 173-180

Beets, P.N., Gilchrist, K., & Jeffreys, M.P., 2001b. Wood density of radiata pine: effect of nitrogen supply. *Forest Ecology and Management, 145*, 173-180

Belwalkar, A., Poblete, T., Hornero, A., & Zarco-Tejada, P.J. 2023. Evaluating the Relative Contribution of Photosystems I and II for Leaf Nitrogen Estimation Using Fractional Depth of Fraunhofer Lines and SIF Derived From Sub-Nanometer Airborne Hyperspectral Imagery. In, *IGARSS 2023-2023 IEEE International Geoscience and Remote Sensing Symposium* (pp. 2819-2822): IEEE

Belwalkar, A., Poblete, T., Longmire, A., Hornero, A., Hernandez-Clemente, R., & Zarco-Tejada, P., 2022. Evaluation of SIF retrievals from narrow-band and sub-nanometer airborne hyperspectral imagers flown in tandem: Modelling and validation in the context of plant phenotyping. *Remote Sensing of Environment, 273*, 112986

Benson, M.L., Myers, B.J., & Raison, R.J., 1992. Dynamics of stem growth of Pinus radiata as affected by water and nitrogen supply. *Forest Ecology and Management, 52*, 117-137

Berger, K., Atzberger, C., Danner, M., D'Urso, G., Mauser, W., Vuolo, F., & Hank, T., 2018. Evaluation of the PROSAIL model capabilities for future hyperspectral model environments: A review study. *Remote Sensing, 10*, 85

Berger, K., Verrelst, J., Féret, J.-B., Hank, T., Wocher, M., Mauser, W., & Camps-Valls, G., 2020. Retrieval of aboveground crop nitrogen content with a hybrid machine learning method. *International Journal of Applied Earth Observation and Geoinformation, 92*, 102174

Blackburn, G.A., 1998. Spectral indices for estimating photosynthetic pigment concentrations: A test using senescent tree leaves. *International Journal of Remote Sensing, 19*, 657-675

Blackburn, G.A., 2007. Wavelet decomposition of hyperspectral data: A novel approach to quantifying pigment concentrations in vegetation. *International Journal of Remote Sensing - INT J REMOTE SENS, 28*, 2831-2855

Blackburn, G.A., & Ferwerda, J.G., 2008. Retrieval of chlorophyll concentration from leaf reflectance spectra using wavelet analysis. *Remote Sensing of Environment, 112*, 1614-1632

Broge, N.H., & Leblanc, E., 2001. Comparing prediction power and stability of broadband and hyperspectral vegetation indices for estimation of green leaf area index and canopy chlorophyll density. *Remote Sensing of Environment, 76*, 156-172

Bürling, K., Hunsche, M., & Noga, G., 2011. Use of blue–green and chlorophyll fluorescence measurements for differentiation between nitrogen deficiency and pathogen infection in winter wheat. *Journal of Plant Physiology, 168*, 1641-1648

Calderón, R., Navas-Cortés, J.A., Lucena, C., & Zarco-Tejada, P.J., 2013. High-resolution airborne hyperspectral and thermal imagery for early detection of Verticillium wilt of olive using fluorescence, temperature and narrow-band spectral indices. *Remote Sensing of Environment, 139*, 231-245

Camino, C., González-Dugo, V., Hernández, P., Sillero, J., & Zarco-Tejada, P.J., 2018a. Improved nitrogen retrievals with airborne-derived fluorescence and plant traits quantified from VNIR-SWIR hyperspectral imagery in the context of precision agriculture. *International journal of applied earth observation geoinformation, 70*, 105-117

Camino, C., González-Dugo, V., Hernández, P., Sillero, J.C., & Zarco-Tejada, P.J., 2018b. Improved nitrogen retrievals with airborne-derived fluorescence and plant traits quantified from VNIR-SWIR hyperspectral imagery in the context of precision agriculture. *International Journal of Applied Earth Observation and Geoinformation, 70*, 105-117

Camino, C., Gonzalez-Dugo, V., Hernandez, P., & Zarco-Tejada, P.J., 2019. Radiative transfer Vcmax estimation from hyperspectral imagery and SIF retrievals to assess photosynthetic performance in rainfed and irrigated plant phenotyping trials. *Remote Sensing of Environment, 231*, 111186

Camino, C., Zarco-Tejada, P.J., & Gonzalez-Dugo, V. 2018c. Effects of Heterogeneity within Tree Crowns on Airborne-Quantified SIF and the CWSI as Indicators of Water Stress in the Context of Precision Agriculture. In, *Remote Sensing*

Cao, C., Wang, T., Gao, M., Li, Y., Li, D., & Zhang, H., 2021. Hyperspectral inversion of nitrogen content in maize leaves based on different dimensionality reduction algorithms. *Computers and Electronics in Agriculture, 190*, 106461

Carstensen, A., Herdean, A., Schmidt, S.B., Sharma, A., Spetea, C., Pribil, M., & Husted, S., 2018. The Impacts of Phosphorus Deficiency on the Photosynthetic Electron Transport Chain. *Plant Physiology, 177*, 271-284

Carter, G.A., 1994. Ratios of leaf reflectances in narrow wavebands as indicators of plant stress. *International Journal of Remote Sensing, 15*, 697-703

Cendrero-Mateo, M.P., Moran, M.S., Papuga, S.A., Thorp, K., Alonso, L., Moreno, J., Ponce-Campos, G., Rascher, U., & Wang, G., 2016. Plant chlorophyll fluorescence: active and passive measurements at canopy and leaf scales with different nitrogen treatments. *Journal of Experimental Botany, 67*, 275-286

Cendrero-Mateo, M.P., Wieneke, S., Damm, A., Alonso, L., Pinto, F., Moreno, J., Guanter, L., Celesti, M., Rossini, M., Sabater, N., Cogliati, S., Julitta, T., Rascher, U., Goulas, Y., Aasen, H., Pacheco-Labrador, J., & Mac Arthur, A., 2019. Sun-Induced Chlorophyll Fluorescence III: Benchmarking Retrieval Methods and Sensor Characteristics for Proximal Sensing. *Remote Sensing, 11*, 962

Chappelle, E.W., Kim, M.S., & McMurtrey III, J.E., 1992. Ratio analysis of reflectance spectra (RARS): an algorithm for the remote estimation of the concentrations of chlorophyll a, chlorophyll b, and carotenoids in soybean leaves. *Remote Sensing of Environment, 39*, 239-247

Chappelle, E.W., Wood Jr, F.M., McMurtrey III, J.E., & Newcomb, W.W., 1984. Laser-induced fluorescence of green plants. 1: A technique for the remote detection of plant stress and species differentiation. *Applied optics, 23*, 134-138

Chen, J.M., 1996. Evaluation of vegetation indices and a modified simple ratio for boreal applications. *Canadian Journal of Remote Sensing, 22*, 229-242

Chen, X., Yan, X., Wang, M., Cai, Y., Weng, X., Su, D., Guo, J., Wang, W., Hou, Y., Ye, D., Zhang, S., Liu, D., Tong, L., Xu, X., Zhou, S., Wu, L., & Zhang, F., 2022. Long-term excessive phosphorus fertilization alters soil phosphorus fractions in the acidic soil of pomelo orchards. *Soil and Tillage Research, 215*, 105214

Cheng, T., Rivard, B., & Sánchez-Azofeifa, A., 2011. Spectroscopic determination of leaf water content using continuous wavelet analysis. *Remote Sensing of Environment, 115*, 659-670

Clevers, J.G., & Gitelson, A.A., 2013a. Remote estimation of crop and grass chlorophyll and nitrogen content using red-edge bands on Sentinel-2 and-3. *International Journal of Applied Earth Observation and Geoinformation, 23*, 344-351

Clevers, J.G.P.W., & Gitelson, A.A., 2013b. Remote estimation of crop and grass chlorophyll and nitrogen content using red-edge bands on Sentinel-2 and -3. *International Journal of Applied Earth Observation and Geoinformation, 23*, 344-351

Cogliati, S., Sarti, F., Chiarantini, L., Cosi, M., Lorusso, R., Lopinto, E., Miglietta, F., Genesio, L., Guanter, L., & Damm, A., 2021. The PRISMA imaging spectroscopy mission: overview and first performance analysis. *Remote Sensing of Environment, 262*, 112499

Cogliati, S., Verhoef, W., Kraft, S., Sabater, N., Alonso, L., Vicent, J., Moreno, J., Drusch, M., & Colombo, R., 2015. Retrieval of sun-induced fluorescence using advanced spectral fitting methods. *Remote Sensing of Environment, 169*, 344-357

Constantine, W., & Kaluzny, S., 2022. ifultools: Insightful Research Tools*, R package version 2.0-26*

Corp, L.A., McMurtrey, J.E., Middleton, E.M., Mulchi, C.L., Chappelle, E.W., & Daughtry, C.S.T., 2003. Fluorescence sensing systems: In vivo detection of biophysical variations in field corn due to nitrogen supply. *Remote Sensing of Environment, 86*, 470-479

Croft, H., Chen, J., & Zhang, Y., 2014. The applicability of empirical vegetation indices for determining leaf chlorophyll content over different leaf and canopy structures. *Ecological Complexity, 17*, 119-130

Croft, H., Chen, J., Zhang, Y., Simic, A., Noland, T., Nesbitt, N., & Arabian, J., 2015. Evaluating leaf chlorophyll content prediction from multispectral remote sensing data within a physically-based modelling framework. *ISPRS journal of photogrammetry and remote sensing, 102*, 85-95

Damm, A., Elbers, J., Erler, A., Gioli, B., Hamdi, K., Hutjes, R., Kosvancova, M., Meroni, M., Miglietta, F., & Moersch, A., 2010. Remote sensing of sun‐induced fluorescence to improve modeling of diurnal courses of gross primary production (GPP). *Global change biology, 16*, 171-186

Damm, A., Erler, A., Hillen, W., Meroni, M., Schaepman, M.E., Verhoef, W., & Rascher, U., 2011. Modeling the impact of spectral sensor configurations on the FLD retrieval accuracy of sun-induced chlorophyll fluorescence. *Remote Sensing of Environment, 115*, 1882-1892

Damm, A., Guanter, L., Laurent, V.C., Schaepman, M.E., Schickling, A., & Rascher, U., 2014. FLD-based retrieval of sun-induced chlorophyll fluorescence from medium spectral resolution airborne spectroscopy data. *Remote Sensing of Environment, 147*, 256-266

Darvishzadeh, R., Atzberger, C., Skidmore, A., & Schlerf, M., 2011. Mapping grassland leaf area index with airborne hyperspectral imagery: A comparison study of statistical approaches and inversion of radiative transfer models. *ISPRS journal of photogrammetry and remote sensing, 66*, 894-906

Darvishzadeh, R., Skidmore, A., Schlerf, M., & Atzberger, C., 2008. Inversion of a radiative transfer model for estimating vegetation LAI and chlorophyll in a heterogeneous grassland. *Remote Sensing of Environment, 112*, 2592-2604

Datt, B., 1998. Remote Sensing of Chlorophyll a, Chlorophyll b, Chlorophyll a+b, and Total Carotenoid Content in Eucalyptus Leaves. *Remote Sensing of Environment, 66*, 111-121

Datta, A., Ghosh, S., & Ghosh, A., 2015. Combination of Clustering and Ranking Techniques for Unsupervised Band Selection of Hyperspectral Images. *IEEE Journal of Selected Topics in Applied Earth Observations and Remote Sensing, 8*, 2814-2823

Daughtry, C.S.T., Walthall, C.L., Kim, M.S., de Colstoun, E.B., & McMurtrey, J.E., 2000. Estimating Corn Leaf Chlorophyll Concentration from Leaf and Canopy Reflectance. *Remote Sensing of Environment, 74*, 229-239

Dawson, T.P., Curran, P.J., & Plummer, S.E., 1998. LIBERTY—Modeling the effects of leaf biochemical concentration on reflectance spectra. *Remote Sensing of Environment, 65*, 50-60

Dechant, B., Ryu, Y., Badgley, G., Zeng, Y., Berry, J.A., Zhang, Y., Goulas, Y., Li, Z., Zhang, Q., Kang, M., Li, J., & Moya, I., 2020. Canopy structure explains the relationship between photosynthesis and sun-induced chlorophyll fluorescence in crops. *Remote Sensing of Environment, 241*, 111733

Dehghan-Shoar, M.H., Orsi, A.A., Pullanagari, R.R., & Yule, I.J., 2023. A hybrid model to predict nitrogen concentration in heterogeneous grassland using field spectroscopy. *Remote Sensing of Environment, 285*, 113385

Demmig-Adams, B., 1990. Carotenoids and photoprotection in plants: a role for the xanthophyll zeaxanthin. *Biochimica et Biophysica Acta (BBA)-Bioenergetics, 1020*, 1-24

Demmig-Adams, B., & Adams III, W.W., 1996. Xanthophyll cycle and light stress in nature: uniform response to excess direct sunlight among higher plant species. *Planta, 198*, 460-470

Demmig-Adams, B., & Adams, W.W., 1996. The role of xanthophyll cycle carotenoids in the protection of photosynthesis. *Trends in Plant science, 1*, 21-26

Duan, S.-B., Li, Z.-L., Wu, H., Tang, B.-H., Ma, L., Zhao, E., & Li, C., 2014. Inversion of the PROSAIL model to estimate leaf area index of maize, potato, and sunflower fields from unmanned aerial vehicle hyperspectral data. *International Journal of Applied Earth Observation and Geoinformation, 26*, 12-20

Eitel, J., Long, D., Gessler, P., & Hunt, E., 2008. Combined spectral index to improve ground-based estimates of nitrogen status in dryland wheat. *Agronomy Journal, 100*, 1694-1702

Evans, J.R., 1989. Photosynthesis and nitrogen relationships in leaves of C3 plants. *Oecologia, 78*, 9-19

Fan, L., Zhao, J., Xu, X., Liang, D., Yang, G., Feng, H., Yang, H., Wang, Y., Chen, G., & Wei, P., 2019. Hyperspectral-Based Estimation of Leaf Nitrogen Content in Corn Using Optimal Selection of Multiple Spectral Variables. *Sensors, 19*, 2898

Fang, H., Baret, F., Plummer, S., & Schaepman-Strub, G., 2019. An overview of global leaf area index (LAI): Methods, products, validation, and applications. *Reviews of Geophysics, 57*, 739-799

Fang, H., Liang, S., & Kuusk, A., 2003. Retrieving leaf area index using a genetic algorithm with a canopy radiative transfer model. *Remote Sensing of Environment, 85*, 257-270

Farmonov, N., Walden, S., Martinée, E., Lampei, C., Schreiber, M., Opgenoorth, L., Rakotomalala, A.A.N.A., Müller, T., Farwig, N., Pinkert, S., Saueressig, L., Wagner, A.R., Junker, R.R., Verrelst, J., & Bendix, J., 2025. Optimizing hybrid models for forest leaf and canopy trait mapping from EnMAP hyperspectral data with limited field samples. *Science of Remote Sensing, 12*, 100253

Féret, J.-B., Berger, K., De Boissieu, F., & Malenovský, Z.J.R.S.o.E., 2021. PROSPECT-PRO for estimating content of nitrogen-containing leaf proteins and other carbon-based constituents*, 252*, 112173

Feret, J.-B., François, C., Asner, G.P., Gitelson, A.A., Martin, R.E., Bidel, L.P., Ustin, S.L., Le Maire, G., & Jacquemoud, S., 2008a. PROSPECT-4 and 5: Advances in the leaf optical properties model separating photosynthetic pigments. *Remote Sensing of Environment, 112*, 3030-3043

Feret, J.-B., François, C., Asner, G.P., Gitelson, A.A., Martin, R.E., Bidel, L.P.R., Ustin, S.L., le Maire, G., & Jacquemoud, S., 2008b. PROSPECT-4 and 5: Advances in the leaf optical properties model separating photosynthetic pigments. *Remote Sensing of Environment, 112*, 3030-3043

Féret, J.-B., Gitelson, A., Noble, S., & Jacquemoud, S., 2017. PROSPECT-D: Towards modeling leaf optical properties through a complete lifecycle. *Remote Sensing of Environment, 193*, 204-215

Fields, S., 2004. Global Nitrogen: Cycling out of Control. *Environmental Health Perspectives, 112*, A556-A563

Forestry Corporation of NSW, 2016. Radiata pine 'the remarkable pine' FOREST FACT NO.04 *Forestry Corporation*

Frankenberg, C., & Berry, J., 2017. Solar Induced Chlorophyll Fluorescence: Origins, Relation to Photosynthesis and Retrieval. *Comprehensive Remote Sensing*

Gamon, J., Serrano, L., & Surfus, J., 1997a. The photochemical reflectance index: an optical indicator of photosynthetic radiation use efficiency across species, functional types, and nutrient levels. *Oecologia, 112*, 492-501

Gamon, J.A., Penuelas, J., & Field, C., 1992a. A narrow-waveband spectral index that tracks diurnal changes in photosynthetic efficiency. *Remote Sensing of Environment, 41*, 35-44

Gamon, J.A., Peñuelas, J., & Field, C.B., 1992b. A narrow-waveband spectral index that tracks diurnal changes in photosynthetic efficiency. *Remote Sensing of Environment, 41*, 35-44

Gamon, J.A., Serrano, L., & Surfus, J.S., 1997b. The photochemical reflectance index: an optical indicator of photosynthetic radiation use efficiency across species, functional types, and nutrient levels. *Oecologia, 112*, 492-501

Gao, H., Liu, S., Lu, W., Smith, A.R., Valbuena, R., Yan, W., Wang, Z., Xiao, L., Peng, X., & Li, Q., 2021. Global analysis of the relationship between reconstructed solar-induced chlorophyll fluorescence (SIF) and gross primary production (GPP). *Remote Sensing, 13*, 2824

Gao, J., Meng, B., Liang, T., Feng, Q., Ge, J., Yin, J., Wu, C., Cui, X., Hou, M., & Liu, J., 2019. Modeling alpine grassland forage phosphorus based on hyperspectral remote sensing and a multi-factor machine learning algorithm in the east of Tibetan Plateau, China. *ISPRS Journal of Photogrammetry and Remote Sensing, 147*, 104-117

Gareth, J., Daniela, W., Trevor, H., & Robert, T., 2013. *An introduction to statistical learning: with applications in R*. Spinger

Garrity, S.R., Eitel, J.U.H., & Vierling, L.A., 2011. Disentangling the relationships between plant pigments and the photochemical reflectance index reveals a new approach for remote estimation of carotenoid content. *Remote Sensing of Environment, 115*, 628-635

Gastellu-Etchegorry, J.-P., Yin, T., Lauret, N., Cajgfinger, T., Gregoire, T., Grau, E., Feret, J.-B., Lopes, M., Guilleux, J., Dedieu, G., Malenovský, Z., Cook, B.D., Morton, D., Rubio, J., Durrieu, S., Cazanave, G., Martin, E., & Ristorcelli, T., 2015. Discrete Anisotropic Radiative Transfer (DART 5) for Modeling Airborne and Satellite Spectroradiometer and LIDAR Acquisitions of Natural and Urban Landscapes. *Remote Sensing, 7*, 1667-1701

Gastellu-Etchegorry, J., Martin, E., & Gascon, F., 2004. DART: a 3D model for simulating satellite images and studying surface radiation budget. *International Journal of Remote Sensing, 25*, 73-96

Gitelson, A., & Merzlyak, M.N., 1994. Spectral reflectance changes associated with autumn senescence of Aesculus hippocastanum L. and Acer platanoides L. leaves. Spectral

features and relation to chlorophyll estimation. *Journal of plant physiology, 143*, 286-292

Gitelson, A., Yacobi, Y., Schalles, J., Rundquist, D., Han, L., Stark, R., & Etzion, D., 2000. Remote estimation of phytoplankton density in productive waters. *Advances in limnology. Stuttgart, 55*, 121-136

Gitelson, A.A., Gritz †, Y., & Merzlyak, M.N., 2003. Relationships between leaf chlorophyll content and spectral reflectance and algorithms for non-destructive chlorophyll assessment in higher plant leaves. *Journal of Plant Physiology, 160*, 271-282

Gitelson, A.A., Keydan, G.P., & Merzlyak, M.N., 2006. Three-band model for noninvasive estimation of chlorophyll, carotenoids, and anthocyanin contents in higher plant leaves. *Geophysical Research Letters, 33*

Gitelson, A.A., & Merzlyak, M.N., 1997. Remote estimation of chlorophyll content in higher plant leaves. *International Journal of Remote Sensing, 18*, 2691-2697

Gitelson, A.A., Zur, Y., Chivkunova, O.B., & Merzlyak, M.N., 2002. Assessing carotenoid content in plant leaves with reflectance spectroscopy¶. *Photochemistry and photobiology, 75*, 272-281

GomezChova, L., AlonsoChorda, L., Amoros Lopez, J., Vila Frances, J., del ValleTascon, S., Calpe, J., & Moreno, J. 2006. Solar induced fluorescence measurements using a field spectroradiometer. In, *AIP Conference Proceedings* (pp. 274-281): American Institute of Physics

Gregoire, N., & Fisher, R.F., 2004. Nutritional diagnoses in loblolly pine (Pinus taeda L.) established stands using three different approaches. *Forest Ecology and Management, 203*, 195-208

Guanter, L., Alonso, L., Gómez-Chova, L., Meroni, M., Preusker, R., Fischer, J., & Moreno, J., 2010. Developments for vegetation fluorescence retrieval from spaceborne high-resolution spectrometry in the O2-A and O2-B absorption bands. *Journal of Geophysical Research: Atmospheres, 115*

Guanter, L., Kaufmann, H., Segl, K., Foerster, S., Rogass, C., Chabrillat, S., Kuester, T., Hollstein, A., Rossner, G., & Chlebek, C., 2015. The EnMAP spaceborne imaging spectroscopy mission for earth observation. *Remote Sensing, 7*, 8830-8857

Guanter, L., Rossini, M., Colombo, R., Meroni, M., Frankenberg, C., Lee, J.-E., & Joiner, J., 2013. Using field spectroscopy to assess the potential of statistical approaches for the retrieval of sun-induced chlorophyll fluorescence from ground and space. *Remote Sensing of Environment, 133*, 52-61

Gueymard, C., 1995a. *SMARTS2: a simple model of the atmospheric radiative transfer of sunshine: algorithms and performance assessment*. Florida Solar Energy Center

Gueymard, C., 1995b. *SMARTS2: a simple model of the atmospheric radiative transfer of sunshine: algorithms and performance assessment*. Florida Solar Energy Center Cocoa, FL, USA

Guo, A., Ye, H., Huang, W., Qian, B., Wang, J., Lan, Y., & Wang, S., 2023. Inversion of maize leaf area index from UAV hyperspectral and multispectral imagery. *Computers and Electronics in Agriculture, 212*, 108020

Guo, P.-T., Shi, Z., Li, M.-F., Luo, W., & Cha, Z.-Z., 2018. A robust method to estimate foliar phosphorus of rubber trees with hyperspectral reflectance. *Industrial Crops and Products, 126*, 1-12

Haboudane, D., Miller, J.R., Pattey, E., Zarco-Tejada, P.J., & Strachan, I.B., 2004a. Hyperspectral vegetation indices and novel algorithms for predicting green LAI of crop canopies: Modeling and validation in the context of precision agriculture. *Remote Sensing of Environment, 90*, 337-352

Haboudane, D., Miller, J.R., Pattey, E., Zarco-Tejada, P.J., & Strachan, I.B.J.R.s.o.e., 2004b. Hyperspectral vegetation indices and novel algorithms for predicting green LAI of crop canopies: Modeling and validation in the context of precision agriculture*, 90*, 337-352

Haboudane, D., Miller, J.R., Tremblay, N., Zarco-Tejada, P.J., & Dextraze, L., 2002. Integrated narrow-band vegetation indices for prediction of crop chlorophyll content for application to precision agriculture. *Remote Sensing of Environment, 81*, 416-426

Harris, P., & Hartley, R., 1976. Detection of bound ferulic acid in cell walls of the Gramineae by ultraviolet fluorescence microscopy. *Nature, 259*, 508-510

Hernández-Clemente, R., Hornero, A., Mottus, M., Peñuelas, J., González-Dugo, V., Jiménez, J., Suárez, L., Alonso, L., & Zarco-Tejada, P.J., 2019a. Early diagnosis of vegetation health from high-resolution hyperspectral and thermal imagery: Lessons learned from empirical relationships and radiative transfer modelling. *Current Forestry Reports, 5*, 169-183

Hernández-Clemente, R., Hornero, A., Mottus, M., Peñuelas, J., González-Dugo, V., Jiménez, J.C., Suárez, L., Alonso, L., & Zarco-Tejada, P.J., 2019b. Early diagnosis of vegetation health from high-resolution hyperspectral and thermal imagery: Lessons learned from empirical relationships and radiative transfer modelling. *Current forestry reports, 5*, 169-183

Hernández-Clemente, R., Navarro-Cerrillo, R.M., Suárez, L., Morales, F., & Zarco-Tejada, P.J., 2011. Assessing structural effects on PRI for stress detection in conifer forests. *Remote Sensing of Environment, 115*, 2360-2375

Hernández-Clemente, R., Navarro-Cerrillo, R.M., & Zarco-Tejada, P.J., 2012. Carotenoid content estimation in a heterogeneous conifer forest using narrow-band indices and PROSPECT+DART simulations. *Remote Sensing of Environment, 127*, 298-315

Hernández-Clemente, R., North, P.R., Hornero, A., & Zarco-Tejada, P.J., 2017a. Assessing the effects of forest health on sun-induced chlorophyll fluorescence using the FluorFLIGHT 3-D radiative transfer model to account for forest structure. *Remote Sensing of Environment, 193*, 165-179

Hernández-Clemente, R., North, P.R.J., Hornero, A., & Zarco-Tejada, P.J., 2017b. Assessing the effects of forest health on sun-induced chlorophyll fluorescence using the FluorFLIGHT 3-D radiative transfer model to account for forest structure. *Remote Sensing of Environment, 193*, 165-179

Herrmann, I., Karnieli, A., Bonfil, D.J., Cohen, Y., & Alchanatis, V., 2010. SWIR-based spectral indices for assessing nitrogen content in potato fields. *International Journal of Remote Sensing, 31*, 5127-5143

Homolová, L., Malenovský, Z., Clevers, J.G.P.W., García-Santos, G., & Schaepman, M.E., 2013. Review of optical-based remote sensing for plant trait mapping. *Ecological Complexity, 15*, 1-16

Hörtensteiner, S., 2013. Update on the biochemistry of chlorophyll breakdown. *Plant Molecular Biology, 82*, 505-517

Jaccard, P., 1901. Etude de la distribution florale dans une portion des Alpes et du Jura. *Bulletin de la Societe Vaudoise des Sciences Naturelles, 37*, 547-579

Jackson, R.D., Idso, S., Reginato, R., & Pinter Jr, P., 1981. Canopy temperature as a crop water stress indicator. *Water resources research, 17*, 1133-1138

Jacquemoud, S., Bacour, C., Poilvé, H., & Frangi, J.P., 2000. Comparison of Four Radiative Transfer Models to Simulate Plant Canopies Reflectance: Direct and Inverse Mode. *Remote Sensing of Environment, 74*, 471-481

Jacquemoud, S., & Baret, F., 1990. PROSPECT: A model of leaf optical properties spectra. *Remote Sensing of Environment, 34*, 75-91

Jia, M., Colombo, R., Rossini, M., Celesti, M., Zhu, J., Cogliati, S., Cheng, T., Tian, Y., Zhu, Y., & Cao, W., 2021. Estimation of leaf nitrogen content and photosynthetic nitrogen use efficiency in wheat using sun-induced chlorophyll fluorescence at the leaf and canopy scales. *European journal of Agronomy, 122*, 126192

Johnston, A.E., Poulton, P.R., Fixen, P.E., & Curtin, D., 2014. Phosphorus: its efficient use in agriculture. *Advances in agronomy, 123*, 177-228

Jordan, C.F., 1969. Derivation of leaf‐area index from quality of light on the forest floor. *Ecology, 50*, 663-666

Julitta, T., Corp, L.A., Rossini, M., Burkart, A., Cogliati, S., Davies, N., Hom, M., Mac Arthur, A., Middleton, E.M., & Rascher, U., 2016. Comparison of sun-induced chlorophyll fluorescence estimates obtained from four portable field spectroradiometers. *Remote Sensing, 8*, 122

Kalousis, A., Prados, J., & Hilario, M., 2007. Stability of feature selection algorithms: a study on high-dimensional spaces. *Knowledge and Information Systems, 12*, 95-116

Kokaly, R.F., Asner, G.P., Ollinger, S.V., Martin, M.E., & Wessman, C.A., 2009a. Characterizing canopy biochemistry from imaging spectroscopy and its application to ecosystem studies. *Remote Sensing of Environment, 113*, S78-S91

Kokaly, R.F., Asner, G.P., Ollinger, S.V., Martin, M.E., & Wessman, C.A.J.R.s.o.e., 2009b. Characterizing canopy biochemistry from imaging spectroscopy and its application to ecosystem studies*, 113*, S78-S91

Krause, a.G., & Weis, E., 1991. Chlorophyll fluorescence and photosynthesis: the basics. *Annual review of plant biology, 42*, 313-349

Krause, G.H., & Jahns, P., 2004. Non-photochemical Energy Dissipation Determined by Chlorophyll Fluorescence Quenching: Characterization and Function. In G.C. Papageorgiou, & Govindjee (Eds.), *Chlorophyll a Fluorescence: A Signature of Photosynthesis* (pp. 463-495). Dordrecht: Springer Netherlands

Krutz, D., Müller, R., Knodt, U., Günther, B., Walter, I., Sebastian, I., Säuberlich, T., Reulke, R., Carmona, E., & Eckardt, A., 2019. The instrument design of the DLR earth sensing imaging spectrometer (DESIS). *Sensors, 19*, 1622

Lambert, M.J., & Turner, J., 1988. Interpretation of nutrient concentrations in Pinus radiata foliage at Belanglo state forest. *Plant and soil, 108*, 237-244

Landi, M., Tattini, M., & Gould, K.S., 2015. Multiple functional roles of anthocyanins in plant-environment interactions. *Environmental and Experimental Botany, 119*, 4-17

Lang, M., & Lichtenthaler, H.K., 1991. Changes in the blue-green and red fluorescence-emission spectra of beech leaves during the autumnal chlorophyll breakdown. *Journal of Plant Physiology, 138*, 550-553

Latorre-Carmona, P., Sotoca, J.M., Pla, F., Bioucas-Dias, J., & Ferré, C.J., 2013. Effect of denoising in band selection for regression tasks in hyperspectral datasets. *IEEE Journal of Selected Topics in Applied Earth Observations and Remote Sensing, 6*, 473-481

le Maire, G., François, C., & Dufrêne, E., 2004. Towards universal broad leaf chlorophyll indices using PROSPECT simulated database and hyperspectral reflectance measurements. *Remote Sensing of Environment, 89*, 1-28

Lee, K.-S., Cohen, W.B., Kennedy, R.E., Maiersperger, T.K., & Gower, S.T., 2004. Hyperspectral versus multispectral data for estimating leaf area index in four different biomes. *Remote Sensing of Environment, 91*, 508-520

Legg, P., Frakes, I., & Garvran, M. 2021a. Australian plantation statistics and log availability report 2021 In. Canberra: Australian Bureau of Agricultural and Resource Economics and Sciences (ABARES)

Legg, P., Frakes, I., & Gavran, M., 2021b. Australian plantation statistics and log availability report 2021. *Australian Bureau of Agricultural and Resource Economics and Sciences: Canberra, Australia*, 119

Li, L., Wang, S., Ren, T., Wei, Q., Ming, J., Li, J., Li, X., Cong, R., & Lu, J., 2018. Ability of models with effective wavelengths to monitor nitrogen and phosphorus status of winter oilseed rape leaves using in situ canopy spectroscopy. *Field Crops Research, 215*, 173-186

Li, P., Poblete, T., Aryal, J., Hornero, A., & Zarco-Tejada, P. 2024. Contribution of Solar-Induced-Fluorescence for Needle Nitrogen and Phosphorus Prediction with Airborne Hyperspectral Imagery. In, *IGARSS 2024-2024 IEEE International Geoscience and Remote Sensing Symposium* (pp. 7893-7897): IEEE

Li, P., Poblete, T., Hornero, A., Aryal, J., & Zarco-Tejada, P.J., 2025. Distinct contribution of the blue spectral region and far-red solar-induced fluorescence to needle nitrogen and phosphorus assessment in coniferous nutrient trials with hyperspectral imagery. *Remote Sensing of Environment, 328*, 114915

Li, Z., & Ahammed, G.J., 2023. Hormonal regulation of anthocyanin biosynthesis for improved stress tolerance in plants. *Plant Physiology and Biochemistry*, 107835

Lichtenthaler, H.K., 1996. Vegetation Stress: an Introduction to the Stress Concept in Plants. *Journal of Plant Physiology, 148*, 4-14

Lichtenthaler, H.K., & Miehé, J.A., 1997. Fluorescence imaging as a diagnostic tool for plant stress. *Trends in Plant science, 2*, 316-320

Lin, D., Chen, Y., Qiao, Y., Qin, D., Miao, Y., Sheng, K., Li, L., & Wang, Y., 2024. A study on an accurate modeling for distinguishing nitrogen, phosphorous and potassium status in summer maize using in situ canopy hyperspectral data. *Computers and Electronics in Agriculture, 221*, 108989

Liu, H.Q., & Huete, A., 1995. A feedback based modification of the NDVI to minimize canopy background and atmospheric noise. *IEEE Transactions on geoscience and remote sensing, 33*, 457-465

Liu, N., Wagner Hokanson, E., Hansen, N., & Townsend, P.A., 2023. Multi-year hyperspectral remote sensing of a comprehensive set of crop foliar nutrients in cranberries. *ISPRS Journal of Photogrammetry and Remote Sensing, 205*, 135-146

Liu, Y., Yang, J., Chen, Y., Tan, K., Wang, L., & Yan, X., 2017. Stability analysis of hyperspectral band selection algorithms based on neighborhood rough set theory for classification. *Chemometrics and Intelligent Laboratory Systems, 169*, 35-44

Liu, Y., & Zhao, H., 2017. Variable importance-weighted random forests. *Quantitative Biology, 5*, 338-351

Lu, B., He, Y., & Dao, P.D., 2019. Comparing the performance of multispectral and hyperspectral images for estimating vegetation properties. *IEEE Journal of Selected Topics in Applied Earth Observations and Remote Sensing, 12*, 1784-1797

Lu, B., Proctor, C., & He, Y., 2021. Investigating different versions of PROSPECT and PROSAIL for estimating spectral and biophysical properties of photosynthetic and non-photosynthetic vegetation in mixed grasslands. *GIScience & Remote Sensing, 58*, 354-371

Lukeš, P., Stenberg, P., Rautiainen, M., Mottus, M., & Vanhatalo, K.M., 2013. Optical properties of leaves and needles for boreal tree species in Europe. *Remote Sensing Letters, 4*, 667-676

Ma, L., Sun, L., Wang, S., Chen, J., Chen, B., Zhu, K., Amir, M., Wang, X., Liu, Y., Wang, P., Wang, J., Huang, M., & Wang, Z., 2022. Analysis on the relationship between sun-induced chlorophyll fluorescence and gross primary productivity of winter wheat in northern China. *Ecological Indicators, 139*, 108905

Mahajan, G., Sahoo, R., Pandey, R., Gupta, V., & Kumar, D., 2014. Using hyperspectral remote sensing techniques to monitor nitrogen, phosphorus, sulphur and potassium in wheat (Triticum aestivum L.). *Precision Agriculture, 15*, 499-522

Mahalingam, S., Srinivas, P., Devi, P.K., Sita, D., Das, S.K., Leela, T.S., & Venkataraman, V.R. 2019. Reflectance based vicarious calibration of HySIS sensors and spectral stability study over pseudo-invariant sites. In, *2019 IEEE Recent Advances in Geoscience and Remote Sensing : Technologies, Standards and Applications (TENGARSS)* (pp. 132-136)

Mahlein, A.K., Rumpf, T., Welke, P., Dehne, H.W., Plümer, L., Steiner, U., & Oerke, E.C., 2013. Development of spectral indices for detecting and identifying plant diseases. *Remote Sensing of Environment, 128*, 21-30

Maier, S.W., Günther, K.P., & Stellmes, M., 2004. Sun‐induced fluorescence: A new tool for precision farming. *Digital imaging and spectral techniques: Applications to precision agriculture and crop physiology 66*, 207-222

Malenovský, Z., Regaieg, O., Yin, T., Lauret, N., Guilleux, J., Chavanon, E., Duran, N., Janoutová, R., Delavois, A., & Meynier, J., 2021a. Discrete anisotropic radiative transfer modelling of solar-induced chlorophyll fluorescence: Structural impacts in geometrically explicit vegetation canopies. *Remote Sensing of Environment, 263*, 112564

Malenovský, Z., Regaieg, O., Yin, T., Lauret, N., Guilleux, J., Chavanon, E., Duran, N., Janoutová, R., Delavois, A., Meynier, J., Medjdoub, G., Yang, P., van der Tol, C., Morton, D., Cook, B.D., & Gastellu-Etchegorry, J.-P., 2021b. Discrete anisotropic radiative transfer modelling of solar-induced chlorophyll fluorescence: Structural impacts in geometrically explicit vegetation canopies. *Remote Sensing of Environment, 263*, 112564

Martin, M.E., Plourde, L.C., Ollinger, S.V., Smith, M.L., & McNeil, B.E., 2008. A generalizable method for remote sensing of canopy nitrogen across a wide range of forest ecosystems. *Remote Sensing of Environment, 112*, 3511-3519

Martínez-Usó, A., Pla, F., Sotoca, J.M., & García-Sevilla, P., 2007. Clustering-based hyperspectral band selection using information measures. *IEEE transactions on geoscience and remote sensing, 45*, 4158-4171

McConnell, I., Li, G., & Brudvig, G.W., 2010. Energy conversion in natural and artificial photosynthesis. *Chemistry & biology, 17*, 434-447

McGill, W., & Figueiredo, C., 1993. Total nitrogen. *Soil sampling and methods of analysis*, 201-211

Mead, D.J., 2013. *Sustainable management of Pinus radiata plantations*. Rome, Italy: Food and Agriculture Organization of the United Nations

Meroni, M., Busetto, L., Colombo, R., Guanter, L., Moreno, J., & Verhoef, W., 2010. Performance of Spectral Fitting Methods for vegetation fluorescence quantification. *Remote Sensing of Environment, 114*, 363-374

Meroni, M., Colombo, R., & Panigada, C., 2004. Inversion of a radiative transfer model with hyperspectral observations for LAI mapping in poplar plantations. *Remote Sensing of Environment, 92*, 195-206

Meroni, M., Rossini, M., Guanter, L., Alonso, L., Rascher, U., Colombo, R., & Moreno, J., 2009. Remote sensing of solar-induced chlorophyll fluorescence: Review of methods and applications. *Remote Sensing of Environment, 113*, 2037-2051

Merzlyak, M.N., Gitelson, A.A., Chivkunova, O.B., & Rakitin, V.Y., 1999. Non‐destructive optical detection of pigment changes during leaf senescence and fruit ripening. *Physiologia Plantarum, 106*, 135-141

Miraglio, T., Adeline, K., Huesca, M., Ustin, S., & Briottet, X. 2020. Monitoring LAI, Chlorophylls, and Carotenoids Content of a Woodland Savanna Using Hyperspectral Imagery and 3D Radiative Transfer Modeling. In, *Remote Sensing*

Mohammed, G.H., Colombo, R., Middleton, E.M., Rascher, U., van der Tol, C., Nedbal, L., Goulas, Y., Pérez-Priego, O., Damm, A., & Meroni, M., 2019. Remote sensing of solar-induced chlorophyll fluorescence (SIF) in vegetation: 50 years of progress. *Remote Sensing of Environment, 231*, 111177

Mu, X., & Chen, Y., 2021. The physiological response of photosynthesis to nitrogen deficiency. *Plant Physiology and Biochemistry, 158*, 76-82

Müller, P., Li, X.-P., & Niyogi, K.K., 2001. Non-Photochemical Quenching. A Response to Excess Light Energy. *Plant Physiology, 125*, 1558-1566

Mutanga, O., & Kumar, L., 2007. Estimating and mapping grass phosphorus concentration in an African savanna using hyperspectral image data. *International Journal of Remote Sensing, 28*, 4897-4911

Naing, A.H., & Kim, C.K., 2021. Abiotic stress‐induced anthocyanins in plants: Their role in tolerance to abiotic stresses. *Physiologia Plantarum, 172*, 1711-1723

Nambiar, E., & Fife, D., 1987a. Growth and nutrient retranslocation in needles of radiata pine in relation to nitrogen supply. *Annals of botany, 60*, 147-156

Nambiar, E.K.S., & Fife, D.N., 1987b. Growth and Nutrient Retranslocation in Needles of Radiata Pine in Relation to Nitrogen Supply. *Annals of Botany, 60*, 147-156

Navarro-Cerrillo, R.M., Trujillo, J., de la Orden, M.S., & Hernández-Clemente, R., 2014. Hyperspectral and multispectral satellite sensors for mapping chlorophyll content in a Mediterranean Pinus sylvestris L. plantation. *International Journal of Applied Earth Observation and Geoinformation, 26*, 88-96

Nex, F., Armenakis, C., Cramer, M., Cucci, D.A., Gerke, M., Honkavaara, E., Kukko, A., Persello, C., & Skaloud, J., 2022. UAV in the advent of the twenties: Where we stand and what is next. *ISPRS journal of photogrammetry and remote sensing, 184*, 215-242

North, P.R., 1996. Three-dimensional forest light interaction model using a Monte Carlo method. *IEEE Transactions on geoscience and remote sensing, 34*, 946-956

North, P.R., 2002. Three-dimensional forest light interaction model using a Monte Carlo method. *IEEE transactions on geoscience and remote sensing, 34*, 946-956

Oliver, M.A., & Webster, R., 1990. Kriging: a method of interpolation for geographical information systems. *International Journal of Geographical Information System, 4*, 313-332

Panigada, C., Rossini, M., Meroni, M., Cilia, C., Busetto, L., Amaducci, S., Boschetti, M., Cogliati, S., Picchi, V., Pinto, F., Marchesi, A., & Colombo, R., 2014. Fluorescence, PRI and canopy temperature for water stress detection in cereal crops. *International Journal of Applied Earth Observation and Geoinformation, 30*, 167-178

Peguero-Pina, J.J., Morales, F., Flexas, J., Gil-Pelegrín, E., & Moya, I., 2008. Photochemistry, remotely sensed physiological reflectance index and de-epoxidation state of the xanthophyll cycle in Quercus coccifera under intense drought. *Oecologia, 156*, 1-11

Penuelas, J., Baret, F., & Filella, I., 1995. Semi-empirical indices to assess carotenoids/chlorophyll a ratio from leaf spectral reflectance. *Photosynthetica, 31*, 221-230

Peñuelas, J., & Filella, I., 1998. Visible and near-infrared reflectance techniques for diagnosing plant physiological status. *Trends in plant science, 3*, 151-156

Peñuelas, J., Filella, I., Lloret, P., Munñoz, F., & Vilajeliu, M., 1995a. Reflectance assessment of mite effects on apple trees. *International Journal of Remote Sensing, 16*, 2727-2733

Peñuelas, J., Filella, I., Lloret, P., Muñoz, F., & Vilajeliu, M., 1995b. Reflectance assessment of mite effects on apple trees. *International Journal of Remote Sensing, 16*, 2727-2733

Peñuelas, J., Gamon, J.A., Fredeen, A.L., Merino, J., & Field, C.B., 1994. Reflectance indices associated with physiological changes in nitrogen- and water-limited sunflower leaves. *Remote Sensing of Environment, 48*, 135-146

Pereira, G.W., Valente, D.S.M., Queiroz, D.M.d., Coelho, A.L.d.F., Costa, M.M., & Grift, T., 2022. Smart-map: An open-source QGIS plugin for digital mapping using machine learning techniques and ordinary kriging. *Agronomy, 12*, 1350

Pérez-Priego, O., Zarco-Tejada, P.J., Miller, J.R., Sepulcre-Cantó, G., & Fereres, E., 2005. Detection of water stress in orchard trees with a high-resolution spectrometer through chlorophyll fluorescence in-filling of the O/sub 2/-A band. *IEEE Transactions on geoscience and remote sensing, 43*, 2860-2869

Pierrat, Z.A., Magney, T., Maguire, A., Brissette, L., Doughty, R., Bowling, D.R., Logan, B., Parazoo, N., Frankenberg, C., & Stutz, J., 2024. Seasonal timing of fluorescence and photosynthetic yields at needle and canopy scales in evergreen needleleaf forests. *Ecology, 105*, e4402

Pimstein, A., Karnieli, A., Bansal, S.K., & Bonfil, D.J., 2011. Exploring remotely sensed technologies for monitoring wheat potassium and phosphorus using field spectroscopy. *Field Crops Research, 121*, 125-135

Plascyk, J.A., & Gabriel, F.C., 1975. The Fraunhofer line discriminator MKII-an airborne instrument for precise and standardized ecological luminescence measurement. *IEEE Transactions on Instrumentation and measurement 24*, 306-313

Poblete, T., Camino, C., Beck, P.S.A., Hornero, A., Kattenborn, T., Saponari, M., Boscia, D., Navas-Cortes, J.A., & Zarco-Tejada, P.J., 2020. Detection of Xylella fastidiosa infection symptoms with airborne multispectral and thermal imagery: Assessing bandset reduction performance from hyperspectral analysis. *ISPRS journal of photogrammetry and remote sensing, 162*, 27-40

Poblete, T., Navas-Cortes, J.A., Hornero, A., Camino, C., Calderon, R., Hernandez-Clemente, R., Landa, B.B., & Zarco-Tejada, P.J., 2023. Detection of symptoms induced by vascular plant pathogens in tree crops using high-resolution satellite data: Modelling and assessment with airborne hyperspectral imagery. *Remote Sensing of Environment, 295*, 113698

Poblete, T., Watt, M.S., Buddenbaum, H., & Zarco-Tejada, P.J., 2025. Chlorophyll content estimation in radiata pine using hyperspectral imagery: A comparison between empirical models, scaling-up algorithms, and radiative transfer inversions. *Agricultural and Forest Meteorology, 362*, 110402

Porcar-Castell, A., Tyystjärvi, E., Atherton, J., Van der Tol, C., Flexas, J., Pfündel, E.E., Moreno, J., Frankenberg, C., & Berry, J.A., 2014. Linking chlorophyll a fluorescence to photosynthesis for remote sensing applications: mechanisms and challenges. *Journal of Experimental Botany, 65*, 4065-4095

Posch, S., Warren, C.R., Adams, M.A., & Guttenberger, H., 2008. Photoprotective carotenoids and antioxidants are more affected by canopy position than by nitrogen supply in 21-year-old Pinus radiata. *Functional Plant Biology, 35*, 470-482

Qi, J., Chehbouni, A., Huete, A.R., Kerr, Y.H., & Sorooshian, S., 1994. A modified soil adjusted vegetation index. *Remote Sensing of Environment, 48*, 119-126

Qiu, J., & Israel, D.W., 1992. Diurnal Starch Accumulation and Utilization in Phosphorus-Deficient Soybean Plants 1. *Plant Physiology, 98*, 316-323

Quan, X., He, B., Yebra, M., Yin, C., Liao, Z., Zhang, X., & Li, X., 2017. A radiative transfer model-based method for the estimation of grassland aboveground biomass. *International Journal of Applied Earth Observation and Geoinformation, 54*, 159-168

Ramoelo, A., Skidmore, A., Cho, M.A., Mathieu, R., Heitkönig, I., Dudeni-Tlhone, N., Schlerf, M., & Prins, H., 2013. Non-linear partial least square regression increases the

estimation accuracy of grass nitrogen and phosphorus using in situ hyperspectral and environmental data. *ISPRS journal of photogrammetry and remote sensing, 82*, 27-40

Rasmussen, C.E., 2004. Gaussian Processes in Machine Learning. In O. Bousquet, U. von Luxburg, & G. Rätsch (Eds.), *Advanced Lectures on Machine Learning: ML Summer Schools 2003, Canberra, Australia, February 2 - 14, 2003, Tübingen, Germany, August 4 - 16, 2003, Revised Lectures* (pp. 63-71). Berlin, Heidelberg: Springer Berlin Heidelberg

Rautiainen, M., Lukeš, P., Homolová, L., Hovi, A., Pisek, J., & Mõttus, M., 2018. Spectral properties of coniferous forests: A review of in situ and laboratory measurements. *Remote Sensing, 10*, 207

Raya-Sereno, M.D., Alonso-Ayuso, M., Pancorbo, J.L., Gabriel, J.L., Camino, C., Zarco-Tejada, P.J., & Quemada, M., 2022. Residual Effect and N Fertilizer Rate Detection by High-Resolution VNIR-SWIR Hyperspectral Imagery and Solar-Induced Chlorophyll Fluorescence in Wheat. *IEEE Transactions on geoscience and remote sensing, 60*, 1-17

Regaieg, O., Malenovský, Z., Siegmann, B., Buffat, J., Krämer, J., Lauret, N., & Le Dantec, V., 2025. DART-based temporal and spatial retrievals of solar-induced chlorophyll fluorescence quantum efficiency from in-situ and airborne crop observations. *Remote Sensing of Environment, 319*, 114636

Riano, D., Vaughan, P., Chuvieco, E., Zarco-Tejada, P.J., & Ustin, S.L., 2005. Estimation of fuel moisture content by inversion of radiative transfer models to simulate equivalent water thickness and dry matter content: analysis at leaf and canopy level. *IEEE transactions on geoscience and remote sensing, 43*, 819-826

Rivard, B., Feng, J., Gallie, A., & Sanchez-Azofeifa, A., 2008. Continuous wavelets for the improved use of spectral libraries and hyperspectral data. *Remote Sensing of Environment, 112*, 2850-2862

Rivera-Caicedo, J.P., Verrelst, J., Muñoz-Marí, J., Camps-Valls, G., & Moreno, J., 2017. Hyperspectral dimensionality reduction for biophysical variable statistical retrieval. *ISPRS journal of photogrammetry and remote sensing, 132*, 88-101

Rivera, J.P., Verrelst, J., Leonenko, G., & Moreno, J. 2013. Multiple Cost Functions and Regularization Options for Improved Retrieval of Leaf Chlorophyll Content and LAI through Inversion of the PROSAIL Model. In, *Remote Sensing* (pp. 3280-3304)

Rondeaux, G., Steven, M., & Baret, F., 1996. Optimization of soil-adjusted vegetation indices. *Remote Sensing of Environment, 55*, 95-107

Roujean, J.-L., & Breon, F.-M., 1995. Estimating PAR absorbed by vegetation from bidirectional reflectance measurements. *Remote Sensing of Environment, 51*, 375-384

Rouse, J.W., Haas, R.H., Schell, J.A., & Deering, D.W. 1974a. Monitoring vegetation systems in the Great Plains with ERTS. In, *Third Earth Resources Technology Satellite-1 Symposium* (pp. 309-317)

Rouse, J.W., Haas, R.H., Schell, J.A., & Deering, D.W., 1974b. Monitoring vegetation systems in the Great Plains with ERTS. *Third Earth Resources Technology Satellite-1 Symposium, 1*, 309-317

Rousseeuw, P.J., 1987. Silhouettes: A graphical aid to the interpretation and validation of cluster analysis. *Journal of Computational and Applied Mathematics, 20*, 53-65

Sachdev, S., Ansari, S.A., Ansari, M.I., Fujita, M., & Hasanuzzaman, M., 2021. Abiotic stress and reactive oxygen species: Generation, signaling, and defense mechanisms. *Antioxidants, 10*, 277

Savitzky, A., & Golay, M.J., 1964. Smoothing and differentiation of data by simplified least squares procedures. *Analytical chemistry, 36*, 1627-1639

Schlerf, M., & Atzberger, C., 2006. Inversion of a forest reflectance model to estimate structural canopy variables from hyperspectral remote sensing data. *Remote Sensing of Environment, 100*, 281-294

Schreiber, U., 2004. Pulse-amplitude-modulation (PAM) fluorometry and saturation pulse method: an overview. *Chlorophyll a fluorescence: a signature of photosynthesis*, 279-319

Shrestha, S., Brueck, H., & Asch, F., 2012. Chlorophyll index, photochemical reflectance index and chlorophyll fluorescence measurements of rice leaves supplied with different N levels. *Journal of Photochemistry and Photobiology B: Biology, 113*, 7-13

Siedliska, A., Baranowski, P., Pastuszka-Woźniak, J., Zubik, M., & Krzyszczak, J., 2021a. Identification of plant leaf phosphorus content at different growth stages based on hyperspectral reflectance. *BMC Plant Biology, 21*, 1-17

Siedliska, A., Baranowski, P., Pastuszka-Woźniak, J., Zubik, M., & Krzyszczak, J., 2021b. Identification of plant leaf phosphorus content at different growth stages based on hyperspectral reflectance. *BMC Plant Biology, 21*, 28

Sims, N.C., Culvenor, D., Newnham, G., Coops, N.C., & Hopmans, P., 2013. Towards the Operational Use of Satellite Hyperspectral Image Data for Mapping Nutrient Status and Fertilizer Requirements in Australian Plantation Forests. *IEEE Journal of Selected Topics in Applied Earth Observations and Remote Sensing, 6*, 320-328

Smith, M.-L., Ollinger, S.V., Martin, M.E., Aber, J.D., Hallett, R.A., & Goodale, C.L., 2002. DIRECT ESTIMATION OF ABOVEGROUND FOREST PRODUCTIVITY THROUGH HYPERSPECTRAL REMOTE SENSING OF CANOPY NITROGEN. *Ecological Applications, 12*, 1286-1302

Smith, M.L., Martin, M.E., Plourde, L., & Ollinger, S.V., 2003. Analysis of hyperspectral data for estimation of temperate forest canopy nitrogen concentration: comparison between an airborne (AVIRIS) and a spaceborne (Hyperion) sensor. *IEEE Transactions on geoscience and remote sensing, 41*, 1332-1337

Song, L., Guanter, L., Guan, K., You, L., Huete, A., Ju, W., & Zhang, Y., 2018. Satellite sun-induced chlorophyll fluorescence detects early response of winter wheat to heat stress in the Indian Indo-Gangetic Plains. *Global change biology, 24*, 4023-4037

Strang, G., & Nguyen, T., 1996. *Wavelets and Filter Banks*. Wellesley-Cambridge Press

Su, H., Yang, H., Du, Q., & Sheng, Y., 2011. Semisupervised Band Clustering for Dimensionality Reduction of Hyperspectral Imagery. *IEEE Geoscience and Remote Sensing Letters, 8*, 1135-1139

Suárez, L., Zarco-Tejada, P., Berni, J., González-Dugo, V., & Fereres, E., 2009a. Modelling PRI for water stress detection using radiative transfer models. *Remote Sensing of Environment, 113*, 730-744

Suárez, L., Zarco-Tejada, P.J., Berni, J.A.J., González-Dugo, V., & Fereres, E., 2009b. Modelling PRI for water stress detection using radiative transfer models. *Remote Sensing of Environment, 113*, 730-744

Suárez, L., Zarco-Tejada, P.J., Sepulcre-Cantó, G., Pérez-Priego, O., Miller, J., Jiménez-Muñoz, J., & Sobrino, J.J.R.S.o.E., 2008. Assessing canopy PRI for water stress detection with diurnal airborne imagery*, 112*, 560-575

Suárez, L., Zhang, P., Sun, J., Wang, Y., Poblete, T., Hornero, A., & Zarco-Tejada, P.J., 2021. Assessing wine grape quality parameters using plant traits derived from physical model inversion of hyperspectral imagery. *Agricultural and Forest Meteorology, 306*, 108445

Subhash, N., Wenzel, O., & Lichtenthaler, H.K., 1999. Changes in blue-green and chlorophyll fluorescence emission and fluorescence ratios during senescence of tobacco plants. *Remote Sensing of Environment, 69*, 215-223

Sun, D., Xu, H., Weng, H., Zhou, W., Liang, Y., Dong, X., He, Y., & Cen, H., 2020. Optimal temporal–spatial fluorescence techniques for phenotyping nitrogen status in oilseed rape. *Journal of Experimental Botany, 71*, 6429-6443

Sun, W., & Du, Q., 2019. Hyperspectral Band Selection: A Review. *IEEE Geoscience and Remote Sensing Magazine, 7*, 118-139

Sun, Y., Frankenberg, C., Jung, M., Joiner, J., Guanter, L., Köhler, P., & Magney, T., 2018. Overview of Solar-Induced chlorophyll Fluorescence (SIF) from the Orbiting Carbon Observatory-2: Retrieval, cross-mission comparison, and global monitoring for GPP. *Remote Sensing of Environment, 209*, 808-823

Townsend, P.A., Foster, J.R., Chastain, R.A., & Currie, W.S., 2003. Application of imaging spectroscopy to mapping canopy nitrogen in the forests of the central Appalachian Mountains using Hyperion and AVIRIS. *IEEE Transactions on geoscience and remote sensing, 41*, 1347-1354

Turner, J., & Lambert, M.J., 1986. Nutrition and nutritional relationships of Pinus radiata. *Annual review of ecology and systematics*, 325-350

Turner, J., & Lambert, M.J., 2011. Analysis of nutrient depletion in a radiata pine plantation. *Forest Ecology and Management, 262*, 1327-1336

Turner, J., & Lambert, M.J., 2017. Analysis of foliage phosphorus requirements of radiata pine plantations. *Communications in Soil Science and Plant Analysis, 48*, 2218-2229

Ulrich, A., & Hills, P., 1967. Principles and practices of plant analysis. *Soil Testing and Plant Analysis. Plant Analysis, Part, 11*, 11-24

Ustin, S.L., Gitelson, A.A., Jacquemoud, S., Schaepman, M., Asner, G.P., Gamon, J.A., & Zarco-Tejada, P., 2009. Retrieval of foliar information about plant pigment systems from high resolution spectroscopy. *Remote Sensing of Environment, 113*, S67-S77

Van der Tol, C., Verhoef, W., Timmermans, J., Verhoef, A., & Su, Z., 2009. An integrated model of soil-canopy spectral radiances, photosynthesis, fluorescence, temperature and energy balance. *Biogeosciences, 6*, 3109-3129

Verhoef, W., & Bach, H., 2007. Coupled soil–leaf-canopy and atmosphere radiative transfer modeling to simulate hyperspectral multi-angular surface reflectance and TOA radiance data. *Remote Sensing of Environment, 109*, 166-182

Verhoef, W., Jia, L., Xiao, Q., & Su, Z., 2007. Unified Optical-Thermal Four-Stream Radiative Transfer Theory for Homogeneous Vegetation Canopies. *IEEE transactions on geoscience and remote sensing, 45*, 1808-1822

Verrelst, J., Rivera-Caicedo, J.P., Reyes-Muñoz, P., Morata, M., Amin, E., Tagliabue, G., Panigada, C., Hank, T., & Berger, K., 2021. Mapping landscape canopy nitrogen content from space using PRISMA data. *ISPRS journal of photogrammetry and remote sensing, 178*, 382-395

Verrelst, J., van der Tol, C., Magnani, F., Sabater, N., Rivera, J.P., Mohammed, G., & Moreno, J., 2016. Evaluating the predictive power of sun-induced chlorophyll fluorescence to estimate net photosynthesis of vegetation canopies: A SCOPE modeling study. *Remote Sensing of Environment, 176*, 139-151

Vilfan, N., van der Tol, C., Muller, O., Rascher, U., & Verhoef, W., 2016. Fluspect-B: A model for leaf fluorescence, reflectance and transmittance spectra. *Remote Sensing of Environment, 186*, 596-615

Vilfan, N., Van der Tol, C., Yang, P., Wyber, R., Malenovský, Z., Robinson, S.A., & Verhoef, W., 2018. Extending Fluspect to simulate xanthophyll driven leaf reflectance dynamics. *Remote Sensing of Environment, 211*, 345-356

Vogelmann, J.E., Rock, B.N., & Moss, D.M., 1993. Red edge spectral measurements from sugar maple leaves. *International Journal of Remote Sensing, 14*, 1563-1575

Wang, N., Yang, P., Clevers, J.G.P.W., Wieneke, S., & Kooistra, L., 2023a. Decoupling physiological and non-physiological responses of sugar beet to water stress from sun-induced chlorophyll fluorescence. *Remote Sensing of Environment, 286*, 113445

Wang, Q., Li, Q., & Li, X., 2019. Hyperspectral Band Selection via Adaptive Subspace Partition Strategy. *IEEE Journal of Selected Topics in Applied Earth Observations and Remote Sensing, 12*, 4940-4950

Wang, Q., Li, Q., & Li, X., 2020. A fast neighborhood grouping method for hyperspectral band selection. *IEEE transactions on geoscience and remote sensing, 59*, 5028-5039

Wang, Q., Li, Q., & Li, X., 2021. A Fast Neighborhood Grouping Method for Hyperspectral Band Selection. *IEEE Transactions on geoscience and remote sensing, 59*, 5028-5039

Wang, Q., Zhang, F., & Li, X., 2018a. Optimal clustering framework for hyperspectral band selection. *IEEE transactions on geoscience and remote sensing, 56*, 5910-5922

Wang, Y., Suarez, L., Hornero, A., Poblete, T., Ryu, D., Gonzalez-Dugo, V., & Zarco-Tejada, P.J., 2025. Assessing plant traits derived from Sentinel-2 to characterize leaf nitrogen variability in almond orchards: modeling and validation with airborne hyperspectral imagery. *Precision Agriculture, 26*, 13

Wang, Y., Suarez, L., Poblete, T., Gonzalez-Dugo, V., Ryu, D., & Zarco-Tejada, P., 2022. Evaluating the role of solar-induced fluorescence (SIF) and plant physiological traits for leaf nitrogen assessment in almond using airborne hyperspectral imagery. *Remote Sensing of Environment, 279*, 113141

Wang, Z., Féret, J.-B., Liu, N., Sun, Z., Yang, L., Geng, S., Zhang, H., Chlus, A., Kruger, E.L., & Townsend, P.A., 2023b. Generality of leaf spectroscopic models for predicting key foliar functional traits across continents: A comparison between physically-and empirically-based approaches. *Remote Sensing of Environment, 293*, 113614

Wang, Z., Skidmore, A.K., Darvishzadeh, R., & Wang, T., 2018b. Mapping forest canopy nitrogen content by inversion of coupled leaf-canopy radiative transfer models from airborne hyperspectral imagery. *Agricultural and Forest Meteorology, 253-254*, 247-260

Wang, Z., Skidmore, A.K., Darvishzadeh, R., & Wang, T., 2018c. Mapping forest canopy nitrogen content by inversion of coupled leaf-canopy radiative transfer models from airborne hyperspectral imagery. *Agricultural and Forest Meteorology, 253*, 247-260

Watt, M.S., Buddenbaum, H., Leonardo, E.M.C., Estarija, H.J., Bown, H.E., Gomez-Gallego, M., Hartley, R.J., Pearse, G.D., Massam, P., & Wright, L., 2020. Monitoring biochemical limitations to photosynthesis in N and P-limited radiata pine using plant functional traits quantified from hyperspectral imagery. *Remote Sensing of Environment, 248*, 112003

Watt, M.S., Coker, G., Clinton, P.W., Davis, M.R., Parfitt, R., Simcock, R., Garrett, L., Payn, T., Richardson, B., & Dunningham, A., 2005a. Defining sustainability of plantation forests through identification of site quality indicators influencing productivity—a national view for New Zealand. *Forest Ecology Management, 216*, 51-63

Watt, M.S., Coker, G., Clinton, P.W., Davis, M.R., Parfitt, R., Simcock, R., Garrett, L., Payn, T., Richardson, B., & Dunningham, A., 2005b. Defining sustainability of plantation forests through identification of site quality indicators influencing productivity—A national view for New Zealand. *Forest Ecology and Management, 216*, 51-63

Watt, M.S., Pearse, G.D., Dash, J.P., Melia, N., & Leonardo, E.M.C., 2019. Application of remote sensing technologies to identify impacts of nutritional deficiencies on forests. *ISPRS journal of photogrammetry and remote sensing, 149*, 226-241

Wei, S., Yin, T., Yuan, B., Lim, K.H., Liew, S.C., & Whittle, A.J., 2025. Optimizing UAV Hyperspectral Imaging for Urban Tree Chlorophyll and Leaf Area Index Retrieval.

IEEE Journal of Selected Topics in Applied Earth Observations and Remote Sensing, 18, 839-852

Wessman, C.A., Aber, J.D., Peterson, D.L., & Melillo, J.M., 1988. Remote sensing of canopy chemistry and nitrogen cycling in temperate forest ecosystems. *Nature, 335*, 154-156

Will, G., & Hodgkiss, P., 1977. Influence of nitrogen and phosphorus stresses on the growth and form of radiata pine. *NZJ For. Sci, 7*, 307-320

Williams, C.K., & Rasmussen, C.E., 2006. *Gaussian processes for machine learning*. MIT press Cambridge, MA

Wold, H., 1966. Estimation of principal components and related models by iterative least squares. *Multivariate Analysis*, 391-420

Wold, S., Johansson, E., & Cocchi, M., 1993. PLS: partial least squares projections to latent structures. *3D QSAR in Drug Design: Theory, Methods and Applications.* (pp. 523-550): Kluwer ESCOM Science Publisher

Wu, C., Niu, Z., Tang, Q., & Huang, W., 2008. Estimating chlorophyll content from hyperspectral vegetation indices: Modeling and validation. *Agricultural and Forest Meteorology, 148*, 1230-1241

Xiao, B., Li, S., Dou, S., He, H., Fu, B., Zhang, T., Sun, W., Yang, Y., Xiong, Y., Shi, J., & Zhang, J., 2024. Comparison of leaf chlorophyll content retrieval performance of citrus using FOD and CWT methods with field-based full-spectrum hyperspectral reflectance data. *Computers and Electronics in Agriculture, 217*, 108559

Xu, S., Atherton, J., Riikonen, A., Zhang, C., Oivukkamäki, J., MacArthur, A., Honkavaara, E., Hakala, T., Koivumäki, N., Liu, Z., & Porcar-Castell, A., 2021. Structural and photosynthetic dynamics mediate the response of SIF to water stress in a potato crop. *Remote Sensing of Environment, 263*, 112555

Yang, G., Zhao, C., Liu, Q., Huang, W., & Wang, J., 2010. Inversion of a radiative transfer model for estimating forest LAI from multisource and multiangular optical remote sensing data. *IEEE transactions on geoscience and remote sensing, 49*, 988-1000

Yang, P., & van der Tol, C., 2018. Linking canopy scattering of far-red sun-induced chlorophyll fluorescence with reflectance. *Remote Sensing of Environment, 209*, 456-467

Ye, X., Abe, S., & Zhang, S., 2020. Estimation and mapping of nitrogen content in apple trees at leaf and canopy levels using hyperspectral imaging. *Precision Agriculture, 21*, 198-225

Zarco-Tejada, P., Camino, C., Beck, P., Calderon, R., Hornero, A., Hernández-Clemente, R., Kattenborn, T., Montes-Borrego, M., Susca, L., & Morelli, M.J.N.P., 2018a. Previsual symptoms of Xylella fastidiosa infection revealed in spectral plant-trait alterations*, 4*, 432-439

Zarco-Tejada, P.J., Berjón, A., Lopez-Lozano, R., Miller, J.R., Martín, P., Cachorro, V., González, M., & De Frutos, A., 2005. Assessing vineyard condition with hyperspectral indices: Leaf and canopy reflectance simulation in a row-structured discontinuous canopy. *Remote Sensing of Environment, 99*, 271-287

Zarco-Tejada, P.J., Berni, J.A.J., Suárez, L., Sepulcre-Cantó, G., Morales, F., & Miller, J.R., 2009. Imaging chlorophyll fluorescence with an airborne narrow-band multispectral camera for vegetation stress detection. *Remote Sensing of Environment, 113*, 1262-1275

Zarco-Tejada, P.J., Camino, C., Beck, P., Calderon, R., Hornero, A., Hernández-Clemente, R., Kattenborn, T., Montes-Borrego, M., Susca, L., & Morelli, M., 2018b. Previsual symptoms of Xylella fastidiosa infection revealed in spectral plant-trait alterations. *Nature Plants, 4*, 432-439

Zarco-Tejada, P.J., Camino, C., Beck, P.S.A., Calderon, R., Hornero, A., Hernández-Clemente, R., Kattenborn, T., Montes-Borrego, M., Susca, L., Morelli, M., Gonzalez-Dugo, V., North, P.R.J., Landa, B.B., Boscia, D., Saponari, M., & Navas-Cortes, J.A., 2018c.

Previsual symptoms of Xylella fastidiosa infection revealed in spectral plant-trait alterations. *Nature Plants, 4*, 432-439

Zarco-Tejada, P.J., Catalina, A., González, M., & Martín, P., 2013a. Relationships between net photosynthesis and steady-state chlorophyll fluorescence retrieved from airborne hyperspectral imagery. *Remote Sensing of Environment, 136*, 247-258

Zarco-Tejada, P.J., Catalina, A., González, M.R., & Martín, P., 2013b. Relationships between net photosynthesis and steady-state chlorophyll fluorescence retrieved from airborne hyperspectral imagery. *Remote Sensing of Environment, 136*, 247-258

Zarco-Tejada, P.J., González-Dugo, V., & Berni, J.A.J., 2012. Fluorescence, temperature and narrow-band indices acquired from a UAV platform for water stress detection using a micro-hyperspectral imager and a thermal camera. *Remote Sensing of Environment, 117*, 322-337

Zarco-Tejada, P.J., González-Dugo, V., Williams, L.E., Suarez, L., Berni, J.A., Goldhamer, D., & Fereres, E., 2013c. A PRI-based water stress index combining structural and chlorophyll effects: Assessment using diurnal narrow-band airborne imagery and the CWSI thermal index. *Remote Sensing of Environment, 138*, 38-50

Zarco-Tejada, P.J., González-Dugo, V., Williams, L.E., Suárez, L., Berni, J.A.J., Goldhamer, D., & Fereres, E., 2013d. A PRI-based water stress index combining structural and chlorophyll effects: Assessment using diurnal narrow-band airborne imagery and the CWSI thermal index. *Remote Sensing of Environment, 138*, 38-50

Zarco-Tejada, P.J., Guillén-Climent, M.L., Hernández-Clemente, R., Catalina, A., González, M., & Martín, P., 2013e. Estimating leaf carotenoid content in vineyards using high resolution hyperspectral imagery acquired from an unmanned aerial vehicle (UAV). *Agricultural and Forest Meteorology, 171*, 281-294

Zarco-Tejada, P.J., Miller, J.R., Harron, J., Hu, B., Noland, T.L., Goel, N., Mohammed, G.H., & Sampson, P., 2004. Needle chlorophyll content estimation through model inversion using hyperspectral data from boreal conifer forest canopies. *Remote Sensing of Environment, 89*, 189-199

Zarco-Tejada, P.J., Miller, J.R., Mohammed, G.H., & Noland, T.L., 2000. Chlorophyll fluorescence effects on vegetation apparent reflectance: I. Leaf-level measurements and model simulation. *Remote Sensing of Environment, 74*, 582-595

Zarco-Tejada, P.J., Miller, J.R., Noland, T.L., Mohammed, G.H., & Sampson, P.H., 2001. Scaling-up and model inversion methods with narrowband optical indices for chlorophyll content estimation in closed forest canopies with hyperspectral data. *IEEE Transactions on geoscience and remote sensing, 39*, 1491-1507

Zarco-Tejada, P.J., Miller, J.R., Noland, T.L., Mohammed, G.H., & Sampson, P.H., 2002. Scaling-up and model inversion methods with narrowband optical indices for chlorophyll content estimation in closed forest canopies with hyperspectral data. *IEEE transactions on geoscience and remote sensing, 39*, 1491-1507

Zarco-Tejada, P.J., Poblete, T., Camino, C., Gonzalez-Dugo, V., Calderon, R., Hornero, A., Hernandez-Clemente, R., Román-Écija, M., Velasco-Amo, M.P., & Landa, B.B., 2021a. Divergent abiotic spectral pathways unravel pathogen stress signals across species. *Nature Communications, 12*, 6088

Zarco-Tejada, P.J., Poblete, T., Camino, C., González-Dugo, V., Calderon, R., Hornero, A., Hernández-Clemente, R., Román-Écija, M., Velasco-Amo, M.P., & Landa, B.B., 2021b. Divergent abiotic spectral pathways unravel pathogen stress signals across species. *Nature Communications, 12*, 6088

Zarco-Tejada, P.J., Suárez, L., & Gonzalez-Dugo, V., 2013f. Spatial resolution effects on chlorophyll fluorescence retrieval in a heterogeneous canopy using hyperspectral

imagery and radiative transfer simulation. *IEEE Geoscience and Remote Sensing Letters, 10*, 937-941

Zhang, Y., Guanter, L., Berry, J.A., Joiner, J., van der Tol, C., Huete, A., Gitelson, A., Voigt, M., & Köhler, P., 2014. Estimation of vegetation photosynthetic capacity from space-based measurements of chlorophyll fluorescence for terrestrial biosphere models. *Global change biology, 20*, 3727-3742

Zhou, J., Wang, B., Fan, J., Ma, Y., Wang, Y., & Zhang, Z., 2022. A systematic study of estimating potato N concentrations using UAV-based hyper-and multi-spectral imagery. *Agronomy, 12*, 2533

Zhu, X., Skidmore, A.K., Darvishzadeh, R., & Wang, T., 2019. Estimation of forest leaf water content through inversion of a radiative transfer model from LiDAR and hyperspectral data. *International Journal of Applied Earth Observation and Geoinformation, 74*, 120-129

Zurita-Milla, R., Laurent, V.C.E., & van Gijsel, J.A.E., 2015. Visualizing the ill-posedness of the inversion of a canopy radiative transfer model: A case study for Sentinel-2. *International Journal of Applied Earth Observation and Geoinformation, 43*, 7-18

Zuromski, L.M., Bowling, D.R., Köhler, P., Frankenberg, C., Goulden, M.L., Blanken, P.D., & Lin, J.C., 2018. Solar-induced fluorescence detects interannual variation in gross primary production of coniferous forests in the Western United States. *Geophysical Research Letters, 45*, 7184-7193

Appendix for Chapter 3

Table A3.1 Results of post-hoc pairwise comparisons using Tukey's honestly significant difference procedure for needle N measurements (g/kg) at the plot level for four datasets. *n* is the sample size. Statistically significant results are highlighted in red. n.s.: not significant. NA: Not applicable if no plots in that treatment were sampled.

	2021-Feb (*n* = 19)		2021-Oct (*n* = 34)		2023-Jan (*n* = 34)		2023-Oct (*n* = 34)	
Comparison	Mean difference	*p*-value	Mean difference	*p*-value	Mean difference	*p*-value	Mean difference	*p*-value
A vs. B	NA	NA	1.80	< 0.05	0.48	n.s.	1.18	n.s.
A vs. C	NA	NA	1.13	n.s.	1.28	n.s.	2.00	n.s.
A vs. D	1.36	n.s.	0.88	n.s.	2.10	n.s.	2.10	n.s.
A vs. E	0.42	n.s.	-0.75	n.s.	-0.07	n.s.	-1.16	n.s.
A vs. F	-1.36	n.s.	-1.40	< 0.05	-0.23	n.s.	-0.47	n.s.
A vs. H	0.78	n.s.	0.20	n.s.	1.51	n.s.	-0.18	n.s.
A vs. G	0.37	n.s.	0.50	n.s.	0.95	n.s.	-0.41	n.s.
A vs. I	1.02	n.s.	1.40	n.s.	2.58	n.s.	0.47	n.s.
B vs. C	NA	NA	-0.67	n.s.	0.80	n.s.	0.82	n.s.
B vs. D	NA	NA	-0.92	n.s.	1.63	n.s.	0.92	n.s.
B vs. E	NA	NA	-2.55	< 0.05	-0.55	n.s.	-2.34	n.s.
B vs. F	NA	NA	-3.20	< 0.05	-0.70	n.s.	-1.65	n.s.
B vs. H	NA	NA	-1.60	< 0.05	1.03	n.s.	-1.36	n.s.
B vs. G	NA	NA	-1.30	n.s.	0.48	n.s.	-1.60	n.s.
B vs. I	NA	NA	-0.40	n.s.	2.10	n.s.	-0.72	n.s.
C vs. D	NA	NA	-0.25	n.s.	0.83	n.s.	0.10	n.s.
C vs. E	NA	NA	-1.88	< 0.05	-1.35	n.s.	-3.16	< 0.05
C vs. F	NA	NA	-2.53	< 0.05	-1.50	n.s.	-2.47	n.s.
C vs. H	NA	NA	-0.93	n.s.	0.23	n.s.	-2.18	n.s.
C vs. G	NA	NA	-0.63	n.s.	-0.32	n.s.	-2.42	n.s.

	2021-Feb (n = 19)		2021-Oct (n = 34)		2023-Jan (n = 34)		2023-Oct (n = 34)	
Comparison	Mean difference	p-value	Mean difference	p-value	Mean difference	p-value	Mean difference	p-value
C vs. I	NA	NA	0.28	n.s.	1.30	n.s.	-1.54	n.s.
D vs. E	-0.93	n.s.	-1.63	< 0.05	-2.18	n.s.	-3.26	< 0.05
D vs. F	-2.71	< 0.05	-2.28	< 0.05	-2.33	n.s.	-2.57	n.s.
D vs. H	-0.58	n.s.	-0.68	n.s.	-0.59	n.s.	-2.28	n.s.
D vs. G	-0.98	n.s.	-0.38	n.s.	-1.15	n.s.	-2.52	n.s.
D vs. I	-0.34	n.s.	0.53	n.s.	0.48	n.s.	-1.63	n.s.
E vs. F	-1.78	n.s.	-0.65	n.s.	-0.15	n.s.	0.69	n.s.
E vs. H	0.36	n.s.	0.95	n.s.	1.58	n.s.	0.98	n.s.
E vs. G	-0.05	n.s.	1.25	n.s.	1.03	n.s.	0.74	n.s.
E vs. I	0.59	n.s.	2.15	< 0.05	2.65	n.s.	1.62	n.s.
F vs. H	2.14	< 0.05	1.60	< 0.05	1.73	n.s.	0.29	n.s.
F vs. G	1.73	n.s.	1.90	< 0.05	1.18	n.s.	0.05	n.s.
F vs. I	2.37	< 0.05	2.80	< 0.05	2.80	< 0.05	0.93	n.s.
H vs. G	-0.41	n.s.	0.30	n.s.	-0.56	n.s.	-0.24	n.s.
H vs. I	0.24	n.s.	1.20	n.s.	1.07	n.s.	0.64	n.s.
G vs. I	0.64	n.s.	0.90	n.s.	1.63	n.s.	0.88	n.s.

Table A3.2 Results of post-hoc pairwise comparisons using Tukey's honestly significant difference procedure for needle P measurements (g/kg) at the plot level for four datasets. *n* is the sample size. Statistically significant results are highlighted in red. n.s.: not significant. NA: Not applicable if no plots in that treatment were sampled.

	2021-Feb (*n* = 19)		**2021-Oct** (*n* = 34)		**2023-Jan** (*n* = 34)		**2023-Oct** (*n* = 34)	
Comparison	Mean difference	*p*-value	Mean difference	*p*-value	Mean difference	*p*-value	Mean difference	*p*-value
A vs. B	NA	NA	-0.31	< 0.05	-0.15	n.s.	-0.45	< 0.05
A vs. C	NA	NA	-0.41	< 0.05	-0.25	n.s.	-0.39	n.s.
A vs. D	-0.31	n.s.	-0.36	< 0.05	-0.23	n.s.	-0.40	n.s.
A vs. E	-0.55	< 0.05	-0.60	< 0.05	-0.74	< 0.05	-0.90	< 0.05
A vs. F	-0.51	< 0.05	-0.58	< 0.05	-0.81	< 0.05	-0.86	< 0.05
A vs. H	-0.48	< 0.05	-0.75	< 0.05	-0.60	< 0.05	-0.81	< 0.05
A vs. G	-0.09	n.s.	-0.07	n.s.	0.05	n.s.	-0.21	n.s.
A vs. I	-0.73	< 0.05	-0.64	< 0.05	-0.46	n.s.	-0.80	< 0.05
B vs. C	NA	NA	-0.10	n.s.	-0.10	n.s.	0.06	n.s.
B vs. D	NA	NA	-0.04	n.s.	-0.08	n.s.	0.05	n.s.
B vs. E	NA	NA	-0.28	< 0.05	-0.59	< 0.05	-0.45	< 0.05
B vs. F	NA	NA	-0.27	< 0.05	-0.66	< 0.05	-0.41	n.s.
B vs. H	NA	NA	-0.44	< 0.05	-0.45	n.s.	-0.36	n.s.
B vs. G	NA	NA	0.24	< 0.05	0.20	n.s.	0.24	n.s.
B vs. I	NA	NA	-0.33	< 0.05	-0.31	n.s.	-0.35	n.s.
C vs. D	NA	NA	0.05	n.s.	0.02	n.s.	-0.01	n.s.
C vs. E	NA	NA	-0.19	n.s.	-0.49	n.s.	-0.51	< 0.05
C vs. F	NA	NA	-0.17	n.s.	-0.57	< 0.05	-0.47	< 0.05
C vs. H	NA	NA	-0.34	< 0.05	-0.36	n.s.	-0.42	n.s.
C vs. G	NA	NA	0.34	< 0.05	0.30	n.s.	0.18	n.s.
C vs. I	NA	NA	-0.23	< 0.05	-0.22	n.s.	-0.41	n.s.
D vs. E	-0.23	n.s.	-0.24	< 0.05	-0.51	< 0.05	-0.50	< 0.05
D vs. F	-0.19	n.s.	-0.23	< 0.05	-0.58	< 0.05	-0.46	< 0.05

	2021-Feb (n = 19)		**2021-Oct** (n = 34)		**2023-Jan** (n = 34)		**2023-Oct** (n = 34)	
Comparison	Mean difference	p-value	Mean difference	p-value	Mean difference	p-value	Mean difference	p-value
D vs. H	-0.17	n.s.	-0.40	< 0.05	-0.37	n.s.	-0.40	n.s.
D vs. G	0.23	n.s.	0.29	< 0.05	0.28	n.s.	0.19	n.s.
D vs. I	-0.42	< 0.05	-0.28	< 0.05	-0.23	n.s.	-0.40	n.s.
E vs. F	0.04	n.s.	0.01	n.s.	-0.07	n.s.	0.03	n.s.
E vs. H	0.07	n.s.	-0.16	n.s.	0.13	n.s.	0.09	n.s.
E vs. G	0.46	< 0.05	0.53	< 0.05	0.79	< 0.05	0.69	< 0.05
E vs. I	-0.19	n.s.	-0.04	n.s.	0.27	n.s.	0.10	n.s.
F vs. H	0.03	n.s.	-0.17	n.s.	0.21	n.s.	0.06	n.s.
F vs. G	0.42	< 0.05	0.51	< 0.05	0.86	< 0.05	0.65	< 0.05
F vs. I	-0.22	n.s.	-0.05	n.s.	0.35	n.s.	0.06	n.s.
H vs. G	0.40	< 0.05	0.68	< 0.05	0.65	< 0.05	0.60	< 0.05
H vs. I	-0.25	n.s.	0.11	n.s.	0.14	n.s.	0.00	n.s.
G vs. I	-0.65	< 0.05	-0.57	< 0.05	-0.51	n.s.	-0.59	< 0.05

Appendix for Chapter 4

Table A4.1 Equations of narrow-band hyperspectral indices (NBHIs). R_λ represents the reflectance at λ nm wavelength.

Index	Equation	Reference
Structural indices		
NDVI	$(R_{800} - R_{670})/(R_{800} + R_{670})$	Rouse *et al.* (1974b)
EVI	$2.5(R_{800} - R_{670})/(R_{800} + 6R_{670} - 7.5R_{400} + 1)$	Liu and Huete (1995)
RDVI	$(R_{800} - R_{670})/\sqrt{(R_{800} + R_{670})}$	Roujean and Breon (1995)
OSAVI	$(1 + 0.16) \times (R_{800} - R_{670})/((R_{800} + R_{670} + 0.16)$	Rondeaux *et al.* (1996)
MSAVI	$[2R_{800} + 1 - \sqrt{(2R_{800} + 1)^2 - 8(R_{800} - R_{670})}]/2$	Qi *et al.* (1994)
TVI	$0.5[120(R_{750} - R_{550}) - 2(R_{670} - R_{550})]$	Broge and Leblanc (2001)
$MTVI_1$	$1.2[1.2(R_{800} - R_{550}) - 2.5(R_{670} - R_{550})]$	Haboudane *et al.* (2004a)
$MTVI_2$	$\frac{1.5[1.2(R_{800} - R_{550}) - 2.5(R_{670} - R_{550})]}{\sqrt{(2R_{800} + 1)^2 - (6R_{800} - 5\sqrt{R_{670}}) - 0.5}}$	Haboudane *et al.* (2004a)
MCARI	$[(R_{700} - R_{670}) - 0.2(R_{700} - R_{550})] \times (R_{700}/R_{670})$	Daughtry *et al.* (2000)
$MCARI_1$	$1.2[2.5(R_{800} - R_{670}) - 1.3(R_{800} - R_{550})]$	Haboudane *et al.* (2004a)
SR	R_{800}/R_{670}	Jordan (1969)
MSR	$[R_{800}/R_{670} - 1]/[(R_{800}/R_{670})^{0.5} + 1]$	Chen (1996)
Chlorophyll *a* + *b* indices		
TCARI	$3[(R_{700} - R_{670}) - 0.2(R_{700} - R_{550}) \times (R_{700}/R_{670})]$	Haboudane *et al.* (2002)
TCARI/ OSAVI	$\frac{3[(R_{700} - R_{670}) - 0.2(R_{700} - R_{550}) \times (R_{700}/R_{670})]}{(1+0.16)(R_{800} - R_{670})/(R_{800} + R_{670} + 0.16)}$	Haboudane *et al.* (2002)
CTR_1	R_{695}/R_{420}	Carter (1994)
CAR	R_{515}/R_{570}	Hernández-Clemente *et al.* (2012)
SRPI	R_{430}/R_{680}	Peñuelas *et al.* (1995b)
$PSSR_a$	R_{800}/R_{675}	Blackburn (1998)
$PSSR_b$	R_{800}/R_{635}	Blackburn (1998)
$PSSR_c$	R_{800}/R_{470}	Blackburn (1998)
$PSND_c$	$(R_{800} - R_{470})/(R_{800} + R_{470})$	Blackburn (1998)
NPCI	$(R_{680} - R_{430})/(R_{680} + R_{430})$	Peñuelas *et al.* (1994)
$DC_{ab}D_{xc}$	$R_{672}/(R_{550} \times 3R_{708})$	Datt (1998)
$DNC_{ab}C_{xc}$	$R_{860}/(R_{550} \times R_{708})$	Datt (1998)
PSRI	$(R_{680} - R_{500})/R_{750}$	Merzlyak *et al.* (1999)
VOG_1	R_{740}/R_{720}	Vogelmann *et al.* (1993)
VOG_2	$(R_{734} - R_{747})/(R_{715} + R_{726})$	Vogelmann *et al.* (1993)
VOG_3	$(R_{734} - R_{747})/(R_{715} + R_{720})$	Vogelmann *et al.* (1993)
GM_1	R_{750}/R_{550}	Gitelson and Merzlyak (1997)

Index	Equation	Reference
GM_2	R_{750}/R_{700}	Gitelson and Merzlyak (1997)
CI	R_{750}/R_{710}	Zarco-Tejada *et al.* (2001)
SIPI	$(R_{800}-R_{445})/(R_{800}+R_{680})$	Penuelas *et al.* (1995)
CRI_{550}	$(1/R_{510})-(1/R_{550})$	Gitelson *et al.* (2002)
CRI_{700}	$(1/R_{510})-(1/R_{700})$	Gitelson *et al.* (2002)
CRI_{550m}	$(1/R_{515})-(1/R_{550})$	Gitelson *et al.* (2006)
CRI_{700m}	$(1/R_{515})-(1/R_{700})$	Gitelson *et al.* (2006)
$RNIR{\cdot}CRI_{550}$	$(1/R_{510})-(1/R_{550})\times R_{770}$	Gitelson *et al.* (2006)
$RNIR{\cdot}CRI_{700}$	$(1/R_{510})-(1/R_{700})\times R_{770}$	Gitelson *et al.* (2006)
PRI indices		
PRI	$(R_{570}-R_{531})/(R_{570}+R_{531})$	Gamon *et al.* (1992b)
PRI_{515}	$(R_{515}-R_{531})/(R_{515}+R_{531})$	Hernández-Clemente *et al.* (2011)
PRI_{m1}	$(R_{512}-R_{531})/(R_{512}+R_{531})$	Hernández-Clemente *et al.* (2011)
PRI_{m2}	$(R_{600}-R_{531})/(R_{600}+R_{531})$	Gamon *et al.* (1992b)
PRI_{m3}	$(R_{670}-R_{531})/(R_{670}+R_{531})$	Gamon *et al.* (1992b)
PRI_{m4}	$(R_{570}-R_{531}-R_{670})/(R_{570}+R_{531}+R_{670})$	Hernández-Clemente *et al.* (2011)
PRI_n	$PRI_{570}/[RDVI\times(R_{700}/R_{670})]$	Zarco-Tejada *et al.* (2013d)
$PRI{\cdot}CI$	$[(R_{570}-R_{530})/(R_{570}+R_{530})](R_{760}/R_{700}-1)$	Garrity *et al.* (2011)
Blue indices		
NPQI	$(R_{415}-R_{435})/(R_{415}+R_{435})$	Peñuelas *et al.* (1995b)
B	R_{450}/R_{490}	Calderón *et al.* (2013)
BF_1	R_{400}/R_{410}	Zarco-Tejada *et al.* (2018a)
BF_2	R_{400}/R_{420}	Zarco-Tejada *et al.* (2018a)
BF_3	R_{400}/R_{430}	Zarco-Tejada *et al.* (2018a)
BF_4	R_{400}/R_{440}	Zarco-Tejada *et al.* (2018a)
BF_5	R_{400}/R_{450}	Zarco-Tejada *et al.* (2018a)
BRI_1	R_{400}/R_{690}	Zarco-Tejada *et al.* (2012)
BRI_2	R_{450}/R_{690}	Zarco-Tejada *et al.* (2012)
RGB indices		
R	R_{700}/R_{670}	Gitelson *et al.* (2000)
G	R_{570}/R_{670}	Calderón *et al.* (2013)
BGI_1	R_{400}/R_{550}	Zarco-Tejada *et al.* (2005)
BGI_2	R_{450}/R_{550}	Zarco-Tejada *et al.* (2005)
RGI	R_{690}/R_{550}	Zarco-Tejada *et al.* (2005)
RARS	R_{746}/R_{513}	Chappelle *et al.* (1992)
LIC_1	$(R_{800}-R_{680})/(R_{800}+R_{680})$	Lichtenthaler (1996)
LIC_2	R_{440}/R_{690}	Lichtenthaler (1996)
LIC_3	R_{440}/R_{740}	Lichtenthaler (1996)
Chlorophyll fluorescence		

Index	Equation	Reference
CUR	$(R_{675} \times R_{690})/R_{683}^2$	Zarco-Tejada *et al.* (2000)
Plant disease index		
HI	$\frac{R_{534} - R_{698}}{R_{534} + R_{698}} - 0.5R_{704}$	Mahlein *et al.* (2013)

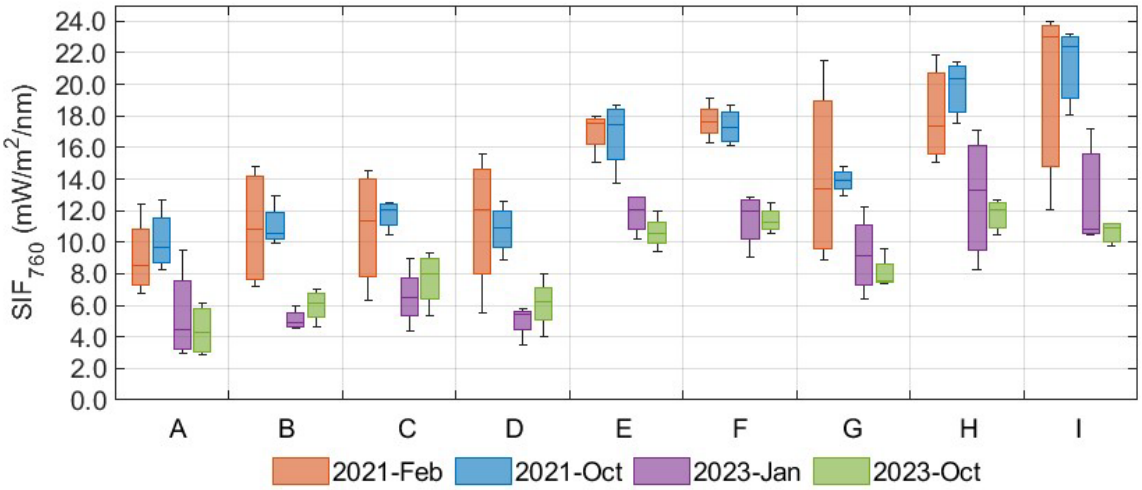

Fig. A4.1. Variability in calibrated SIF_{760} quantified through 3FLD method at the treatment level for four dates.

Table A4.2 Needle N and P estimation performance of GPR models with inputs including TCARI/OSAVI (T/O), PRI, NPQI and CUR at plot level and treatment level.

Dataset	N = *f*(T/O, PRI, NPQI, CUR)		P = *f*(T/O, PRI, NPQI, CUR)	
	R^2	NRMSE	R^2	NRMSE
Plot level				
2021-Feb (n = 19)	0.66***	0.17	0.15^{ns}	0.30
2021-Oct (n = 34)	0.54***	0.19	0.50***	0.19
2023-Jan (n = 34)	0.01^{ns}	0.26	0.34***	0.25
2023-Oct (n = 34)	0.10^{ns}	0.31	0.12^{ns}	0.30
Treatment level				
2021-Feb (n = 7)	0.86**	0.11	0.46^{ns}	0..25
2021-Oct (n = 9)	0.88***	0.12	0.87***	0.15
2023-Jan (n = 9)	0.01^{ns}	0.34	0.82***	0.18
2023-Oct (n = 9)	0.46*	0.24	0.55*	0.24

Appendix for Chapter 6

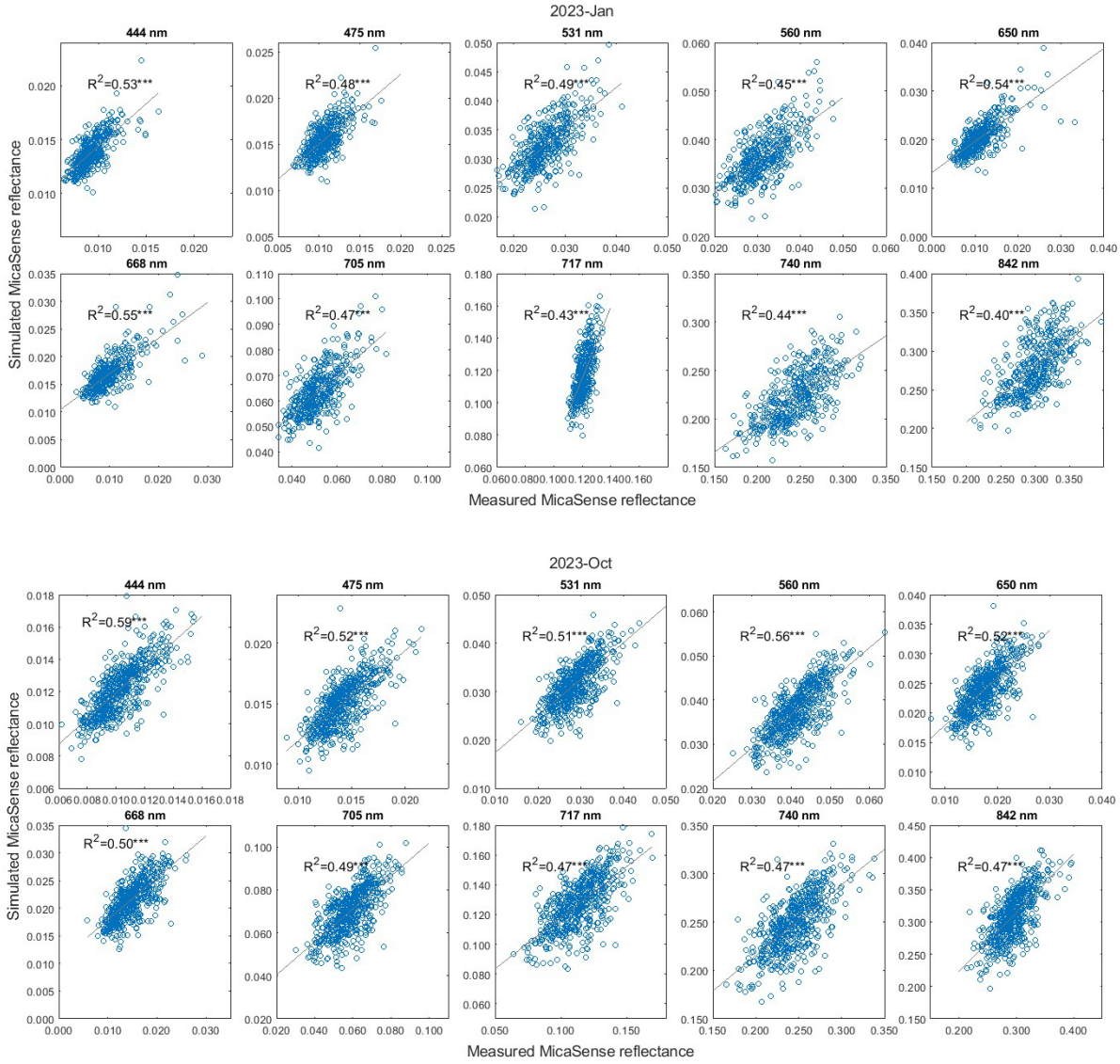

Fig. A6.1. Tree-level comparison of reflectance values between measured and simulated MicaSense data across 10 MicaSense spectral bands for the (top) 2023-Jan and (bottom) 2023-Oct datasets. ******p*-value < 0.001; *****p*-value < 0.01; ****p*-value < 0.05; n.s. = not significant.